NONLINEAR SEISMIC ANALYSIS OF ARCH DAMS

Thesis by

Michael J. Dowling

In Partial Fulfillment of the Requirements

for the Degree of

Doctor of Philosophy

California Institute of Technology

Pasadena, California

1988

(Submitted 17 September 1987)

ACKNOWLEDGEMENTS

My thanks go primarily to my thesis advisor, John Hall, firstly because his enormous input to this thesis cannot be overstated, and secondly because his advice, help and friendship over the past four years are greatly appreciated. Thanks also to his wife, Nancy, for several excellent meals over the past four years.

My thanks also go to the inhabitants of Thomas Laboratory, most of whom, to one degree or another, have helped make my stay here enjoyable, rewarding and memorable. In particular, I wish to thank Zee Duron and his family for being good to me.

In the production of this thesis, my thanks go in particular to Cecelia Lin for producing many of the figures, and to Krista Potter for her help in preparing some of the text. My thanks also go to Garret Jeong for his patience and help with the Prime computer.

I would like to thank my parents for their unfailing and unconditional love and support, for guiding me in what to do when they knew best and, later, for encouraging me to do what I wanted to do when they felt (mistakenly or otherwise) that I knew best, and most of all for never suggesting that I get a real job. My gratitude also goes to the many other members of my immediate and not so immediate family who have always been supportive to me.

TABLE OF CONTENTS

ABSTRACT

A nonlinear finite element procedure for arch dams is described in which the gradual opening and closing of vertical contraction joints and predetermined horizontal cracking planes are considered. A special joint element approximately represents the deformations due to plane sections not remaining plane at each open joint and allows a single shell element discretization in the thickness direction to be used for the dam. Compressive and sliding nonlinearities are not included. Finite element treatments are also used for the water, assumed incompressible, and for the foundation rock, assumed massless, with all degrees of freedom (dof) off the dam condensed out. For efficiency in the computations, the condensed water and foundation matrices are localized in a way which maintains good accuracy. The response of Pacoima Dam to the 1971 San Fernando ground motion recorded on a ridge over one abutment and scaled by two-thirds is computed first for water at the intermediate level that existed during the 1971 earthquake and then for full reservoir. In the first analysis, the dam exhibits pronounced opening and separation of the contraction joints, allowing violation of the no-slip assumption. The presence of a full reservoir greatly increases the dam response, enough to bring some of the assumptions of the analysis into question. Reducing the ground motion scale to 0.44 with full reservoir drops the response back to a reasonable level, but the contraction joint separations remain.

CHAPTER I
INTRODUCTION

1.1 General Introduction and Background

Finite element methods for linear elastic analysis of the response of arch dams to earthquake motions are well established [1–5]. Analyses of a number of dams have been carried out, many in response to the state of California's ongoing program to ensure the safety of dams in the state. One common characteristic of these analyses is the computation of high tensile stresses which occur during the dynamic response. The tensile stresses are generally largest in the arch direction in the upper portions of a dam, and, depending on the dam geometry, can reach values of 6 MPa (1 MPa = 145 psi) under moderately strong ground shaking and higher under severe motions [6–12].

The large tensile stresses computed in linear finite element analyses are unrealistic as the tensile strength of concrete under static loads is typically about 3 MPa, with perhaps a 50% increase under dynamic loading due to strain rate effects [13]. In addition, arch dams are often built with vertical contraction joints spaced at regular intervals. The contraction joints may be grouted, in which case they might be able to carry some small tensile stress, or they may be ungrouted, in which case no tensile stress can be transmitted across the joints. Also, an arch dam is constructed in a series of lifts, each lift being several feet high. The bond between the concrete in successive lifts is imperfect, possibly giving rise to planes of weakness. Imperfect bond may also be present at the foundation interface. Thus, even the limited tensile strength of concrete may not be attained over the major portion of the dam.

The occurrence of computed tensile stresses in excess of those capable of being carried presents a dilemma for the analyst seeking to design a new dam or to determine the safety of an existing dam. In essence, the nonlinear response and stability of the dam must be predicted from linear elastic analysis. Typically, concern over large tensile stresses is alleviated using a load transfer argument [14]; for example,

the load carried artificially by computed arch tensions is assigned to the cantilevers which are often more lightly stressed. Along this line, tensile arch stresses from a linear analysis have been converted to equivalent radial loads and then applied to the cantilevers in a subsequent static analysis [10,12]. In another case [11], the stiffness of the center portion of the upper arches was reduced in a subsequent dynamic analysis. However, such procedures cannot account for cantilever cracking [15,16] which has been shown to occur in model tests [17,18], estimate increased compressive stresses resulting from opening or impact at joints and cracks, and include the effects of sliding at joints or cracks which involve friction and the presence of shear keys; nor are they rigorous enough upon which to base important seismic safety decisions. Clearly, some analysis procedure for including nonlinear features of the seismic response of arch dams is needed.

A survey of the literature on finite element modeling of cracks and joints shows that two approaches are common: the smeared crack approach and the use of joint elements. In the smeared crack method [19–23], cracks and joints are modeled in an average or smeared sense by appropriately modifying the material properties at the integration points of regular finite elements. Smeared cracks are convenient when the crack orientations are not known beforehand because the formation of a crack involves no remeshing or new degrees of freedom (dof). Compressive and sliding nonlinearities have been included. However, smeared crack methods have only limited ability to model sharp discontinuities, and work best when the cracks to be modeled are themselves smeared out as in reinforced concrete applications.

Joint elements are more appropriate for modeling opening and closing of discrete cracks and joints. The simplest joint element is a nonlinear spring [24] which has infinite strength in compression, finite strength in tension, and spans the joint connecting the nodes of the finite elements on opposite sides. More sophisticated joint elements [25–28] have been borrowed from those used in rock mechanics [29,30] where the joints between rocks are of finite width and filled with a soft, no-tension material. A disadvantage of joint elements is the additional dof associated with the double-node arrangements. Joint elements can be constructed to include slid-

ing [31], while nonlinear behavior in compression can be included in the adjacent finite elements. Of major concern is the mechanism of opening and closing of the joints and cracks which probably takes place continuously, i.e., gradual opening and closing without impact, although some localized impact may occur following joint separation. Representation of the gradual opening and closing with the use of joint springs requires a multiple finite element discretization in the thickness direction (assuming linearly interpolated elements are used) which, for an arch dam, typically modeled with a single shell element in the thickness direction, would be very expensive. The rock mechanics type joint element does exhibit gradual opening and closing of a sort, even with a single, linearly interpolated finite element in the thickness direction; however, the behavior differs from that at an interface joint or a crack which is characterized by plane sections not remaining plane during opening. Thus, this approach is thought not to be valid; in any case, its accuracy has never been established. A similar problem exists with the smeared crack approach.

A number of other joint treatments have been developed [32–34], but have drawbacks and have not been applied to three-dimensional arch dams. The interface smeared crack model [32,33] represents cracks discretely like joint elements but, like smeared crack elements, does not introduce additional dof. Its behavior is similar to that resulting from the use of joint springs and, thus, similarly requires extra through-thickness discretization to represent gradual opening and closing. In [34], the finite element interpolation functions were modified to account for a partially open joint at the element boundary. Although the bi-linear displacement interpolation in the thickness direction may be too restrictive, the technique does have potential. Apparently, the only previous attempt to account for joint opening in a dynamic analysis of a three-dimensional arch dam is [26].

1.2 Objectives and Scope

The purpose of the research described in this dissertation is to examine the effect of the opening of vertical contraction joints and predetermined cracking planes

within the dam and along the dam-foundation interface on the earthquake response of arch dams. Both nonlinearities are modeled similarly with a special joint element designed to efficiently represent the gradual opening and closing of a joint and to be used in conjunction with a single shell element discretization in the thickness direction of the dam. A number of important nonlinear effects are excluded from the joint model. First, it is assumed that the stress-strain relationship for the concrete in compression remains linear throughout the analysis. Second, sliding along the joints and crack planes is assumed to be prevented by friction and/or built-in shear keys. This assumption is questionable under conditions of complete separation at a crack or joint. Third, when a joint located below the top surface of the water opens on the upstream face, water, to some degree, will enter the joint and exert a pressure which will tend to pry the joint open further. This effect is not modeled, though it is briefly addressed. Fourth, cavitation, which will occur in the water if the dynamic component of pressure reduces the absolute pressure to the vapor pressure, is also not included. In addition to the assumptions on nonlinear behavior, this study employs simplified treatments of foundation interaction, omits spatial variations in free-field ground motions, and neglects water compressibility.

1.3 Outline of Present Work

Chapter II describes the development of a special joint element which efficiently and accurately represents gradual opening and closing in two-dimensional slabs and arches using a single slab finite element discretization in the thickness (depth) direction. The joint element introduces two extra dof in addition to the three regular dof at each node of the structure. The manner in which the joint element is incorporated in a regular finite element mesh and the solution procedure for the nonlinear finite element equations are described.

In Chapter III, an analysis of a two-dimensional jointed arch (which is a representative horizontal cross-section of a concrete arch dam), in which the arch material is modeled by slab elements and the joints by the special joint elements, is compared

to an analysis of the same arch in which the arch material is modeled by means of many plane strain elements and the joints are modeled by means of several no-tension springs rigid in compression. The comparison illustrates the accuracy and relative efficiency of the former method. In addition, the special joint element is used in a comprehensive earthquake response analysis of the arch. Responses of the arch with and without joints are compared to assess the effect of joint opening.

Chapter IV describes the generalization of the two-dimensional joint element in a simple, approximate way for use in analysis of three-dimensional arch dams. Finite element treatments for the water, assumed incompressible, and for the foundation region, assumed massless, are described. For efficiency in the computations, all the water and foundation dof off the dam are condensed out, and it is shown that the condensed water and foundation matrices can be localized in a way which maintains accuracy. A method is described by which the dead weight of the dam is applied in steps in order to approximately simulate a construction sequence.

Chapter V describes a full three-dimensional nonlinear analysis of Pacoima (arch) Dam subjected to the 1971 San Fernando earthquake ground motion recorded on a ridge over one abutment of the dam and scaled by two-thirds. The response of the dam is computed first for water at the intermediate level that existed during the 1971 earthquake and then for the full reservoir. A third response analysis is also described for the case of the dam with a full reservoir subjected to less intense ground shaking.

Chapter VI, the final chapter, summarizes the major findings of this study and presents conclusions regarding the range of applicability of the analytical technique described herein.

CHAPTER II
TWO-DIMENSIONAL JOINT ELEMENT [35]

This chapter outlines the development of the two-dimensional joint element, showing how the gradual opening and closing of joints in two-dimensional slabs and arches can be accurately and efficiently modeled by a two-dof nonlinear spring element. Some important features, as well as the limitations of the element, are described. The nonlinear equations of motion of a two-dimensional arch or slab are developed, and the solution scheme is presented.

2.1 Joint Modeling, Analytical Considerations

Idealized behavior of an interface joint in a simply supported slab of unit width (perpendicular to the plane of the page), depth h and length $2d$ is shown in Figure 2.1. Material properties of the slab are assumed to be homogeneous, isotropic and linearly elastic, and small displacement and strain conditions are assumed. The presence of friction and/or built-in shear keys is assumed sufficient to prevent sliding along the joint. The slab is subjected to an axial force P and a varying end moment M, both applied to the ends of the slab as shown. For stability, P must be compressive (negative). Initially, when M is zero or very small, the whole joint is in compression and remains closed. When M is increased to a value of $-Ph/6$, then from simple beam theory, the normal stress at the bottom of the joint becomes zero. As M is increased beyond this value, the joint opens gradually. The maximum value of M is $-Ph/2$, obtained when the joint opening reaches the top. Failure of the joint would actually precede $M = -Ph/2$ because of the large compressive stress across the joint when the contact area reduces to a small value.

Figure 2.2 shows the $M - \theta_T$ and $M - U_T$ relations where θ_T and U_T are the total rotation and axial translation, respectively, at the support. For $M < -Ph/6$, the joint remains closed, and

$$\theta_T = \theta_E \approx 12Md(1-\nu^2)/Eh^3 \quad \text{by beam theory neglecting shear deformations}$$
$$U_T = U_E = -Pd/Eh, \tag{2.1}$$

where E = Young's modulus; ν = Poisson's ratio; and the subscript E denotes elastic behavior. For $M > -Ph/6$ the joint opens; θ_T increases nonlinearly, as does U_T due to a prying action at the joint. The joint may be considered to cause an additional rotation and axial translation at the support; i.e., in addition to the elastic values θ_E and U_E which would occur if the joint were absent. The displacements due to the joint are

$$\begin{aligned} \theta_J &= \theta_T - \theta_E \\ U_J &= U_T - U_E \end{aligned} \tag{2.2}$$

and are also plotted in Figure 2.2.

If, instead of being subjected to a constant axial load P and moment M varying from 0 to $-Ph/2$, the joint were subjected to a constant end moment M and an axial load varying from some large compressive value ($< -6M/h$, M positive) up to a value of $-2M/h$, behavior similar to that described above and illustrated in Figures 2.1 and 2.2 would be observed. Initially, with a large negative axial load, the joint would remain closed, but as P decreases in magnitude, gradual opening of the joint would result until P reaches a value of $-2M/h$, at which point the opening would reach the top. For this case, two additional sets of curves, analogous to those shown in Figure 2.2 relating total and joint rotations and total and joint translations at the support to axial load P, would be obtained.

It will be convenient to view the joint as a structural element with its own tangent stiffness defined by

$$\begin{Bmatrix} \mathrm{d}M \\ \mathrm{d}P \end{Bmatrix} = [K_J] \begin{Bmatrix} \mathrm{d}\theta_J \\ \mathrm{d}U_J \end{Bmatrix}, \tag{2.3}$$

where

$$[K_J] = \begin{bmatrix} k_{\theta\theta} & k_{\theta U} \\ k_{U\theta} & k_{UU} \end{bmatrix}, \tag{2.4}$$

and M and P are the moment and axial force across the joint. The tangent stiffness matrix $[K_J]$ is the inverse of the tangent flexibility matrix $[F_J]$ where

$$\begin{Bmatrix} \mathrm{d}\theta_J \\ \mathrm{d}U_J \end{Bmatrix} = [F_J] \begin{Bmatrix} \mathrm{d}M \\ \mathrm{d}P \end{Bmatrix} \tag{2.5}$$

and

$$[F_J] = \begin{bmatrix} f_{\theta\theta} & f_{\theta U} \\ f_{U\theta} & f_{UU} \end{bmatrix}. \tag{2.6}$$

The terms $f_{\theta\theta}$ and $f_{U\theta}$ in $[F_J]$ are the slopes $\mathrm{d}\theta_J/\mathrm{d}M$ and $\mathrm{d}U_J/\mathrm{d}M$ from the curves in Figure 2.2. The other terms $f_{\theta U}$ and f_{UU} are $\mathrm{d}\theta_J/\mathrm{d}P$ and $\mathrm{d}U_J/\mathrm{d}P$ where $\mathrm{d}\theta_J$ and $\mathrm{d}U_J$ are caused by an increment in $\mathrm{d}P$ keeping M constant. The matrices $[F_J]$ and $[K_J]$ are symmetric, i.e., $f_{\theta U} = f_{U\theta}$ and $k_{\theta U} = k_{U\theta}$. The terms of $[F_J]$ and $[K_J]$ can be shown, by dimensional analysis, to depend only on the elastic modulus E, Poisson's ratio ν, slab depth h, length d, and the dimensionless parameter $-M/Ph$. Independence of d results if d/h is sufficiently large (see next section). The functional dependence on $-M/Ph$ is one-to-one except at M and P both equal to zero. Alternatively, $[K_J]$ and $[F_J]$ can be expressed as one-to-one functions of $\theta_J h/U_J$ except when both U_J and θ_J equal zero. Thus, the behavior of the joint is independent of loading and deformation history.

The structural element represented by $[K_J]$ is equivalent to a three parameter spring system. The three parameters are a rotational spring of tangent stiffness k_θ, a translational spring of tangent stiffness k_U, and the location $\bar{h}$ of the translational spring (Figure 2.3). With a large d and a set value of Poisson's ratio, dimensional analysis leads to the following expressions for the spring parameters,

$$\begin{aligned} k_U &= E \cdot f_1(-M/Ph \quad \text{or} \quad \theta_J h/U_J) \\ k_\theta &= Eh^2 \cdot f_2(-M/Ph \quad \text{or} \quad \theta_J h/U_J) \\ \bar{h} &= h \cdot f_3(-M/Ph \quad \text{or} \quad \theta_J h/U_J). \end{aligned} \tag{2.7}$$

Relation to the components of $[K_J]$ is given by

$$\begin{aligned} k_{\theta\theta} &= k_\theta + \bar{h}^2 k_U \\ k_{\theta U} &= k_{U\theta} = -\bar{h} k_U \\ k_{UU} &= k_U . \end{aligned} \tag{2.8}$$

2.2 Joint Modeling, Numerical Treatment

Computation of $[K_J]$ or $[F_J]$ is difficult analytically because of the mixed boundary condition at the joint, i.e., zero displacement along that part of the joint which is in contact, zero tractions along that part of the joint which is open. However, a nonlinear finite element solution of the problem illustrated in Figure 2.1 is possible. Only half the joint and slab (to one side of the plane of symmetry) need be considered. The finite element mesh of this system, shown in Figure 2.4, uses 8 elements through the depth of the slab and 20 elements along the length from the plane of symmetry to the end of the slab. The elements are four-node, linearly elastic, plane strain elements. Each node of the mesh has two dof, namely translations in the z and x directions. Nodes at the joint have their x dof free and their z dof connected by horizontal springs to the fixed plane of symmetry. These springs have zero stiffness within the open portion of the joint and have large stiffness ($\approx \infty$) within the closed portion of the joint, i.e., they are rigid in compression and have zero stiffness and strength in tension.

The z translations of the 9 dof at the right end of the mesh in Figure 2.4 move nearly as a straight line, but not exactly; this makes the computation of θ_T and U_T somewhat arbitrary. Therefore, these nine z dof were constrained to move as a straight line by transforming to the two dof θ_T and U_T using a penalty method.

The nondimensionalized $M - \theta_J$ and $M - U_J$ curves obtained from the finite element system are shown in Figure 2.5. The elastic portions θ_E and U_E of the support displacements (computed with the mesh of Figure 2.4 with all springs intact) have been subtracted out. Note that, in contrast to the smooth curves of Figure 2.2, those of Figure 2.5 are piecewise linear; slope changes occur every time a spring

opens or closes. The joint condition is denoted by i where $|i|$ is the number of open springs at the bottom (positive i) or top (negative i). Slopes of the linear segments give $f^i_{\theta\theta}$ and $f^i_{U\theta}$; the superscript denotes the joint condition. The curves in Figure 2.5 were obtained by applying a constant axial load and a varying moment to the right hand end of the slab. A second pair of curves (not shown) was obtained by applying a constant moment and a varying axial load to the end of the slab. Then solution for a load increment $\mathrm{d}P$ with a particular joint condition leads to $f^i_{\theta U}$ and f^i_{UU}.

Inversion of $\left[F_J\right]^i$ yields $\left[K_J\right]^i$, which is given in Table 2.1 in the form of the equivalent spring parameters k^i_θ, k^i_U and $\bar{h}^i$. These parameters are constant within ranges of $-M/Ph$ or $\theta_J h/U_J$ which correspond to particular joint conditions. Note that as the joint opens, $\bar{h}$ increases and the springs soften. Under complete separation, stiffnesses of the equivalent springs are zero.

The behavior of the joint shown in Figure 2.4, modeled by 9 spring elements through the depth of the beam, is intended to approximate the continuous opening behavior shown in Figure 2.1. The error in the finite element model depends on the number of spring elements employed, and consequently on the number of plane elements. The results presented for the mesh with eight plane elements in the depth direction differed significantly from those obtained using a coarser mesh with four elements through the depth; however, they agreed well with results obtained with a finer mesh using 16 elements in the depth direction. Use of the latter results would require 35 possible conditions (0,$\pm$1,...$\pm$17) for each joint, as opposed to 19 possible conditions (0,$\pm$1,...$\pm$9) using the results obtained from the mesh with eight elements through the depth. This would require many more iterations and a significant increase in computation time for solution of an actual problem without giving any significant improvement in the accuracy of the analysis. Therefore, all the analyses described in this thesis were performed using the results presented in this chapter obtained from the mesh in Figure 2.4.

Numerical experience has shown that the joint spring parameters are independent of the distance d between joint and support if d exceeds $0.7h$. Thus, for

multiply jointed structures, some error will be present when the joint spacing is less than $0.7h$ due to interference between adjacent joints. However, this error is small for joints spaced as closely as $0.5h$. At closer spacings, the error becomes significant. Chapter V presents results for Pacoima Dam, a typical arch dam. It will be seen in that chapter that the minimum spacing of the vertical contraction joints approaches $0.5h$ only in the lower part of the dam, where little or no joint opening occurs. Numerical experience has also shown only a weak dependence of the joint spring parameters on Poisson's ratio. All results presented in this thesis will be for $\nu = 0.2$, a value typical for concrete.

As pointed out in Chapter I, nonlinearities arising from large compressive stresses acting across the joint are not taken into account. These large stresses can occur at times of high axial compression when the bending moment is large enough to cause significant opening. Nonlinear behavior in compression is an important feature in the failure response of an arch dam [36], and thus the analysis methods described in this study may be unable to predict ultimate stability. Also, cracking within the finite elements and sliding along the joints is not permitted. In the experimental results of [36], no cracking occurred within the discrete blocks comprising the arch rib, and the pressure of friction was sufficient to prevent sliding between the blocks. Thus, based on these results, the last two assumptions may be reasonable except in the case of severe ground motion. The effect of complete joint separation on the no sliding assumption is discussed in Chapters IV and V.

A feature of a joint model which may be desirable is the ability to carry some tensile stress. Vertical contraction joints in an arch dam may be grouted, in which case they could have some tensile strength. This is accounted for in the following manner. If at a closed joint the moment is sufficient to cause tension on a face which has not opened previously, then that tensile stress is computed assuming a linear stress distribution through the depth of a joint and then compared to a specified limiting tensile stress. If the stress at the face does not exceed the limiting stress, the joint is held in the closed position. If the limiting tensile stress is exceeded, joint opening is allowed to take place from that face in the manner described previously.

Further, once opening has taken place at a face, the limiting tensile stress for opening at that face is set to zero.

For output purposes, when a joint is completely closed, the values of M and P at the joint are converted to normal stresses by assuming a linear stress distribution across the full depth of the joint. At a partially open joint, the normal stress at the closed face is computed using a triangular stress distribution with a no-tension zone (Figure 2.6). In both cases, M and P are sufficient to determine the stress distribution. However, as joint condition ± 8 (only end spring in contact) is approached; the depth of the triangular stress block goes to zero, and the peak compressive stress goes to infinity. Such behavior often occurs either as a joint completely separates or as it reestablishes contact after complete separation and is a result of using only a finite discretization in the thickness direction (Figure 2.4). Consequently, these high stresses are thought to be fictitious, or at worst, to lead to minor chipping of the concrete at the edge of the joint. As an arbitrary fix to this problem, the depth of the triangular stress block for joint conditions ± 7 and ± 8 was assumed to vary linearly from the depth computed from M and P at $\theta_J h/U_J = \pm 3.1306$ (i.e., when the third spring from the face just breaks) to a zero depth at $\theta_J h/U_J = \pm 2.0$, with the peak stress adjusted to maintain the total force at P. However, peak stresses which were felt to be unrealistically high still resulted, so as an additional measure, a minimum stress block depth was established at $1/8$ of the joint depth.

In addition to the stresses at a joint, a second important computation for output purposes is that of the joint opening displacement at the upstream and downstream faces. If the material on either side of the open portion of the joint deforms as a straight line, then the opening at the face of the joint is simply the relative rotation of the joint, θ_J, times the depth of the joint opening. Tests with the mesh shown in Figure 2.4 have shown that only if the contact depth is small can the joint opening be computed reliably in this manner. If a significant portion of the joint is closed, the joint opening at a face exceeds that predicted by the method described above. In this case, the joint opening displacement can be more accurately computed as

the relative rotation, θ_J, times a depth h^* which is greater than the depth of joint opening. Results from the mesh of Figure 2.4 for the actual value of h^* for each joint condition are given in nondimensionalized form in Table 2.1. For any value of $-M/Ph$ other than those given in Table 2.1, h^* can be determined by linear interpolation.

2.3 Solution Scheme

The finite element used is a two-dimensional slab element which includes shear deformations [37]. Figure 2.7 shows the element in its parent and mapped forms. The element has 2 nodes located at the mid-thickness, each of which has three dof associated with the local $\hat{z}$,$\hat{x}$ axes. The $\hat{z}$ axis is in the mapped η direction and lies along the nodal 'normal', and $\hat{x}$ is perpendicular to $\hat{z}$. The three dof are $\hat{z}$ and $\hat{x}$ translations of the nodal normal and a counterclockwise rotation $\hat{\theta}$ of the nodal normal. Linear shape functions are used for all dof. Two conditions imposed are zero normal strain perpendicular to the plane of the element, and zero in plane normal stress in a direction perpendicular to the mapped ξ direction. The 6×6 linearly elastic element stiffness matrix is denoted by $[K_e]$.

Joint planes are located at element intersections and create a double-node condition, as shown in Figure 2.8. Five dof to define the positions of the nodal 'normals' a–b and A–B are associated with such an arrangement. The five dof are average translations $\hat{W}_{av}$ and $\hat{U}_{av}$ along $\hat{z}$ and $\hat{x}$, the average rotation $\hat{\theta}_{av}$, the relative translation $\hat{U}_{rel}$ along $\hat{x}$ (opening positive), and the relative rotation $\hat{\theta}_{rel}$ (positive for opening at the bottom, or negative $\hat{z}$ edge of the joint). The relative displacement along $\hat{z}$ is zero since sliding is not allowed. At the joint (Figure 2.8), the nodal dof (numbered 1 and 2) are related to the average and relative dof by

$$\begin{aligned} \hat{U}_1 &= \hat{U}_{av} - \hat{U}_{rel} \qquad & \hat{U}_2 &= \hat{U}_{av} + \hat{U}_{rel} \\ \hat{\theta}_1 &= \hat{\theta}_{av} + \hat{\theta}_{rel} \qquad & \hat{\theta}_2 &= \hat{\theta}_{av} - \hat{\theta}_{rel}. \end{aligned} \tag{2.9}$$

Stiffness terms associated with the average dof are the same ones which would be used if the joint plane were absent. Stiffness terms associated with the relative

dof are provided by the 2×2 tangent stiffness matrix $[K_J]^i$ of the joint element defined in the preceding section and by the adjacent finite elements. For an end joint at a plane of symmetry or at a support, $[K_J]^i$ can be used directly; it must be multiplied by 2 at an interior joint. With the unmodified $[K_J]^i$, equation 2.3 (and also equation 2.21) apply only for an end joint; the resulting values of M and P or $\mathrm{d}M$ and $\mathrm{d}P$ must be divided by 2 at an interior joint. These considerations follow from the fact that the spring elements in the mesh in Figure 2.4 represent a joint at a plane of symmetry or fixed support and from the transformations defined by equation 2.9. Nonlinearities are associated only with the relative joint dof.

The time integration scheme for the nonlinear equations of motion employs Bossak's extension of the standard Newmark method. This extension [38,39] involves the introduction of a parameter, α_B, to provide algorithmic damping in the high frequency range where spurious (numerical) oscillations can result from certain types of nonlinearities. The solution scheme employs Newton iterations within time steps to establish equilibrium. (In static problems, time steps are employed as a convenient way to increment the load.)

Development of the solution scheme proceeds from the time integration equations,

$$\{\dot{a}^{l+1}(t-\Delta t)\} = \{\dot{a}(t)\} + \{(1-\gamma)\ddot{a}(t) + \gamma\ddot{a}^{l+1}(t+\Delta t)\}\Delta t \tag{2.10}$$

and

$$\{\ddot{a}^{l+1}(t+\Delta t)\} = \frac{1}{\beta\Delta t^2}\{a^l(t+\Delta t) + \Delta a^l - a(t)\} - \frac{1}{\beta\Delta t}\dot{a}(t) - \left(\frac{1}{2\beta} - 1\right)\{\ddot{a}(t)\}, \tag{2.11}$$

and the general equation of motion which expresses equilibrium attained after the lth iteration in time stepping from t to $t+\Delta t$, altered from standard form, i.e.,

$$\{p^{l+1}(t+\Delta t)\} + [C]\{\dot{a}^{l+1}(t+\Delta t)\} + [M]\{\ddot{a}^{l+1}(t+\Delta t)\} \approx \{f(t+\Delta t)\}, \tag{2.12}$$

to Bossak's form,

$$\{p^{l+1}(t+\Delta t)\} + [C]\{\dot{a}^{l+1}(t+\Delta t)\} + \alpha_B [M]\{\ddot{a}(t)\} +$$

$$(1-\alpha_B)[M]\{\ddot{a}^{l+1}(t+\Delta t)\} \approx \{f(t+\Delta t)\}, \tag{2.13}$$

where $\{a(t)\}$, $\{\dot{a}(t)\}$ and $\{\ddot{a}(t)\}$ are vectors of nodal displacements, velocities and accelerations at time t relative to any earthquake motions, and $\{a(t)\}$ includes static displacements; notations $^{l}(t+\Delta t)$ and $^{l+1}(t+\Delta t)$ signify the approximations to the state at time $t+\Delta t$ after $(l-1)$ and l iterations, respectively, with $^{1}(t+\Delta t) = (t)$; γ and β are integration parameters where, for unconditional stability (guaranteed only for the linear solution), $\gamma \geq \frac{1}{2}$ and $\beta \geq \frac{1}{4}(\frac{1}{2}+\gamma)^2$; Δ denotes incremental quantity; $\{p^{l+1}(t+\Delta t)\}$ = vector of stiffness forces which corresponds to the state $\{a^{l+1}(t+\Delta t)\}$; $\{f(t+\Delta t)\}$ = vector of applied nodal forces on the dam at time $(t+\Delta t)$; and $[C]$ and $[M]$ are the damping and mass matrices of the structure. Substitution of equations (2.10) and (2.11) into the linearized form of equation (2.13) leads to the following algorithm for the lth iteration step in the computation of the state at time $t+\Delta t$, with the state at time t known.

1. Compute the incremental displacement $\{\Delta a^l\}$ from

$$\left[\frac{(1-\alpha_B)}{\beta\Delta t^2}M + \frac{\gamma}{\beta\Delta t}C + K\right]\{\Delta a^l\} = \{f(t+\Delta t)\} - \{p^l(t+\Delta t)\}$$

$$-\left[\frac{(1-\alpha_B)}{\beta\Delta t^2}M + \frac{\gamma}{\beta\Delta t}C\right]\{a^l(t+\Delta t)\} + \left[\frac{(1-\alpha_B)}{\beta\Delta t^2}M + \frac{\gamma}{\beta\Delta t}C\right]\{a(t)\}$$

$$+\left[\frac{(1-\alpha_B)}{\beta\Delta t}M + \left(\frac{\gamma}{\beta}-1\right)C\right]\{\dot{a}(t)\}$$

$$+\left[\left(\left(\frac{1}{2\beta}-1\right)(1-\alpha_B)-\alpha_B\right)M + \left(\frac{\gamma}{2\beta}-1\right)\Delta t C\right]\{\ddot{a}(t)\}, \tag{2.14}$$

where

$$\begin{aligned}\{p^l(t+\Delta t)\} &= \{p(\{a^l(t+\Delta t)\})\}\\ \{a^1(t+\Delta t)\} &= \{a(t)\}\\ \{p^1(t+\Delta t)\} &= \{p(\{a(t)\})\}\end{aligned} \tag{2.15a}$$

and where $\{p^{l+1}(t+\Delta t)\}$ has been linearized by

$$\{p^{l+1}(t+\Delta t)\} = \{p^l(t+\Delta t)\} + [K]\{\Delta a^l\}. \tag{2.15b}$$

2. Compute the new approximation to $\{a(t+\Delta t)\}$ from

$$\{a^{l+1}(t+\Delta t)\} = \{a^l(t+\Delta t)\} + \{\Delta a^l\}. \tag{2.16}$$

Compute $\{p^{l-1}(t+\Delta t)\}$ from $\{p^l(t+\Delta t)\}$ and $\{\Delta a^l\}$. After convergence, compute

$$\begin{aligned}\{\dot{a}(t+\Delta t)\} &= \{\dot{a}(t)\} + \{(1-\gamma)\ddot{a}(t) + \gamma\ddot{a}(t+\Delta t)\}\Delta t\\ \{\ddot{a}(t+\Delta t)\} &= \frac{1}{\beta\Delta t^2}\{a(t+\Delta t) - a(t)\} - \frac{1}{\beta\Delta t}\dot{a}(t) - \left(\frac{1}{2\beta} - 1\right)\{\ddot{a}(t)\}\end{aligned} \tag{2.17}$$

and proceed to the next time step.

In the above,

$[M]$ = the mass matrix of the stucture. Mass terms are associated with both the average and relative dof at a joint. The mass terms associated with the average dof are the same ones associated with a single node which would be used if the joint plane were absent. The mass terms associated with the relative dof come from the adjacent finite elements through the transformations defined by equation 2.9. No mass is associated with the joint elements. To account for interaction effects with an incompressible water domain, $[M]$ can be augmented by an added mass matrix $[M_a]$ in equations 2.13 and 2.14 above and equations 2.18 and 2.19 below.

$[C]$ = the damping matrix of the structure. Rayleigh damping [40] is assumed; i.e., $[C]$ is constructed as a linear combination of the mass matrix $[M]$ and the linearly elastic stiffness matrix $[K']$ as

$$[C] = \alpha_0 [M] + \alpha_1 [K'], \tag{2.18}$$

where $[K']$ is the stiffness matrix of the structure excluding all joint element stiffness terms. Thus, no structural damping is associated with the joint elements.

$[K]$ = the tangent stiffness matrix of the structure. $[K]$ is assembled from the linearly elastic matrices $[K_e]$ of the finite elements and the current tangent matrices $[K_J]^i$ of the joint elements. Due to large changes in the terms of $[K_J]^i$ for different values of i (as the joints open and close), the current matrix $[K]$ is always used in each iteration. The modified Newton method, which uses a tangent matrix from a previous configuration that is updated from time to time, results in fewer matrix factorizations but requires an excessive number of iterations. This difficulty is common in analysis of contact problems.

$\{f(t+\Delta t)\}$ = specified nodal load vector at time $t + \Delta t$. For static plus earthquake loading [40],

$$\{f(t+\Delta t)\} = \{f_{st}\} - [M\ M_g]\{r\}\ddot{a}_g(t+\Delta t), \tag{2.19}$$

where $\{f_{st}\}$ = static load due to, say, water pressure; $[M_g]$ is the portion of the mass matrix which couples support dof (i.e., dof which are fixed) and non-support (free) dof; $\{r\}$ is an influence vector which depends on the direction of earthquake motion; and $\ddot{a}_g(t+\Delta t)$ is the ground acceleration at time $t + \Delta t$ in the given direction.

$\{p^l(t+\Delta t)\}$ = nodal load vector which is in equilibrium with the stresses that correspond to the strains in the configuration $\{a^l(t+\Delta t)\}$. $\{p^l(t+\Delta t)\}$ is assembled from vectors $\{p_e^l(t+\Delta t)\}$ of the finite elements and vectors $\{p_J^l(t+\Delta t)\}$ of the joint elements. For the finite elements

$$\{p_e^l(t+\Delta t)\} = [K_e]\{a_e^l(t+\Delta t)\}, \tag{2.20}$$

where $\{a_e^l(t+\Delta t)\}$ is the element displacement vector. The joint load vector $\{p_J^l(t+\Delta t)\}$ contains the two terms $M^l(t-\Delta t)$ and $P^l(t+\Delta t)$ computed from

$$\begin{Bmatrix} M^l(t+\Delta t) \\ P^l(t+\Delta t) \end{Bmatrix} = \left[K_J\right]^i \begin{Bmatrix} \hat{\theta}^l_{rel}(t+\Delta t) \\ \hat{U}^l_{rel}(t+\Delta t) \end{Bmatrix} \tag{2.21}$$

where the joint condition i is determined from the value of the parameter $\hat{\theta}^l_{rel}(t+\Delta t)\cdot h/\hat{U}^l_{rel}(t+\Delta t)$. Note that no integration is required to compute $M^l(t+\Delta t)$ and $P^l(t+\Delta t)$ as is implied by equation 2.3. The reason is the independence of the stress state from the deformation history; i.e., the same $M^l(t+\Delta t)$ and $P^l(t+\Delta t)$ would result from any deformation path including the one in which $\hat{U}^l_{rel}(t-\Delta t)$ and $\hat{\theta}^l_{rel}(t+\Delta t)$ increase from zero to their final values maintaining the same ratio throughout, which takes place entirely under joint condition i.

Additional features of the solution algorithm are the following:

1. The choice

$$\begin{aligned} \gamma &= \frac{1}{2} - \alpha_B \\ \beta &= \frac{1}{4}\left(1-\alpha_B\right)^2 \end{aligned} \tag{2.22}$$

is convenient because it produces no algorithmic damping at $\alpha_B = 0$ (constant average acceleration method) and results in minimal damping at low frequencies for nonzero α_B. The variation of damping with frequency for nonzero (negative) values of α_B is shown in Figure 2.9.

2. The Rayleigh damping matrix $\left[C\right]$, expressed by equation 2.18, gives any mode with natural frequency ω (radians/sec) a damping ratio given by

$$\xi = \frac{\alpha_0\omega}{2} + \frac{\alpha_1}{2\omega}. \tag{2.23}$$

Specifying ξ at two frequencies ω is sufficient to determine α_0 and α_1. As ξ from equation 2.23 can often be made to vary slowly over the frequency range of interest, the modal frequencies do not have to be found precisely.

3. The solution at time $t+\Delta t$ is obtained following an iteration in which no joint condition changes occur.

4. Use of the current tangent matrix $\left[K\right]$ is expensive because it must be reformed and recomputed in each iteration of each time step. This would be

particularly true for three-dimensional problems, and Chapter IV describes methods to ensure maximum computational efficiency in that case.

5. For linear matrix equations, the Bossak-Newmark time integration scheme with the Bossak parameter $\alpha_B \leq 0$ is unconditionally stable. In the application here to a nonlinear matrix equation, no instabilities were encountered which allowed the choice of Δt to be based solely on accuracy criteria.

6. The algorithm described above is for a nonlinear analysis. A linear analysis may be performed simply by specifying the condition of each joint to be 0 at all times.

7. Removal of the dynamic terms (mass, damping, velocity and acceleration) from the algorithm described above gives the static solution scheme.

8. A basic requirement of any proposed algorithm is that the computed values of M and P at the joints under linear analysis (no opening) be accurate. In the present algorithm, M and P are computed directly from the displacements of the joint springs. Comparison to analytical solutions of linear slabs and arches under static loading has shown M and P to be very accurate. Results presented in Chapter III will reinforce this.

Table 2.1 Parameters of the Joint Element

Joint Condition i	Range of $-M/Ph$	k_θ^i/Eh^2	k_u^i/E	$\bar{h}^i/h$	Range of $h\theta_J/U_J$	Range of h^*/h
0	0 to ±0.181515	0.686400E5	0.800000E6	0	0 to ∓2.115581	1.000 to 2.905
±1	±0.181515 to ±0.208654	0.149009E1	0.578035E6	±0.181511	∓2.115581 to ∓∞ or ±∞ to ±5.512184	2.905 to 1.370
±2	±0.208654 to ±0.245145	0.324072E0	0.257321E4	±0.202751	±5.512184 to ±5.005502	1.370 to 1.040
±3	±0.245145 to ±0.287020	0.125015E0	0.263496E3	±0.228791	±5.005502 to ±4.532209	1.040 to 0.910
±4	±0.287020 to ±0.332713	0.572333E-1	0.540538E2	±0.260362	±4.532209 to ±4.069550	0.910 to 0.870
±5	±0.332713 to ±0.381015	0.266024E-1	0.148260E2	±0.299084	±4.069550 to ±3.607720	0.870 to 0.880
±6	±0.381015 to ±0.431850	0.109213E-1	0.462551E1	±0.347379	±3.607720 to ±3.130602	0.880 to 0.920
±7	±0.431850 to ±0.500000	0.286902E-2	0.143287E1	±0.409660	±3.130602 to ±2.580636	0.920 to 1.000
±8	±0.500000	0	0.282278E0	±0.500000	±2.580636 to ±2.000000	1.0
±9	---	0	0	---	---	1.0

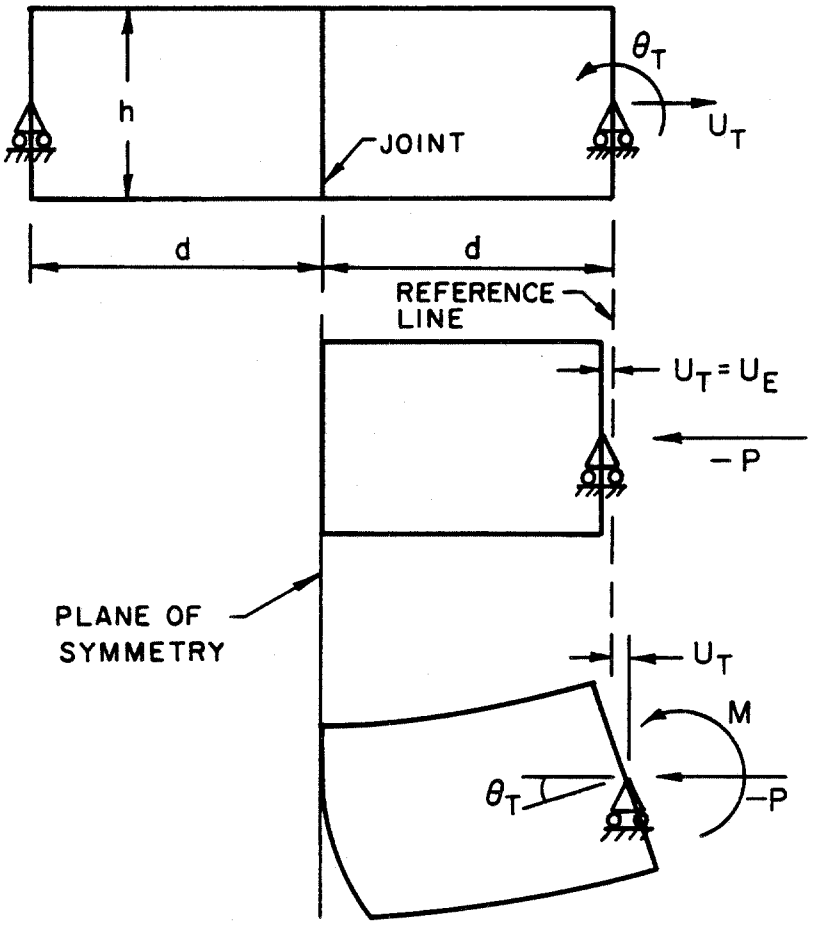

Figure 2.1 Idealized Behaviour of an Interface Joint.

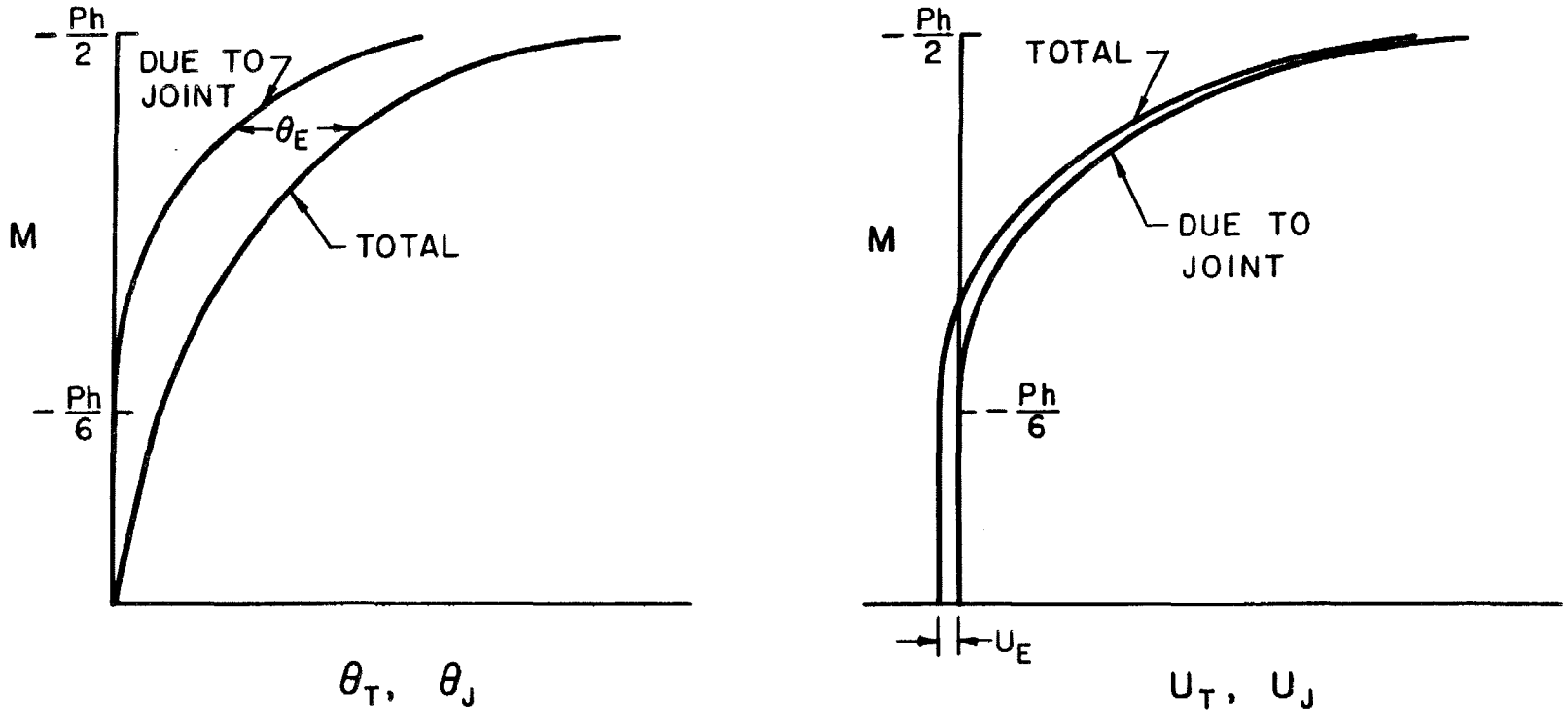

Figure 2.2 Moment versus support displacements of idealized joint under constant axial force.

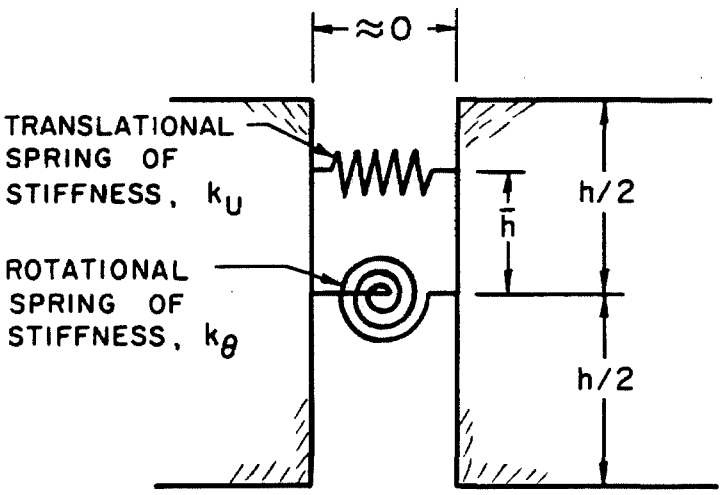

Figure 2.3 Equivalent joint element.

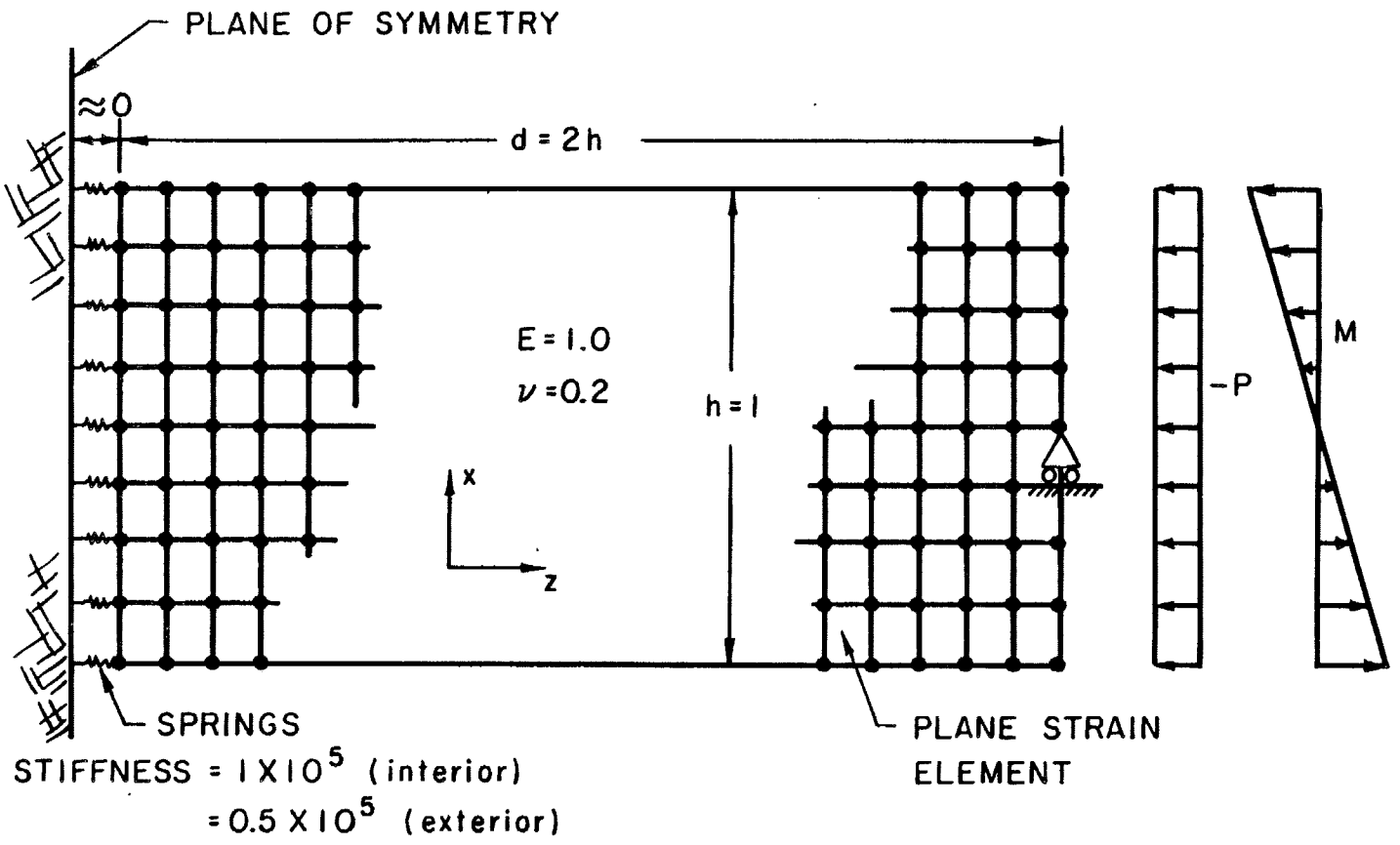

Figure 2.4 Finite element model for computation of equivalent joint element.

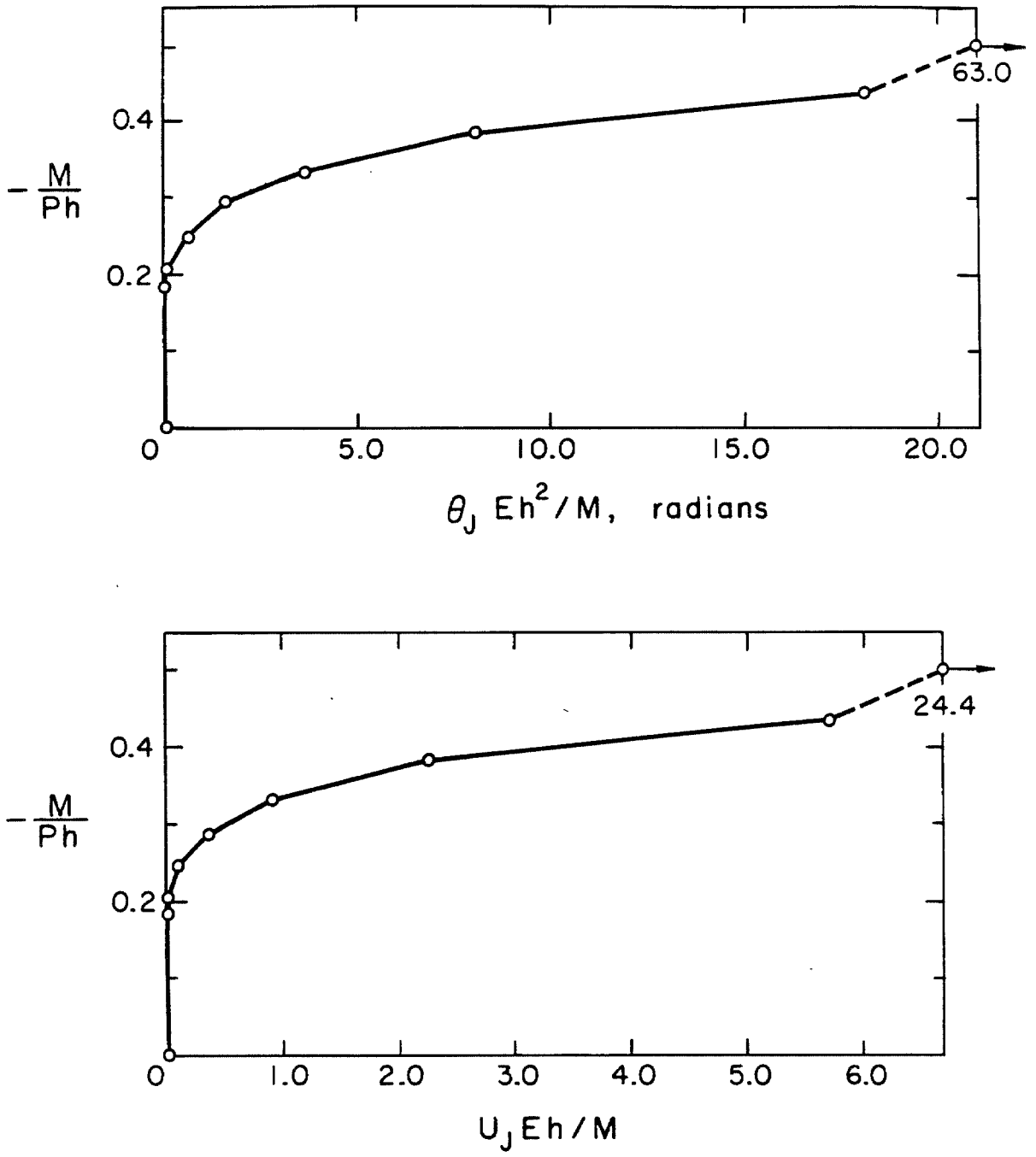

Figure 2.5 Moment versus support displacements due to joint action under constant axial force. Results are from the finite element model.

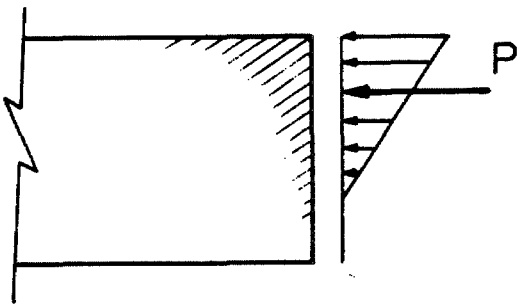

Figure 2.6 Determination of the compressive stresses at a partially open joint using a triangular stress block with a no-tension zone.

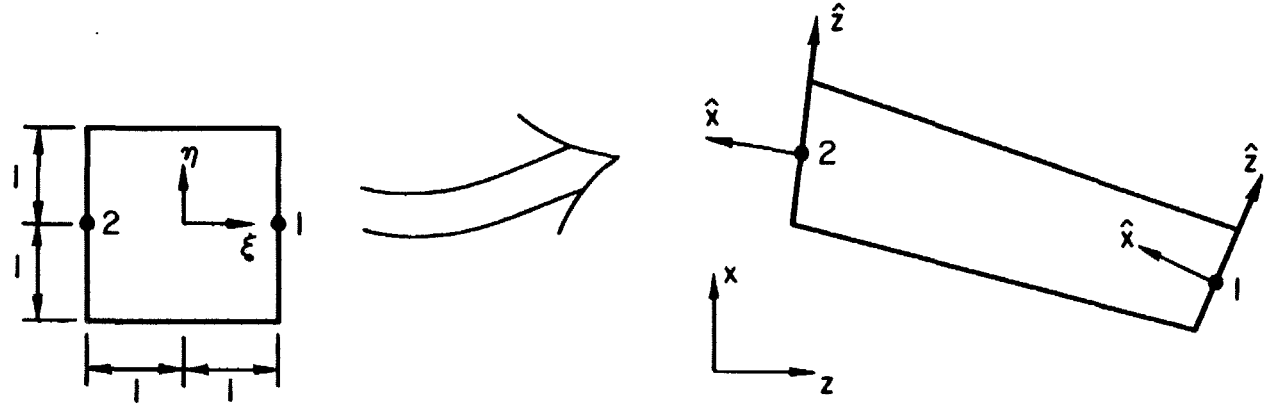

Figure 2.7 Two-node slab element.

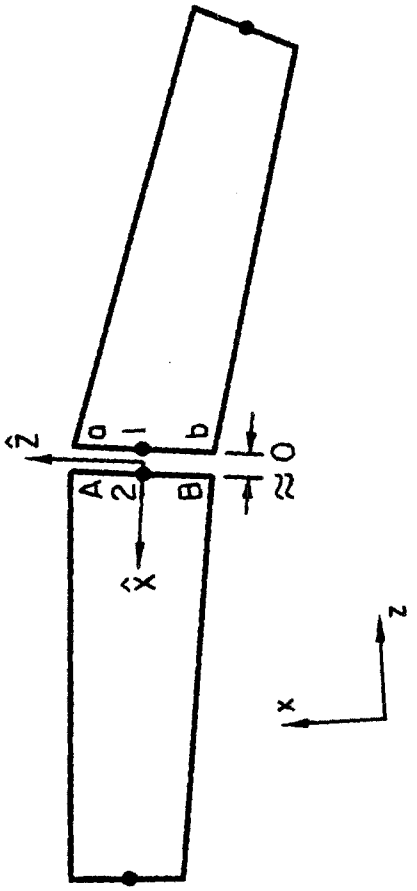

Figure 2.8 Joint plane at slab element intersection.

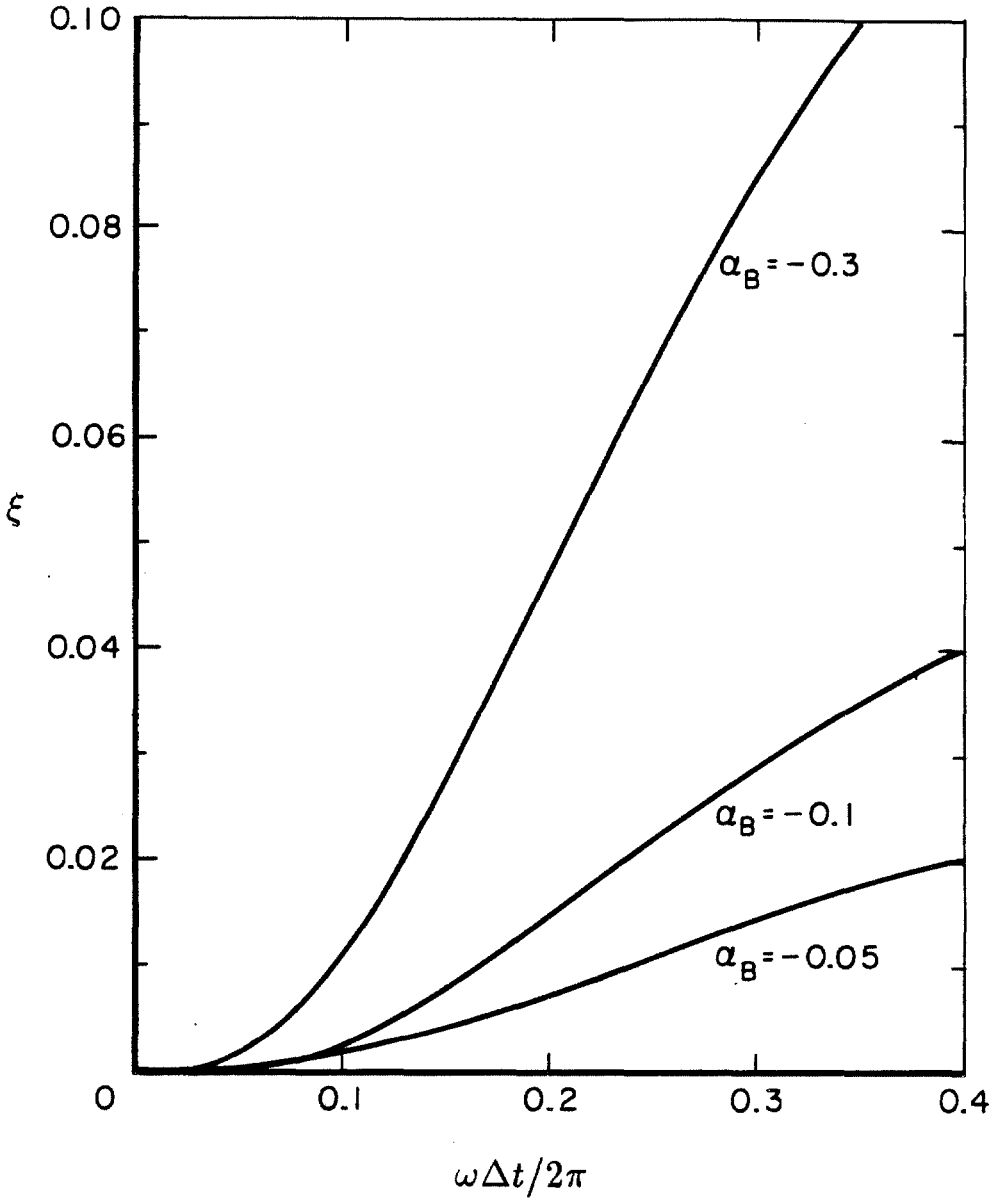

Figure 2.9 Algorithmic damping ratio, ξ, as a fraction of critical, plotted against $\omega\Delta t/2\pi$ for $\alpha_B = -0.05, -0.1, -0.3$ for a single degree of freedom oscillator, natural frequency ω radians/sec (source, [39]).

CHAPTER III
TWO-DIMENSIONAL ANALYSIS RESULTS

This chapter compares some results of static and dynamic analyses of a two-dimensional jointed arch, for the purpose of demonstrating the accuracy and usefulness of the equivalent joint element developed in Chapter II. In one case the arch is modeled with slab finite elements connected by these joint elements, and in the other case, a fine discretization through the depth of plane finite elements and joint springs is employed.

Thereafter, a more extensive analysis of the arch structure, using the slab elements, is performed in which the arch is subjected to a series of successively stronger ground motions in order to observe the increasing amount of joint opening which occurs and its effect on the dynamic response of the arch, and also to compare the linear and nonlinear behavior of the structure.

3.1 Accuracy and Efficiency of Joint Element

Chapter II outlined the development of the equivalent two-dimensional joint element designed to model the gradual opening and closing mechanism of an interface joint in a slab using a single slab element discretization through the depth. This technique produces a much more efficient solution than that obtained by the type of mesh shown in Figure 2.4, which uses nine spring elements and eight plane elements through the depth. Regarding accuracy, both techniques should be comparable for a simple slab such as shown in Figure 2.1 because this was the calibration problem for the equivalent joint element. Of interest, however, is the performance of the joint element in a more complex arch structure containing several joints and subjected to a dynamic load, such as an earthquake excitation.

The jointed circular arch pictured in Figure 3.1a will be used as a test problem and is intended to represent a horizontal cross-section of an arch dam. It has a unit height of 1 meter and a uniform depth of 5.5 meters. The radius to the mid-depth

of the arch is 45 meters. Material properties of the concrete are Young's modulus E of 27,500 MPa, Poissons's ratio of ν 0.2, and mass density of 2500 kg/m^3. Due to symmetry, only half the arch is modeled, subtending an angle of 60°. The five blocks are separated by contraction joints which, along with the abutment joint, have no assigned tensile strength.

The arch is located at a depth of 45 meters below the water surface and is precompressed by a static pressure of 0.44 MPa. Using this value of water pressure in a design of the arch by circular ring theory (uniform axial force, zero bending moments) where the circumferential compressive stress is given by

$$\sigma = pr/h \tag{3.1}$$

(p = water pressure, r = radius, h = depth), then the arch depth of 5.5 meters corresponds to an allowable compressive stress of 3.6 MPa.

Two finite element models are employed in analysis of the arch: one of slab finite elements and equivalent joint elements (Figure 3.1a) and one of plane finite elements and joint springs (Figure 3.1b). The latter model contains nine spring and eight plane elements through the depth, a discretization similar to that in Figure 2.4. Translational dof of the plane element nodes are transformed to radial and tangential components. Joints are numbered 1 (abutment) through 6 (center), and no joint sliding is permitted. To enforce this constraint in the mesh of Figure 3.1b, the two opposing center nodes at each joint are connected by a rigid radial spring (not shown in the figure).

The structure is first subjected to the forces due to the static pressure of the water as shown in Figure 3.1a. In the slab element mesh, the forces are applied in the radial direction at each of the six nodes. In the plane element mesh, the static pressure is distributed along all the nodes on the upstream face of the mesh. Figure 3.2 shows that the resulting circumferential stress distributions at the joints in the slab element mesh (a) and the plane element mesh (b) are very similar. Departures from the uniform stress distribution due to the presence of bending moments are

well approximated. No joint opening occurs.

With the static loads still acting, the arch is subjected to earthquake ground motions applied in the x (stream) direction. The ground motion applied is the 1940 El Centro record shown in Figure 3.3 which has a peak acceleration of about 0.34g. Only the first four seconds of the record are employed but contain the maximum accelerations. The time step Δt equals 0.02 seconds. Interaction with the water is approximately accounted for by added masses which, in the case of the shell element mesh, are attached to the radial dof at each of the six nodes, and, in the case of the plane element mesh, are attached to and uniformly distributed among the radial dof on the upstream face of the arch. The values of added mass shown in Figure 3.1a are reasonable for water at a depth of 45 meters. Values of the Rayleigh damping coefficients α_0 and α_1 in equation 2.18 are chosen to give damping ratios of 5% at frequencies of 4Hz and 20Hz, giving a minimum damping ratio of 3.7% at about 9 Hz. The Bossak high frequency dissipation parameter α_B described in Chapter II is chosen as -0.2. This value of α_B gives algorithmic damping ratios increasing from 0.3% at 4 Hz to $2\frac{1}{2}$% at 10 Hz to 6% at 20 Hz. At high frequencies both the Rayleigh and algorithmic damping increase rapidly. Incidentally, the first six eigenvalues of the linear structure (including added mass) range from about 3.5 Hz to 24 Hz.

Linear dynamic analyses of the structure are performed by not allowing any joint to open. Figures 3.4 a to i present the results; slab element mesh results are shown solid and the plane element mesh results are shown dashed. Included are time histories at joints 1 and 6 of radial displacement (joint 6 only), axial force, moment, and circumferential stress at the upstream and downstream faces. The two sets of curves in Figure 3.4 agree well. Some differences do exist and are attributed to the different discretizations; i.e., slab elements vs. the refined plane element mesh.

Figures 3.5 a to n present results for the nonlinear dynamic analyses of the arch using the slab and plane element discretizations. The time history responses plotted include those of Figure 3.4 as well as the amount of opening at the upstream face of joint 1 and at the upstream and downstream faces of joint 6 and the position of

the contact point at each joint, i.e., "crack tip" location. In Figures 3.5 b and i, the upper and lower traces represent opening from the upstream and downstream faces, respectively, of the joint. Agreement between the two sets of curves, while not quite of the quality obtained with the linear responses, is still reasonable. Indications are that accuracy of the equivalent joint element improves for more severe openings (Figures d and j).

In conclusion, taking into account the different finite element discretizations, it may be said that the equivalent joint element developed in Chapter II represents the opening behavior of an interface joint reasonably well including opening width and joint axial force, moment and stress. The effect of the joint on the overall response of the structure is well captured. Needless to say, use of the mesh shown in Figure 3.1a is computationally much more efficient than use of the mesh shown in Figure 3.1b. The nonlinear analysis of the arch using the plane element mesh required about 50,000 seconds of CPU time on a PRIME 500 computer. The corresponding analysis using the slab element mesh took less than 700 seconds of CPU time. In addition, since much of the 700 seconds was set-up time, which remains constant regardless of the earthquake duration, a longer duration would show an even more dramatic difference in computation time.

3.2 Nonlinear Analyses of Jointed Arch

With the ability of the equivalent joint element to adequately model the opening and closing mechanism of an interface joint in a structure as well as its effect on the overall behavior of the structure confirmed, a more comprehensive study of the same arch structure described previously using the slab element discretization is performed here. The effect of nonlinearities on the arch response is revealed by examining the response to the El Centro ground motion (Figure 3.3) with acceleration scaled by $f = 0.50$, $f = 0.75$, $f = 1.00$ and $f = 1.25$. Again, the first four seconds are applied in the x direction. All parameters of the previous solution including geometry, static loads, added masses and damping are kept the same except that a

2 MPa tensile strength is assigned to the abutment (joint number 1).

Results from the nonlinear analyses are shown in Figures 3.6 a to f and include time histories of radial displacement (joint number 6), upstream opening (joint number 1), axial force, $-M/P$, position of joint contact and maximum compressive stress (the latter quantities at both joints). The quantity $-M/P$ represents the position of the axial force P (measured from the mid-depth line), and varies between $+2.75$ meters (upstream face) and -2.75 meters (downstream face). In plotting the maximum compressive stress at a joint, no distinction is made between whether the stress occurs at the upstream face or downstream face. This information can be determined from the sign of $-M/P$. As described in Chapter II and illustrated by Figure 2.6, the location of the joint contact point and the value of the maximum compressive stress across a joint are computed from M and P using a linear compressive stress distribution with a no-tension zone.

Each part of Figures 3.6 a to f contains the responses to all four earthquake ground motions. All curves are solid lines. In each part, the curve for $f = 1.25$ exhibits the greatest response; the curves for $f = 1.00$, 0.75 and 0.50 show progressively less response. The radial displacement curves in Figure 3.6a indicate that the displacement response of the dam increases approximately linearly with the level of excitation even though significant joint opening occurs (see discussion of Figure 3.6e below). The amplitudes of the displacement curves closely correspond to those obtained from linear analysis using the same excitation levels (not shown). Evident in Figure 3.6a, as well as the other figures, is a slight period elongation in the response which becomes more pronounced as the excitation level increases. This period elongation is due to a reduction in stiffness caused by joint opening. Where the response and joint opening are smaller near the ends of the time histories, the period elongation is less.

The axial force response in Figure 3.6c is similar at joints 1 and 6, and, in fact, at all joints. This feature is also true under static loading. In one cycle, at time $t = 2.3$ seconds, P is reduced to about 12% of its static value for the case where the ground acceleration is scaled by a factor of 1.25. Therefore, a somewhat more

intense excitation would cause a complete separation and a possible violation of the no-slip assumption.

Examination of Figures 3.6d and e reveals the joint opening behavior. At $f = 0.50$, joint opening is essentially confined to joint 1 where the penetration depth is about 2.5 meters (less than one-half of the joint depth). At $f = 1.25$, joints 1 and 6 open severely to depths of about 4 meters (about three-quarters of the joint depth). Figure 3.6f shows that the maximum compressive stress reaches about 20 MPa at both joints. These stress levels are probably permissible for many concrete dams for an unusual loading condition. Additionally, if the ultimate concrete strength exceeds about 30 MPa (a reasonable value if $E = 27{,}500$ MPa) then the assumption of a linear stress-strain relation is not too bad. To put the joint opening in perspective, Figure 3.6b shows the time history of the opening at the upstream face of joint number 1. At $f = 1.25$, the maximum opening is about 0.2 cm with a duration of 0.18 seconds. This time history may prove useful in a future analysis to determine the extent of water entering an open joint, an effect not considered here.

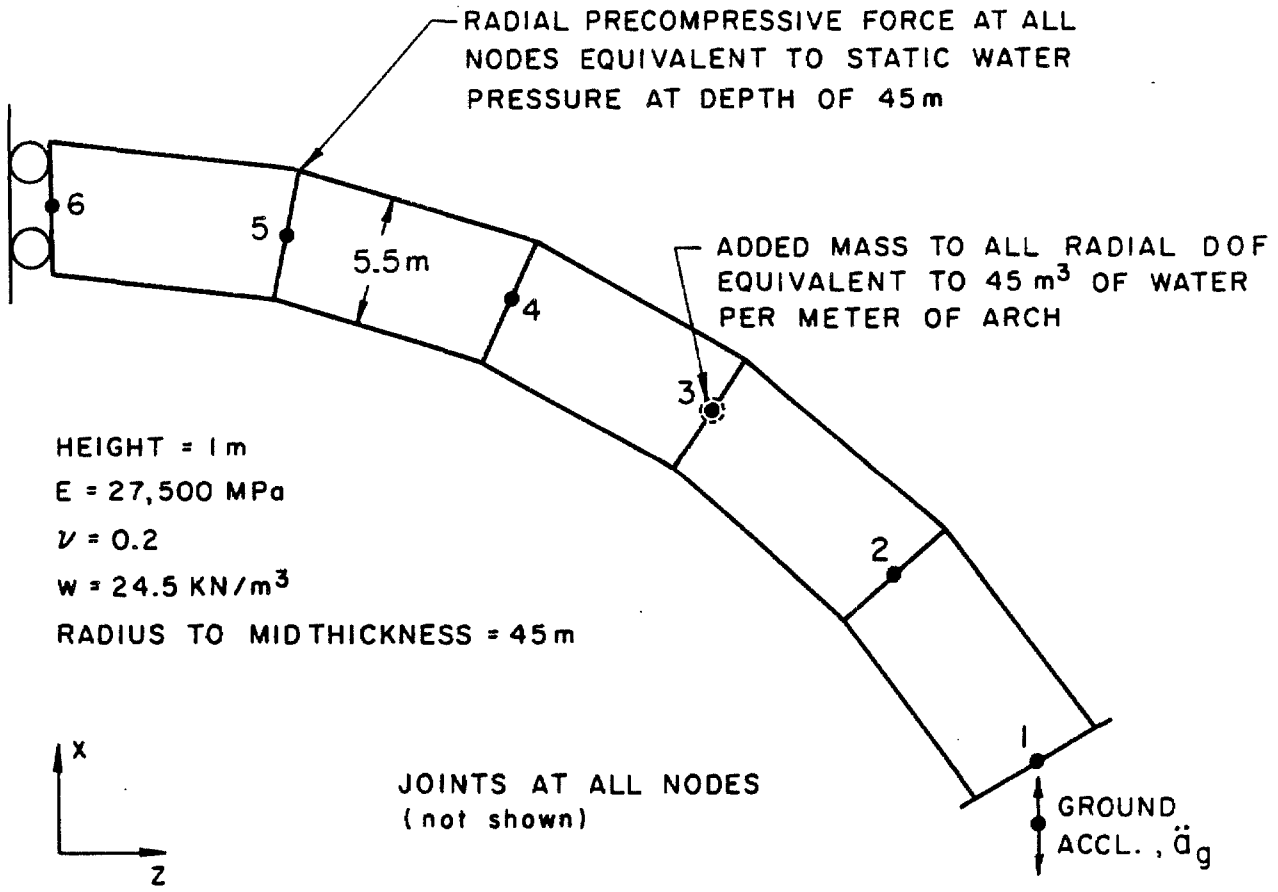

a. Slab element mesh with equivalent joint elements.

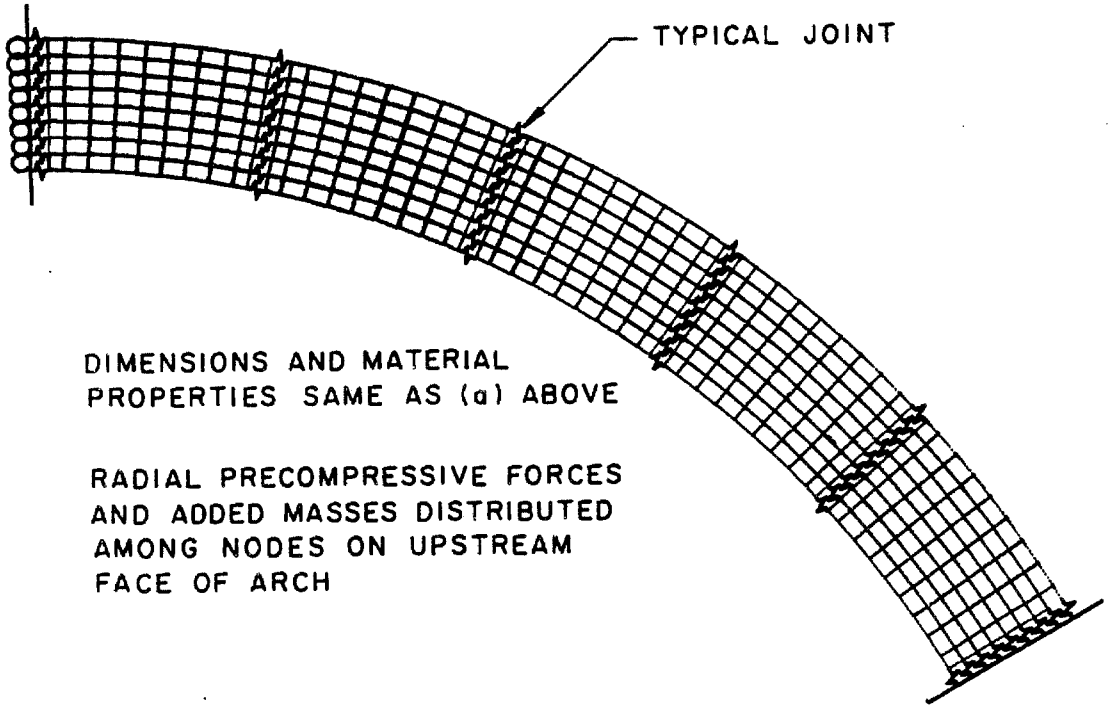

b. Plane element mesh with joint springs. Joint widths are exaggerated.

Figure 3.1 Fixed ended arch used to verify the equivalent joint element.

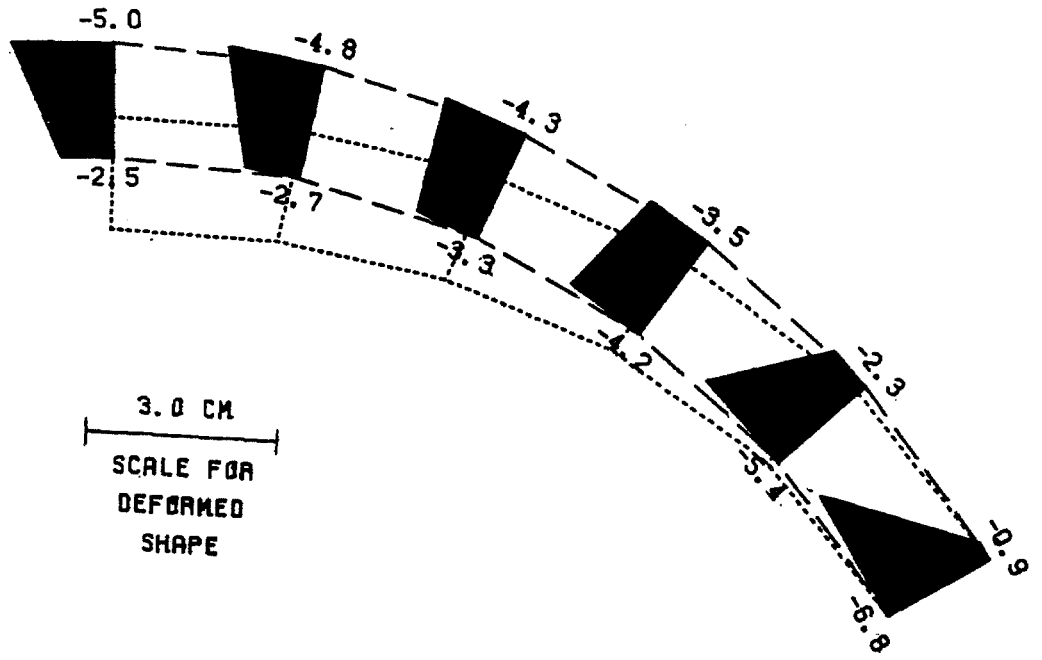

a. Slab element mesh with equivalent joint elements.

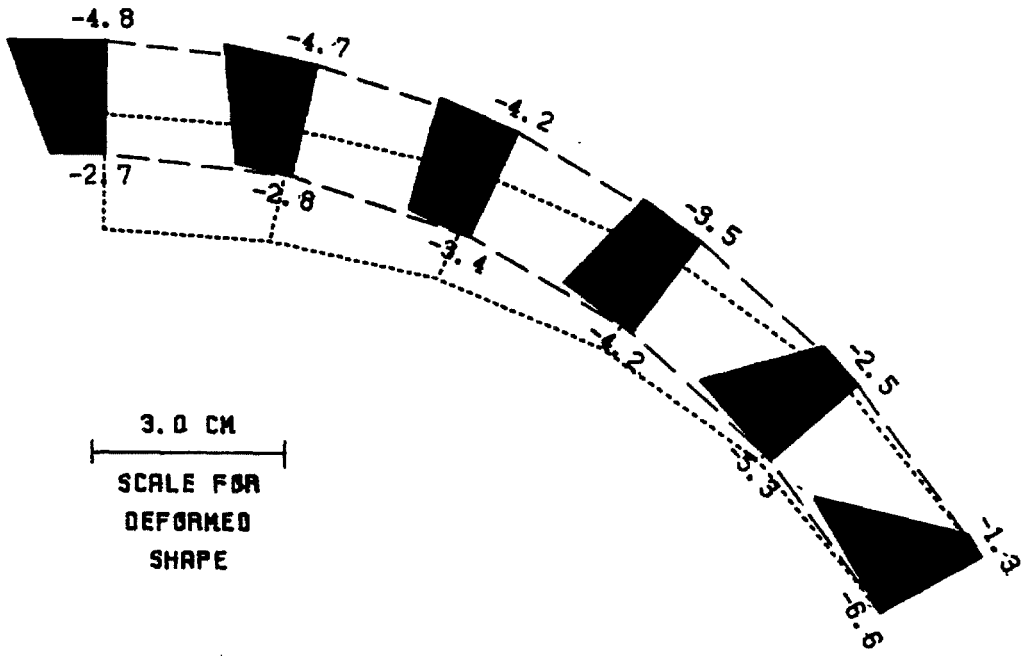

b. Plane element mesh with joint springs.

Figure 3.2 Compressive stresses (in MPa) due to hydrostatic pressure. Deformed shape shown dotted.

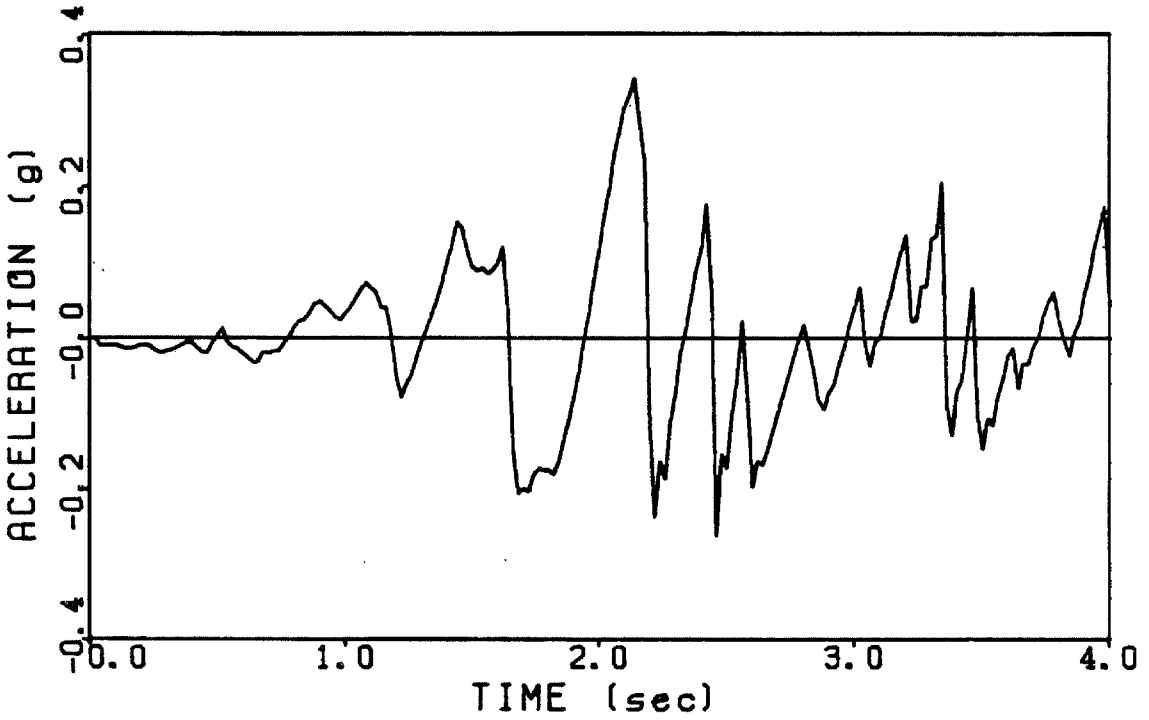

Figure 3.3 North-south component of 1940 El Centro ground acceleration.

Figure 3.4 a to i (next 5 pages). Comparison of the dynamic linear responses computed from the slab-equivalent joint element mesh and the plane element-joint spring mesh.

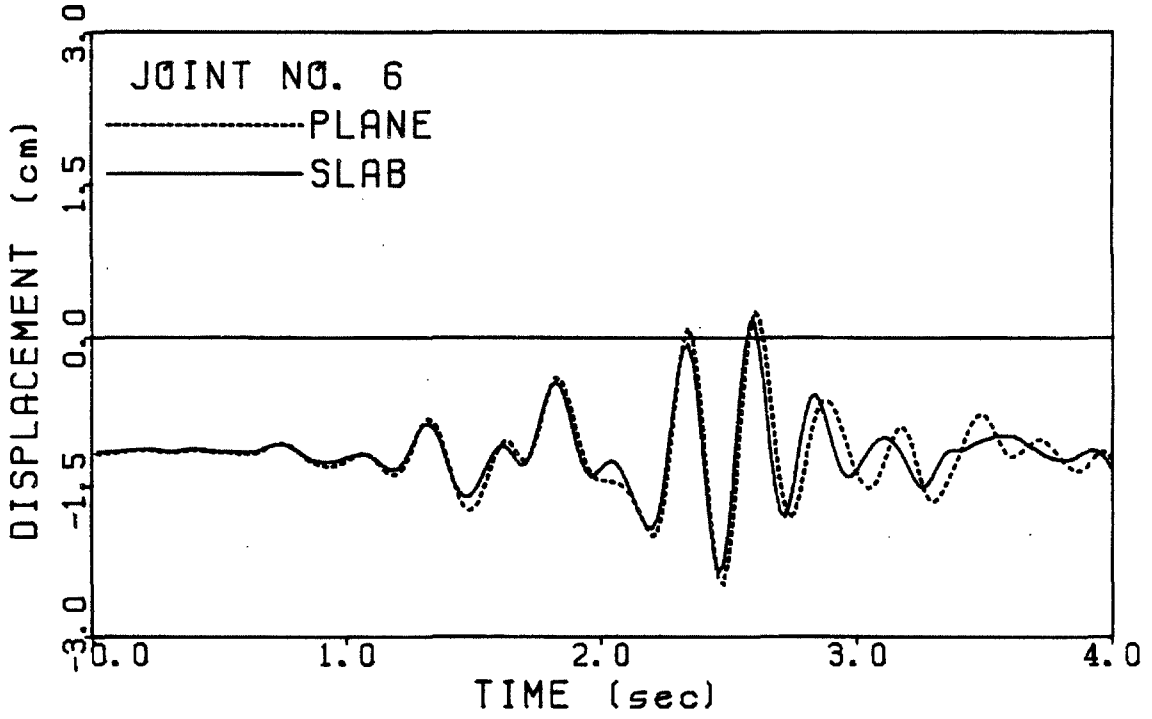

a. Radial displacement at joint 6 versus time.

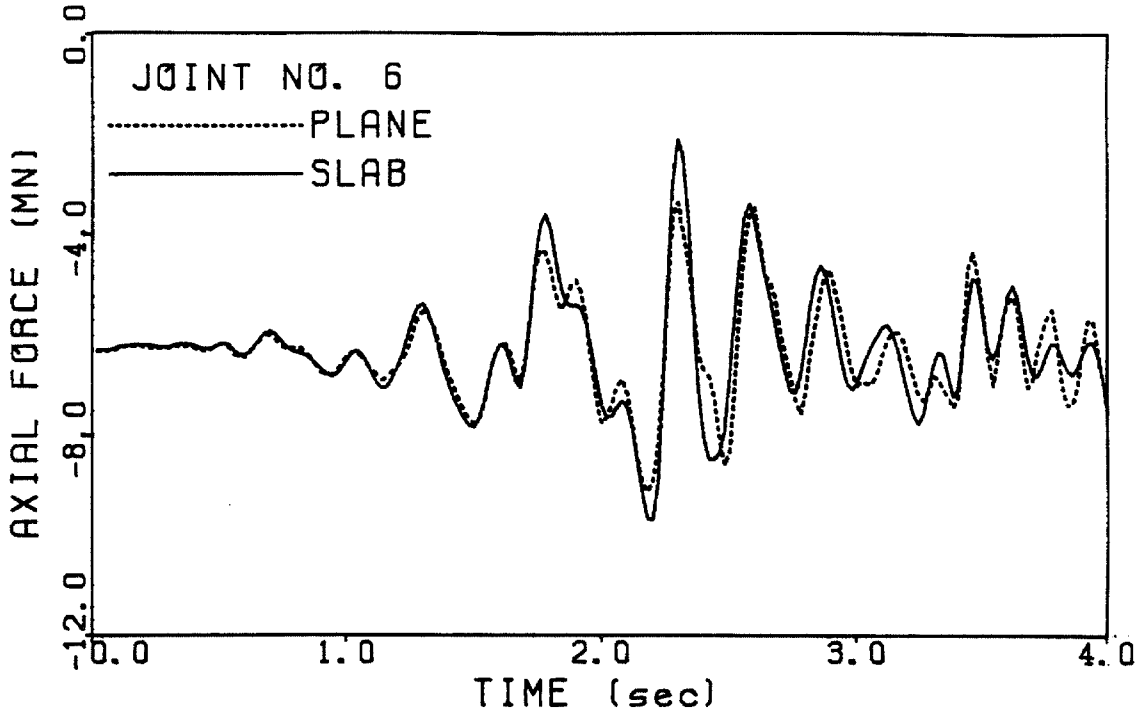

b. Axial force at joint 6 versus time.

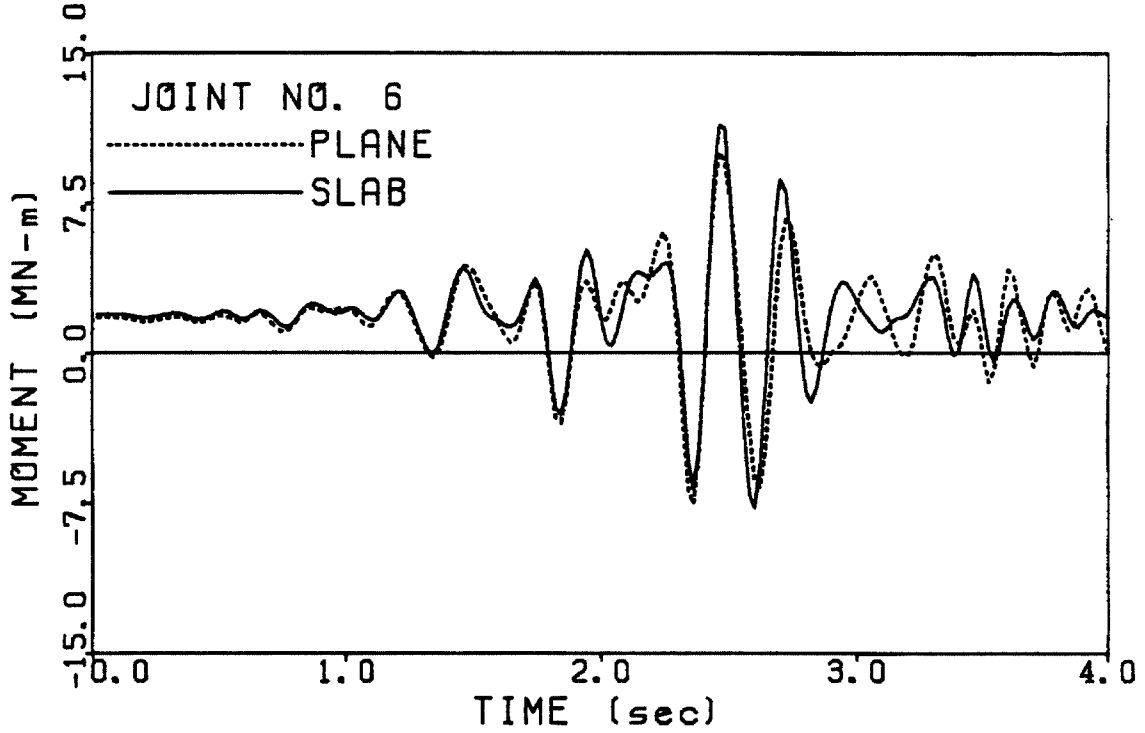

c. Moment at joint 6 versus time.

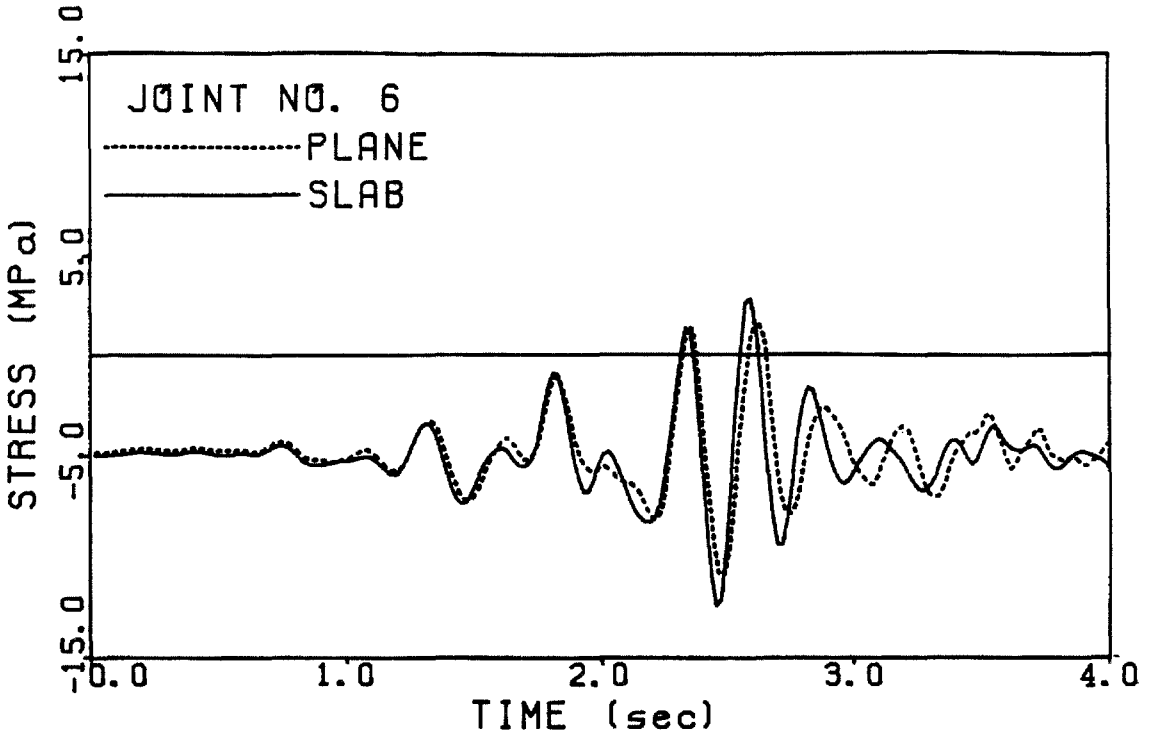

d. Circumferential stress at upstream face at joint 6 versus time.

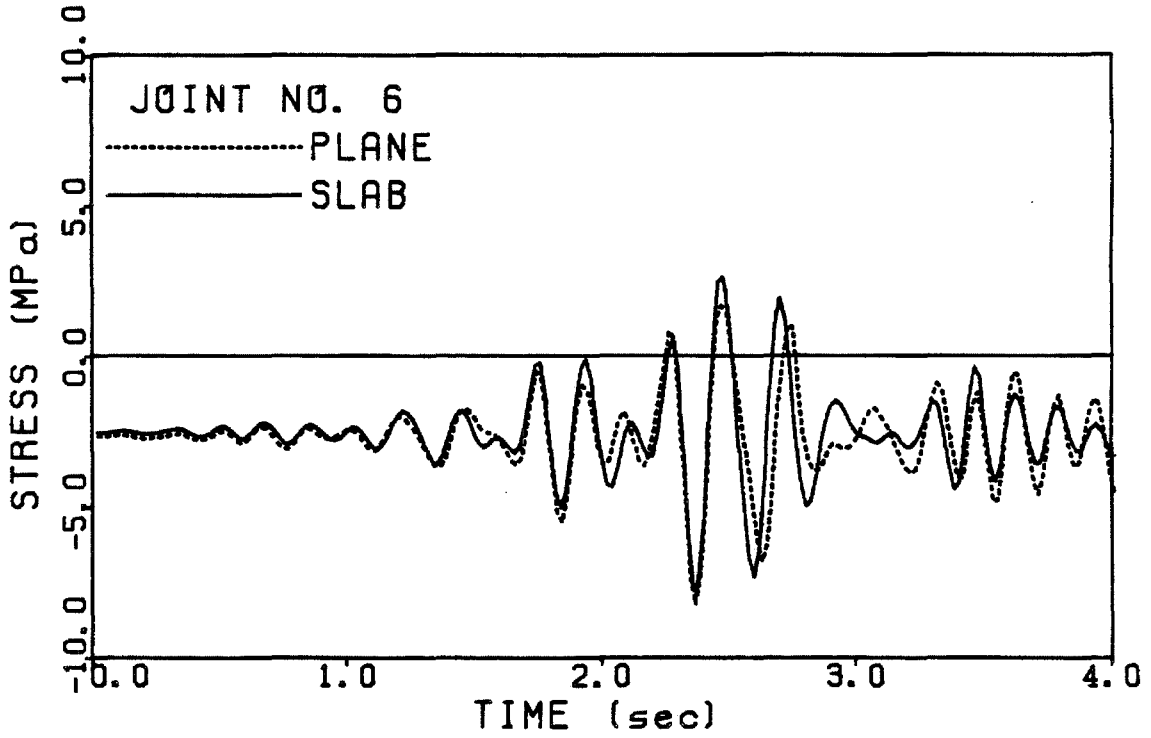

e. Circumferential stress at downstream face at joint 6 versus time.

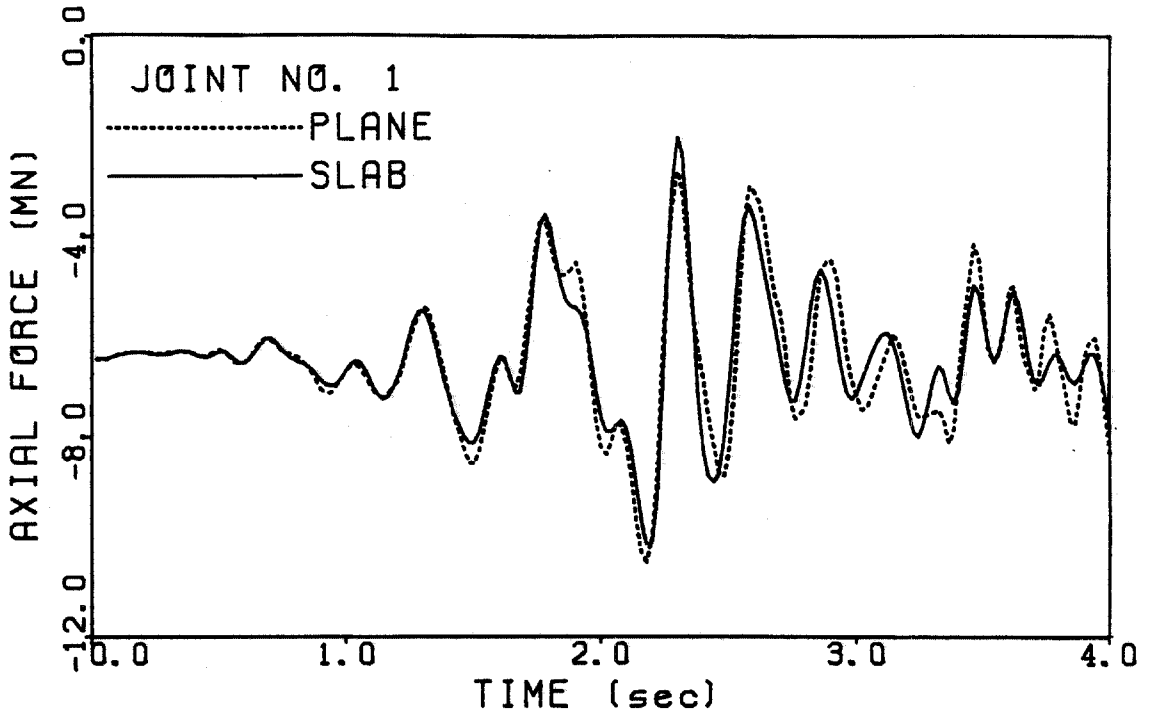

f. Axial force at joint 1 versus time.

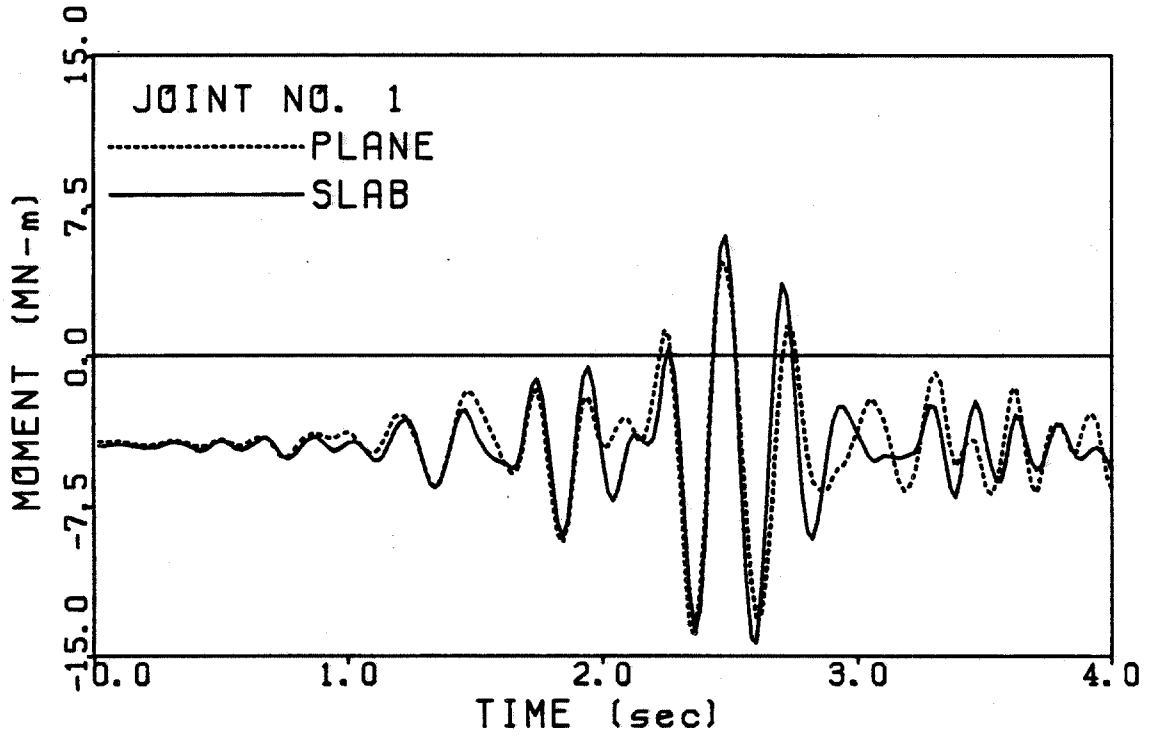

g. Moment at joint 1 versus time.

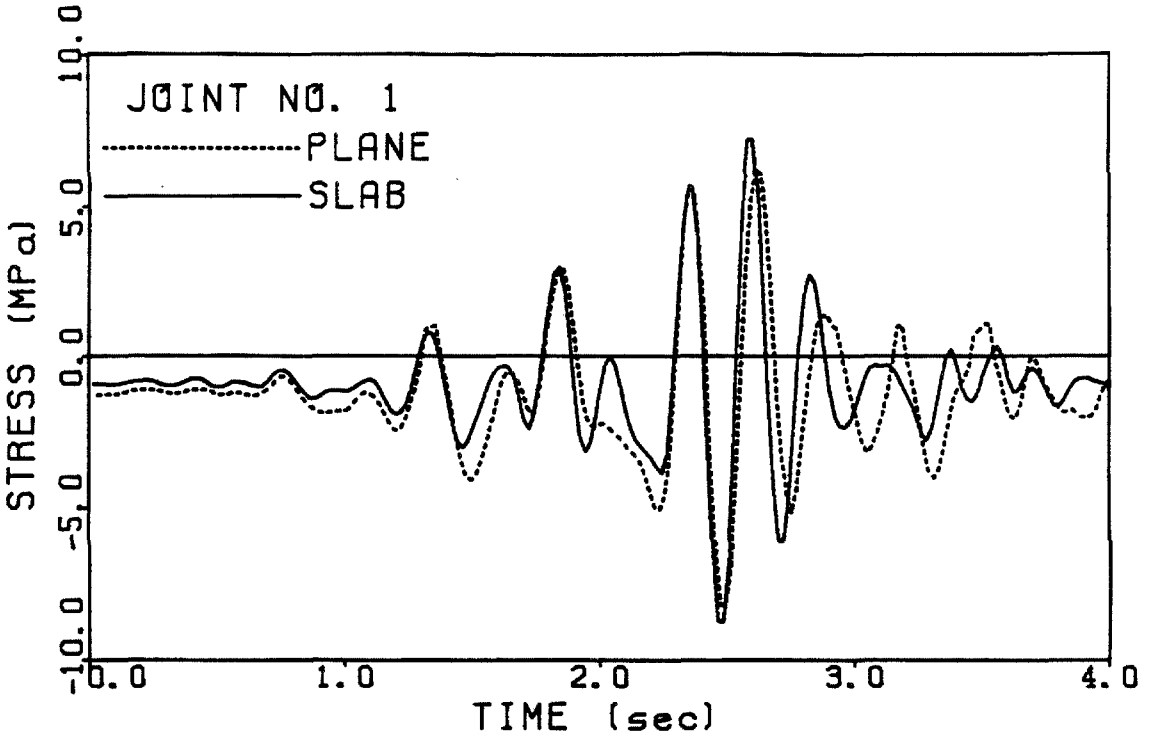

h. Circumferential stress at upstream face at joint 1 versus time.

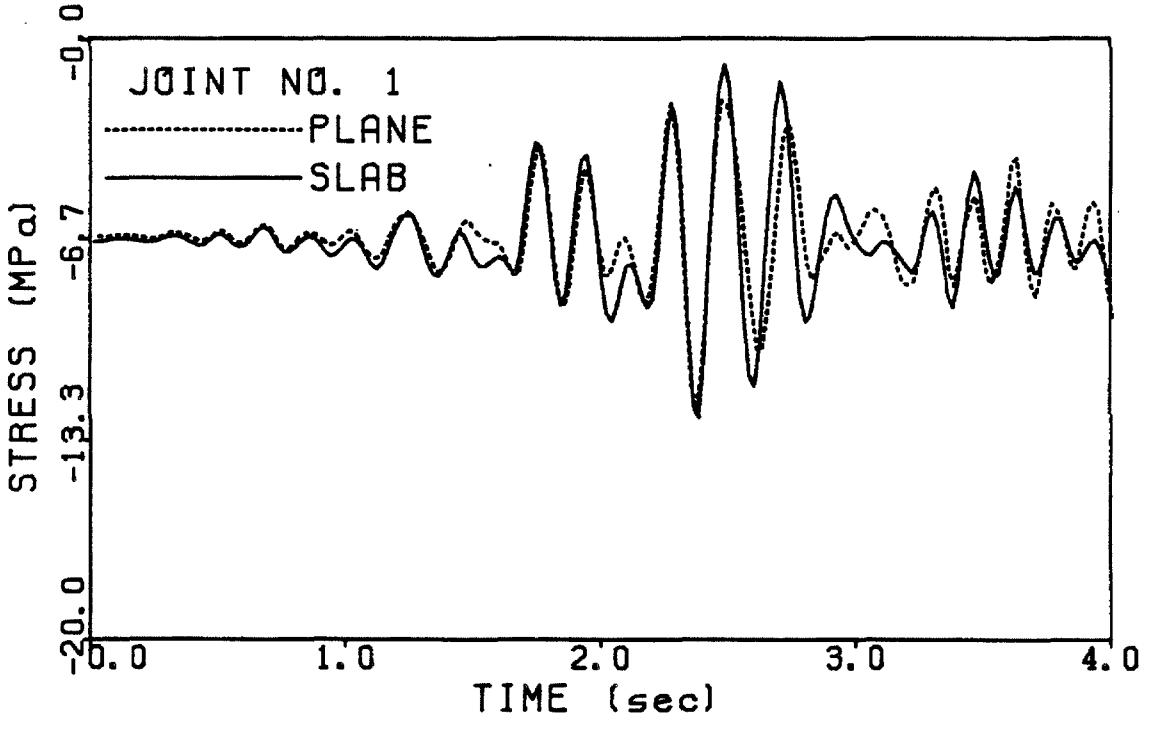

i. Circumferential stress at downstream face at joint 1 versus time.

Figure 3.5 a to n (next 7 pages). Comparison of the dynamic nonlinear responses computed from the slab-equivalent joint element mesh and the plane element-joint spring mesh.

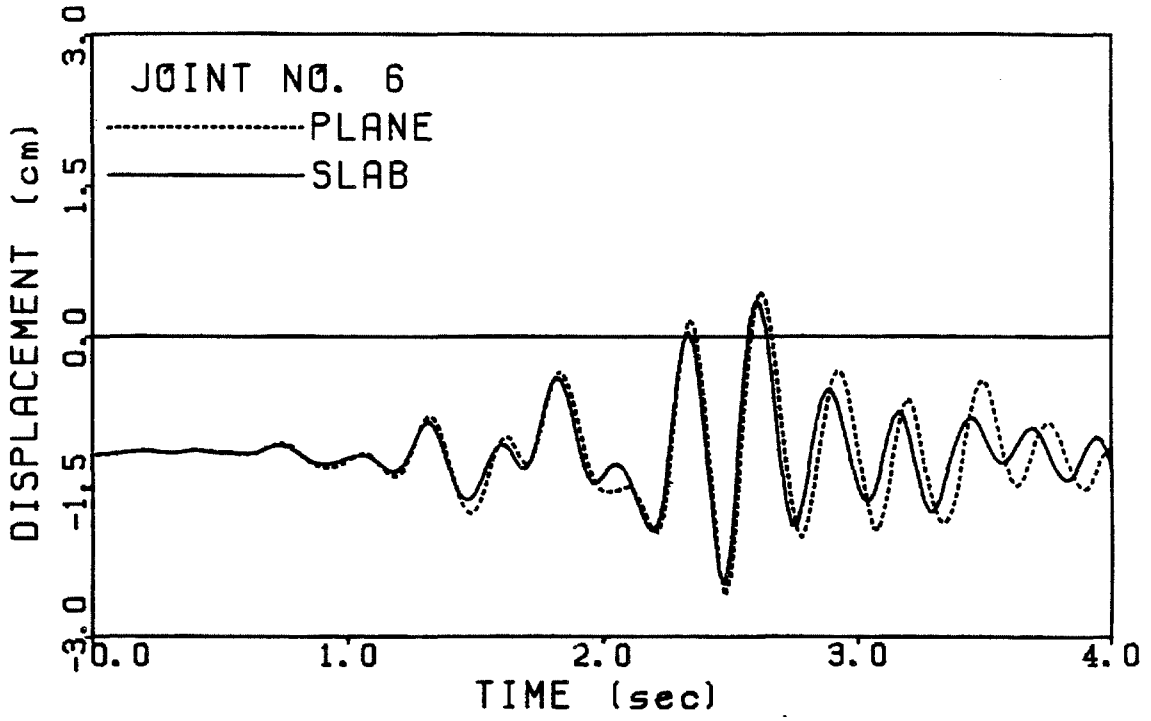

a. Radial displacement at joint 6 versus time.

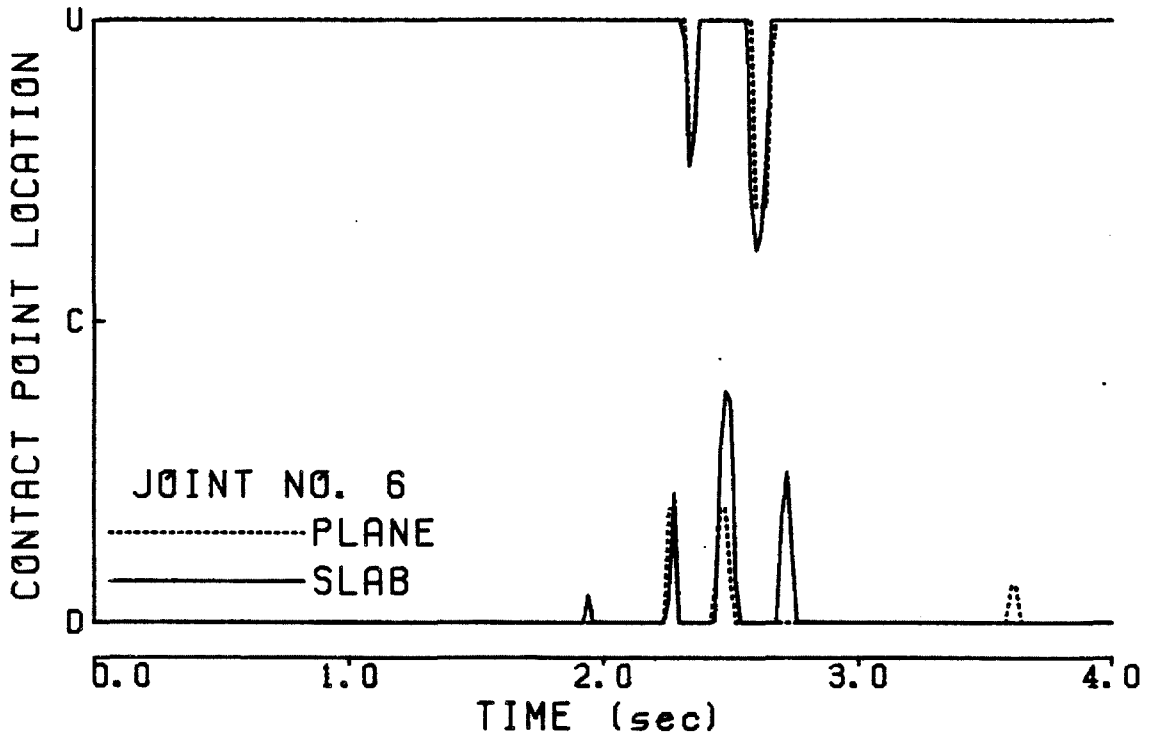

b. Position of joint contact at joint 6 versus time.

(U = upstream face. D = downstream face. C = center plane).

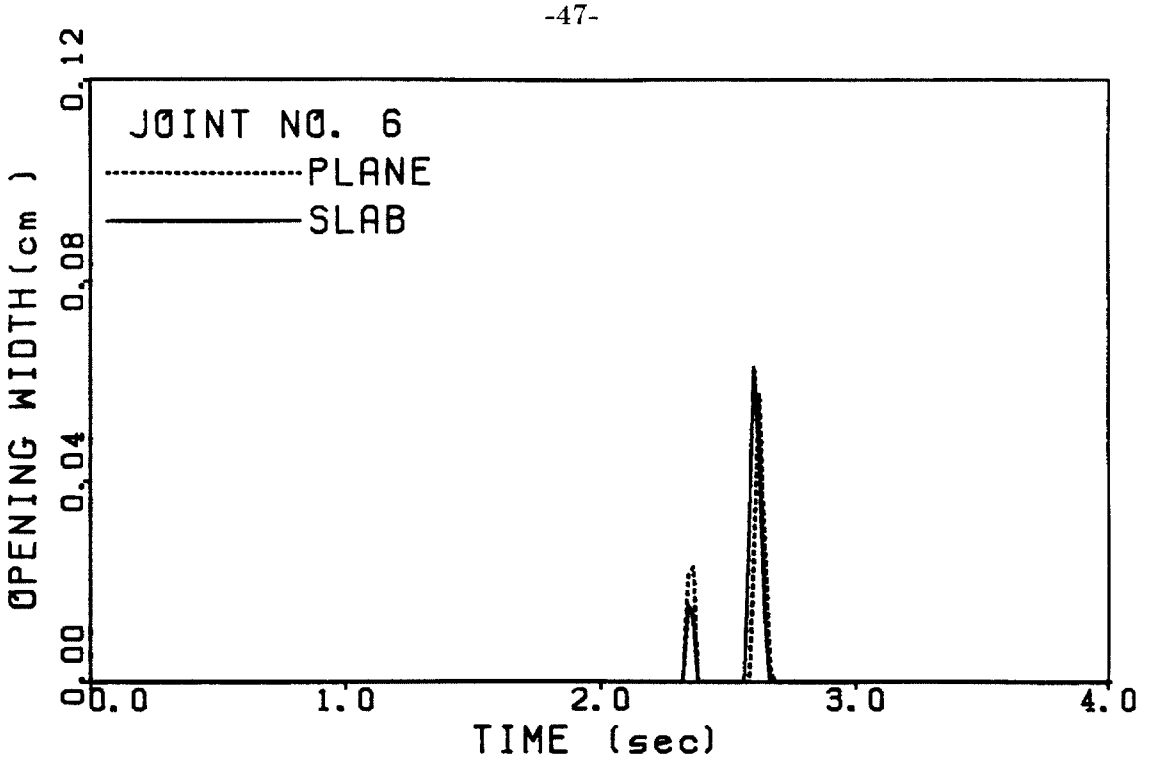

c. Opening of joint 6 at upstream face versus time.

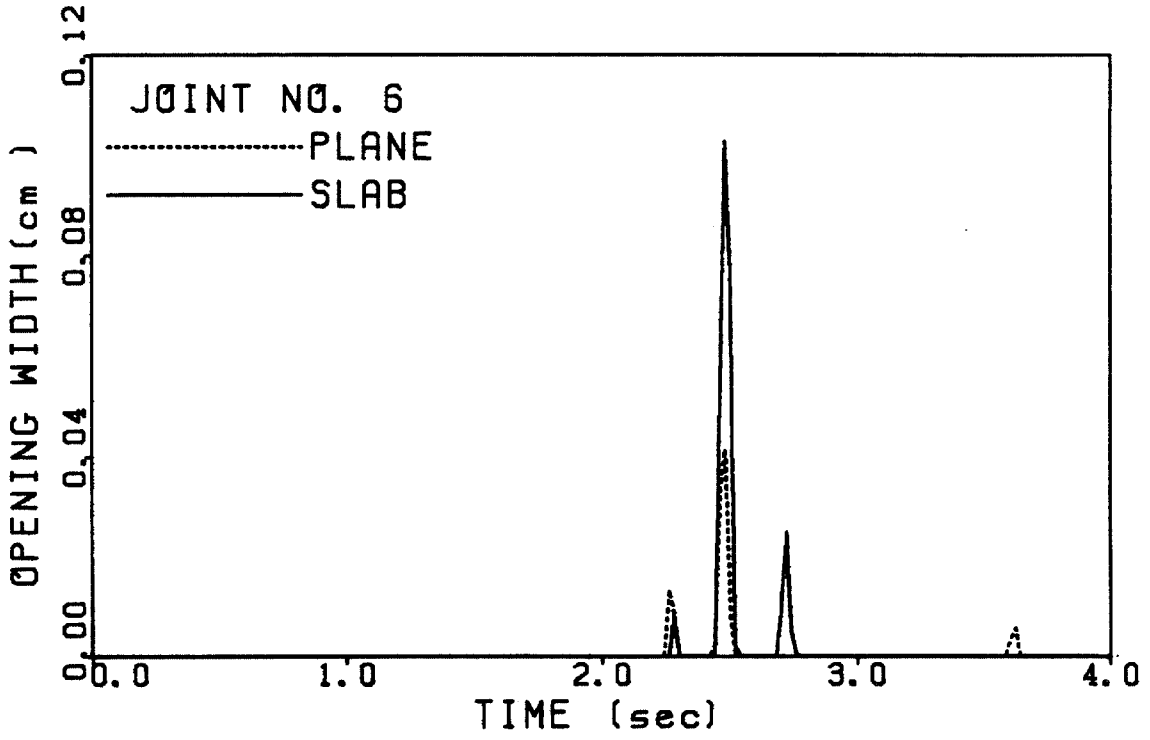

d. Opening of joint 6 at downstream face versus time.

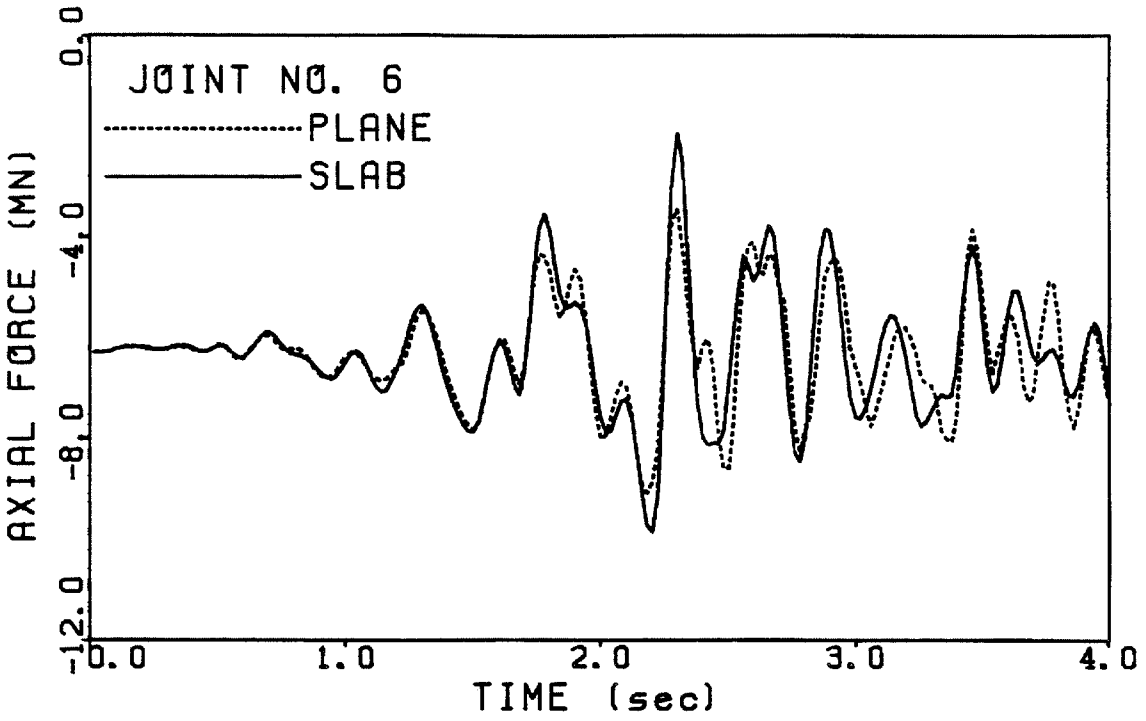

e. Axial force at joint 6 versus time.

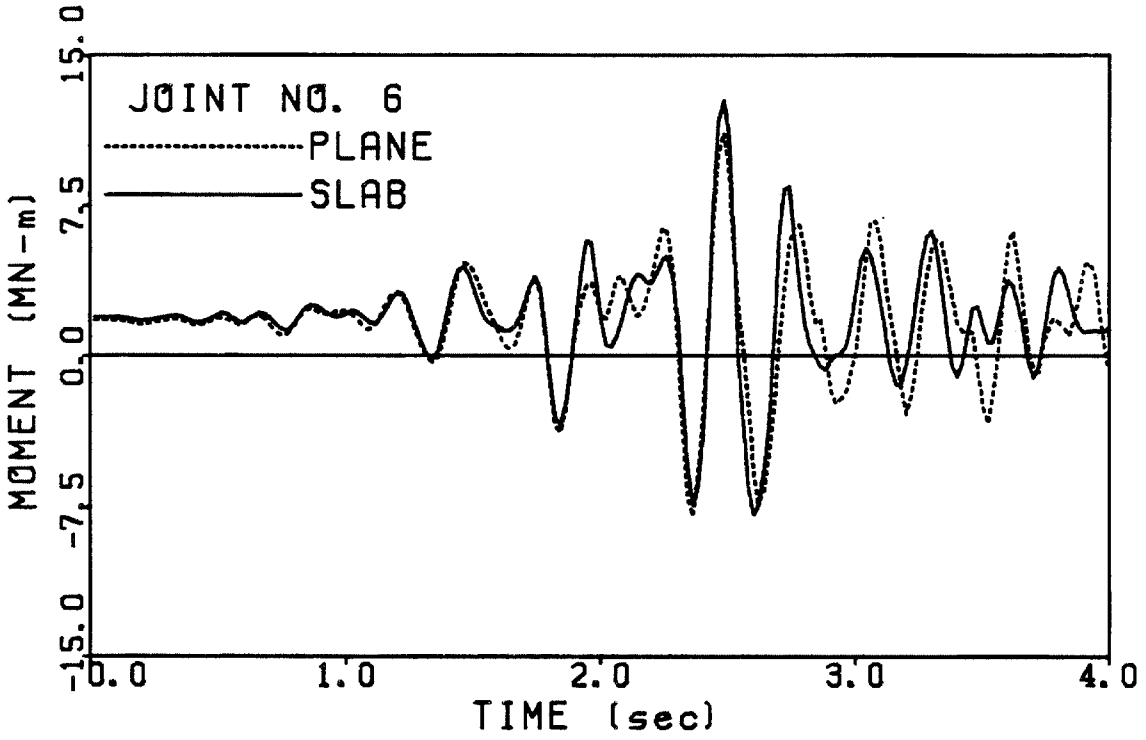

f. Moment at joint 6 versus time.

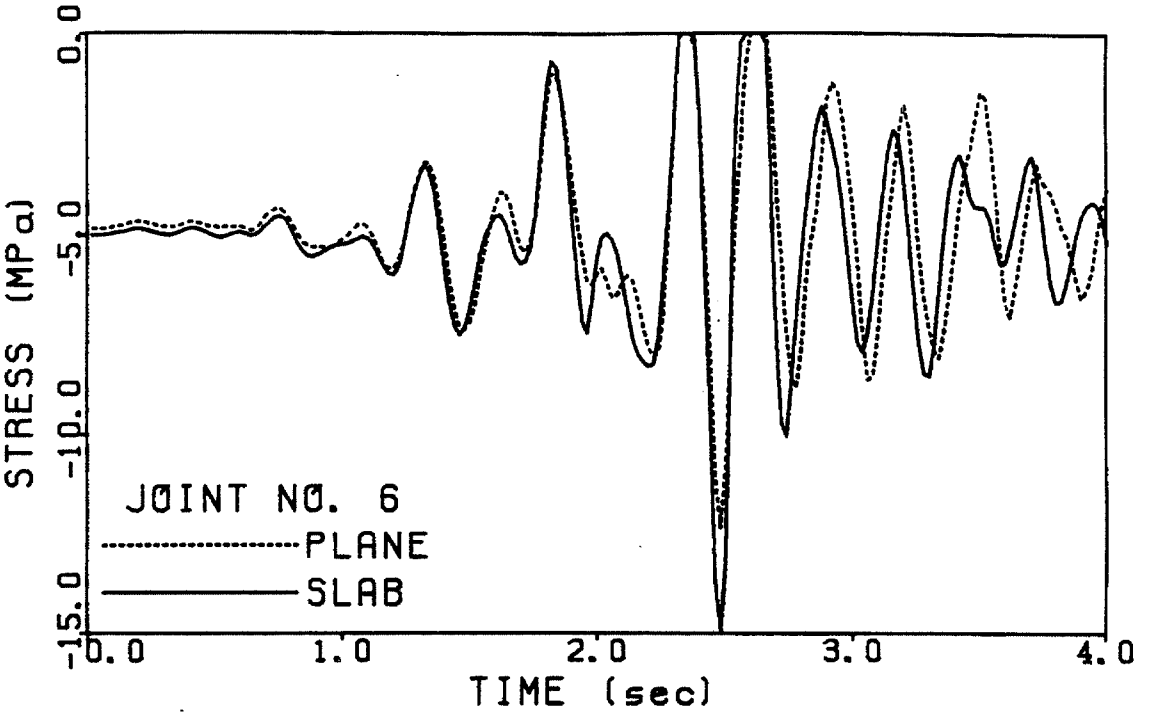

g. Circumferential stress at upstream face at joint 6 versus time.

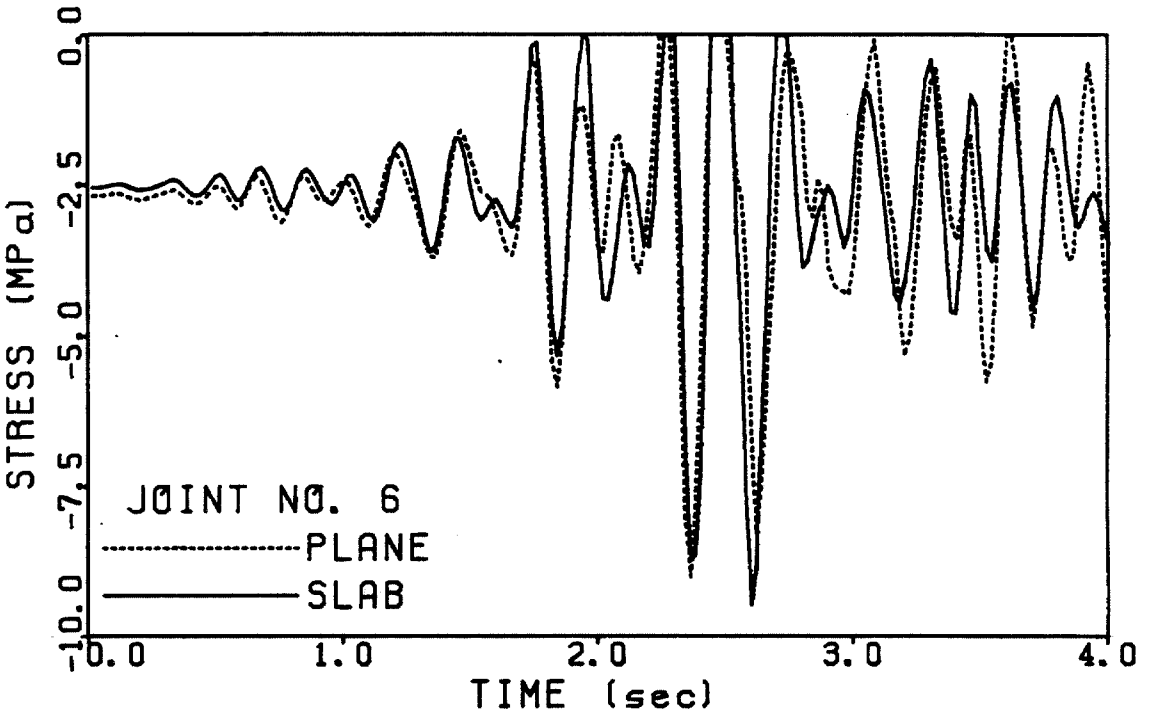

h. Circumferential stress at downstream face at joint 6 versus time.

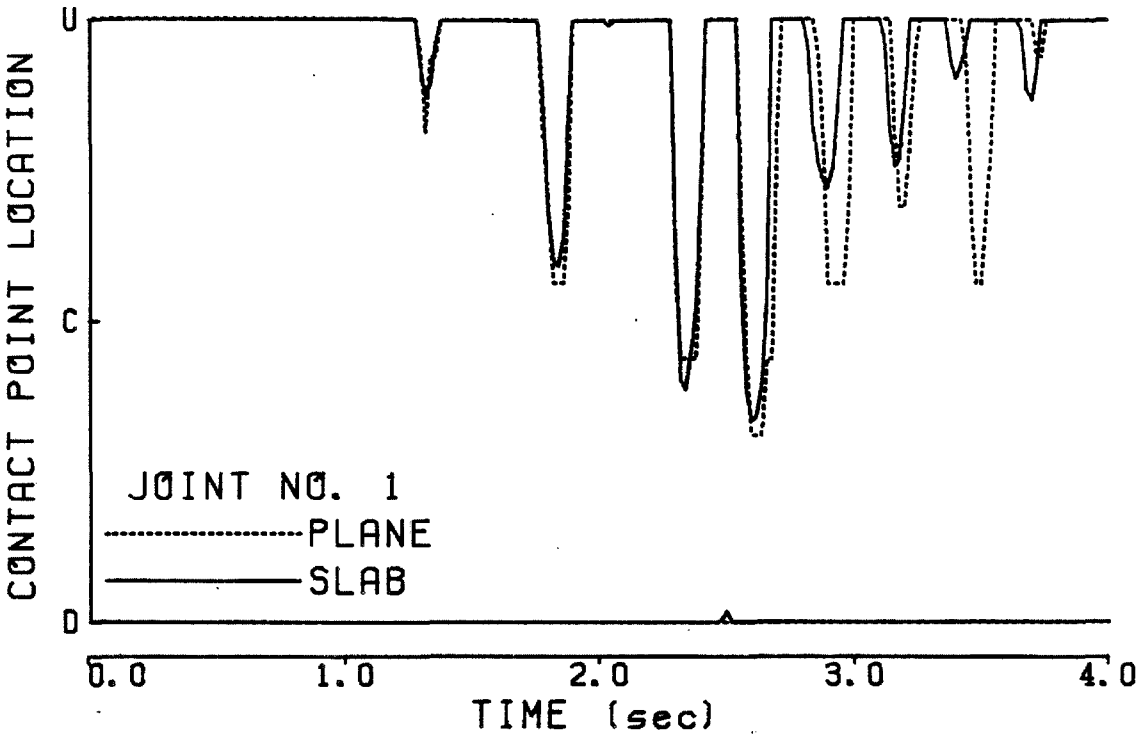

i. Position of joint contact at joint 1 versus time.
(U = upstream face. D = downstream face. C = center plane).

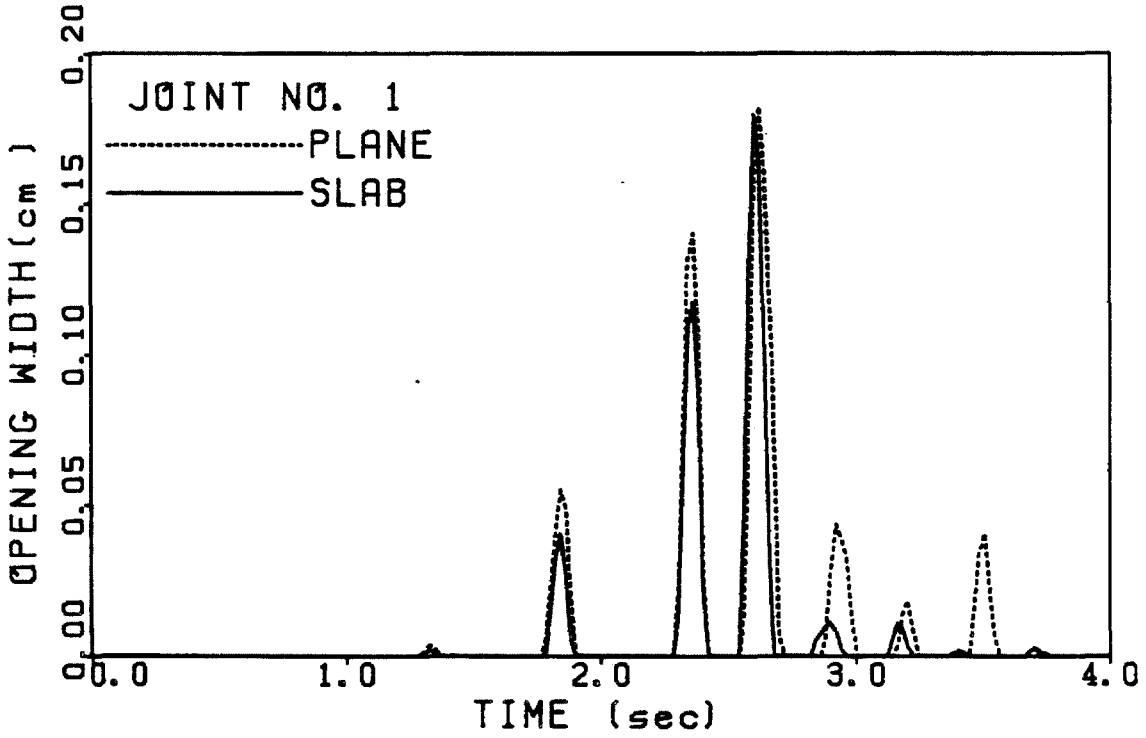

j. Opening of joint 1 at upstream face versus time.

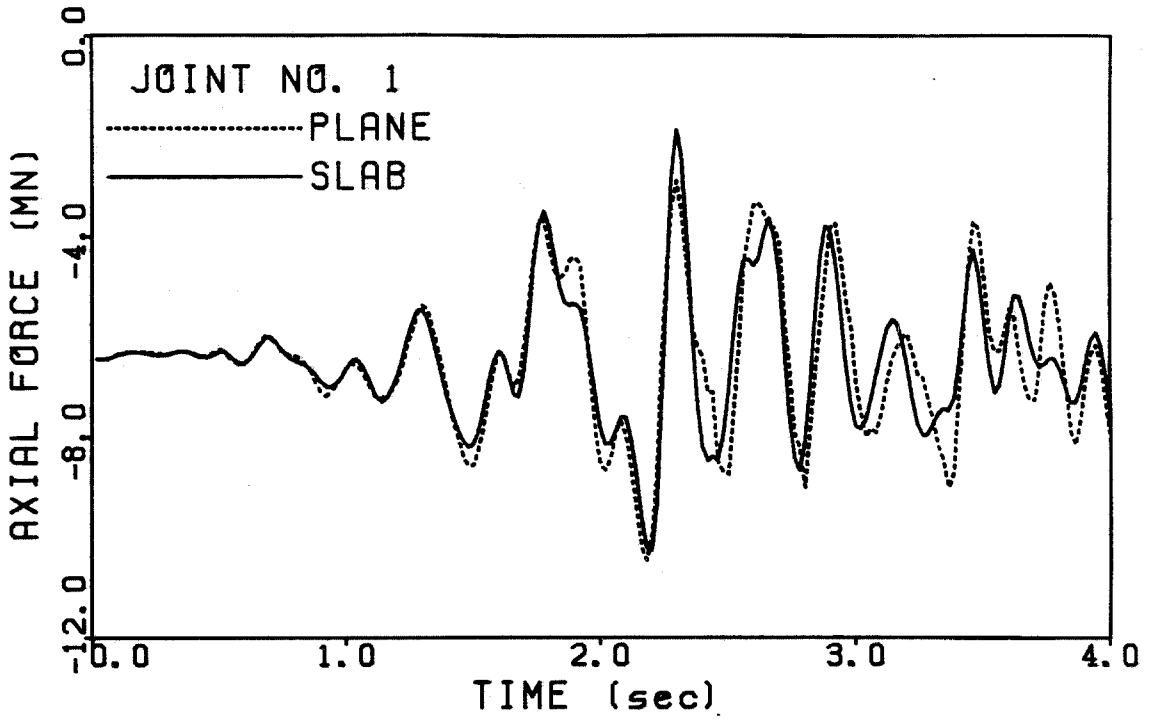

k. Axial force at joint 1 versus time.

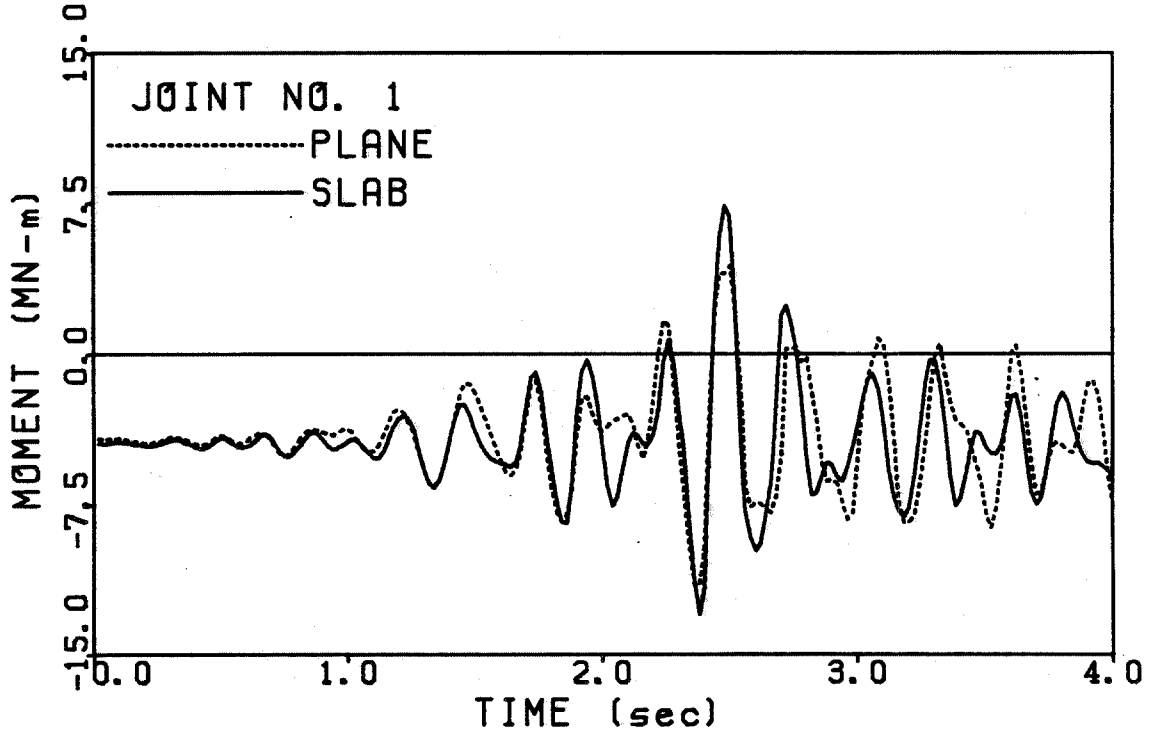

l. Moment at joint 1 versus time.

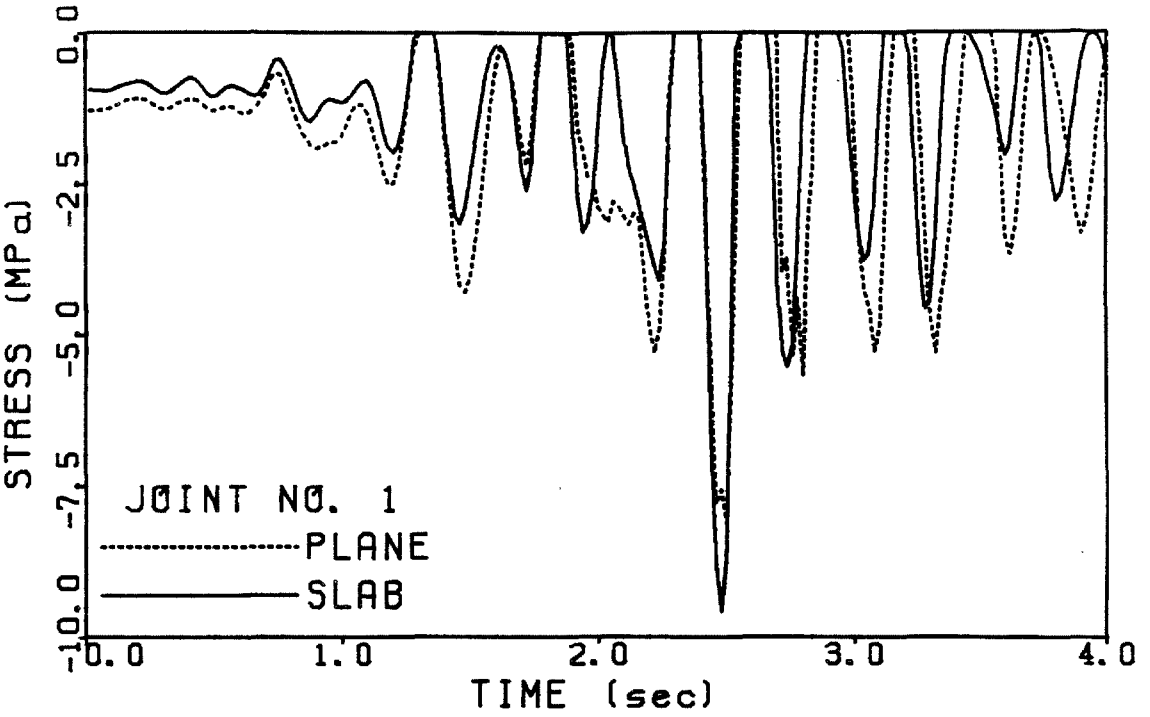

m. Circumferential stress on upstream face at joint 1 versus time.

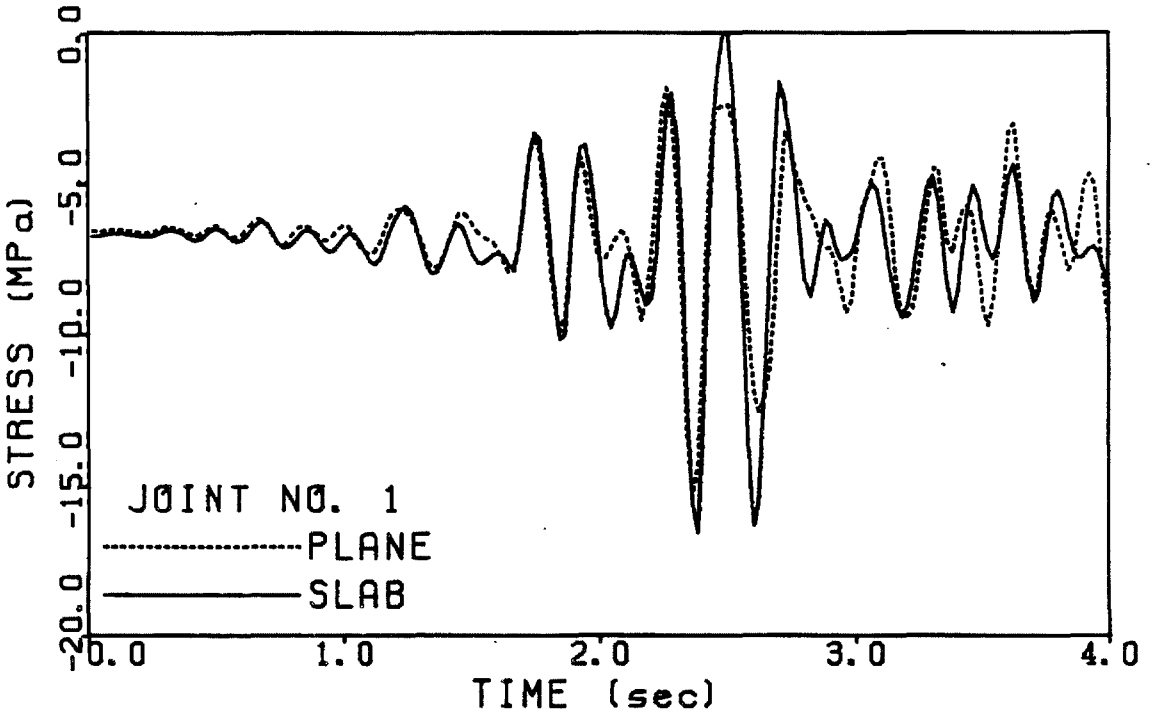

n. Circumferential stress at downstream face at joint 1 versus time.

Figure 3.6 a to f (next 5 pages). Dynamic nonlinear responses of the arch with the slab-equivalent joint spring mesh for various intensities of ground motion as specified by the scale factor f.

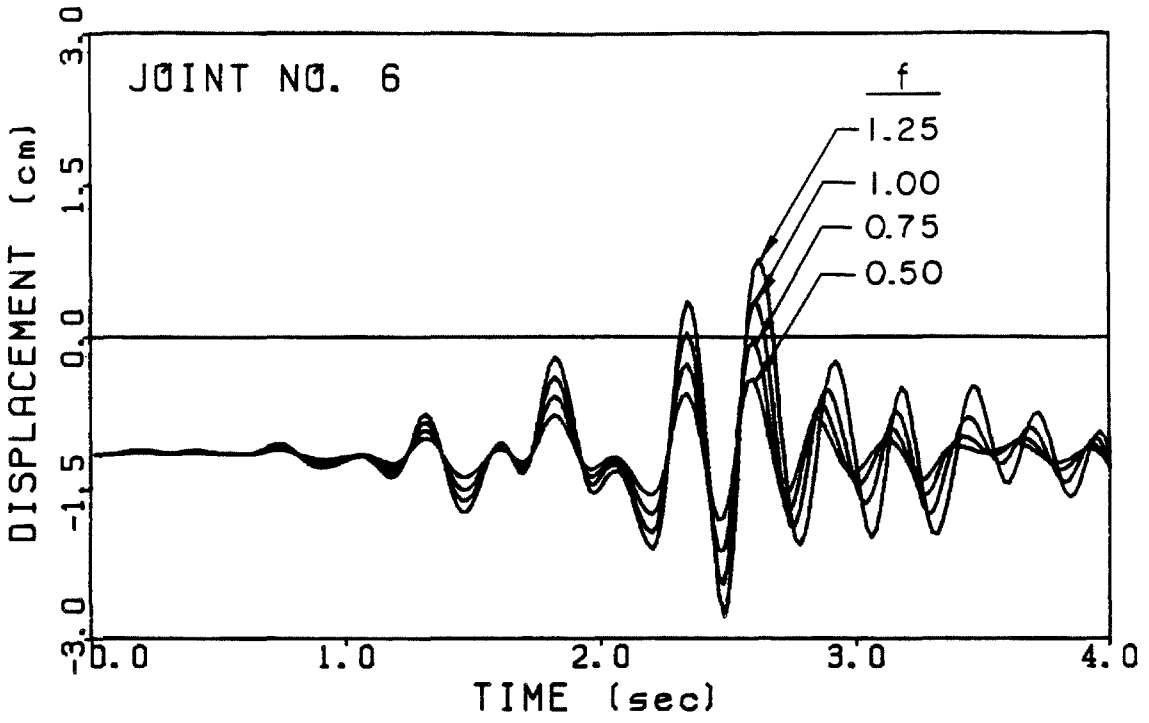

a. Radial displacement at joint 6 versus time.

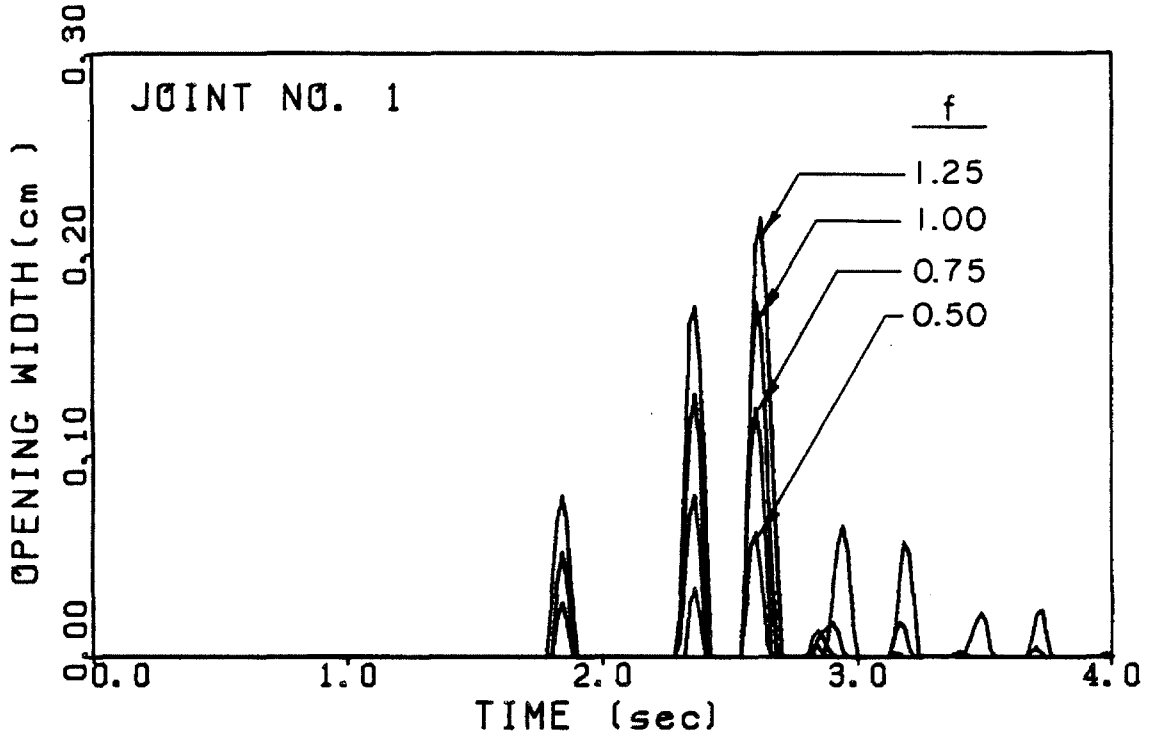

b. Opening of joint 1 at upstream face versus time.

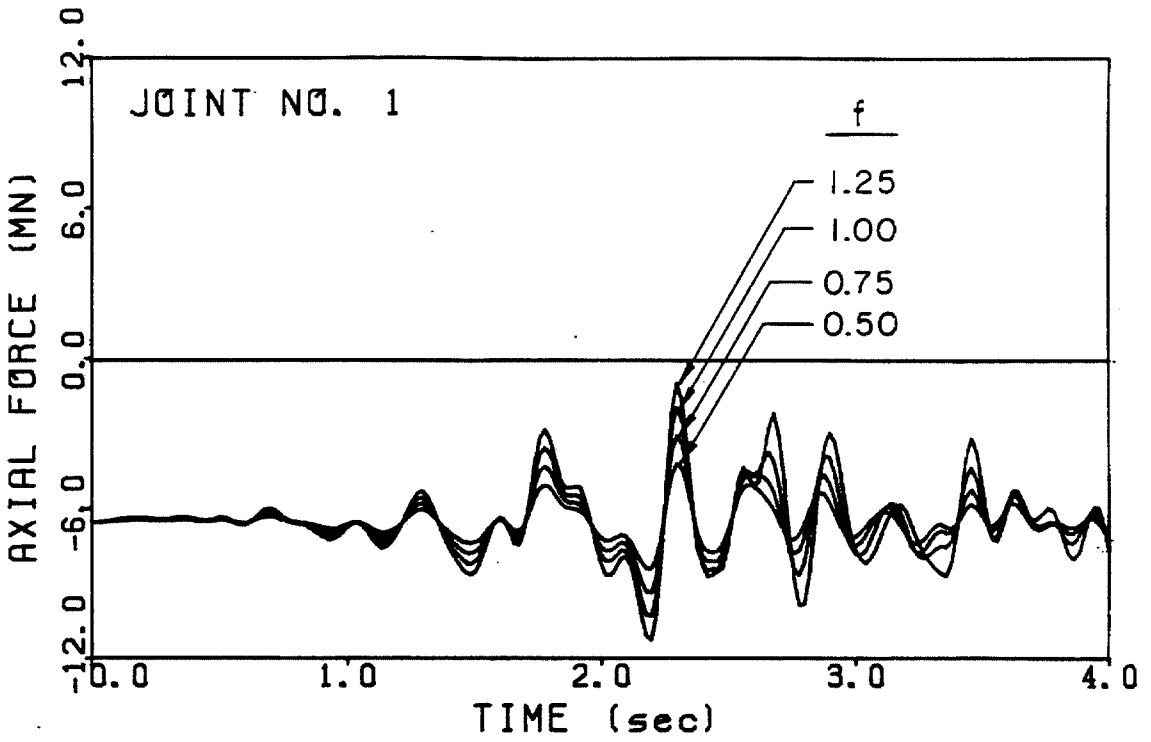

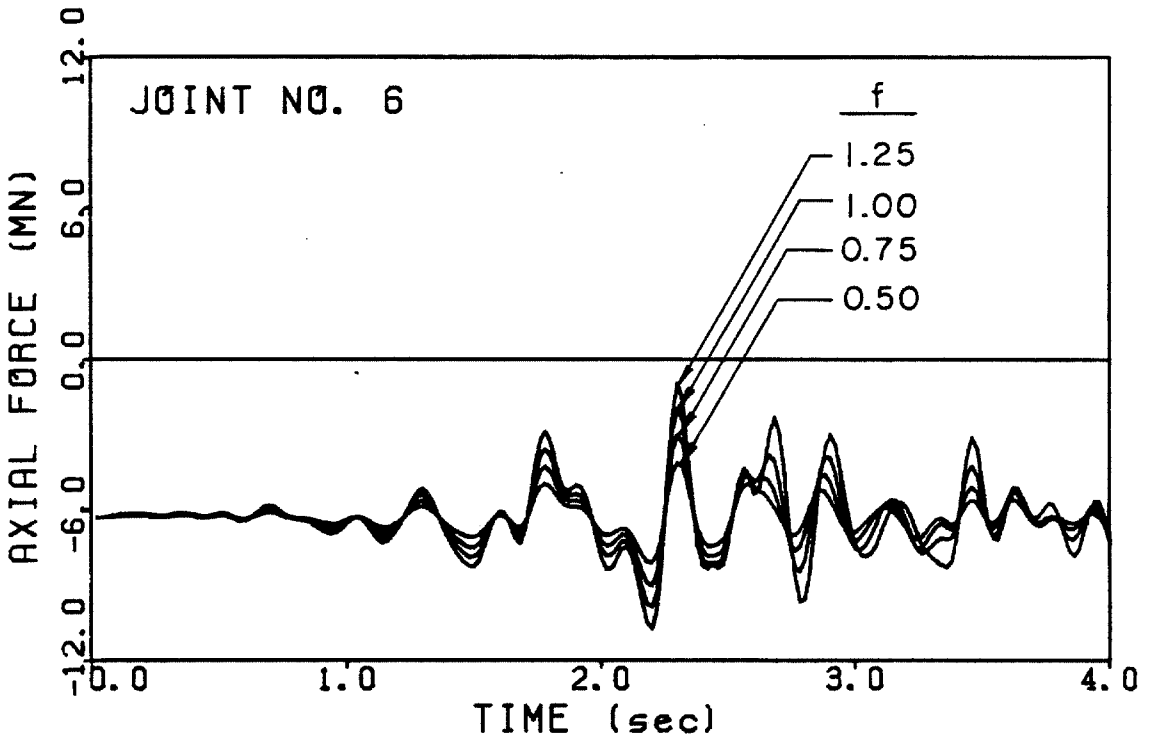

c. Axial force versus time at joints 1 and 6.

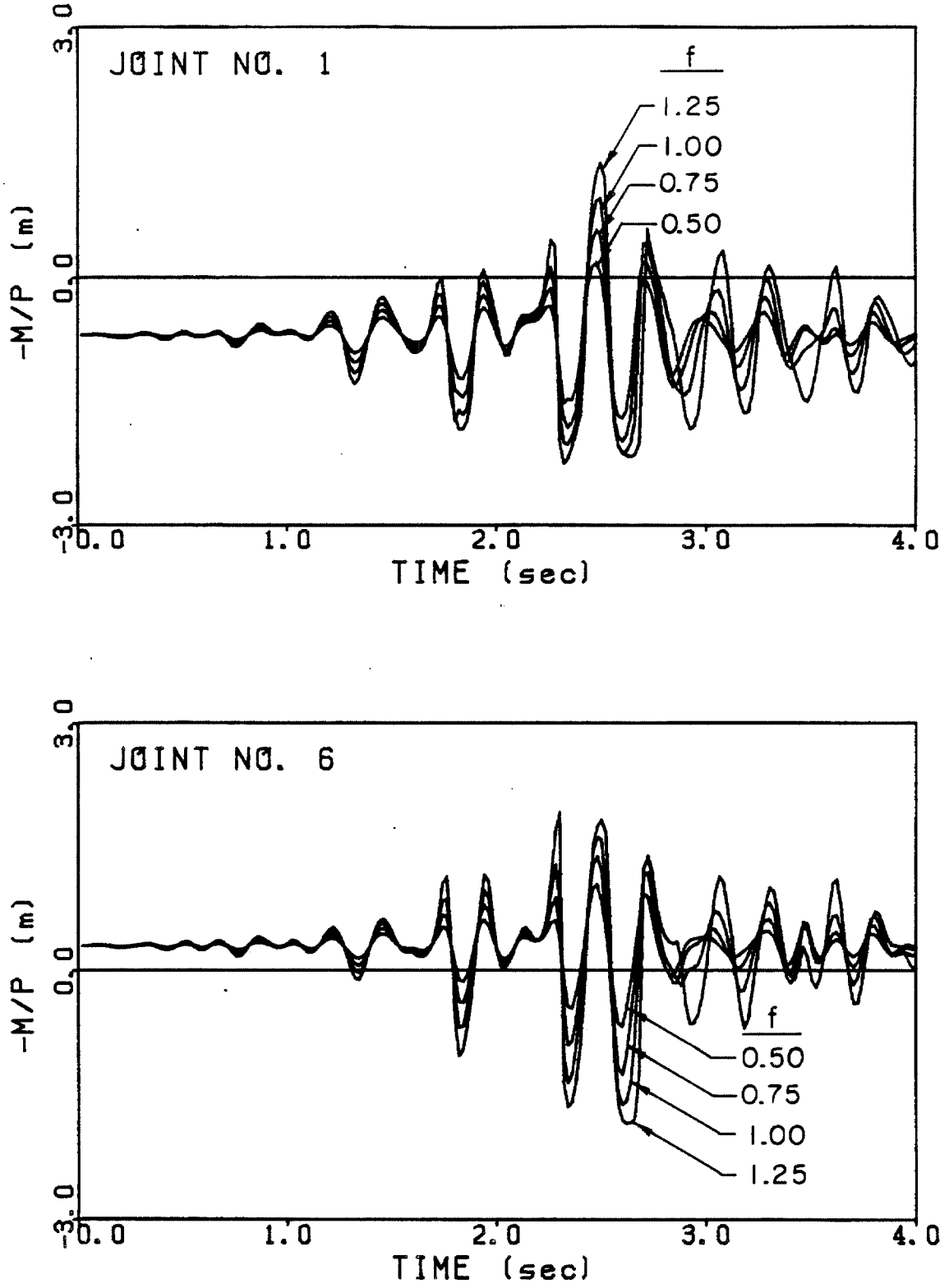

d. Ratio of moment to axial force versus time at joints 1 and 6.

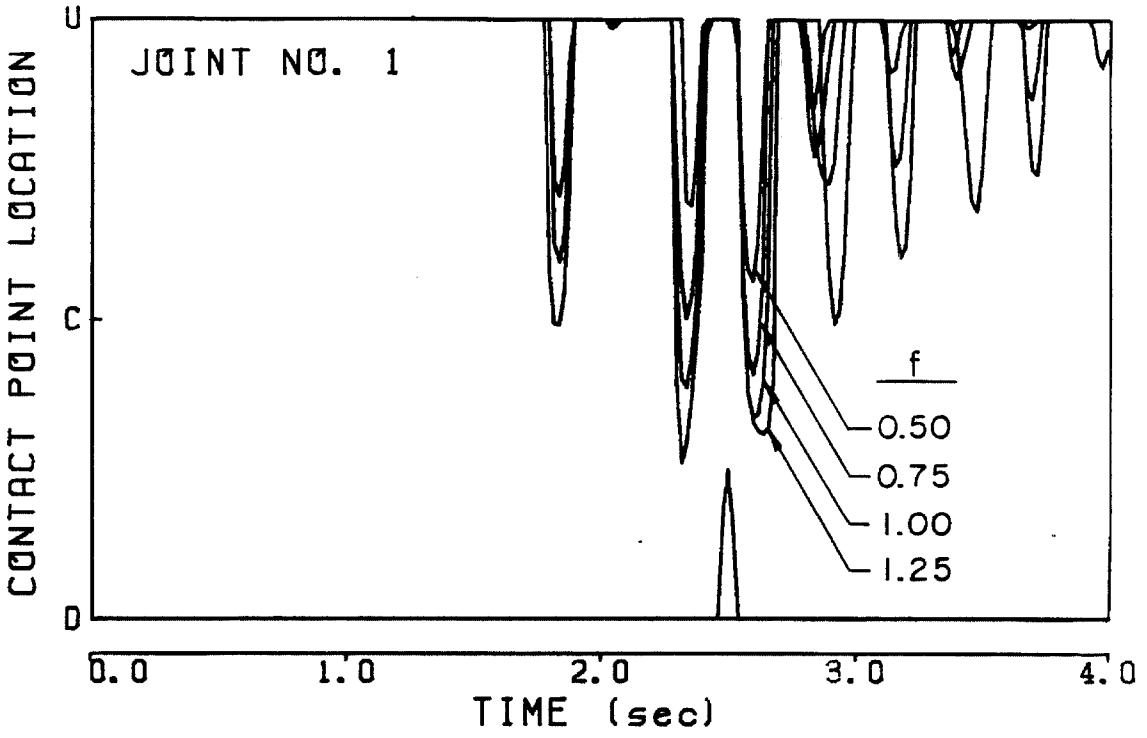

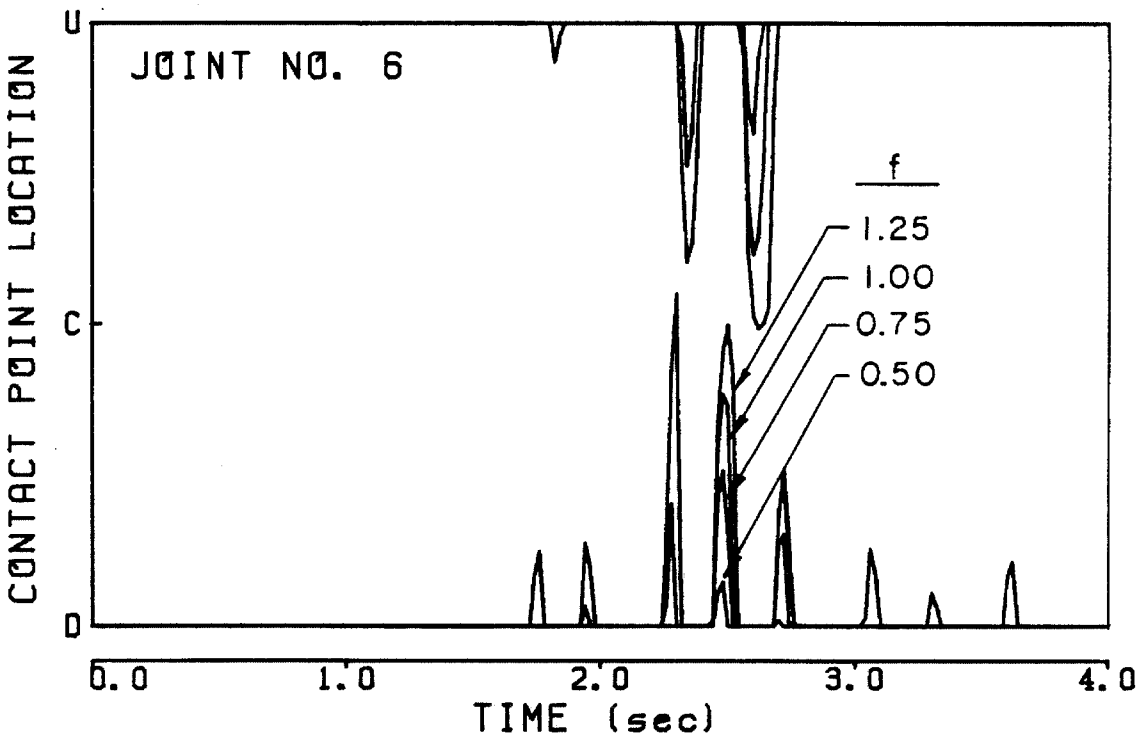

e. Position of joint contact versus time at joints 1 and 6.

(U = upstream face. D = downstream face. C = center plane).

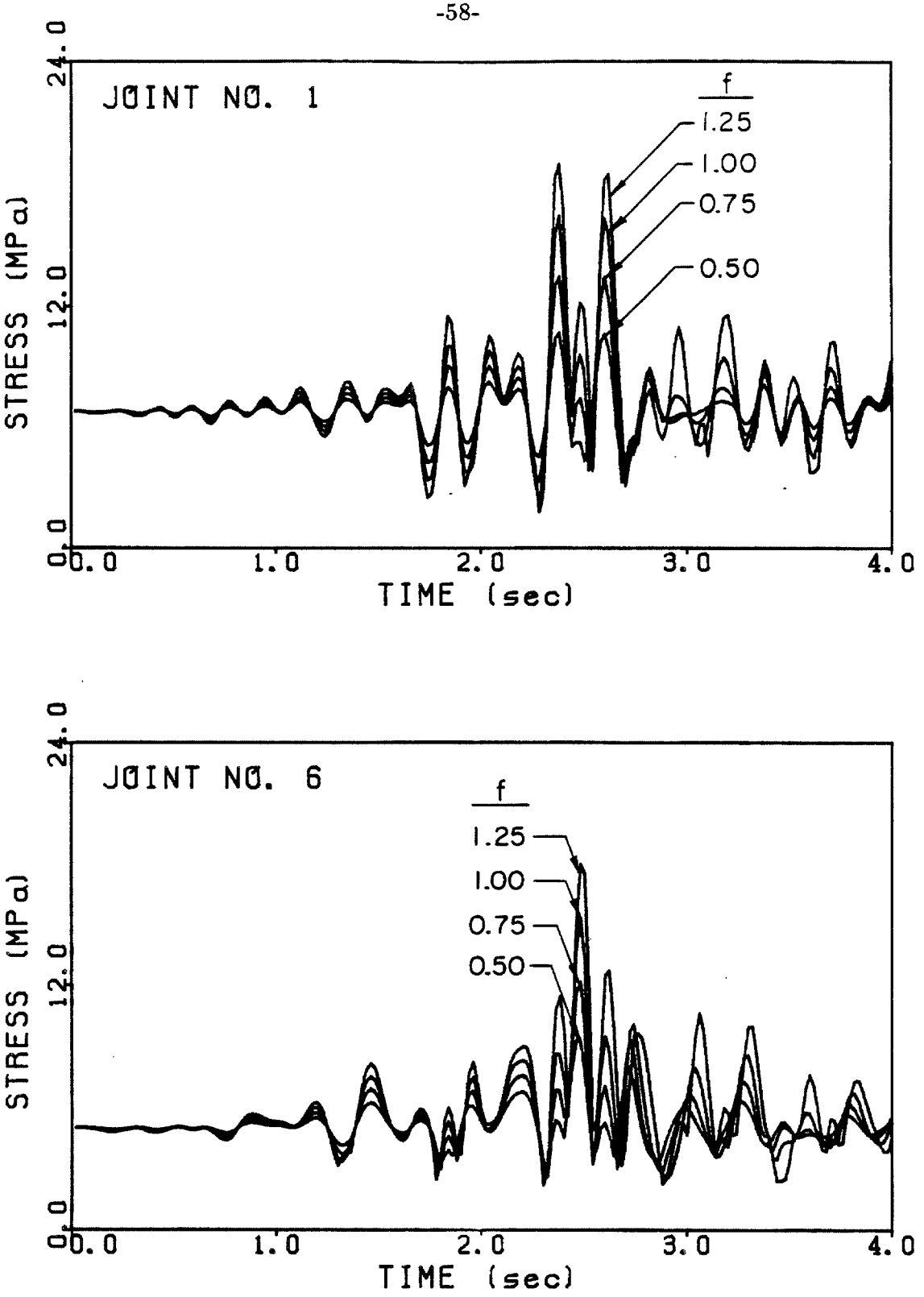

f. Maximum compressive stress versus time at joints 1 and 6.

CHAPTER IV
ANALYSIS OF THREE-DIMENSIONAL ARCH DAMS [41]

This chapter describes how the two-dimensional joint element whose development and use was outlined in Chapters II and III can be generalized in a simple but approximate way for use in analysis of a three-dimensional arch dam (Figure 4.1). It describes how the effects of both foundation-structure interaction and fluid-structure interaction can be accounted for with only a minimal increase in storage requirements and with little loss of computational efficiency. The solution algorithm presented in Chapter II is generalized for the three-dimensional problem. Lastly, a method is described whereby the dead weight of the structure can be applied in a manner which simulates the actual construction sequence for a typical arch dam.

4.1 Body of the Dam

Chapter II outlined the development of a special element to model gradual opening and closing of interface joints in a two-dimensional arch or slab. The results of Chapter III showed the element to be both accurate and efficient for this purpose. However, for realistic analysis of arch dams, generalization needs to be made to the three-dimensional situation. This can be done in a simple but approximate way.

The dam is divided horizontally and vertically into blocks, each of which is represented by a single shell element. The vertical joint planes are the actual contraction joints in the dam. Typically, these might be spaced at intervals of about 15 meters, with perhaps ten or twelve such planes across the crest of the dam. Consequently, all of the contraction joints can be modeled without undue computational effort. The horizontal joints represent predetermined planes where cantilever cracking is constrained to occur. Horizontal crack orientations are suggested by the vertical orientation of the contraction joints [15] and by the possible horizontal planes of weakness in the lift joints, and are supported by shaking table studies [17,18] on small scale models built with contraction joints (but probably with keys

omitted). As typical lift heights are small, the spacing of horizontal joints in the finite element model is governed by computational limitations. As described in Chapter II, cracking at the face of a joint occurs when the tensile stress there exceeds an assigned tensile strength. Approximations regarding cracking, i.e., the predetermined locations and an absence of fracture mechanics criteria, are noted.

As in the two-dimensional treatment, no joint sliding is permitted. At a horizontal joint, the validity of this constraint requires that contact be maintained with sufficient friction. In the contraction joints, however, slip would be constrained even under a condition of complete separation if right angled keys were present. Typically, though, keys have beveled geometries which permit an amount of free slip during joint separation dependent on the bevel angle (Figure 4.2). Although omitted here, joint slip is certainly a desirable feature to include in a nonlinear analysis of an arch dam. Inclusion of joint slip would entail a considerable increase in complexity of formulation and in computational effort and is not included for these reasons.

Discretization of the dam employs linearly interpolated shell elements which include shear deformations (the type with independent interpolations for translation and rotation [37]). A single element discretization through the thickness of the dam is utilized. The element may be three-noded (for use in the vicinity of the dam-foundation interface) or four-noded. Figure 4.3 shows the four-noded element in its parent and mapped forms. The element uses mid-thickness nodes, each node having five dof associated with the local $\hat{x}$,$\hat{y}$ and $\hat{z}$ axes. The $\hat{z}$ is in the mapped η direction and lies along the nodal 'normal', or through-thickness direction; $\hat{x}$ is perpendicular to $\hat{z}$ and lies in the horizontal $x-z$ plane; $\hat{y}$ is perpendicular to both $\hat{z}$ and $\hat{x}$ and oriented so that $\hat{x}$,$\hat{y}$ and $\hat{z}$ form a right-handed system. The five dof needed to describe the position of the nodal 'normal' are translations $\hat{U}$,$\hat{V}$ and $\hat{W}$ in the $\hat{x}$,$\hat{y}$ and $\hat{z}$ directions, respectively, and rotations $\hat{\theta}$ and $\hat{\alpha}$ about $\hat{y}$ and $\hat{x}$, respectively.

The joint planes are located at element boundaries and can produce four types of nodal arrangements. At a node where no joint planes intersect, the standard

five dof are used. In Figure 4.4a, where a vertical joint plane is present, seven dof are used for the double node arrangement involved; five average translations and rotations ($\hat{U}_{av}, \hat{V}_{av}, \hat{W}_{av}, \hat{\theta}_{av}$ and $\hat{\alpha}_{av}$) of the nodal normals a–b and A–B, plus the relative translation $\hat{U}_{rel}$ (opening positive) and relative rotation $\hat{\theta}_{rel}$ (opening on downstream face positive). The joint plane in Figure 4.4b is horizontal. Again, seven dof are used to define the position of the nodal normals c–d and C–D; the same five average translations and rotations ($\hat{U}_{av} \ldots \hat{\alpha}_{av}$) as for the vertical joint, plus the relative translation $\hat{V}_{rel}$ (opening positive) and rotation $\hat{\alpha}_{rel}$ (opening on downstream face positive). Lastly, the intersection of a vertical and horizontal joint plane provides the fourth nodal arrangement. Nine dof are required here; $\hat{U}_{av}, \hat{V}_{av}, \hat{W}_{av}, \hat{\theta}_{av}, \hat{\alpha}_{av}, \hat{U}_{rel}, \hat{\theta}_{rel}, \hat{V}_{rel}$ and $\hat{\alpha}_{rel}$. A single joint suffices along the dam-foundation interface and represents the interface itself. In this case, the local $\hat{y}$ axis is rotated to make $\hat{x}$ perpendicular to the interface, and the joint is treated as vertical.

The shell elements contribute stiffness to both the average and relative dof at a node as determined by transformations which, where both horizontal and vertical joints are present, are given by

$$\begin{array}{llll}
\hat{U}_1 = \hat{U}_{av} + \hat{U}_{rel} & \hat{U}_2 = \hat{U}_{av} + \hat{U}_{rel} & \hat{U}_3 = \hat{U}_{av} - \hat{U}_{rel} & \hat{U}_4 = \hat{U}_{av} - \hat{U}_{rel} \\
\hat{V}_1 = \hat{V}_{av} - \hat{V}_{rel} & \hat{V}_2 = \hat{V}_{av} + \hat{V}_{rel} & \hat{V}_3 = \hat{V}_{av} + \hat{V}_{rel} & \hat{V}_4 = \hat{V}_{av} - \hat{V}_{rel} \\
\hat{\theta}_1 = \hat{\theta}_{av} - \hat{\theta}_{rel} & \hat{\theta}_2 = \hat{\theta}_{av} - \hat{\theta}_{rel} & \hat{\theta}_3 = \hat{\theta}_{av} + \hat{\theta}_{rel} & \hat{\theta}_4 = \hat{\theta}_{av} + \hat{\theta}_{rel} \\
\hat{\alpha}_1 = \hat{\alpha}_{av} - \hat{\alpha}_{rel} & \hat{\alpha}_2 = \hat{\alpha}_{av} + \hat{\alpha}_{rel} & \hat{\alpha}_3 = \hat{\alpha}_{av} + \hat{\alpha}_{rel} & \hat{\alpha}_4 = \hat{\alpha}_{av} - \hat{\alpha}_{rel},
\end{array} \tag{4.1}$$

where the nodal numbering refers to that of the unassembled elements appearing in Figure 4.5. The resulting stiffness terms associated with the average dof are the same ones associated with the single node which would be used if the joint planes were absent. The 2×2 joint stiffness matrices $\left[K_J\right]^i$ assemble into the $\hat{U}_{rel}$ and $\hat{\theta}_{rel}$ dof at each node containing a vertical joint and into the $\hat{V}_{rel}$ and $\hat{\alpha}_{rel}$ dof at each node containing a horizontal joint.

Table 2.1 presents sets of values of the elements of $\left[K_J\right]^i$ together with

the ranges of $-M/Ph$ and $\theta_J h/U_J$ for which each $\left[K_J\right]^i$ holds, all in nondimensionalized form. To determine the 2×2 joint stiffness matrix at a particular node, the values shown in Table 2.1 must be scaled:

(a) by the elastic modulus at the node. Since a node may be associated with several elements, the elastic modulus would normally be taken as the average of the elastic moduli of the adjacent finite elements.

(b) by the effective height V (in the case of a vertical joint, Figure 4.4a), width H (horizontal joint, Figure 4.4b), or length (dam-foundation interface joint, not shown) at the node.

(c) by the depth of the joint, computed by an averaging procedure using linear weighting functions varying from one at the node to zero at the adjacent nodes. This procedure actually results in little difference except at the vertical joints at the nodes on the crest where the averaging picks up only the increased dam thickness below the crest.

Then for a joint at a particular node, the translational and rotational stiffnesses and location of the translational spring are given by

$$\begin{aligned} k_\theta^i &= \left(\frac{k_\theta^i}{Eh^2}\right)\cdot E_{\text{av}}\cdot h_{\text{av}}^2\cdot b_{\text{eff}} \\ k_U^i &= \left(\frac{k_U^i}{E}\right)\cdot E_{\text{av}}\cdot b_{\text{eff}} \\ \bar{h}^i &= \left(\frac{\bar{h}^i}{h}\right)\cdot h_{\text{av}}, \end{aligned} \tag{4.2}$$

where k_θ^i/Eh^2, k_U^i/E and $\bar{h}^i/h$ are the nondimensionalized values from Table 2.1; E_{av} is the average elastic modulus at the node, h_{av} is the average depth of the joint; and b_{eff} is the effective height, width or length of the joint. Then the terms of the 2×2 stiffness matrix for the joint are given by equation 2.8.

4.2 Seismic Input

The earthquake excitation can be defined by three components of free-field ground acceleration, one horizontal in the upstream-downstream direction, one hor-

izontal in the cross-stream direction, and one vertical. In reality, considerable variation in the amplitude and phase around the canyon occurs. While nonuniform boundary excitations can be included in finite element analysis of structures [40], no accepted procedure for defining realistic free-field motions for a canyon geometry exists. Therefore, only uniform free-field motions are employed in this thesis as excitation to both dam and water.

4.3 Foundation of the Dam

Only a finite portion of the foundation rock, fixed at its far end, is included. To avoid system resonances with artificially low frequencies, foundation mass is omitted. This technique has not prevented reasonable correlations from being obtained to forced vibration field test results [42,43]. An extent of massless foundation region (measured radially away from the dam) of about the dam height is required for a converged eigensolution of the dam-foundation system [44]. Radiation damping is represented indirectly by including the foundation stiffness matrix in the Rayleigh damping matrix and choosing the Rayleigh damping coefficients appropriately. The mathematical formulation of the damping appears in Section 4.5.

The foundation is meshed using standard 8 to 20 node rectangular prism and 6 to 15 node triangular prism elements. Figure 4.6 shows the 20 node element in its parent form. Three dof are associated with each node, namely translations in the global x, y and z directions. The stiffness matrix of the foundation is formed element by element and assembled in the standard way. Since only the response of the dam is of interest, to avoid carrying all the foundation dof (which would necessitate much extra storage and computation time), the foundation dof off the interface are condensed out prior to assembly (condensation is possible because the foundation is massless). The disadvantage of this procedure is that the resulting condensed foundation stiffness matrix is full (i.e., no bandedness), and, on assembly into the global stiffness matrix, couples together dof st all nodes on the dam-foundation interface, thus destroying the bandwidth of the dam stiffness matrix. This results

in an unacceptably large problem in a computational sense which is avoided by localizing the condensed foundation stiffness matrix.

Figure 4.7 shows a diagram of a dam mesh with its associated foundation mesh. A consequence of the condensation process is that the dof at, for example, node number 3 are coupled to all the dof at nodes 1,3,6,...58 along the interface. To avoid this coupling, in a row of the stiffness matrix corresponding to a particular dof at node number 3, only the diagonal stiffness term and the coupling terms between that dof and the other dof at node number 3 and the neighbouring nodes 1 and 6 are retained. All other stiffness terms are set to zero. This procedure is repeated for all the dof along the dam-foundation interface and results in an approximate foundation stiffness matrix which assembles only into nonzero terms of the dam stiffness matrix and, thus, produces no nodal coupling not already present. This procedure enables foundation-structure interaction to be modeled with no penalty other than the addition of some extra dof along the dam-foundation interface which, in the rigid foundation case, would be fixed. Results presented in Chapter V will show that the errors incurred by the localization process described above are very small and well within acceptable limits.

4.4 Water Domain

While water compressibility can be important in the earthquake response of arch dams [44,45], its inclusion requires a considerable computational effort. Many pressure dof must be carried, especially since the frequency domain transmitting boundary employed for the water domain in [44,45] has no exact counterpart in the time domain. Since the focus of this study is on the effect of joint opening, water compressibility is omitted in order to keep the computational effort to a reasonable level. A finite element model is employed rather than the more conventional lumped added mass approach which has been shown to be a poor representation of an incompressible water domain [46].

Incompressible water is governed by the three-dimensional Laplace equation,

$$\frac{\partial^2 P}{\partial x^2} + \frac{\partial^2 P}{\partial y^2} - \frac{\partial^2 P}{\partial z^2} = 0, \quad P = \text{dynamic pressure (compression positive)} \quad (4.3a)$$

subject to the boundary conditions

$$\begin{aligned} &\frac{\partial P}{\partial n} + \rho_w A_n = 0 \quad \text{along accelerating boundaries} \\ &P = 0 \quad \text{at the free surface,} \end{aligned} \quad (4.3b)$$

where A_n is the boundary acceleration in the direction of the inward normal n, and ρ_w is the water density. The reservoir floor and sides are assumed to accelerate rigidly at the specified earthquake motions; i.e., no water-foundation interaction is included.

The water domain is meshed by means of linearly interpolated, 6 or 8 node, three-dimensional finite elements. Figure 4.8 shows the 8-node element in its parent form. One dof, namely dynamic water pressure, is associated with each node. The nodes of the water mesh at the upstream face of the dam should lie along the nodal 'normals' of the shell element mesh. The water mesh is extended upstream for a sufficient distance (about twice the dam height) to approximate an infinite reservoir. The omission of water compressibility allows the condensing out of any dof which does not need to be carried; this set includes all dof off the upstream face of the dam.

The finite element formulation for the water is

$$[K_{pp}]\{a_p\} = \{f_p\} - [M_p]\{\ddot{a}\}, \quad (4.4)$$

where $[K_{pp}]$ is the "stiffness" matrix of the water domain [47] condensed to those dof on the dam-water interface (symmetric matrix, but full); $\{a_p\}$ is the vector of dynamic water pressures at the interface; $\{f_p\}$ is the vector of nodal acceleration quantities which arise from rigid accelerations of the dam face and the reservoir floor and side walls at the uniform earthquake motions [48]; $[M_p]$ is a matrix which transforms nodal accelerations of the dam to nodal acceleration quantities of the

water [47]; and $\{\ddot{a}\}$ is the dam nodal acceleration vector. The last term in equation 4.4 is the water domain load arising from the accelerations of the dam relative to the uniform free-field motions. Because of the proximity of the nodal 'normal' to the true normal at the upstream face of the dam, the contribution to this load term is included only for the average translational dof of the dam.

4.5 Solution Scheme

The equation of motion for the dam-foundation system which expresses equilibrium attained after the lth iteration in time stepping from t to $t + \Delta t$ is

$$\{p^{l+1}(t+\Delta t)\} + [\bar{K}]\{a^{l+1}(t+\Delta t)\} + [C]\{\dot{a}^{l+1}(t+\Delta t)\} + [M]\{\ddot{a}^{l+1}(t+\Delta t)\}$$
$$= \{f(t+\Delta t)\} - [K_{\mathrm{p}}]\{a_{\mathrm{p}}^{l+1}(t+\Delta t)\}, \tag{4.5}$$

where $\{p^{l+1}(t+\Delta t)\}$= vector of nodal stiffness forces of the dam which corresponds to the state $\{a^{l+1}(t+\Delta t)\}$; $\{a\}$, $\{\dot{a}\}$ and $\{\ddot{a}\}$ are vectors of nodal displacements, velocities and accelerations relative to the earthquake motions, and $\{a\}$ includes static displacements; the notation $^{l+1}(t+\Delta t)$ signifies the approximation to the state at time $t + \Delta t$ after l iterations, with $^{1}(t+\Delta t) = (t)$; and

$[\bar{K}]$ = the condensed and localized foundation matrix whose translational dof have been transformed into shell compatible dof and assembled into the average translational and rotational dof at the interface.

$[M]$ = the mass matrix of the dam. Mass terms come from the shell elements and are associated with both the average and relative dof at a joint as determined by the transformations of equation 4.1.

$[C]$ is the Rayleigh damping matrix,

$$[C] = \alpha_0[M] + \alpha_1[K' + \bar{K}], \tag{4.6}$$

where $[K']$ is the linear stiffness matrix of the shell elements only (all joint stiffness terms excluded). Thus no structural damping from the joint elements is present.

$\{f(t+\Delta t)\}$ = specified nodal load vector at time $t+\Delta t$ given by

$$\{f(t+\Delta t)\} = \{f_{st}\} - [M][r]\{\ddot{a}_g(t+\Delta t)\}, \tag{4.7}$$

where $\{f_{st}\}$ contains the dead loads of the dam concrete and the static water forces; $[r]$ = matrix of influence vectors, one for each component of ground motion; and $\{\ddot{a}_g(t+\Delta t)\}$ contains the x, y and z components of the free-field ground acceleration at time $t+\Delta t$.

$[K_p]$ = a matrix which transforms dynamic water pressures at nodes on the upstream dam face to nodal forces on the average translational dof on the dam [47], and

$$[K_p] = -\frac{1}{\rho_w}[M_p]^T, \tag{4.8}$$

where $[M_p]$ is defined for equation 4.4.

Equations 4.4 and 4.5 are coupled, and they may be combined into a single partitioned matrix equation as

$$\begin{Bmatrix} p^{l+1}(t+\Delta t) \\ 0 \end{Bmatrix} + \begin{bmatrix} \bar{K} & K_p \\ 0 & K_{pp} \end{bmatrix} \begin{Bmatrix} a^{l+1}(t+\Delta t) \\ a_p^{l+1}(t+\Delta t) \end{Bmatrix} + \begin{bmatrix} C & 0 \\ 0 & 0 \end{bmatrix} \begin{Bmatrix} \dot{a}^{l+1}(t+\Delta t) \\ 0 \end{Bmatrix} +$$

$$\begin{bmatrix} M & 0 \\ M_p & 0 \end{bmatrix} \begin{Bmatrix} \ddot{a}^{l+1}(t+\Delta t) \\ 0 \end{Bmatrix} = \begin{Bmatrix} f(t+\Delta t) \\ f_p(t+\Delta t) \end{Bmatrix}. \tag{4.9}$$

This global partitioning between the dam and the water dof is for notational convenience only. In practice, each pressure dof is assembled immediately following those dof of the adjacent dam node.

One method of solving this set of equations is to solve the lower part (i.e., equation 4.4) for $\{a_p^{l+1}(t+\Delta t)\}$ as

$$\{a_p^{l+1}(t+\Delta t)\} = [K_{pp}]^{-1}\Big\{ - [M_p]\{\ddot{a}^{l+1}(t+\Delta t)\} + \{f_p(t+\Delta t)\}\Big\} \tag{4.10}$$

and substitute into the upper part to get

$$\{p^{l+1}(t+\Delta t)\} + [\bar{K}]\{a^{l+1}(t+\Delta t)\} + [C]\{\dot{a}^{l+1}(t+\Delta t)\} +$$
$$[M + M_a]\{\ddot{a}^{l+1}(t+\Delta t)\} = \{f(t+\Delta t)\} + \{f_a(t+\Delta t)\}, \qquad (4.11)$$

where

$$[M_a] = -[K_p][K_{pp}]^{-1}[M_p] \qquad (4.12a)$$

and

$$\{f_a(t+\Delta t)] = -[K_p][K_{pp}]^{-1}\{f_p(t+\Delta t)\}. \qquad (4.12b)$$

The physical interpretation of $[M_a]$ is an added mass matrix; the term in row i, column j of $[M_a]$ is the force from the water on dam dof i resulting from a unit acceleration of dam dof j. $\{f_a\}$ contains the dam loads due to the water pressures resulting from the rigid accelerations of the dam face and the reservoir floor and side walls at the uniform earthquake motions.

The difficulty with the method of solution outlined above is that $[M_a]$ is a full matrix and couples together average translational dof of the dam at all nodes associated with the dam-water interface. Consequently, the bandedness of the global mass matrix is lost and solution of equation 4.11 becomes computationally prohibitive. A possible remedy for the loss of bandedness is to localize $[M_a]$ in the same manner as was previously described for the condensed foundation stiffness matrix. However, unlike the foundation stiffness matrix, where such a localization process resulted in minimal errors, localization of $[M_a]$ led to unacceptably large errors.

To see the reason why localization of $[M_a]$ fails, consider the membrane analogy to the two-dimensional form of equations 4.3a and b, where P represents the out-of-plane displacement and A_n the out-of-plane boundary traction. In this analogy, $[K_{pp}]$ in the finite element formulation, equation 4.4, is a stiffness matrix. Thus, from equation 4.12a, $[M_a]$ must have the characteristics of a flexibility matrix. The intrinsic nature of a flexibility matrix makes it unamenable to localization.

The stiffness characteristics of $[K_{\rm pp}]$, which is also full due to the condensation procedure, suggest that the preferable solution scheme is to solve equation 4.9 with a localized $[K_{\rm pp}]$. The penalty in dealing with equation 4.9 is an extra dof at each dam node due to the adjacent pressure unknown which is carried. Compared to solving equation 4.11, the penalty (assuming each dam node has 9 dof; i.e., both horizontal and vertical joints are present) is approximately $\frac{10^2}{9^2}-1 = 23\%$ on storage and $\frac{10^3}{9^3}-1 = 37\%$ on computation time, which are acceptable if the localization is accurate. For the example of Chapter V, this is the case.

Rewriting equation 4.9 in the Bossak form followed by linearization of $\{p^{l+1}(t+\Delta t)\}$ (equation 2.15b) and substitution of equations 2.10 and 2.11 leads to the finite element solution scheme,

$$\begin{bmatrix} \frac{(1-\alpha_B)}{\beta\Delta t^2}M + \frac{\gamma}{\beta\Delta t}C + K + \bar{K} & K_{\rm p} \\ \frac{(1-\alpha_B)}{\beta\Delta t^2}M_{\rm p} & K_{\rm pp} \end{bmatrix} \begin{Bmatrix} \Delta a^l \\ \Delta {a_{\rm p}}^l \end{Bmatrix} = \begin{Bmatrix} f(t+\Delta t) \\ f_{\rm p}(t+\Delta t) \end{Bmatrix} -$$

$$\begin{Bmatrix} p^l(t+\Delta t) \\ 0 \end{Bmatrix} - \begin{bmatrix} \frac{(1-\alpha_B)}{\beta\Delta t^2}M + \frac{\gamma}{\beta\Delta t}C + \bar{K} & K_{\rm p} \\ \frac{(1-\alpha_B)}{\beta\Delta t^2}M_{\rm p} & K_{\rm pp} \end{bmatrix} \begin{Bmatrix} a^l(t+\Delta t) \\ a^l_{\rm p}(t+\Delta t) \end{Bmatrix}$$

$$+ \begin{bmatrix} \frac{(1-\alpha_B)}{\beta\Delta t^2}M + \frac{\gamma}{\beta\Delta t}C \\ \frac{(1-\alpha_B)}{\beta\Delta t^2}M_{\rm p} \end{bmatrix} \{a(t)\} + \begin{bmatrix} \frac{(1-\alpha_B)}{\beta\Delta t}M + \left(\frac{\gamma}{\beta}-1\right)C \\ \frac{(1-\alpha_B)}{\beta\Delta t}M_{\rm p} \end{bmatrix} \{\dot{a}(t)\} +$$

$$\begin{bmatrix} \left(\left(\frac{1}{2\beta}-1\right)(1-\alpha_B)-\alpha_B\right)M + \left(\frac{\gamma}{2\beta}-1\right)\Delta t C \\ \left(\left(\frac{1}{2\beta}-1\right)(1-\alpha_B)-\alpha_B\right)M_{\rm p} \end{bmatrix} \{\ddot{a}(t)\}, \qquad (4.13)$$

where $[K]$ = tangent stiffness matrix of the dam (linear shell elements and tangent joint elements), and $\{p^l(t+\Delta t)\}$ = vector of nodal stiffness forces of the dam corresponding to the state $\{a^l(t+\Delta t)\}$. Construction of $[K]$ and $\{p^l(t+\Delta t)\}$ in each iteration proceeds as is described in Chapter II. Multiplication of the lower partitioned equation by $\frac{-\beta\Delta t^2}{(1-\alpha_B)\rho_{\rm w}}$ together with the identity defined by equation 4.8 results in a symmetric left hand side matrix.

This equation corresponds to equation 2.14 of the two-dimensional treatment, and the solution procedure outlined in Chapter II carries over to the present case.

As emphasis has been on obtaining the dynamic part of the solution, the next section presents a few details on the static part.

4.6 Static Solution

Three different techniques of computing static stresses in an arch dam due to the dead weight of the concrete are in use.

(a) The dead weight acts instantly on the continuous and completely finished structure.

(b) The dead weight is taken by independently acting cantilevers [3,10,49].

(c) A staged construction sequence is simulated. In each stage, the dam is raised by independent extension of the cantilevers, and the contraction joints are grouted up to the level attained in a previous stage [3,50].

The first method, the simplest and most often used, is to be avoided since the stresses in the upper portion of the dam are largely due to it being pulled down by the portion of the dam below. The last method is the most realistic, and a version which corresponds to continuous grouting of the cantilevers as they are raised is employed here. The description will make use of the mesh in Figure 4.7.

The condensed, localized foundation stiffness matrix is first assembled into the global stiffness matrix followed by the 2×2 joint element stiffness matrices for each joint in the mesh, which are held in the closed position during the application of the dam self-weight. The shell element stiffness matrices $[K_e]$ and self-weight vectors $\{f_e\}$ for the bottom row of elements (numbers 21,27,33 and 39) are assembled into the global stiffness matrix and force vector, respectively, and the resulting system of equations is solved for the incremental displacements. These displacements are nonzero only for the dof on the dam-foundation interface and dof associated with the bottom row of elements. The shell element stiffness matrices and self-weight vectors for the second row of elements (numbers 15,20,...44) are then assembled, and the resulting incremental displacements are computed. Nonzero increments result only for the dof associated with the dam-foundation interface and the bottom

two rows of elements. This process is continued until the total stiffness matrix is assembled and the total self-weight vector is applied. The consequence of applying the self-weight via this construction sequence method is that the stresses in any row of elements result only from the weight of that row of elements and the elements above, as opposed, for example, to the method whereby the dead load is applied instantaneously to the completely finished structure where stresses, say in the top row of elements, result in part from the weight of the bottom row of elements, an unrealistic situation. Results presented in Chapter V will show that the stress distribution resulting from the construction sequence method of application differs significantly from that resulting from the instantaneous application method. The assumption that no joint opening occurs during application of the dead load is not violated.

Following application of the concrete dead load, the static water pressure is applied. This is performed in a single "time step" with iterations to allow for joint opening. The equation solved is a specialized version of equation 4.5 with dynamic terms omitted and $\left\{a_{\mathrm{p}}^{l+1}(t+\Delta t)\right\}$ replaced by the vector of static water pressures. The static solution for the concrete dead load and the static water pressure, thus computed, is used as the initial condition for the dynamic computation.

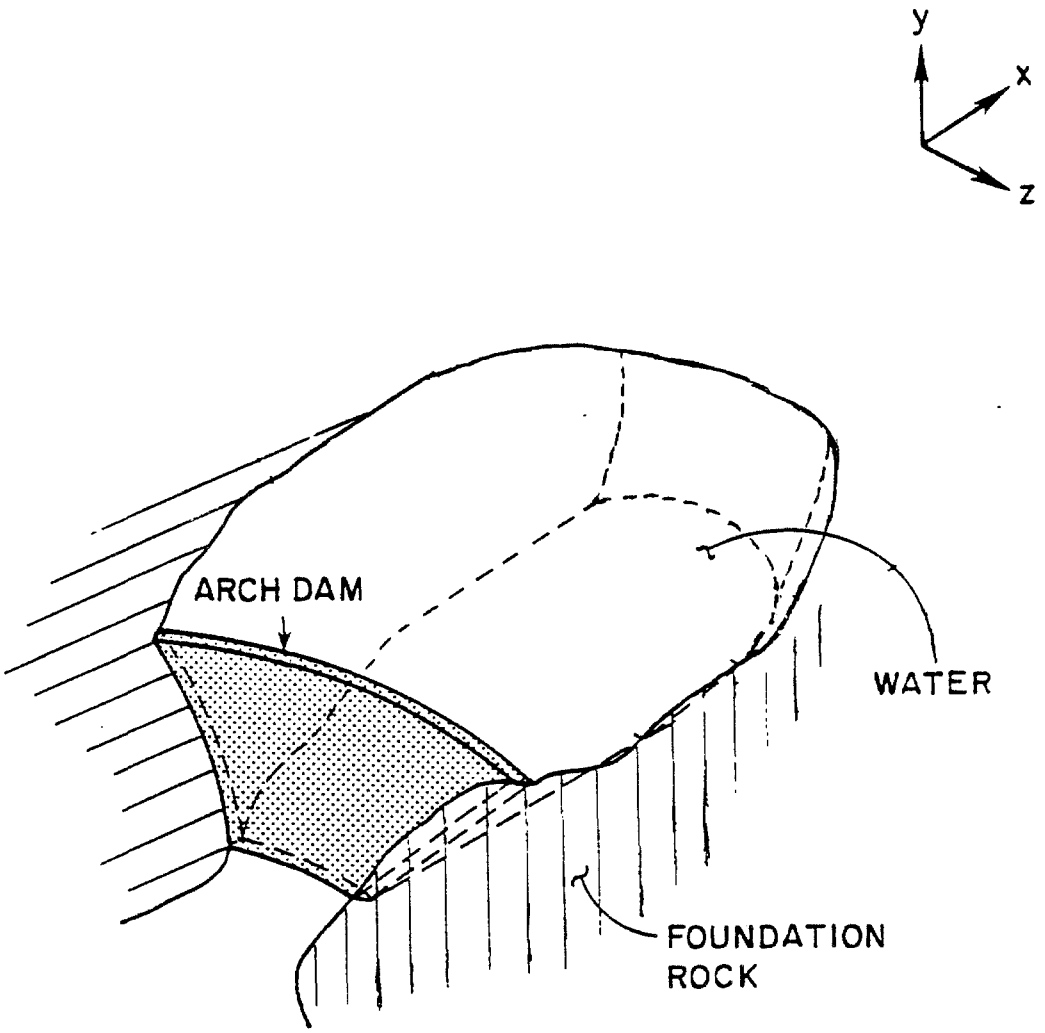

Figure 4.1 Arch dam-water-foundation rock system (adapted from [5]).

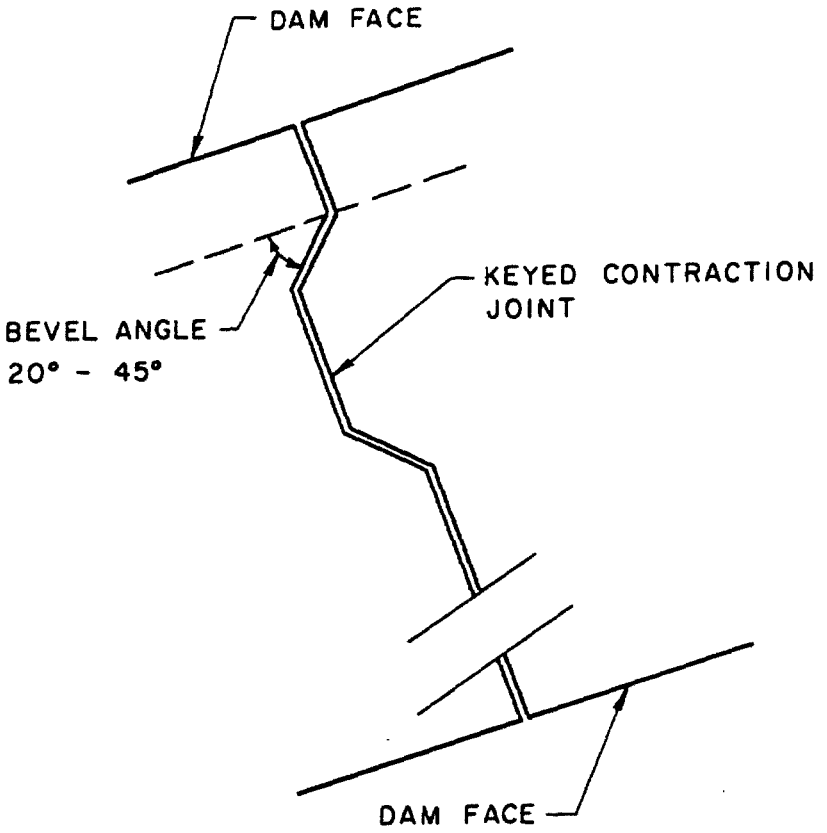

PLAN VIEW OF CONTRACTION JOINT

Figure 4.2 Typical detail of a contraction joint in an arch dam showing beveled keys.

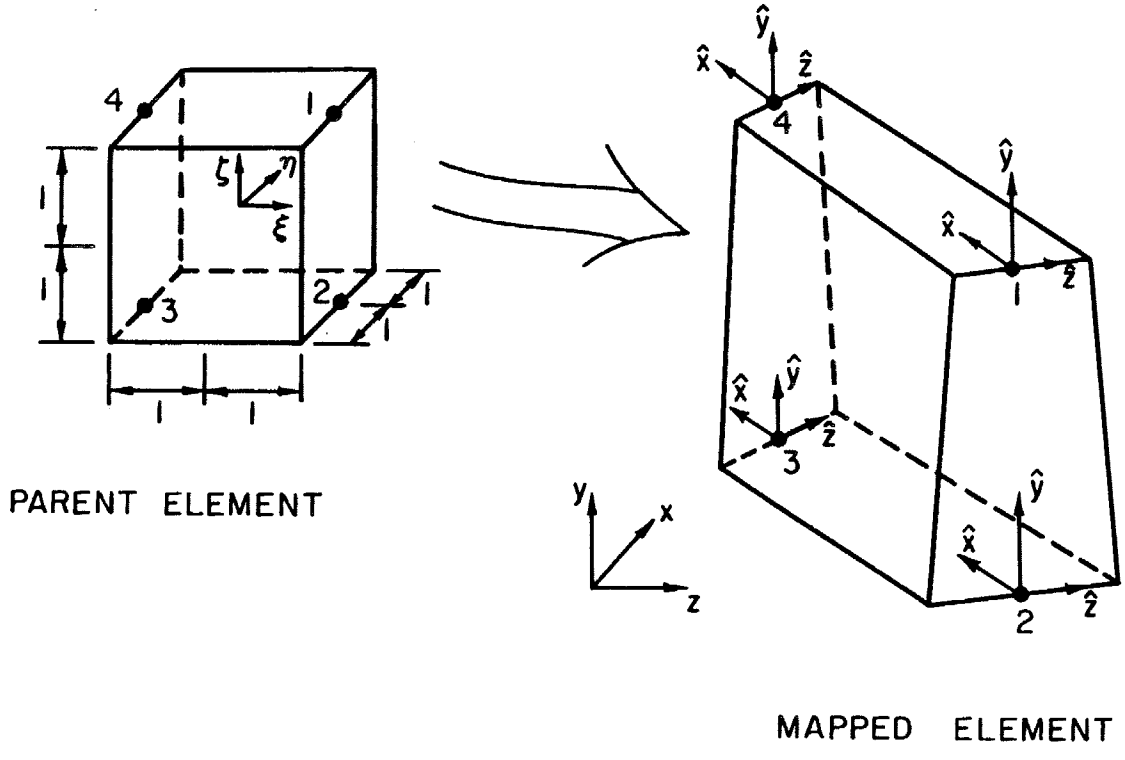

Figure 4.3 Four-node shell element.

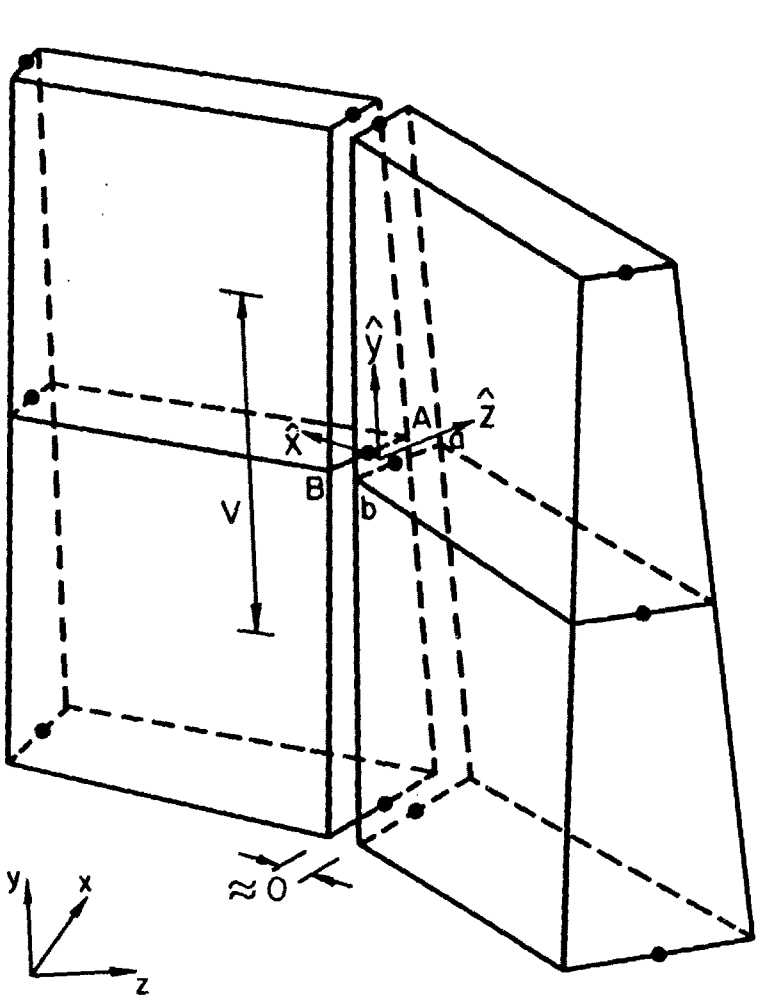

a. Vertical joint plane (contraction joint).

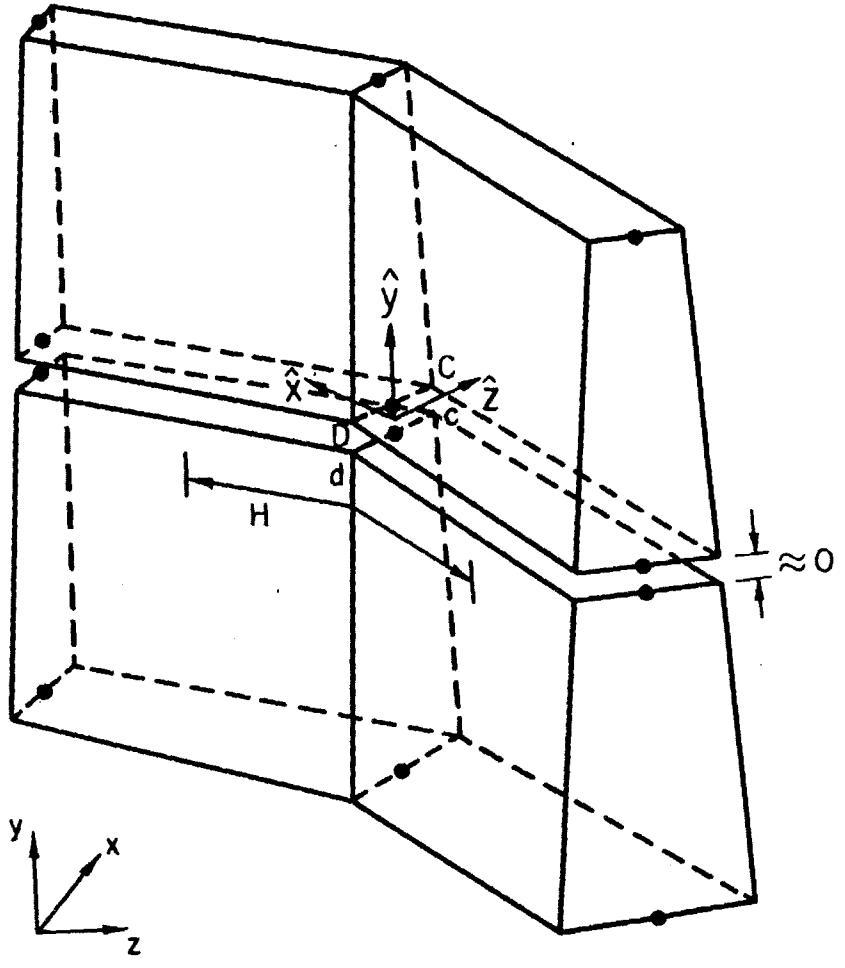

b. Horizontal joint plane (cracking plane).

Figure 4.4 Joint Planes at Shell Element Intersections.

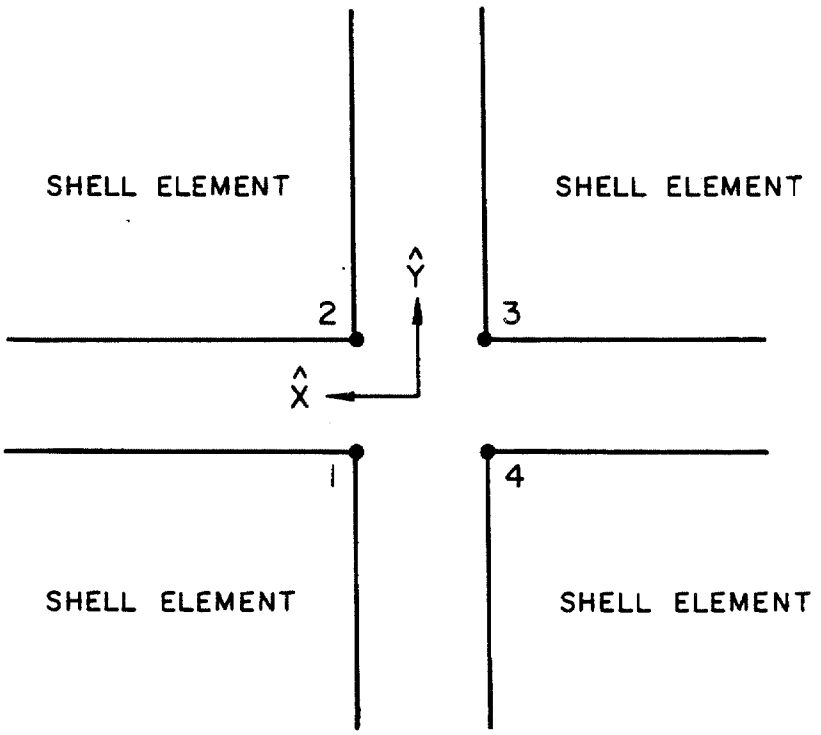

Figure 4.5 Node at Intersection of Horizontal and Vertical Joint.

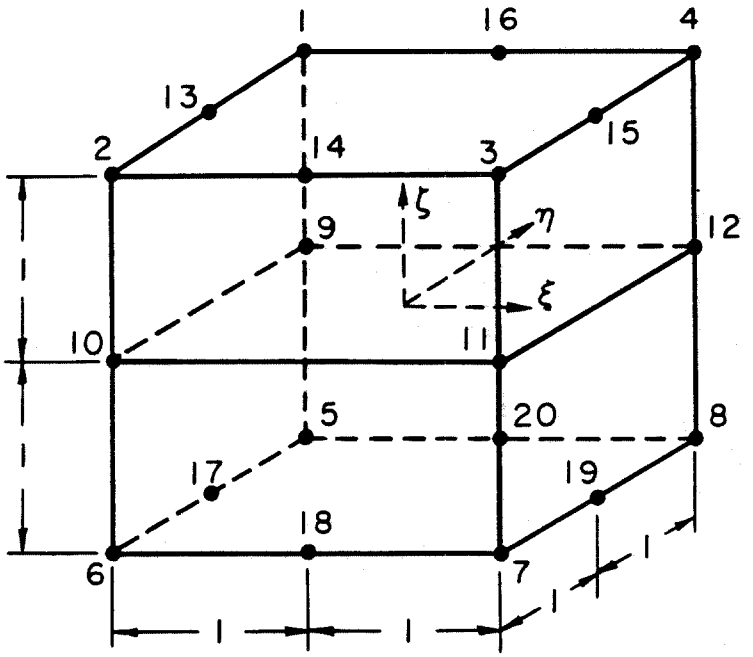

Figure 4.6 20-node solid element.

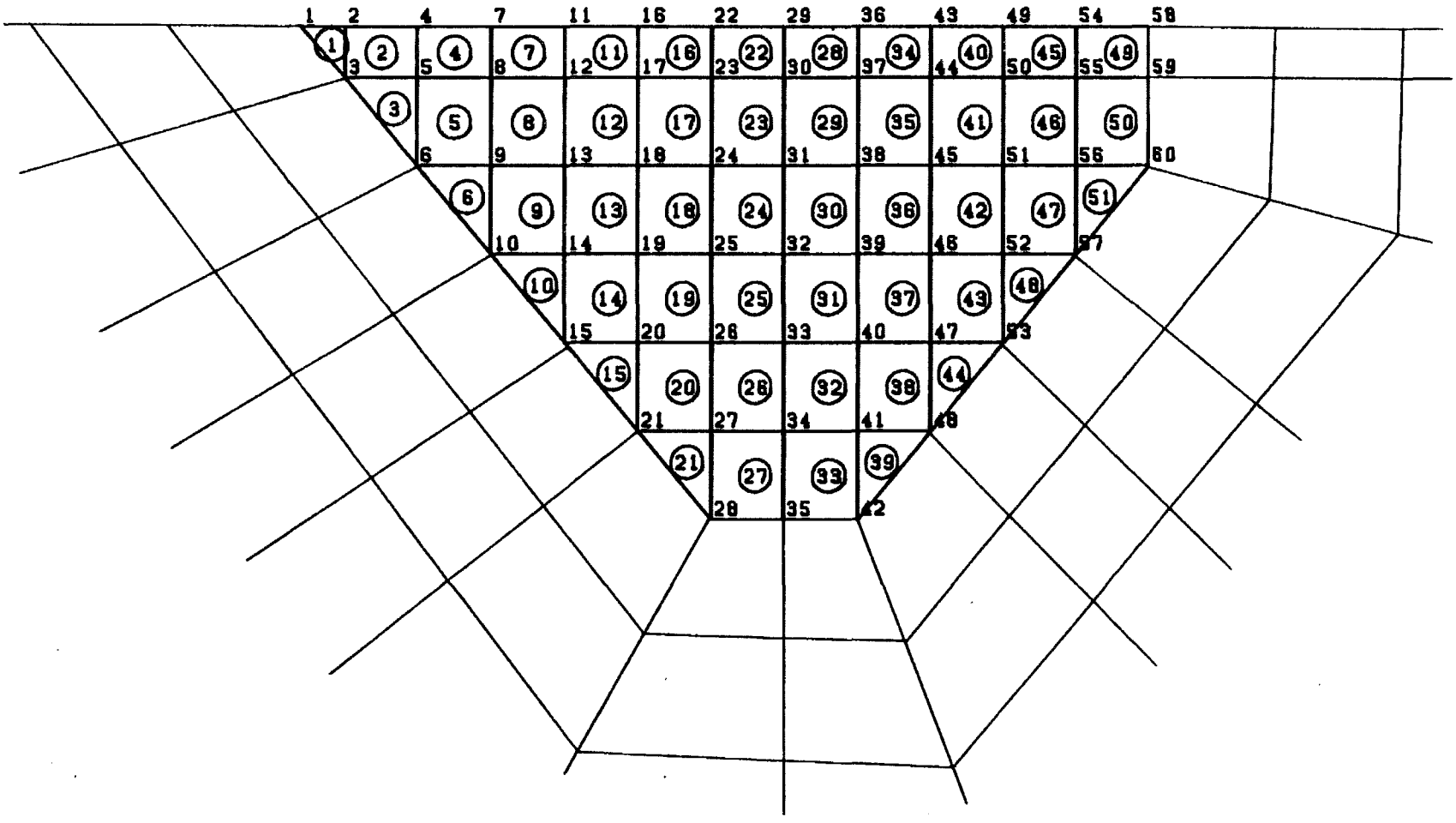

Figure 4.7 Diagram of a typical dam mesh with connected foundation region.

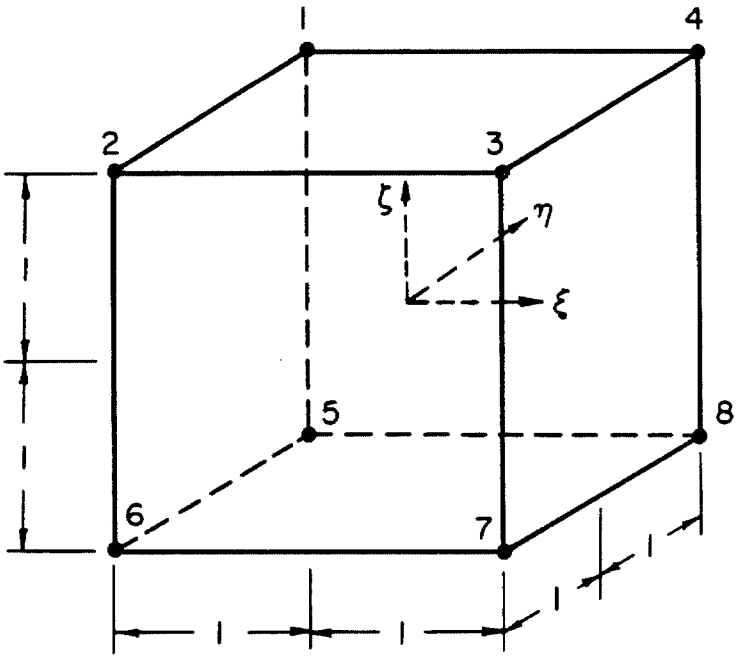

Figure 4.8 8-node element used to discretize the water domain.

CHAPTER V
THREE-DIMENSIONAL ANALYSIS OF PACOIMA DAM

This chapter describes the studies carried out on Pacoima Dam which investigate techniques for application of dead load, effects of the localization of the foundation and water domain discretizations, earthquake responses under full and partially full reservoir conditions using different ground motion intensities, and the effect of the no-slip constraint in the joints as pertains to possible collapse of the dam. Of the three earthquake analyses presented, one attempts to simulate the 1971 earthquake experience when the reservoir was only partially full, another repeats this analysis with full reservoir, and the third employs a full reservoir with a more typical, less severe ground motion.

5.1 Description of dam and ground motion

Pacoima Dam is a 111 meter high constant angle arch dam. It has a crest length of 180 meters and contains about 170,000 cubic meters of concrete. The thickness of the dam's center cantilever varies from about 3.2 meters at the crest to 30 meters at the base. The dam, which was constructed between 1925 and 1929, is located approximately 7 kilometers northeast of Central San Fernando, California.

The February 9, 1971, San Fernando earthquake had a Richter magnitude of 6.6 and caused moderately strong (15–25%g) to very strong ($\geq$ 25%g) shaking over a wide area. The earthquake was generated by slip on a fault making an angle of approximately 45° with the horizontal. While the surface expression of the fault was located several miles from Pacoima Dam, the epicenter was almost directly beneath the dam [51]. The earthquake caused permanent differential movement of the sides of Pacoima Canyon, opened the previously grouted contraction joint on the thrust block at the left abutment to nearly a centimeter, and caused a small crack near the base of the thrust block. (During construction, a volume of insecure rock from the left abutment had been removed and replaced by the concrete thrust

block.) In addition, the earthquake cracked the gunite cover on both abutments, caused slumping of an 8,000 m^2 area on the left abutment, cracked the lining of the spillway outlet tunnel, and started a number of rock slides from the canyon walls in the vicinity of the dam [6]. The ground motions recorded by a strong motion accelerograph located on a ridge about 15 meters above the left abutment of the dam were the highest earthquake accelerations ever recorded (Figure 5.1). Peaks in excess of 1 g occurred in both horizontal components, and a maximum peak of about 0.7 g occurred in the vertical component. The strong motion had a duration of approximately 7.5 seconds. Thus, despite the severe shaking, the body of the dam suffered only slight damage. However, at the time of the earthquake, the water level stood 45 meters below the crest.

5.2 Dam, water and foundation discretizations

Finite element meshes of the dam, foundation region and water are shown in Figures 5.2, 5.4 and 5.5, respectively.

The dam mesh consists of 60 mid-thickness nodes and 51 three- and four- node linearly interpolated shell elements. Note that the dam is not perfectly symmetric because of the thrust block at the left abutment where the dam terminates in an approximately vertical plane. The thrust block is modeled as part of the foundation. Reduced, one-point integration to prevent shear locking is used for the dam stiffness. Both vertical and horizontal joints are present at each node of the dam, except along the crest where vertical joints only are present and along the foundation interface where a single joint suffices. The vertical joints coincide with the vertical contraction joints, spaced at intervals of approximately 15 meters in the actual dam. The topmost horizontal joint is approximately 11 meters below the crest. The other horizontal joints are spaced at intervals of about 20 meters. Material properties of concrete used in the finite element calculations are as follows:

tensile strength = 2.1 MPa in the vertical joints

= 3.1 MPa in the horizontal joints

= 2.1 MPa in the foundation interface joints

Young's modulus = 20,700 MPa

Poisson's ratio = 0.2

Specific gravity = 2.4.

The tensile strength of the horizontal joints is set equal to $0.5\sqrt{f'_c}$ plus a 15% increase to allow for strain rate effects, where f'_c is the compressive strength of the concrete determined from cylinder tests to be about 29 MPa [6]. The strength of the grouting in the vertical joints and that of the bond between the dam and the foundation is unknown, so the lower value of 2.1 MPa is arbitrarily assigned to both. The value of Young's modulus is based on seismic surveys [52], and it and the values for Poisson's ratio and specific gravity were used in previous analyses [6]. Figure 5.3 shows the developed downstream profile of the dam. The nodes are numbered 1 to 60; the arches are labelled A0 to A6 and the cantilevers C−7 to C5. This figure will serve as a reference drawing for later discussions.

The foundation mesh shown in Figure 5.4 employs 296 nodes and 158 eight-node linearly interpolated brick elements. Reduced integration is used for the foundation stiffness. The foundation mesh extends outward from it's interface with the dam a distance of about 70 meters. The material properties of the foundation used in the analysis are as follows:

Young's modulus = 13,800 MPa

Poisson's ratio = 0.25.

The foundation modulus is an average value based on seismic surveys [52], but does not account for possibly softer material on the left abutment.

Figure 5.5 shows the finite element mesh of the water in the full reservoir condition. It consists of 420 nodes and 306 six- and eight-node fluid elements. The mesh extends radially outward from the dam for a short distance and then extends in the upstream direction for 180 meters. Note that since water-foundation interaction is not modeled, the boundaries of the water and foundation meshes need not coincide. The finite element mesh for the water used in the simulation of the 1971 earthquake had its free surface 45 meters below the dam crest and is not

shown.

5.3 Static load application

Chapter IV describes various methods whereby the dead weight of the dam can be applied. Two will be considered here. In the first, which will be referred to as the instantaneous application method, the dead load is applied instantaneously to the continuous and completely finished structure. In the second, referred to as the construction sequence method, the dead weight is applied in a manner which attempts to simulate a construction operation using continuous grouting of the contraction joints. Figures 5.6 a and b compare the results of analyses of Pacoima Dam obtained using these two methods to apply the dead weight; also included are results for combined dead weight and hydrostatic load (for the full reservoir case). Both figures show the normal stresses in the joints at the crest of the dam (arch A0, see Figure 5.3 for arch and cantilever numbers) and the normal stresses on the horizontal cracking planes at the crown cantilever (cantilever C0). The deformed shapes of the top arch and crown cantilever are also shown.

Comparison of Figures 5.6a and 5.6b shows that the arch stresses are sensitive to the manner in which the dead load is applied, while the cantilever stresses are less so. Application via the construction sequence results in stresses along the top arch of the dam which are typically less than or equal to 0.1 MPa tension or compression, while the instantaneous application results in stresses in the top arch which range from -0.4 MPa (compression) to 1.5 MPa (tension). (Recall that the joints are grouted and hence able to carry some tensile stress.) Since the hydrostatic load is applied in the same manner in the two cases, differences in the stresses under the combined loading are not as striking as in the case where the dead weight acts alone; nonetheless significant differences do occur at and near the abutments in the top arch. The smaller displacements which occur for the construction sequence calculation are attributed to the fact that the reference displacements for each row of elements are taken as zero when added. Thought to be more realistic, the

static solution obtained via the construction sequence method is used as the initial condition for the earthquake responses presented later.

5.4 Localization of foundation and water stiffness matrices

As outlined in Chapter IV, the condensed foundation and water stiffness matrices, $[\bar{K}]$ and $[K_{pp}]$, respectively, are localized to preserve the bandwidth of the global stiffness matrix of the dam. In order to assess the loss of accuracy incurred by the localization process, the first six eigenfrequencies of the finite element system (with the joints in the closed position) are presented in Table 5.1 for the cases indicated. Comparison of case 1 (empty reservoir, original foundation stiffness matrix) and case 2 (empty reservoir, localized $[\bar{K}]$) shows that localizing $[\bar{K}]$ loses little accuracy; the errors in the computed eigenvalues range from 0.1% to 1.2%. Cases 3 and 4 both have the original foundation stiffness matrix and a full reservoir, case 3 having the original $[K_{pp}]$ and case 4 the localized $[K_{pp}]$. Comparison shows that some noticeable error is incurred by localizing $[K_{pp}]$. The error is largest (about 5%) for the first and fourth modes and ranges from about 0.1% to 2% for the other modes. Case 5 is included in Table 5.1 to illustrate the fact that use of the localized $[K_{pp}]$ is, despite the errors incurred, a big improvement over the conventional lumped added mass representation of incompressible water (technique described in [46,53]), albeit at a cost of one dof per node. Comparison of cases 3 and 5 shows errors of 17% to 21% in the latter. Incidentally, the resonant frequencies of Pacoima Dam for empty reservoir or low water condition, as determined by forced vibration tests [54,55] are in the range 5.1 Hz to 5.5 Hz for the fundamental symmetric mode and about 5.6 Hz for the fundamental antisymmetric mode. These values are in reasonable agreement with the finite element results.

In order to further investigate the errors incurred in localizing $[\bar{K}]$, the foundation region as described by the original and local $[\bar{K}]$ is loaded by nodal forces and the resulting displacements plotted (Figure 5.7). Agreement between the two sets of displacements is nearly exact at the load point, and, although some errors

are evident at distant nodes, the displacements there are small. The agreement evident in Figure 5.7 is consistent with that for the eigenvalues in Table 5.1.

Results of an investigation of the errors incurred in localizing $[K_{pp}]$ are presented in Figure 5.8. The water domain as described by the original and local $[K_{pp}]$ is excited by accelerations at the dam face, and the resulting hydrodynamic forces acting on the dam are plotted. Agreement between the two sets of forces is good, but not quite of the quality attained in Figure 5.7. These results are again consistent with those of Table 5.1.

5.5 Dynamic analysis of Pacoima Dam under severe ground motion; full and partially full reservoir.

Nonlinear dynamic analysis of Pacoima Dam is performed to simulate the 1971 earthquake experience (water level 45 meters below the crest). As stated previously, ground motion records were obtained by an accelerograph located at the site. However, a question of the degree of influence of the accelerograph location upon the record obtained can be raised. The instrument was located on the edge of a narrow, badly fractured ridge about 15 meters above the dam crest. Observation of the disturbance of topsoil and loose rock on the ridge crest as compared to other areas in the vicinity of the dam indicated that the ground motion on the ridge was unusually high [6]. Consequently, the applied ground motions used in this analysis are those of Figure 5.1 (all three components employed) reduced by a third to approximately account for amplification effects on the ridge. This reduction has been used in previous analyses [6]. It is expected that a more severe case for the stability of the dam is the full reservoir condition. To determine how the dam might have fared in this case, a second nonlinear analysis is carried out with the water level at the crest. Further, to assess the effect of joint opening, and to compare the nonlinear analysis results with conventional linear analysis results, additional linear analyses (joint opening prevented) at the two water levels are performed. For all the computations, the Rayleigh damping parameters α_0 and α_1 are chosen to yield

5% damping at 4 Hz and 20 Hz, while $\Delta t = 0.01$ seconds, and $\alpha_B = -0.2$ to provide moderate high frequency dissipation (0.5% at 10 Hz, 2% at 20 Hz). Each nonlinear analysis required about 40 minutes of CPU time on a Cray X-MP/48 computer. By comparison, each linear analysis required about 10 minutes of CPU time.

Results of the analyses, including the static stresses and the maximum tensile and compressive stresses and joint openings reached during the earthquake, are shown in Figure 5.9. (All earthquake responses include the static component.) Figure 5.9a, for example, shows the top arch of the dam (Arch A0). Results are presented both for the partially full and full reservoir cases. For each case, the stresses across the arch under static (dead weight of concrete plus hydrostatic) loading, the maximum tensile stresses at the joints computed via a linear analysis, the maximum joint opening widths computed via a nonlinear analysis, the maximum compressive stresses at the joints computed via a linear analysis and the maximum compressive stresses computed via a nonlinear analysis are shown. Thus, for example, from the plot labelled "MAX. TENSIONS LINEAR ANALYSIS" for the partially full reservoir case, the maximum tensile stress at the left abutment of the arch reached 5.0 MPa (tensile stress positive) during the earthquake. It occurs at the downstream face of the joint and, at the time of its occurrence, the stress at the upstream face of the joint is -3.7 MPa (compressive). The maximum tensile stress reached across the crest during the earthquake is 6.5 MPa at node 22 (for node numbers see Figure 5.3), and it may occur at a different time from that at which the maximum tensile stress occurs at, say, the left abutment. Thus, the stress distribution shown is not the distribution at any particular time; rather, each joint is shown at the time the tensile stress reaches a maximum there. Similarly, for any of the plots in Figure 5.9a, the stresses (shaded, amplitudes given to one decimal place) or openings (unshaded, amplitudes given to two decimal places) shown at each joint occur at the time the indicated quantity (MAX. TENSIONS LINEAR ANALYSIS, for example) reaches a maximum there, except, of course, for the static stress pictures. Note that in the plots of maximum openings, if no opening occurs at a joint, the joint is shown at the time the tensile stress reaches a maximum there (e.g. node 49, partially full

reservoir case), and that in the nonlinear analysis, the maximum compressive stress at a joint often coincides with partial opening of the joint. Figures 5.9c, 5.9e, 5.9g and 5.9i show the maximum stresses and openings at arches A1 to A4 displayed in the same manner as Figure 5.9a, while Figure 5.9b, 5.9d, 5.9f, 5.9h and 5.9j show the corresponding results for cantilevers C−2 to C2. Incidentally, none of the maximum compressive stresses shown in Figure 5.9 occurred with a contact depth less than the 1/8 joint thickness minimum discussed in Chapter II.

Results of the linear analyses to the earthquake motions show whether or not nonlinear behavior will occur and roughly indicate the amount of nonlinearity to be expected. Tensile stresses computed from the linear analyses with the reservoir partially full reach 6.5 MPa in arch A0 (node 22) and about 2.5 MPa in a number of cantilevers, showing that opening of the contraction joints will take place. In addition, this opening will transfer considerable load to the cantilevers and lead to an increase in the cantilever tensions. Presence of the full reservoir increases the tensile stress to 9.1 MPa in arch A0 (node 36) and to 4.0 MPa in several cantilevers, showing that significant joint opening and cracking will occur. Maximum compressive stresses (12.5 MPa in arch A0, node 29, full reservoir) from the linear analyses are not in the nonlinear range, but impacts and partial joint openings may result in significantly higher values.

The nonlinear response of the dam with the partially full reservoir (earthquake simulation case) exhibits complete separation in the upper portions (top 50m) of most of the contraction joints with the maximum opening of 2.3 cm occurring on the upstream face at node 16. As outlined in previous chapters, it is assumed in this study that slip is prevented in the vertical contraction joints by friction and/or shear keys and in the horizontal cracking planes by friction. Even in the case of complete separation of a vertical contraction joint, slip would be prevented if the shear keys (30 cm deep in Pacoima Dam) were perfectly "square". However, the side walls of these keys are actually beveled at 20° to 30° (measured from the normal to the contraction joint) and would allow some free slip under complete separation with unknown consequences on the dam response. (If a joint opens uniformly by

1 cm, relative radial displacement of up to 0.5 cm, a significant amount, would be permitted.) Although the openings of the contraction joints increase the loads carried by the cantilevers; nonetheless, the cantilever tensions remain below the 3.1 MPa tensile strength except at the downstream face at node 24 where a small amount of cracking occurs. Thus, for the cantilevers, the no-slip assumption may not be violated.

The predicted openings of the contraction joints are not necessarily in conflict with the lack of observed cracking following the 1971 earthquake since such evidence may have been hard to detect. On the other hand, a 2.4 cm permanent narrowing of the canyon which occurred as a result of the earthquake [6] and is not included in the analysis would, assuming that it occurred simultaneously with the strong ground motion, offset much of the computed openings of the contraction joints and consequently reduce the cantilever tensions. Also, the uniform ground motion assumption (i.e., the assumption of spatially uniform free-field motion of the canyon) is generally felt to result in an overestimation of the dam response [56]. The only joint opening predicted by the analysis which is known to have occurred is that at the left abutment of the dam. However, the actual opening may have been caused by the slumping of the rock mass on the left abutment which was not included in the analysis.

The maximum arch compressive stress in the nonlinear response with the reservoir partially full is 12.7 MPa which occurs on the crest at node 43 and is less than half the value of f'_c (29 MPa). Consequently it does not violate the assumption of a linear stress-strain relation in the concrete. No other arch compression exceeds 10 MPa and compressions in arches A1, A2 etc. are much smaller. The maximum cantilever compressive stresss is 6.3 MPa. It occurs at the upstream face at node 24 and corresponds to a partial opening on the downstream face at that node.

Although the times at which the openings and compressive stresses reach maximum values are not shown in Figure 5.9, most of the larger openings and compressive stresses in the dam for the partially full reservoir occur between $t = 8$ seconds and $t = 9$ seconds. To further examine the nonlinear behavior during this time period,

Figure 5.10 presents a sequence of 12 'snapshots' taken from $t = 8.21$ to $t = 8.30$ seconds and from $t = 8.54$ to $t = 8.98$ seconds. The layout of each snapshot is the same as that in Figure 5.6; i.e., the stress distributions along the top arch (A0) and crown cantilever (C0) are presented together with the deformed shapes, including joint openings, of the arch and cantilever. The first three pictures, at $t = 8.21$, $t = 8.25$ and $t = 8.30$ illustrate the behavior during the period when the maximum downstream displacement occurs. The magnitude of this symmetric deformation is about 5.0 cm at node 22. The deformation is accompanied by compressive arch stresses, reaching 8.6 MPa at the left abutment (node 58) at $t = 8.25$. The accompanying cantilever stresses are much smaller (max. 1.6 MPa compression, 1.5 MPa tension) suggesting that much of the load is taken by arch action.

Both the maximum joint opening and maximum compressive stress on the dam occur during the period $t = 8.54$ and $t = 8.98$ seconds. The maximum joint opening (2.3 cm at node 16) occurs at $t = 8.63$ seconds at the time of the maximum upstream displacement of the dam (about 6.0 cm radial displacement at node 22) and is accompanied by significant opening at several other joints along the arch and by a significant increase in cantilever stresses (up to 4.3 MPa compression, 2.3 MPa tension). Approximately half a cycle later, at $t = 8.73$ seconds, the arch has displaced into an axisymmetric configuration, and the maximum compressive stress of 12.7 MPa occurs at node 43 under a condition of partial opening. Another half a cycle later, at $t = 8.91$ seconds, significant opening occurs at several joints across the arch, and the displacement and stress patterns are very similar to those at the previous large upstream excursion at $t = 8.63$ seconds.

The full reservoir significantly increases the dam response (Figure 5.9) with openings in the contraction joints reaching 5.3 cm at node 29 and openings in the cracking planes reaching 6.7 cm at node 37; both maxima occur under complete separations. The maximum compressive arch and cantilever stresses reach values of 19.7 MPa (at node 58) and 25.2 MPa (at node 23), respectively. Note that both of these maximum compressive stresses are accompanied by partial opening of the joint from the opposite face with a corresponding reduction in the stress

block depth. However, unlike the partially full reservoir case, where large ($\geq$ 9 MPa) compressive stresses only occur at partially open joints, in the full reservoir case compressive stresses up to 18 MPa occur at joints which are completely closed (node 29). Further, in the full reservoir case, the arch compressive stresses at the crest and the cantilever compressive stresses in the top horizontal joint are large enough to bring the linear stress-strain assumption for the concrete into question. In addition, both the large separations which occur in the contraction joints and the large lift-off in the top horizontal joint violate the no-slip assumption. As pointed out previously, the beveled contraction joints allow some relative radial motion to accompany complete opening, while the assumption that friction along the cracking planes prohibits slip is obviously violated in the case of complete lift-off.

Figure 5.11 presents a sequence of 11 'snapshots' of the top arch and crown cantilever for the nonlinear response with full reservoir taken between $t = 8.04$ and $t = 8.53$ seconds. During this period, maximum values are reached for joint openings in the top arch and crown cantilever as well as for the cantilever compressive stresses. The maximum arch compressive stress of 19.7 MPa occurs at node 58 at a slightly later time, but this is an isolated stress event occurring over a much reduced contact area for a very short duration and not accompanied by other large compressions along the arch. Consequently, the large compressive stress occurring at and near the crown of the arch during the time period encompassed by Figure 5.11 may be of greater importance.

Significant contraction joint opening, up to about 2.0 cm at node 36, occurs during the upstream displacement of the arch from $t = 8.04$ to about $t = 8.20$ seconds, and is accompanied by small partial openings of the cantilever joints. Complete separation of a cantilever joint (node 30) occurs at $t = 8.22$ seconds when the dam is beginning its downstream excursion. Approximately one quarter of a cycle later, at $t = 8.28$ seconds, the dam reaches its maximum downstream displacement, about 11.0 cm at node 29, coinciding with high compressive stresses across almost the full length of the arch. The maximum stress of 18 MPa occurs at the crown of the arch and is at about the upper limit for the linear stress-strain assumption. Shortly

thereafter, another cantilever separation occurs at node 30 followed by recontact and development of a large cantilever compressive stress (18.4 MPa) at maximum upstream displacement (t = 8.37 seconds). After reversal, complete cantilever separation again occurs culminating in the maximum opening of 6.6 cm in the top cracking plane at t = 8.47 seconds and coinciding with the maximum contraction joint opening (node 29) of 5.3 cm. The cycle concludes at about 8.53 seconds. Thereafter, no joint openings or compressive stresses occur which are comparable to those occurring during the time period encompassed by Figure 5.11. However, because of the violation of the material linearity (25.2 MPa compression in cantilever -1) and no-slip assumptions, a more sophisticated analysis would be required to determine the fate of the dam in the full reservoir condition subjected to the specified ground motions. The cantilever lift-offs also warrant further investigation, as the source of this feature of the response is not evident.

Selected time histories of the dam response, shown in Figure 5.12, provide additional insight into the nonlinear behavior. Each quantity plotted is displayed from t = 6.0 seconds to t = 10.0 seconds since most of the important activity takes place in this time range. Plots of average radial dynamic displacement at node 29 (Figure 5.12a) show larger peak amplitudes and some period elongation due to joint opening, although the period elongation for the full reservoir case is obscured by a high frequency component of the response. For the nonlinear responses, displacements are generally greater upstream than downstream because of joint opening although an occasional large downstream displacement is seen as, for example, in the full reservoir case at t = 8.28 seconds giving rise to high arch compressive stresses (see Figure 5.11).

Time histories of the contraction joint openings at node 29 (Figure 5.12b) show that the precompression provided by a full reservoir significantly reduces the number of joint openings; i.e., the joints tend to rattle less. On the other hand, the openings which do occur are typically of greater amplitude and longer duration (0.1 to 0.15 seconds for the larger openings) than in the partially full reservoir case (about 0.08 seconds duration). As was pointed out in Chapter III, joint opening

may allow for water intrusion with unknown consequences on the dam response. The effect may not be large at node 29 where water pressures are low, but could be important at, say, node 31, approximately 30 meters below the surface. Figure 5.12c shows the time histories of joint opening at node 31 at the upstream faces of the vertical and horizontal joints (full reservoir). At the vertical joint, a single significant opening of 0.6 cm with a duration of 0.09 seconds occurs at $t = 8.42$ seconds, while at the horizontal joint, a considerable amount of opening occurs in the time period $t = 6$ to $t = 10$ seconds, with a maximum opening width of 3 cm and duration of 0.11 seconds at $t = 8.31$ seconds. The time history of the absolute water pressure (atmospheric plus hydrostatic plus hydrodynamic) at node 31 (Figure 5.12d) shows values at $t = 8.31$ and $t = 8.42$ seconds of 0.45 MPa and 0.15 MPa (compression positive for water pressure), respectively. These are not close to the peak compressive pressure (0.85 MPa) because the large upstream openings in the joints occur during an upstream excursion when the dam is accelerating away from the water. Still, water intrusion is possible and warrants investigation.

The time histories of arch compressive stresses at node 29, presented in Figures 5.12e exhibit very high frequency oscillations, mitigated somewhat by the dissipation parameter α_B, which may be partly numerical and partly due to impacts. With the dilatational wave velocity in concrete about 3300 m/s and with an element dimension of, at most, 20 meters, the time for a stress wave to traverse an element would be about 0.006 seconds, or about half the time step length (0.01 seconds). Consequently the high frequency impact behavior of the stress responses probably cannot be accurately captured by the element and time step size employed.

Another phenomenon which was not included in this study, but was mentioned briefly in Chapter III is cavitation, which occurs where the absolute pressure reduces below zero (actually below the vapor pressure of water, about 0.002 MPa). The plot of the absolute pressure at node 30 (full reservoir) in Figure 5.12f shows that while it drops below zero several times between $t = 6.0$ and $t = 10.0$ seconds, the negative pressure peaks are isolated and of short duration, and only two (-0.15 MPa at $t = 8.40$ seconds and -0.1 MPa at $t = 8.90$ seconds) are significantly less than zero.

In addition, node 30 along line C0 is the only one where cavitation is indicated. Further, no cavitation occurs at all with a partially full reservoir. These results suggest that, at least for this analysis, cavitation may be a relatively unimportant effect. The dependence of the pressure responses on water compressibility (not included) is noted.

The most important conclusion from the analysis of the dam with a full reservoir subjected to severe ground shaking is that the primary assumptions on which this analysis method are based, namely the no-slip assumption in the joints and the linear stress-strain assumption in the concrete, are violated to too great an extent to draw any definite conclusions regarding the dam's stability, and thus how it might have fared during the 1971 earthquake had the reservoir been full.

5.6 Dynamic analysis with lower intensity ground motion

A further study was undertaken to examine the response of the dam with a full reservoir to ground motions somewhat less intense than those used in the analysis described above. For this analysis, the records in Figure 5.1 are scaled to give a maximum horizontal ground acceleration of 0.5g. The scaling factor required is about 0.44, and results in a maximum vertical acceleration of about 0.3g. While considerably less intense than the ground motions measured at the site, this still represents a substantial earthquake. Both linear and nonlinear analyses were performed. Results of the analyses, including static stresses, maximum dynamic tensile and compressive stresses and maximum dynamic joint openings are shown in Figure 5.13, displayed in the same manner as the results for previous analyses (Figure 5.9).

It is apparent that the dam response is considerably reduced from that which occurs due to the more intense ground motion. However, maximum tensile stresses from the linear analysis are still large enough (5.2 MPa arch at node 36) to indicate that nonlinear behavior will be present. In fact, significant separations occur in several contraction joints near the top of the dam, reaching a maximum of 2.2 cm at node 36. This is a violation of the no-slip assumption. Below the top arch of

the dam, much less opening takes place. No cracking of the joints along the crown cantilever occurs, but significant partial opening takes place in the top two joints in cantilevers C−1 and C1 (Figures 5.13b and c). The maximum arch and cantilever compressive stresses are 10.8 MPa (node 58) and 8.3 MPa (node 38, coinciding with the maximum opening at that joint), respectively. The magnitudes of these stresses are well within the linear stress-strain realm. Stresses in the lower reaches of the dam are much smaller.

Figure 5.14 presents a sequence of 'snapshots' of arch A0 and cantilever C1 (rather than C0 which does not experience any cracking or high stresses) for the nonlinear response taken between $t = 8.93$ and $t = 9.40$ seconds, during which time the most significant joint openings and compressive stresses occur. At $t = 8.93$ seconds, complete lift-off of the uppermost block of cantilever C1 is present. However, the amount of lift-off is small (about 0.1 cm on the upstream face) and is of very short (about 0.02 seconds) duration. The maximum arch compressive stress (9.3 MPa at node 36) occurs at $t = 8.95$ seconds and is associated with a downstream excursion causing compression across the arch. At $t = 8.97$ seconds, the arch is still on the downstream excursion, but the peak compressive stress (8.6 MPa) has shifted to node 29. Another small and brief separation at the horizontal joint at node 37 occurs at $t = 9.02$ seconds. A short time later ($t = 9.23$ seconds), the arch is once again displaced in the downstream direction. During the following upstream excursion of the arch, at $t = 9.33$ seconds, the maximum cantilever compressive stress (8.3 MPa) occurs at node 38 while the maximum contraction joint opening (2.2 cm at node 36) and cantilever joint opening (1.8 cm at node 37) occur one time step later at $t = 9.34$ seconds. Note also that complete separation of the left abutment joint occurs at $t = 9.33$ seconds. Lastly, the downstream displacement at $t = 9.40$ seconds results in a stress pattern in the arch very similar to that at $t = 8.95$ seconds.

Figure 5.15 presents time histories of average radial dynamic displacement at node 29 for linear and nonlinear analyses. These time histories are similar both in terms of amplitudes and periods, reflecting the limited amount of nonlinear activity

which takes place. However, this activity is sufficient to cause a 2.2 cm separation in the contraction joint at node 36 which, as mentioned earlier, is of some concern regarding violation of the no-slip assumption. The minor lift-offs seen in several horizontal joints may be less important.

5.7 Investigation of no-slip constraint in joints

An additional calculation was made to investigate some features of not permitting any slip in the joints as pertains to possible collapse of the dam. The pseudo-static response of the dam was computed for a constant ground acceleration in the downstream and cross-stream directions. The tensile strength of all joints was set to zero, the reservoir was taken to be empty, and no dead load was applied. Figure 5.16 shows the results for a 1 g ground acceleration applied in the downstream direction. The stresses and openings along each of the arches A0 to A5 and cantilevers C−4 to C4 are displayed in a manner similar to Figure 5.6. In addition, the deformed shape (openings omitted) of each arch and cantilever is shown in dashed lines. The maximum opening at any joint is 3.69 cm on the downstream face of the dam-foundation interface joint at node 10. Most of the vertical contraction joints and interface joints are completely or almost completely open except in the lower reaches of the dam where some joints have significant contact depths. Most of the horizontal cracking planes are open (by as much as 1.45 cm) on their downstream faces but are closed on their upstream faces. The maximum radial displacement of the crest relative to the ground is 19.8 cm. If the ground acceleration is increased beyond 1 g, the joint openings and compressive stresses increase linearly but the dam remains stable. Thus, the no-slip constraint on the joint provides sufficient stiffness to prevent collapse even though joints are free to open. The results of the pseudo-static analysis with a ground acceleration of 1 g in the cross-stream direction also showed the dam to be stable, with a maximum radial displacement of the crest of 3.1 cm. Thus, joint slip appears to be an important ingredient for collapse, and the present analytical technique cannot be used for collapse simulations.

	Case 1	Case 2	Case 3	Case 4	Case 5
$\bar{K}$	original	local	original	original	original
reservoir	empty	empty	full	full	full
water	—	—	FEM	FEM	LAM
K_{pp}	—	—	original	local	—
mode 1 (S)	5.203	5.213	4.140	4.363	3.392
mode 2 (A)	5.245	5.270	4.324	4.405	3.588
mode 3 (S)	7.888	7.896	6.624	6.672	5.486
mode 4 (S)	8.878	8.967	7.363	7.755	5.824
mode 5 (A)	10.032	10.129	9.119	9.105	7.164
mode 6 (A)	10.432	10.565	9.346	9.358	7.357

Table 5.1. Eigenfrequencies (hz.) of Pacoima Dam-water-foundation system under various conditions. FEM = finite element. LAM = lumped added mass. S = symmetric mode. A = antisymmetric mode. $[\bar{K}]$ = foundation stiffness matrix. $[K_{pp}]$ = water stiffness matrix.

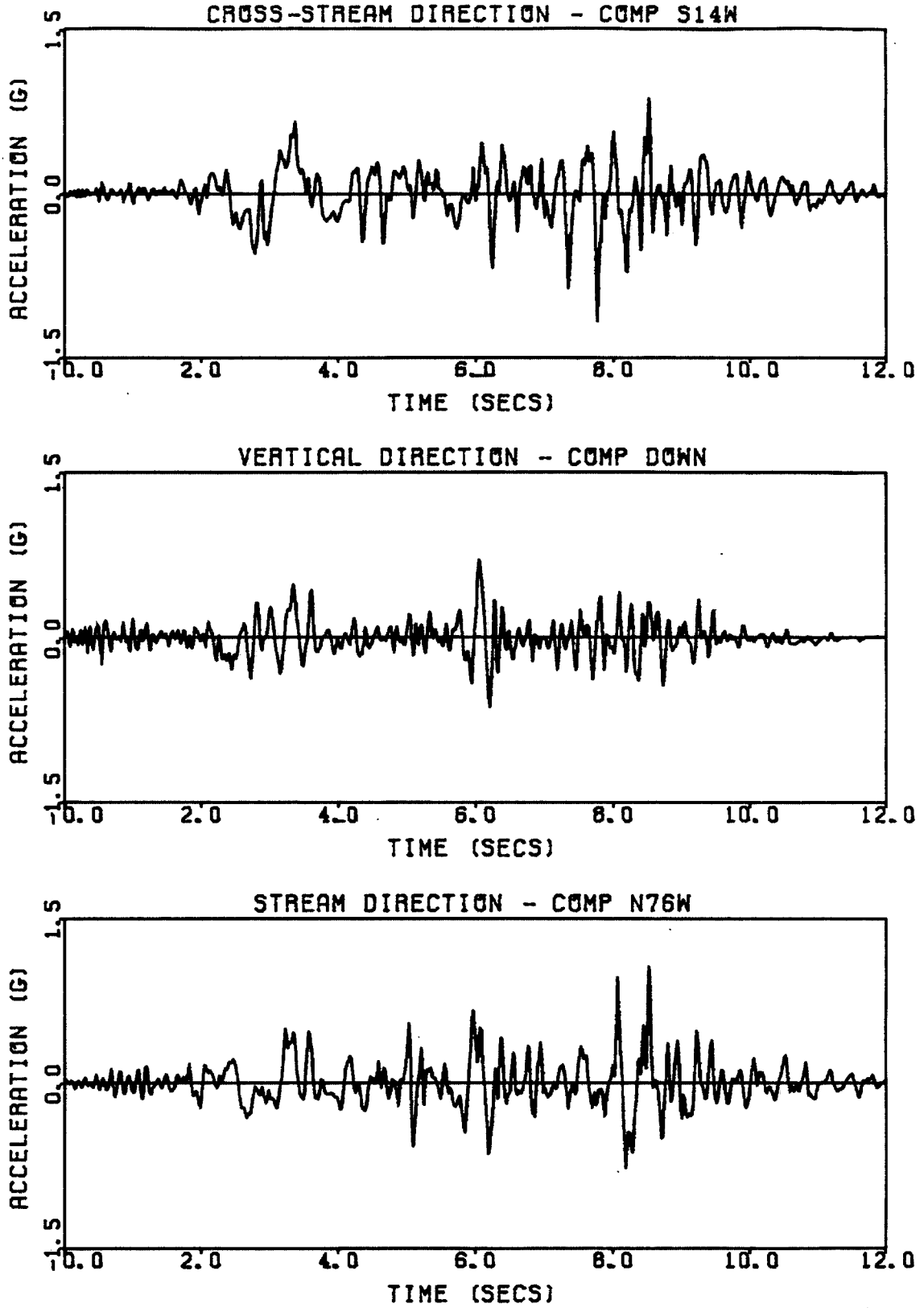

Figure 5.1 Accelerograms obtained at Pacoima Dam during 1971 San Fernando earthquake.

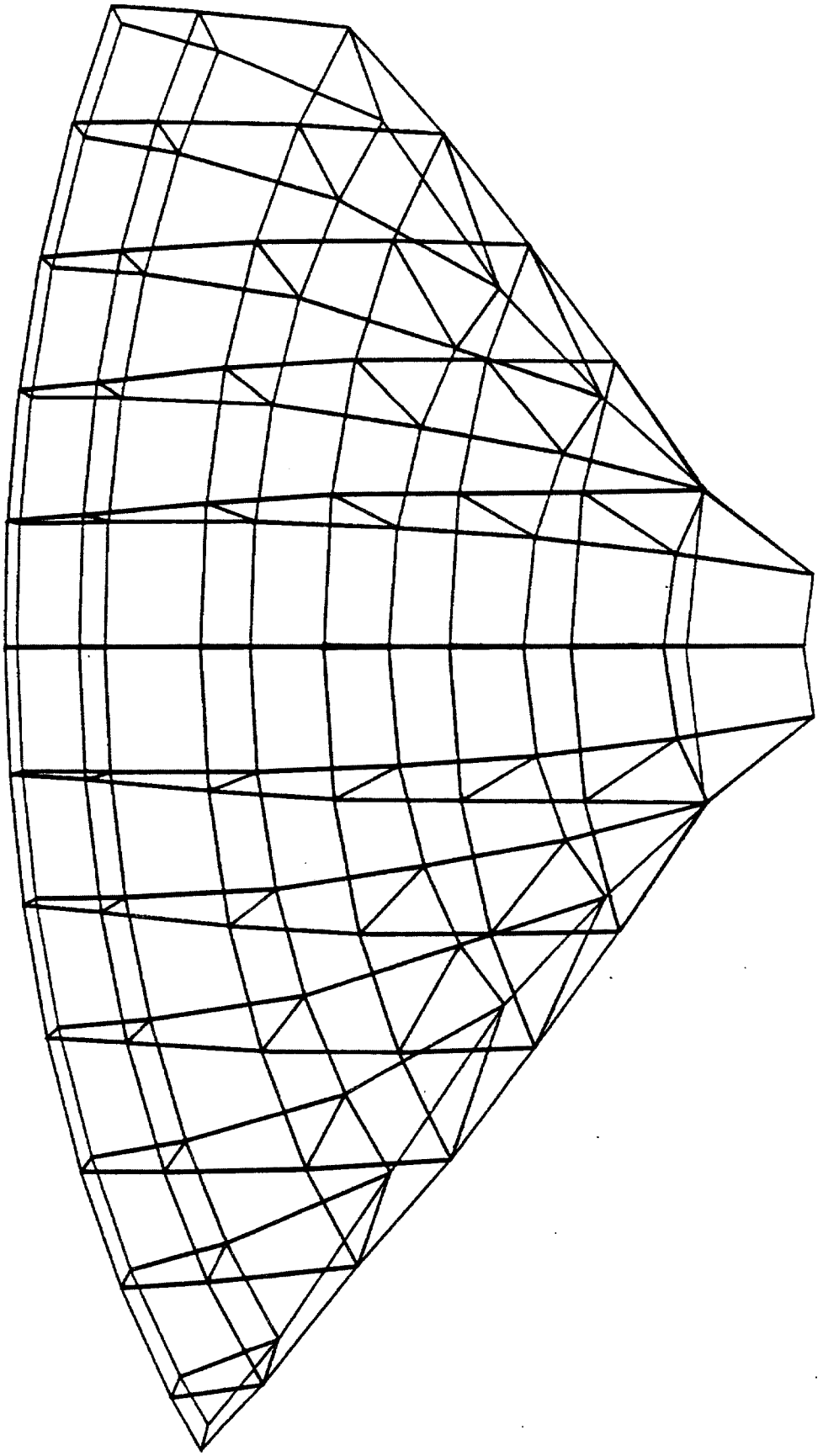

Figure 5.2 Finite element mesh of Pacoima Dam.

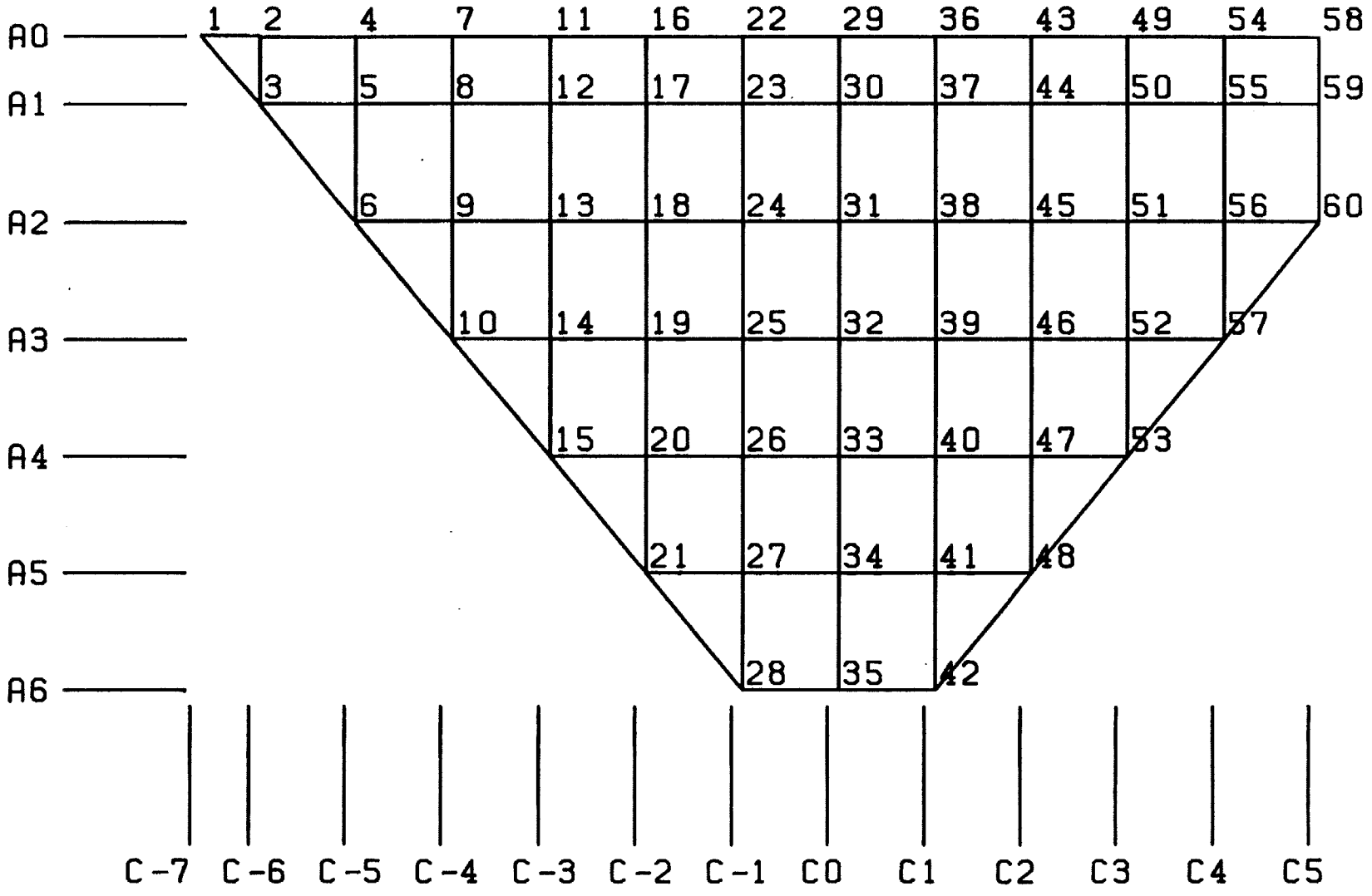

Figure 5.3 Dam mesh showing node numbers and the arch and cantilever reference lines.

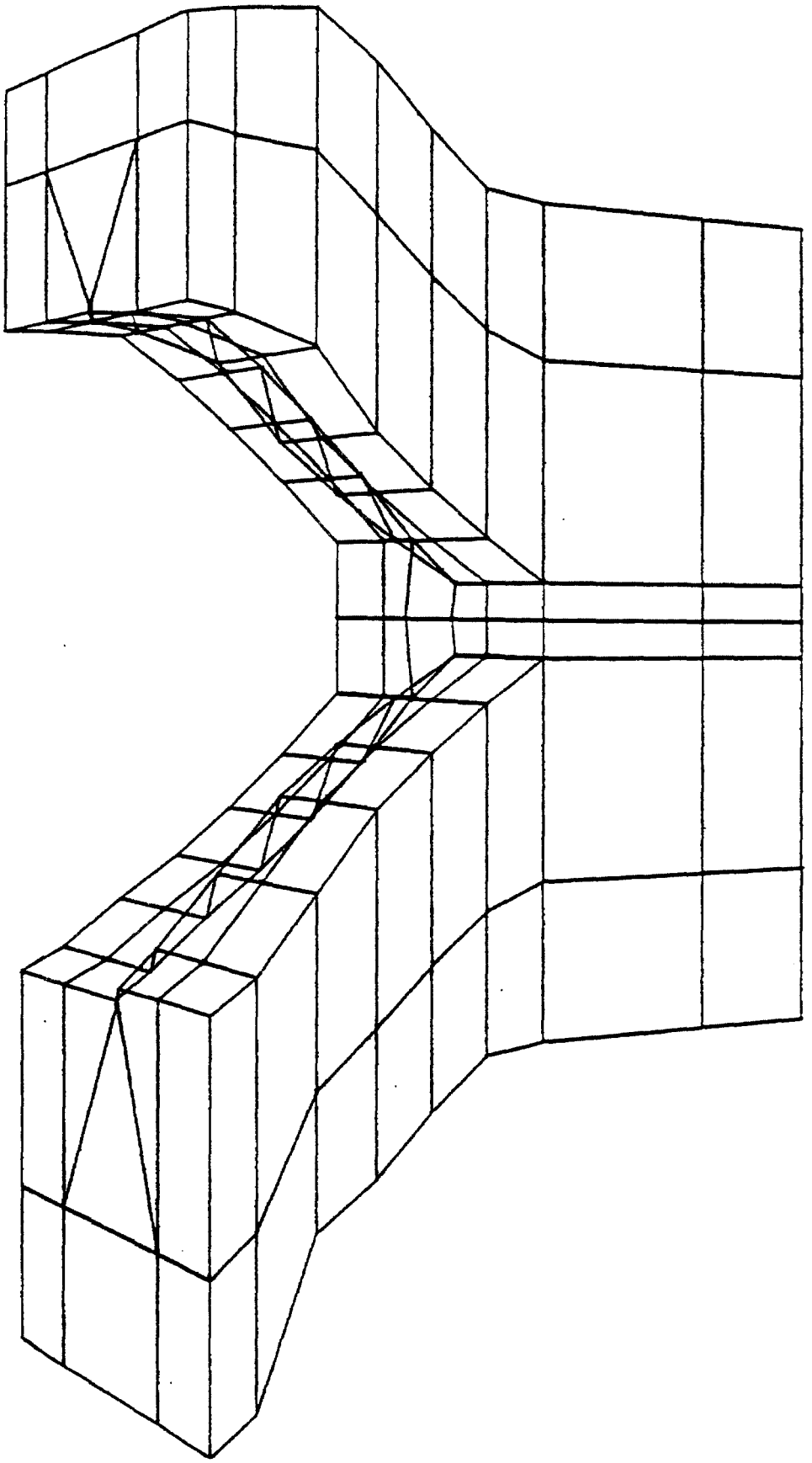

Figure 5.4 Finite element mesh of foundation.

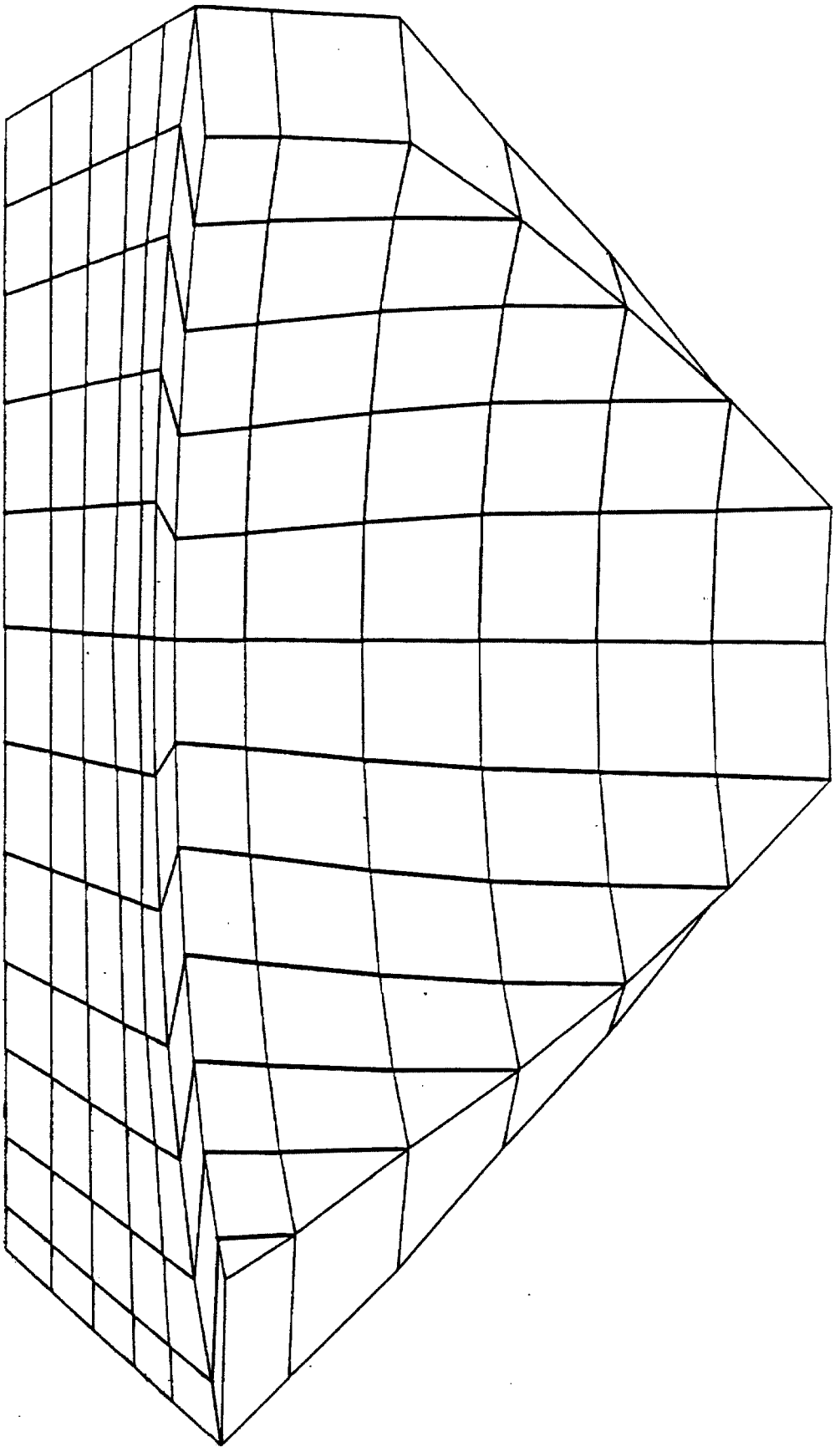

Figure 5.5 Finite element mesh of water domain (full condition).

Figure 5.6 a and b (next 2 pages). Results of static load application to Pacoima Dam showing normal stresses (MPa, tension positive, compression negative) in arch A0 and cantilever C0 and their deformed shapes (solid line, original profile dashed line).

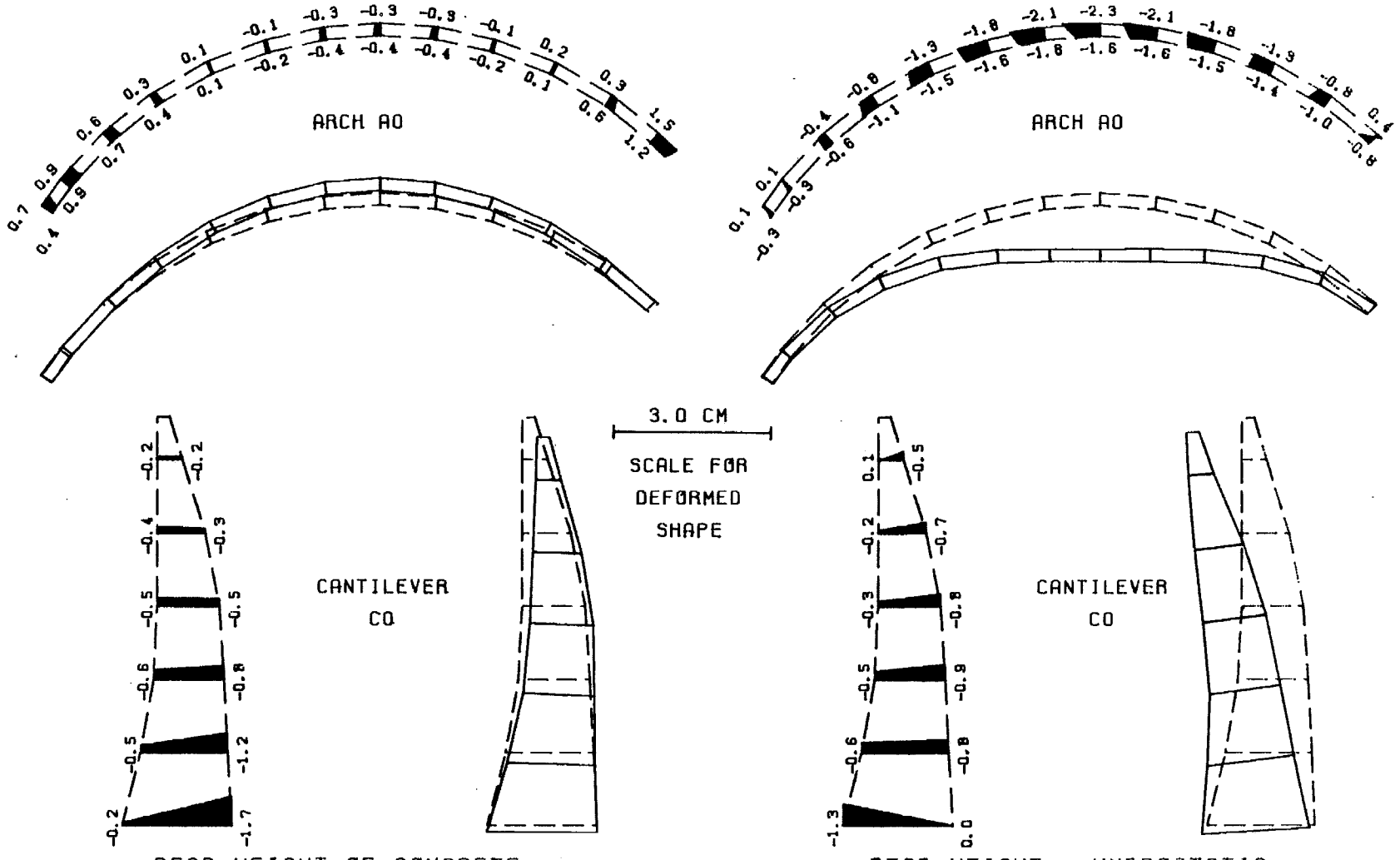

Figure 5.6a Dead weight applied instantaneously to the continuous and completely finished structure.

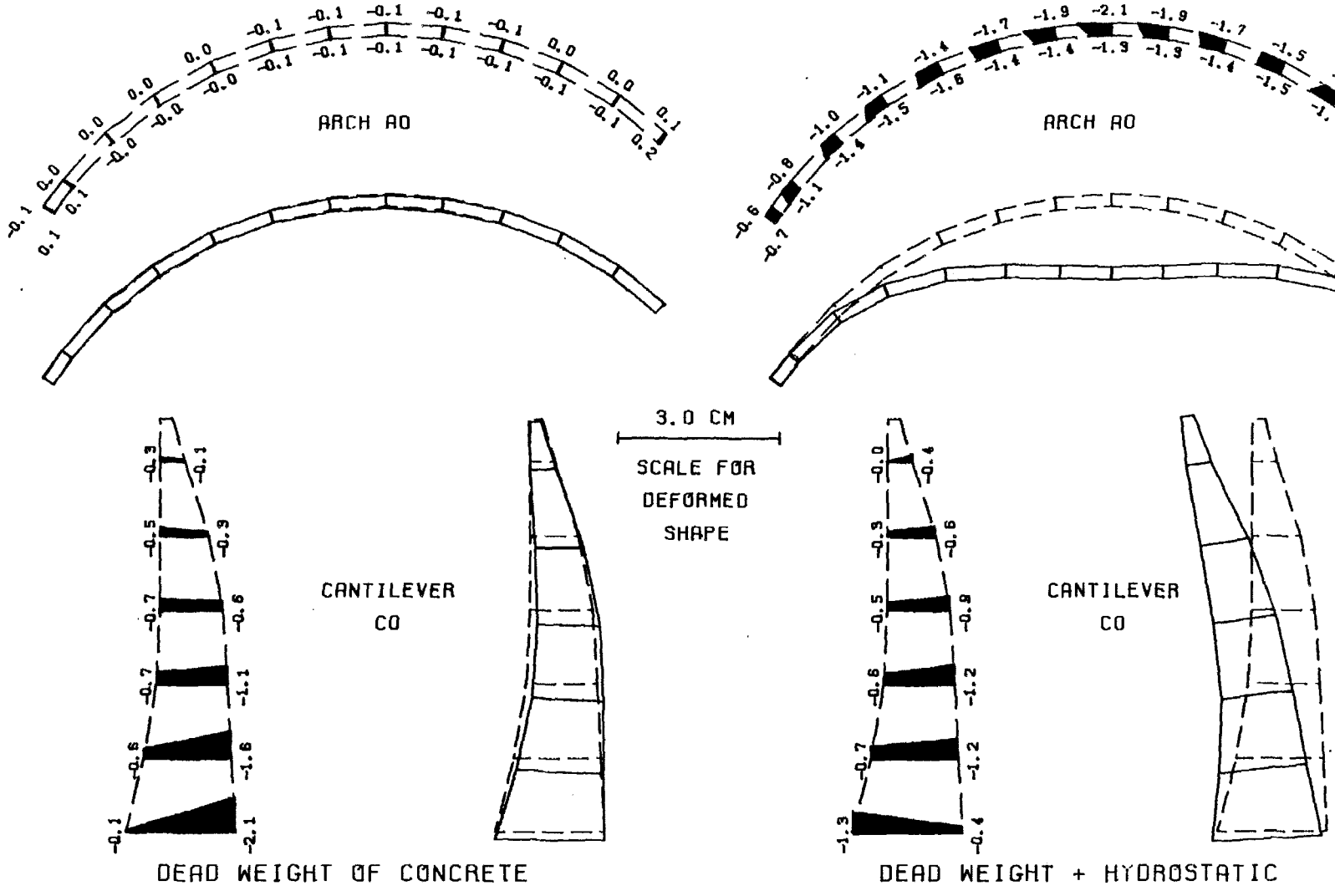

Figure 5.6b Dead weight applied via a construction sequence.

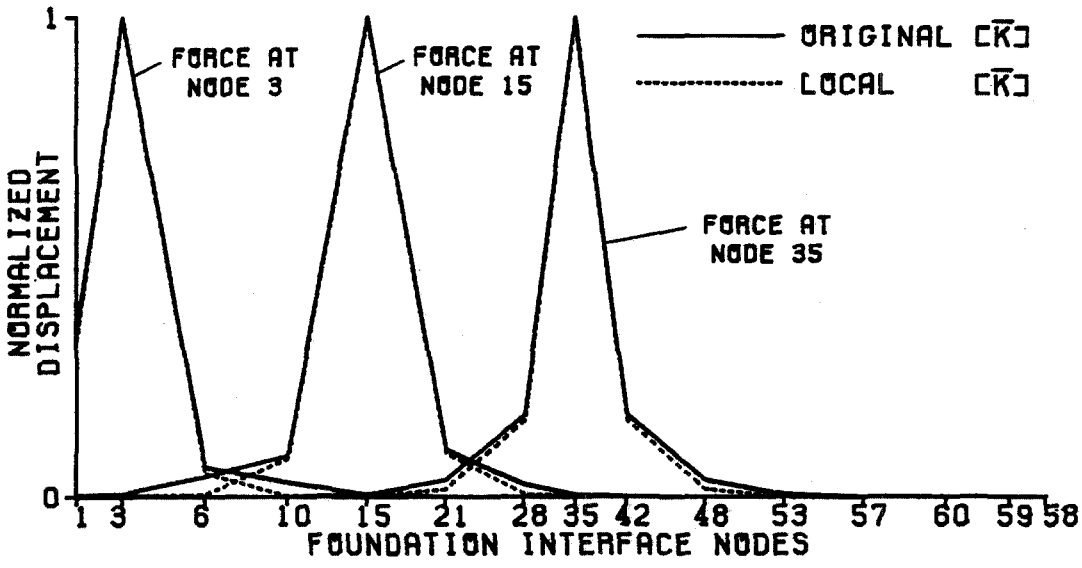

a. Applied forces and plotted displacements are in the $\hat{z}$ direction (approximately normal to the dam midsurface).

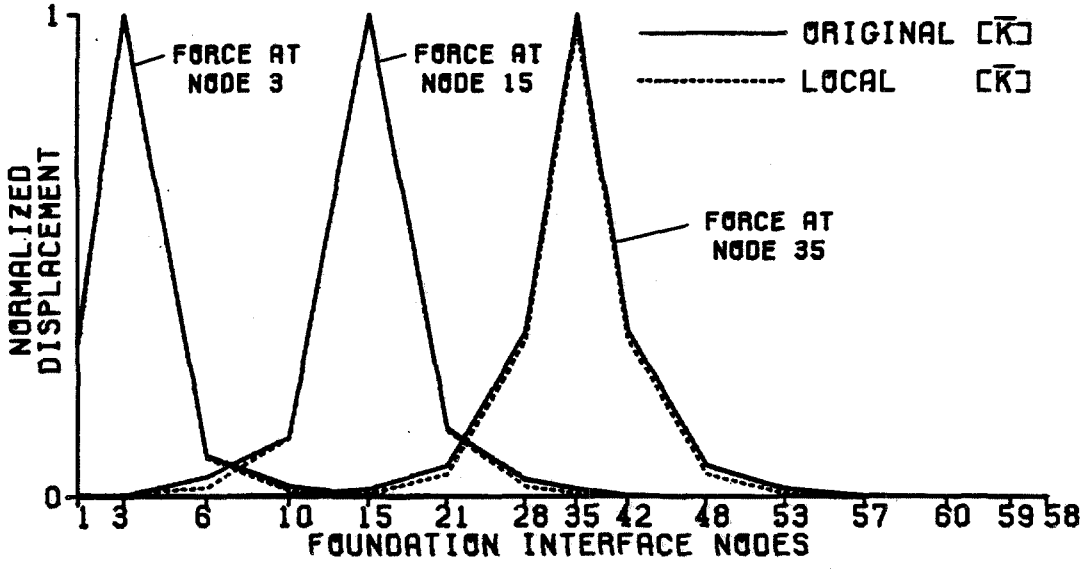

b. Applied forces and plotted displacements are in the $\hat{x}$ direction (normal to the foundation interface).

Figure 5.7 Results of investigation to assess localization of $[\bar{K}]$. Forces are applied at nodes 3, 15 and 35 on the foundation interface, and the displacements are plotted around the interface. Each displacement profile from the original $[\bar{K}]$ is normalized to a peak value of one and the scale factor required is also used to scale the corresponding displacement profile from the local $[\bar{K}]$.

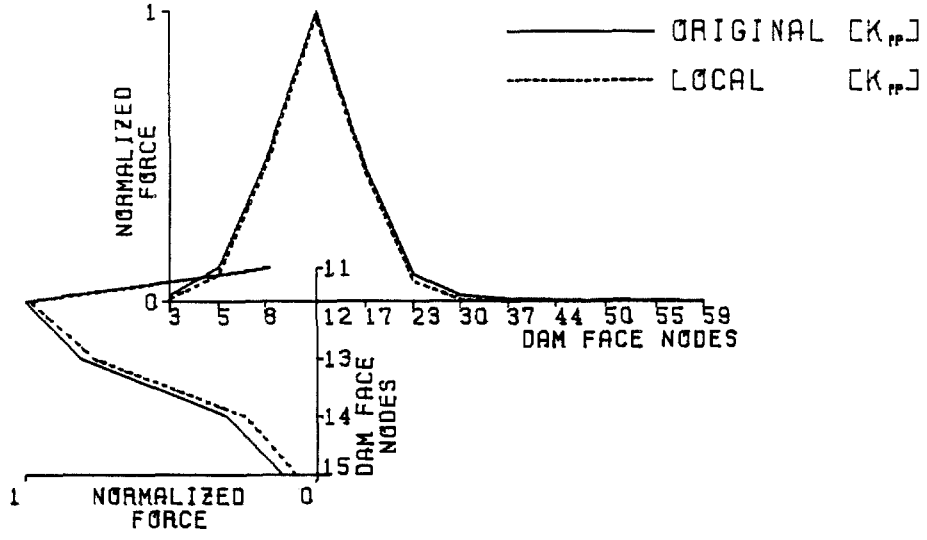

a. Acceleration of node 12.

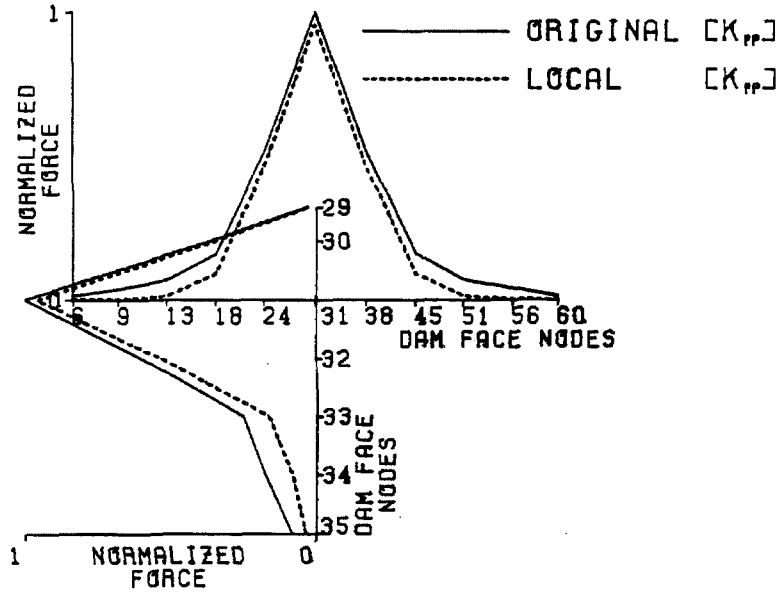

b. Acceleration of node 31.

Figure 5.8 Results of investigation to assess localization of $[K_{pp}]$. Applied accelerations and plotted hydrodynamic forces are in the $\hat{z}$ direction (approximately normal to the dam mid-surface). Each hydrodynamic force profile from the original $[K_{pp}]$ is normalized to a peak value of one and the scale factor required is also used to scale the corresponding hydrodynamic force profile from the local $[K_{pp}]$.

Figure 5.9 a to j (next 10 pages). Summary of the earthquake responses of Pacoima Dam to the records of Figure 5.1 scaled by 2/3. Results for both the partially full and full reservoirs are presented: static stresses, maximum tensions for linear analysis, maximum openings for nonlinear analysis, and maximum compressions for linear and nonlinear analysis. Stresses (MPa) are shaded with amplitudes given to one decimal place. Openings (cm) are unshaded with amplitudes given to two decimal places.

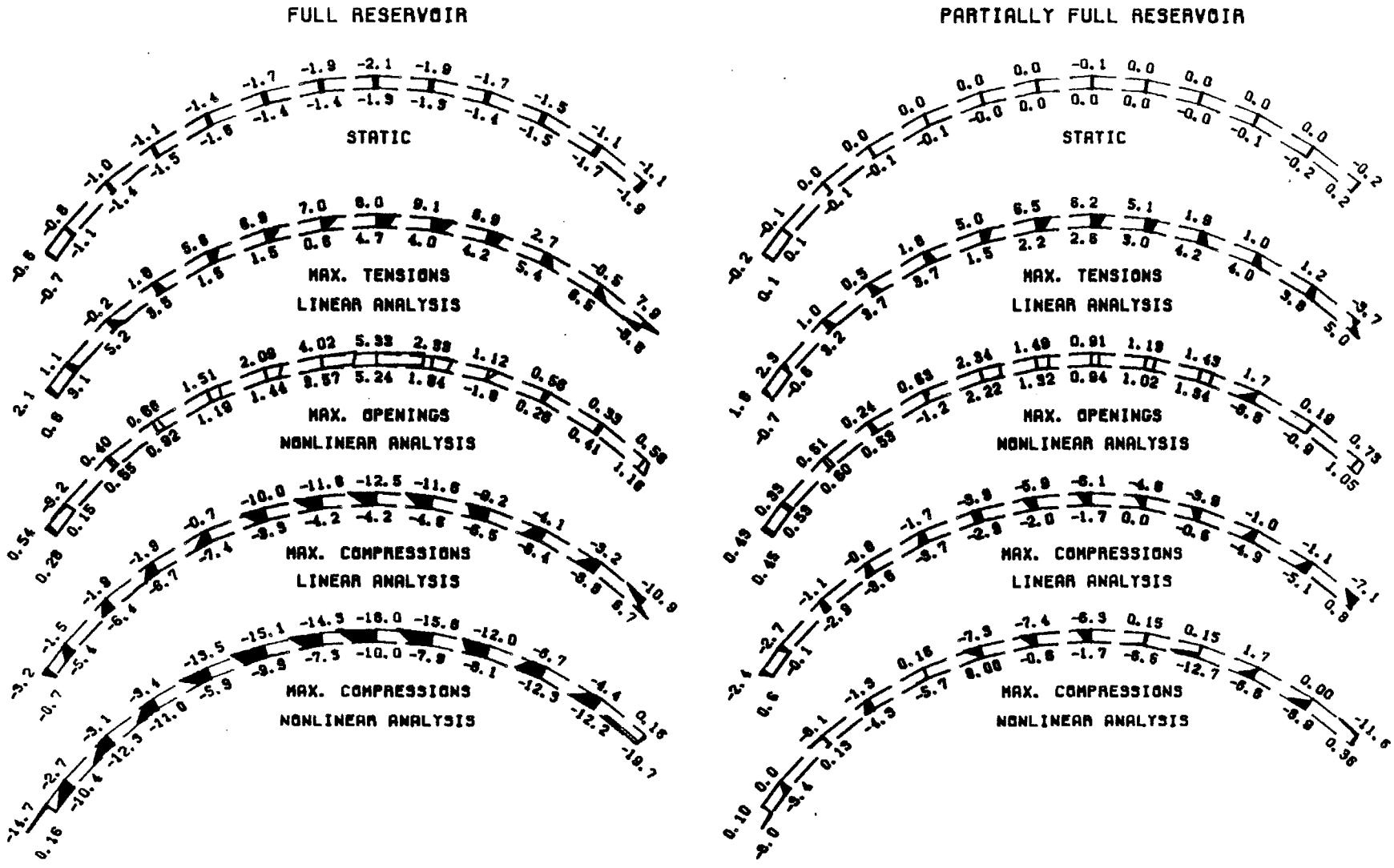

Figure 5.9a. Arch 0 (ground motion scale = 2/3).

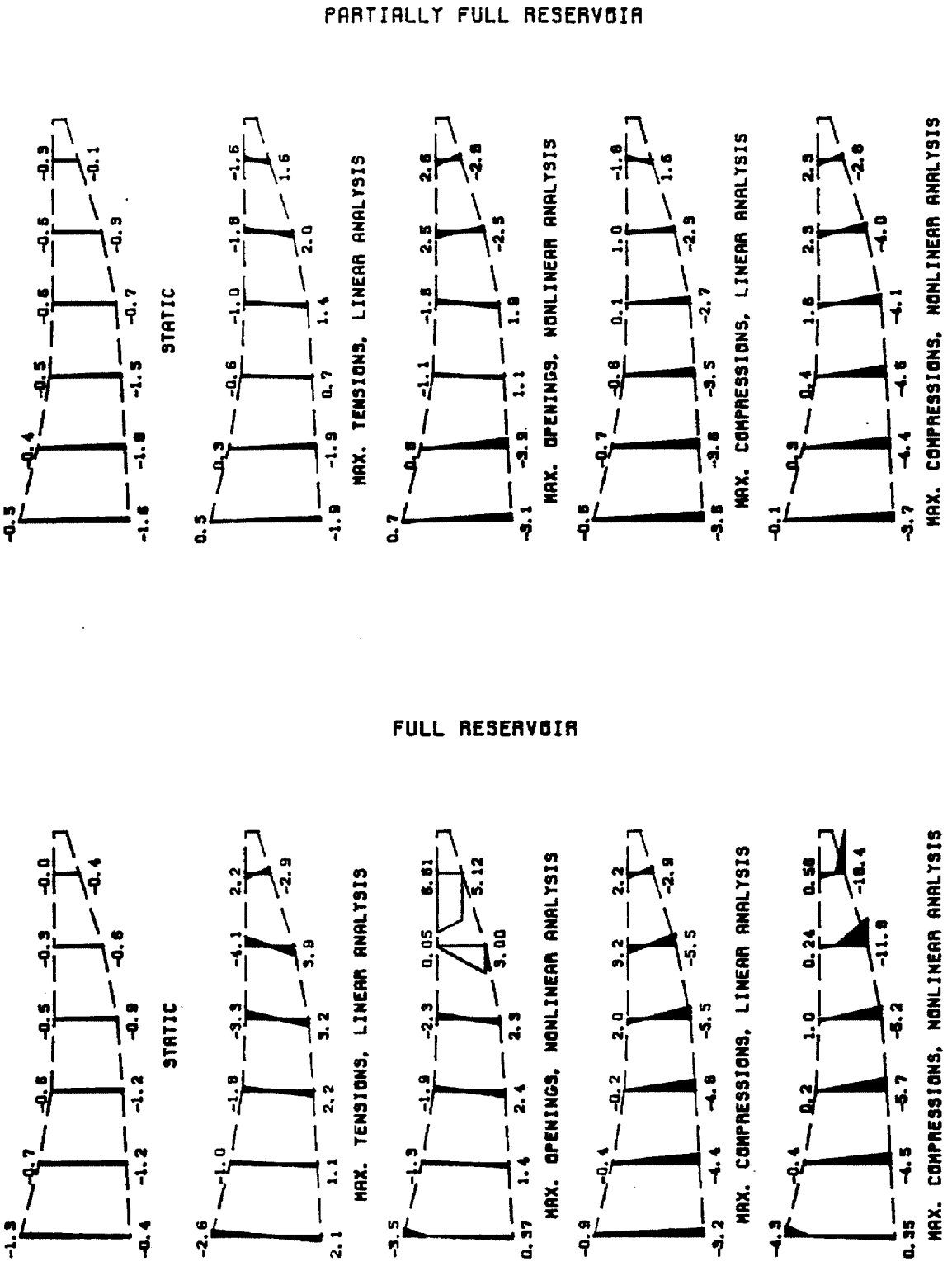

Figure 5.9b. Cantilever 0 (ground motion scale = 2/3).

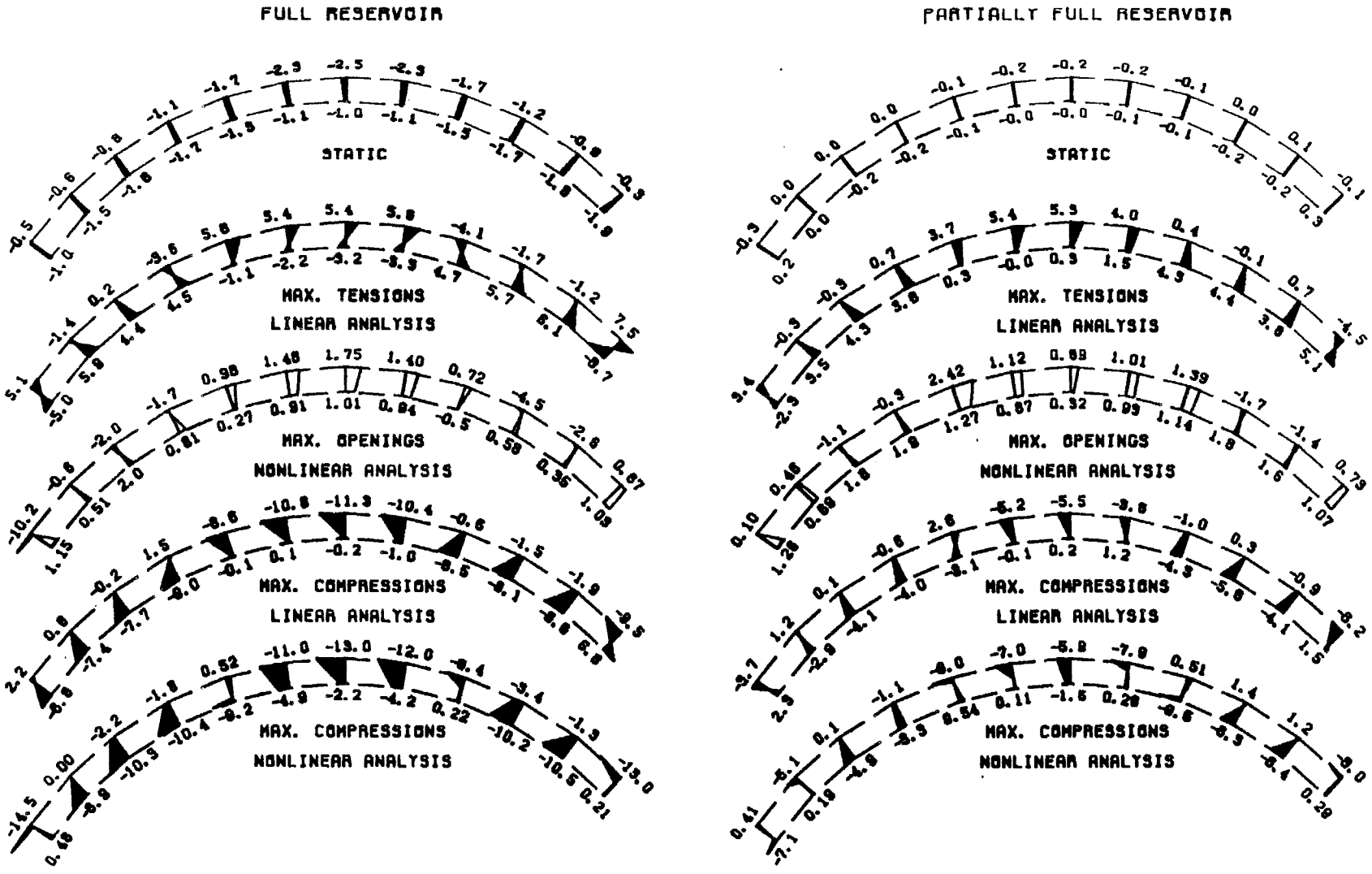

Figure 5.9c. Arch 1 (ground motion scale = 2/3).

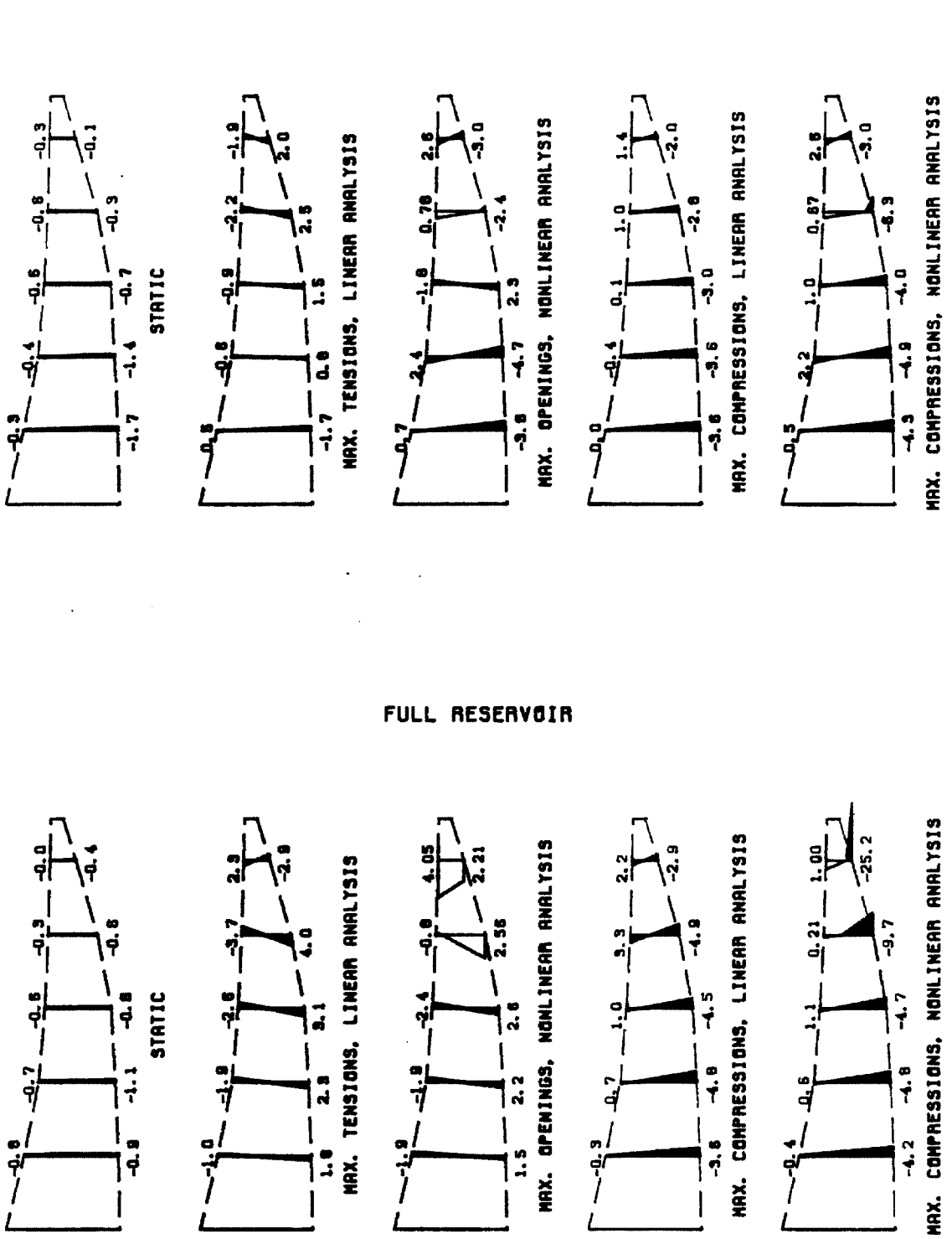

Figure 5.9d. Cantilever −1 (ground motion scale = 2/3).

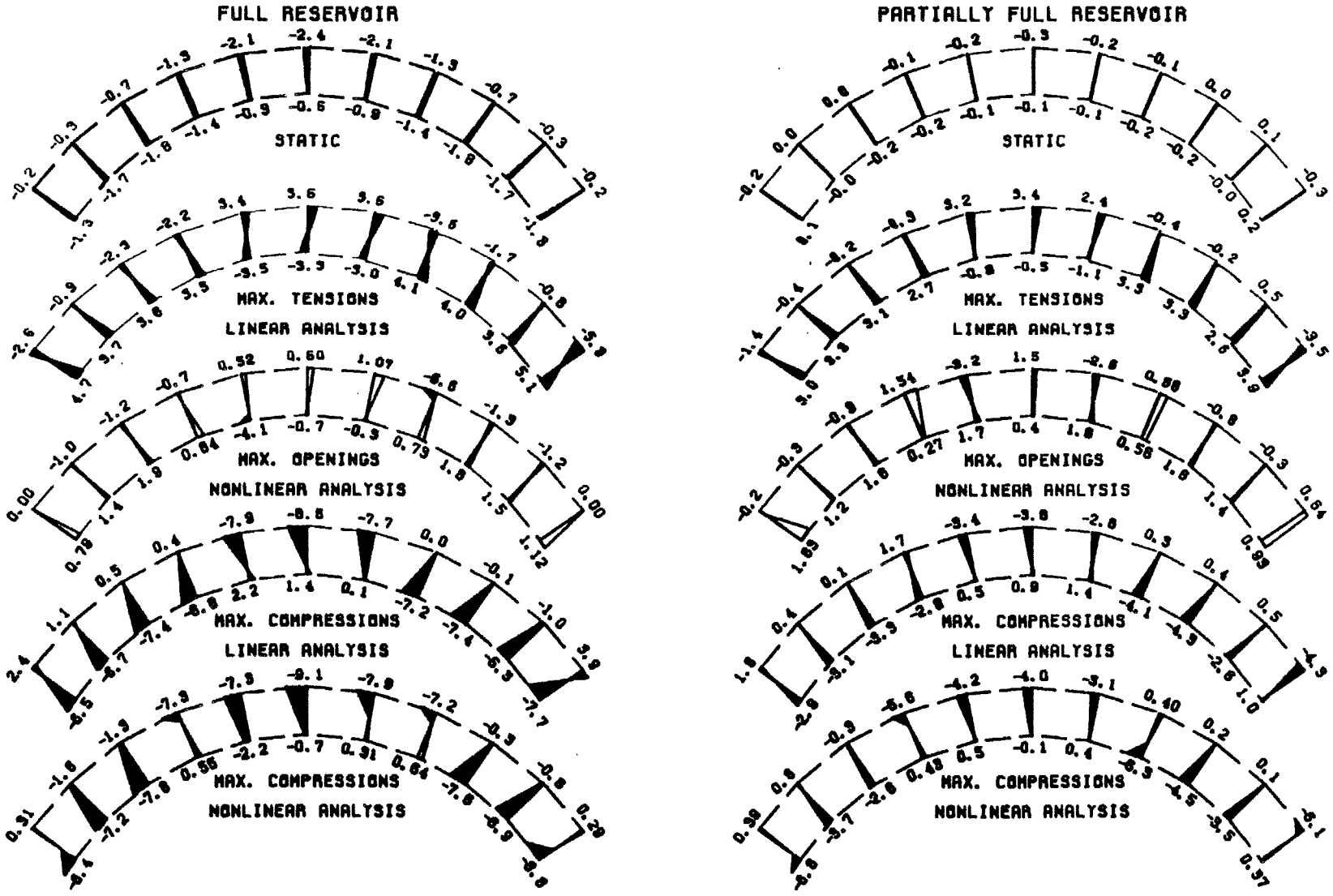

Figure 5.9e. Arch 2 (ground motion scale = 2/3).

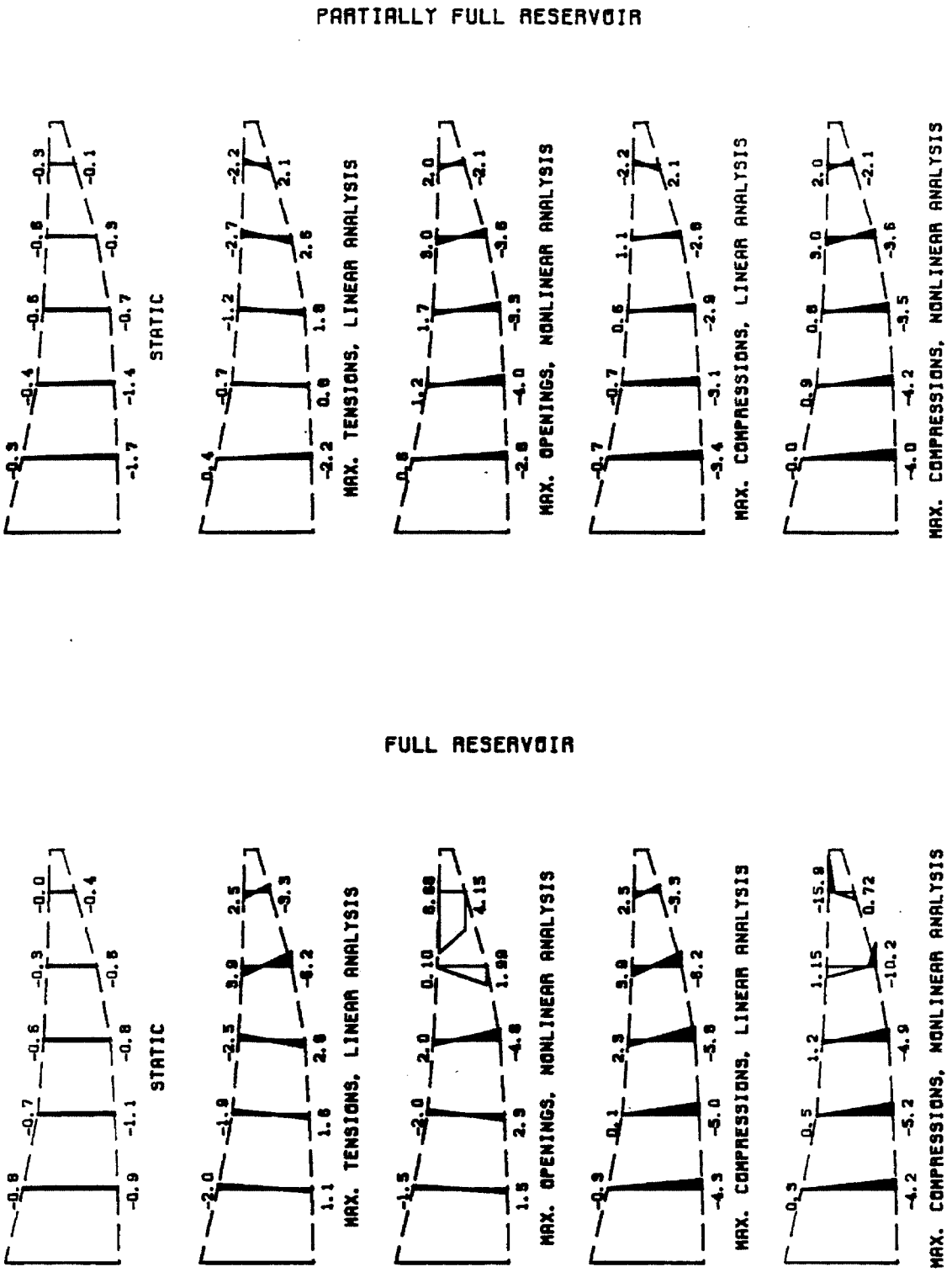

Figure 5.9f. Cantilever 1 (ground motion scale = 2/3).

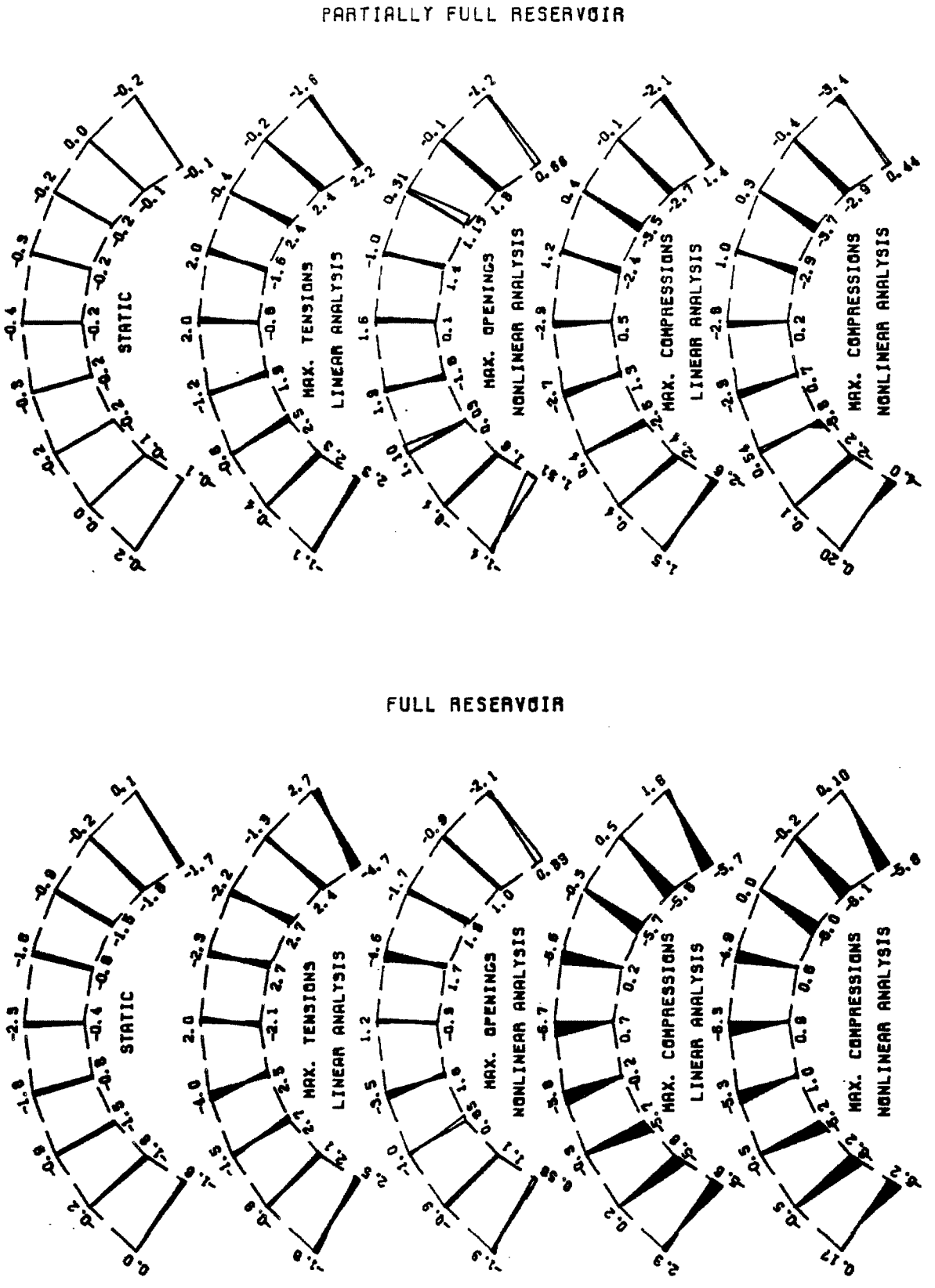

Figure 5.9g. Arch 3 (ground motion scale = 2/3).

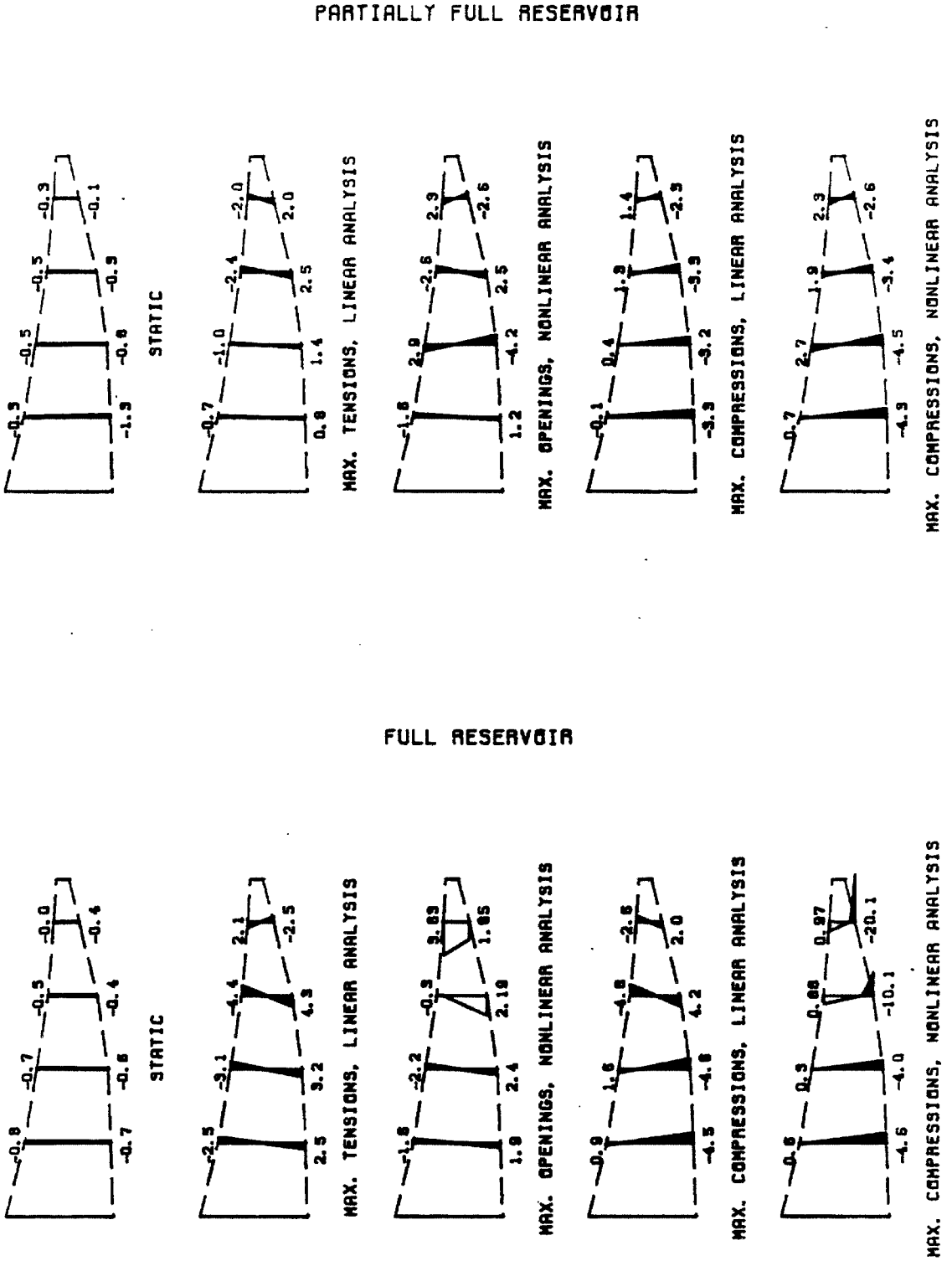

Figure 5.9h. Cantilever -2 (ground motion scale $= 2/3$).

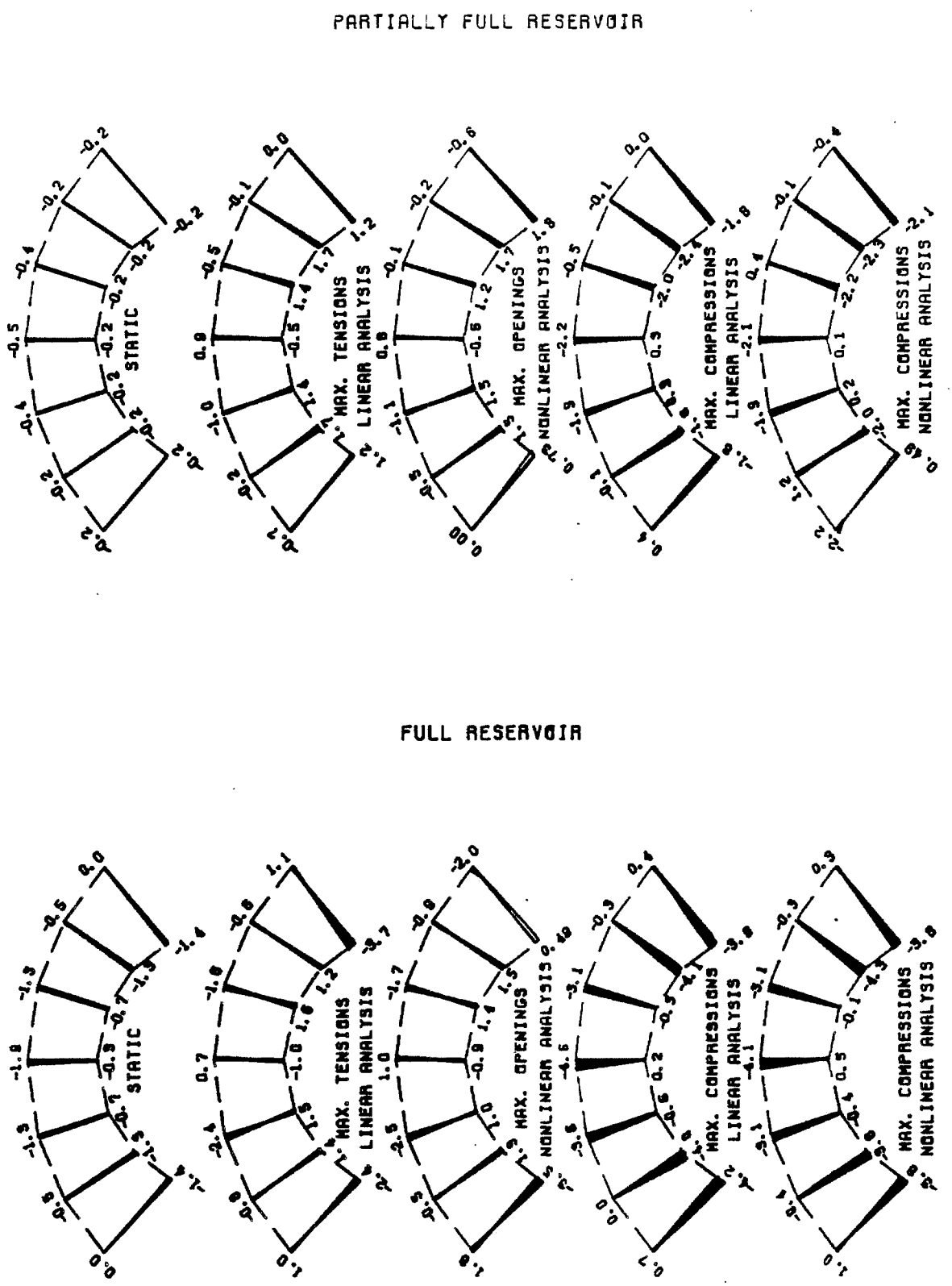

Figure 5.9i. Arch 4 (ground motion scale = 2/3).

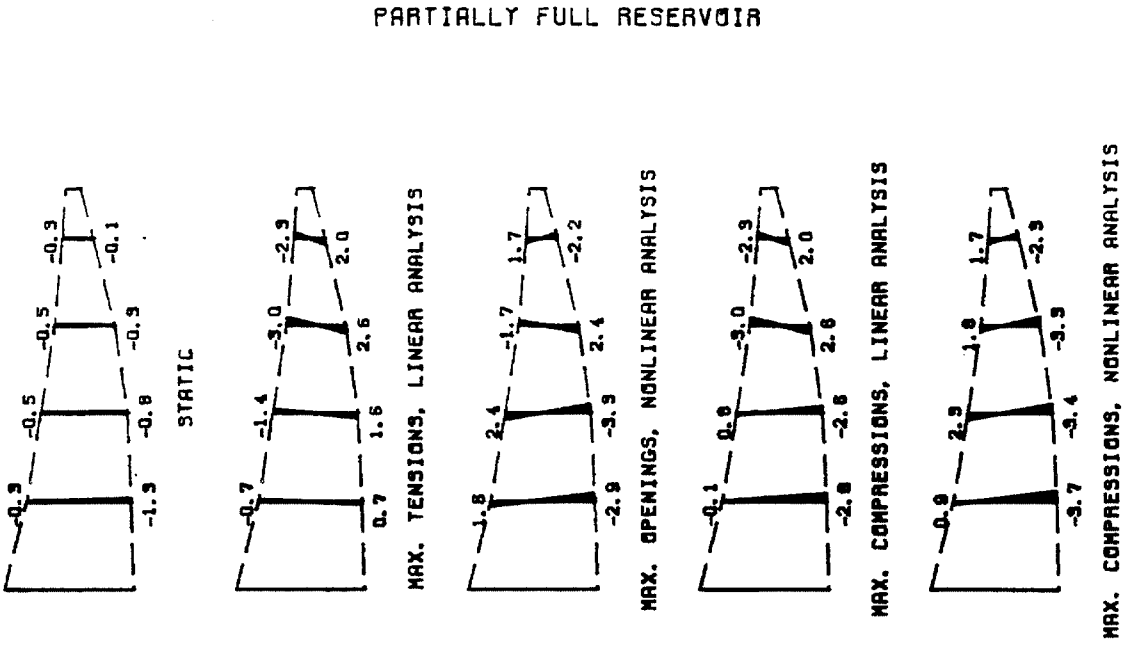

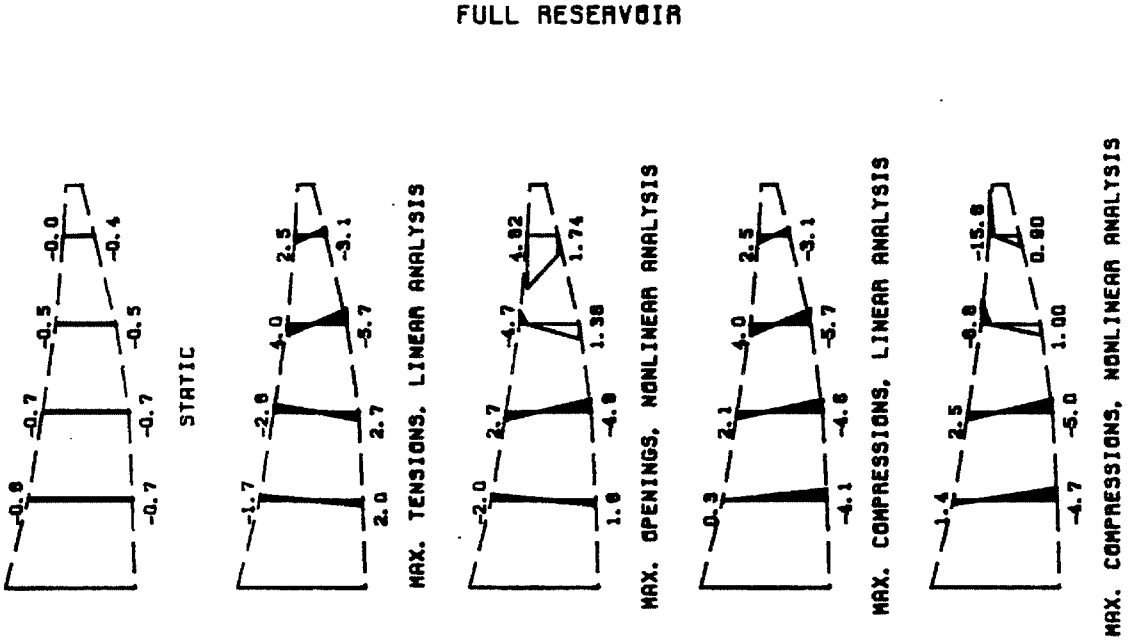

Figure 5.9j. Cantilever 2 (ground motion scale = 2/3).

Figure 5.10 (next 6 pages). Sequence of snapshots of arch A0 and cantilever C0 from the nonlinear earthquake response of Pacoima Dam to the records of Figure 5.1 scaled by 2/3. Results are for the partially full reservoir: normal stresses (shaded, tension positive, compression negative, amplitude given in MPa to one decimal place), joint openings (unshaded, amplitude given in cm to two decimal places), and deformed shape (solid line, original profile dashed line).

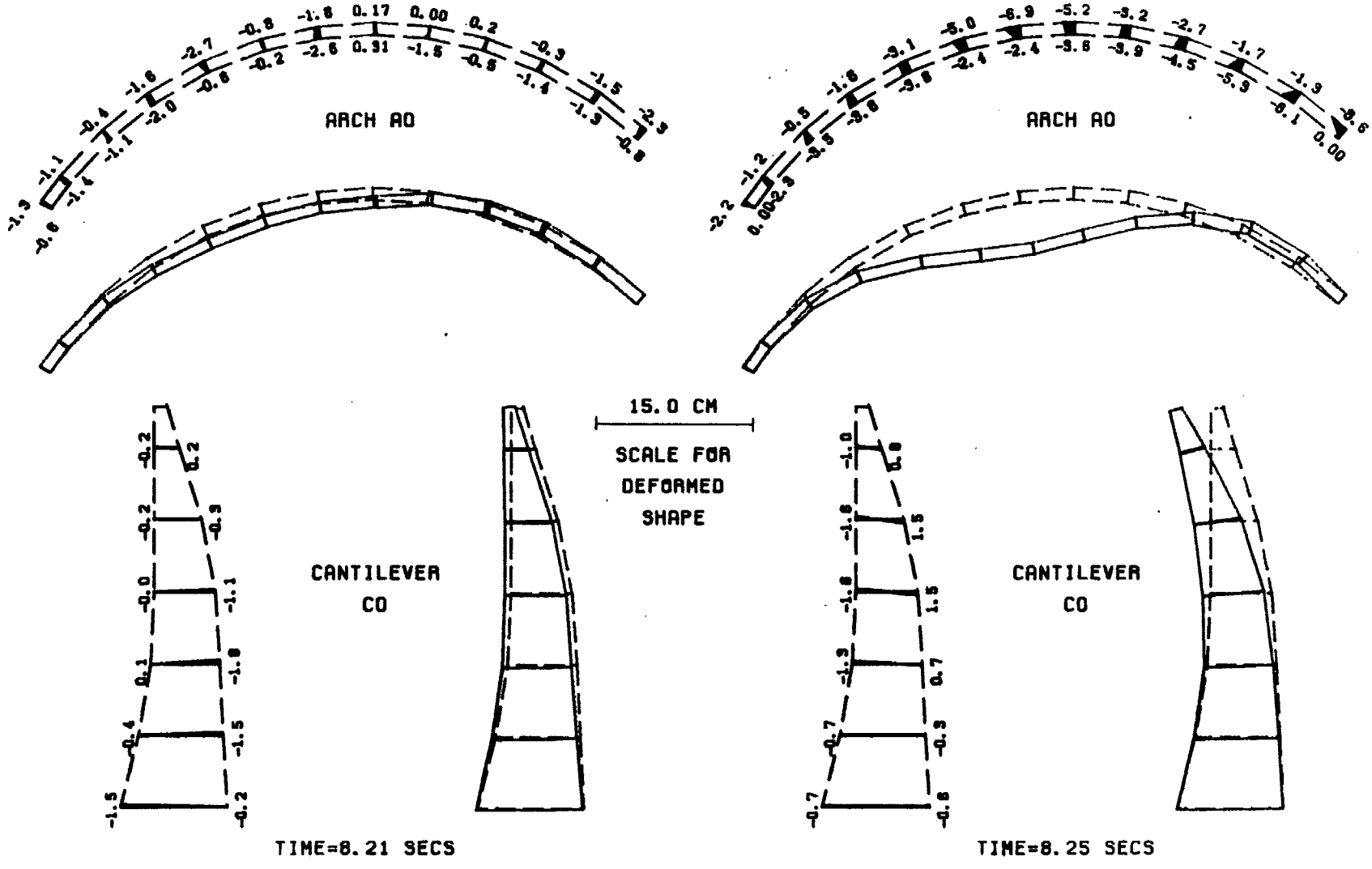

Figure 5.10 (ground motion scale = 2/3, partially full reservoir).

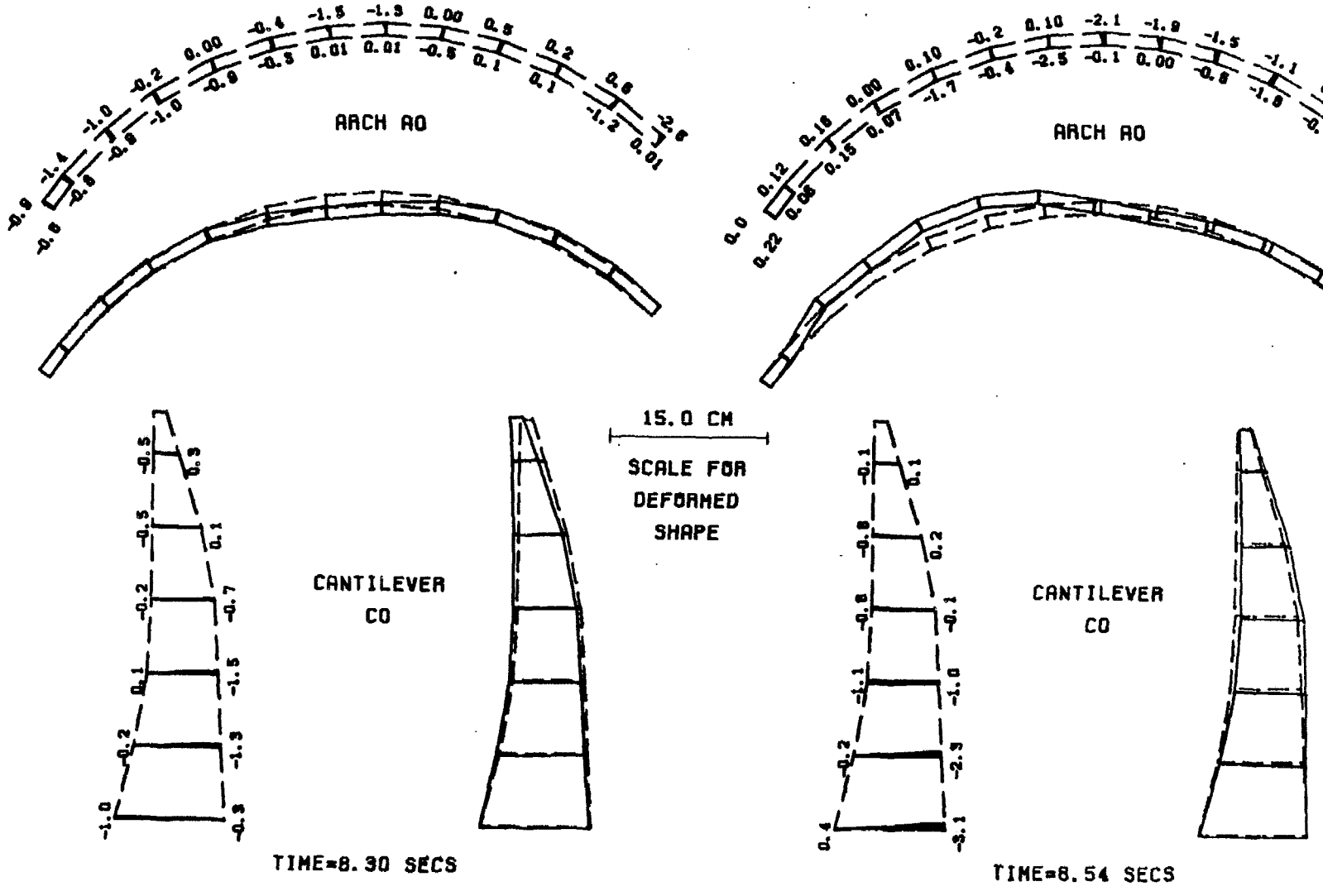

Figure 5.10 (continued, ground motion scale = 2/3, partially full reservoir).

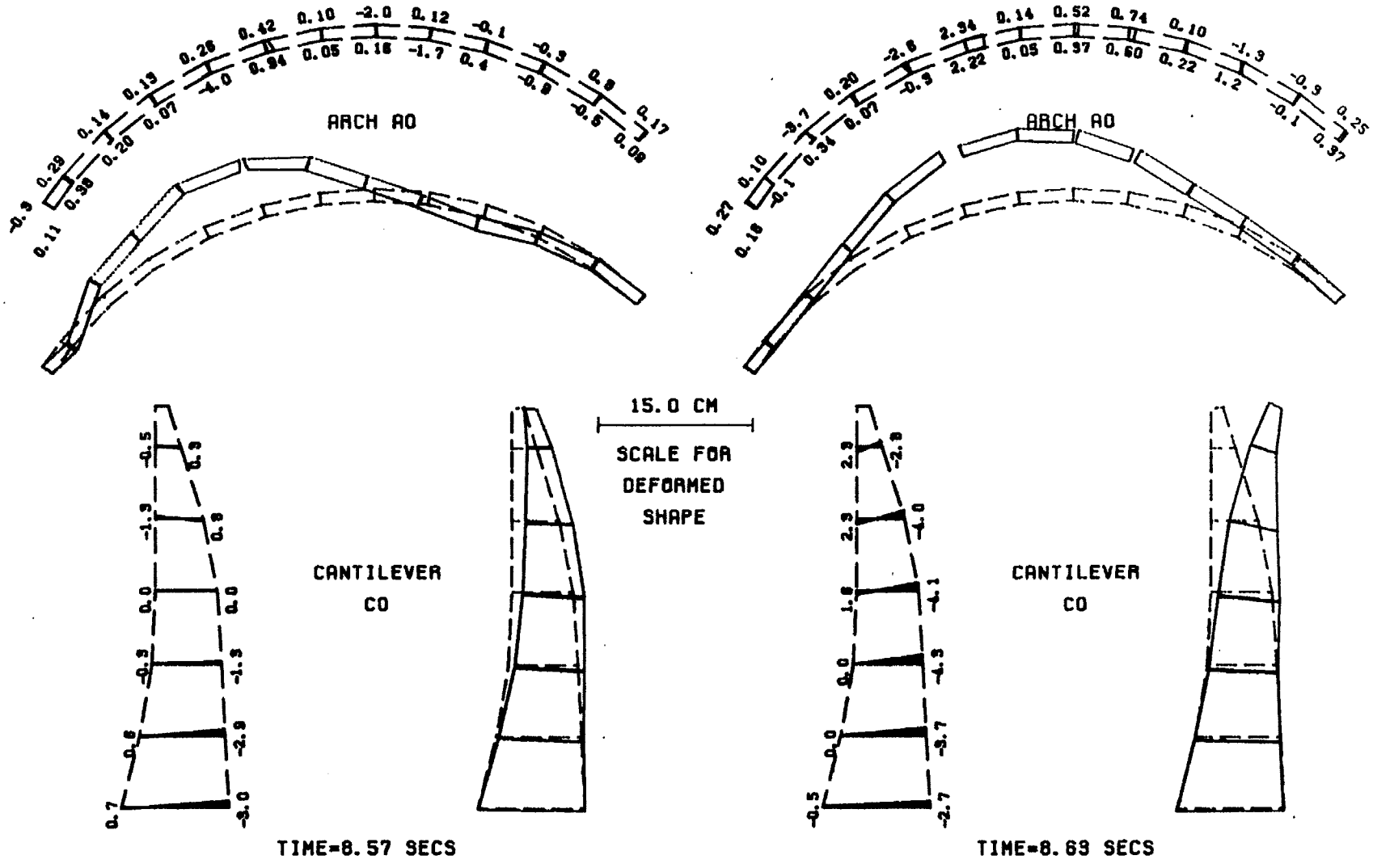

Figure 5.10 (continued, ground motion scale = 2/3, partially full reservoir).

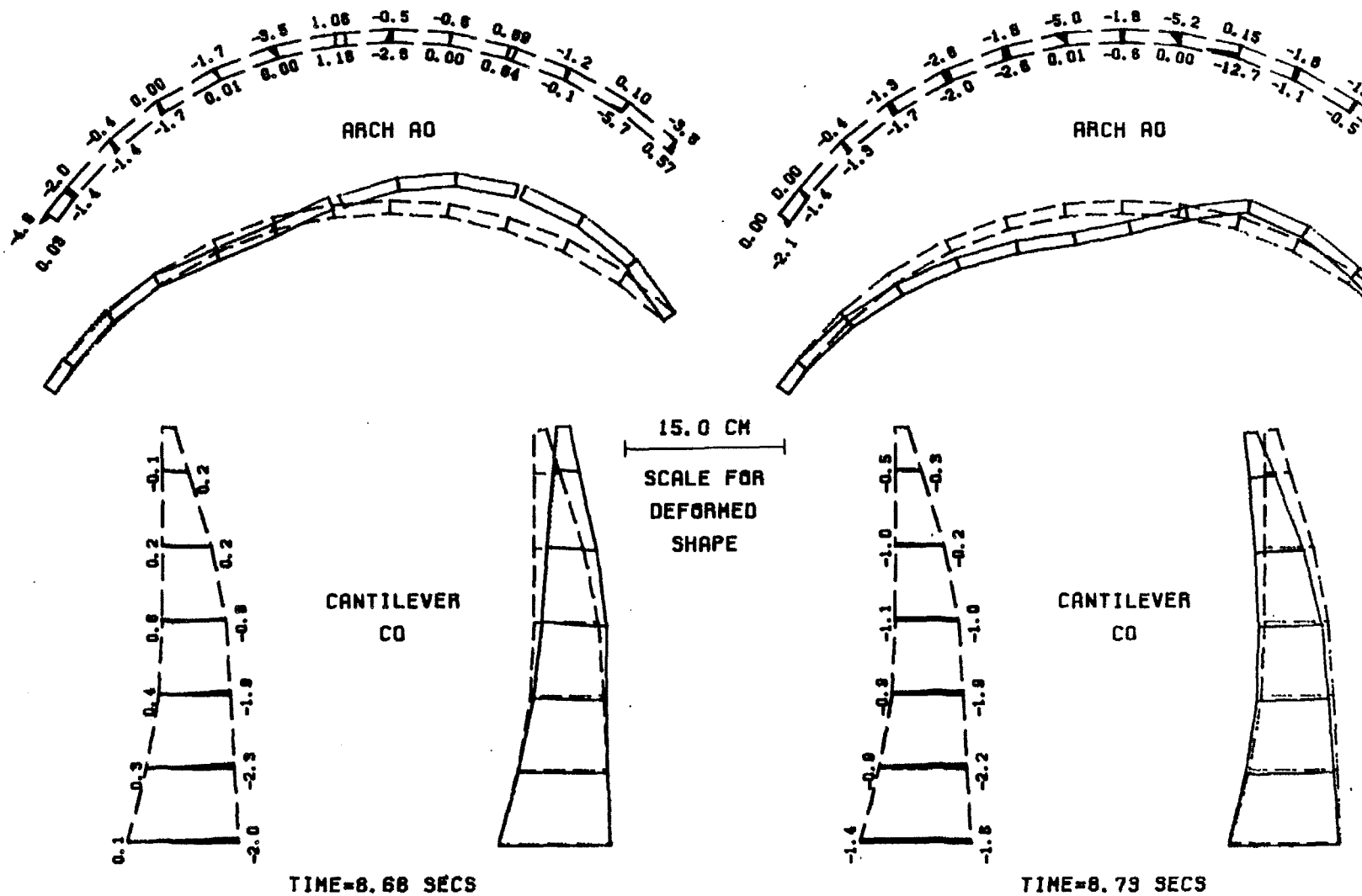

Figure 5.10 (continued, ground motion scale = 2/3, partially full reservoir).

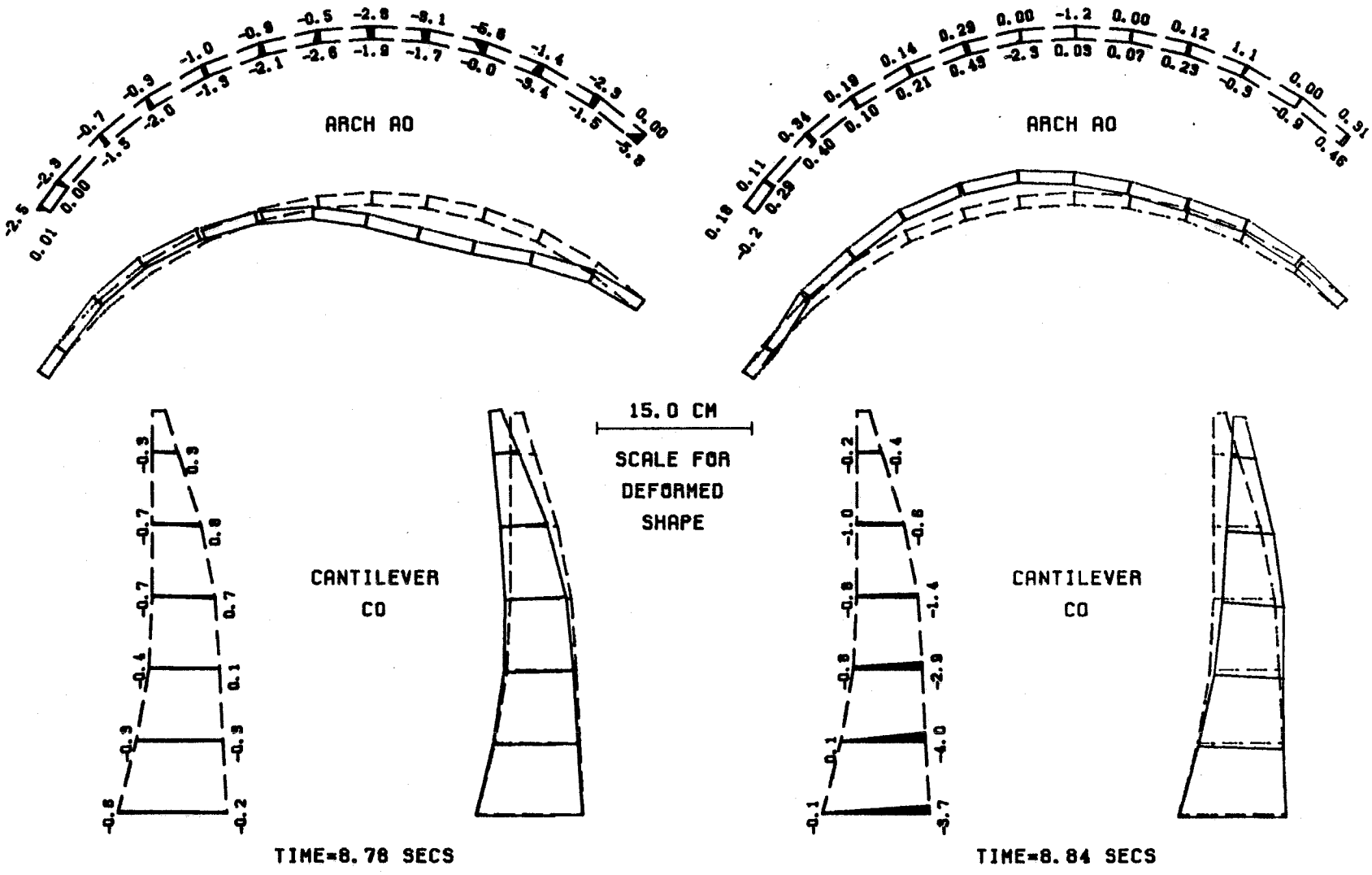

Figure 5.10 (continued, ground motion scale = 2/3, partially full reservoir).

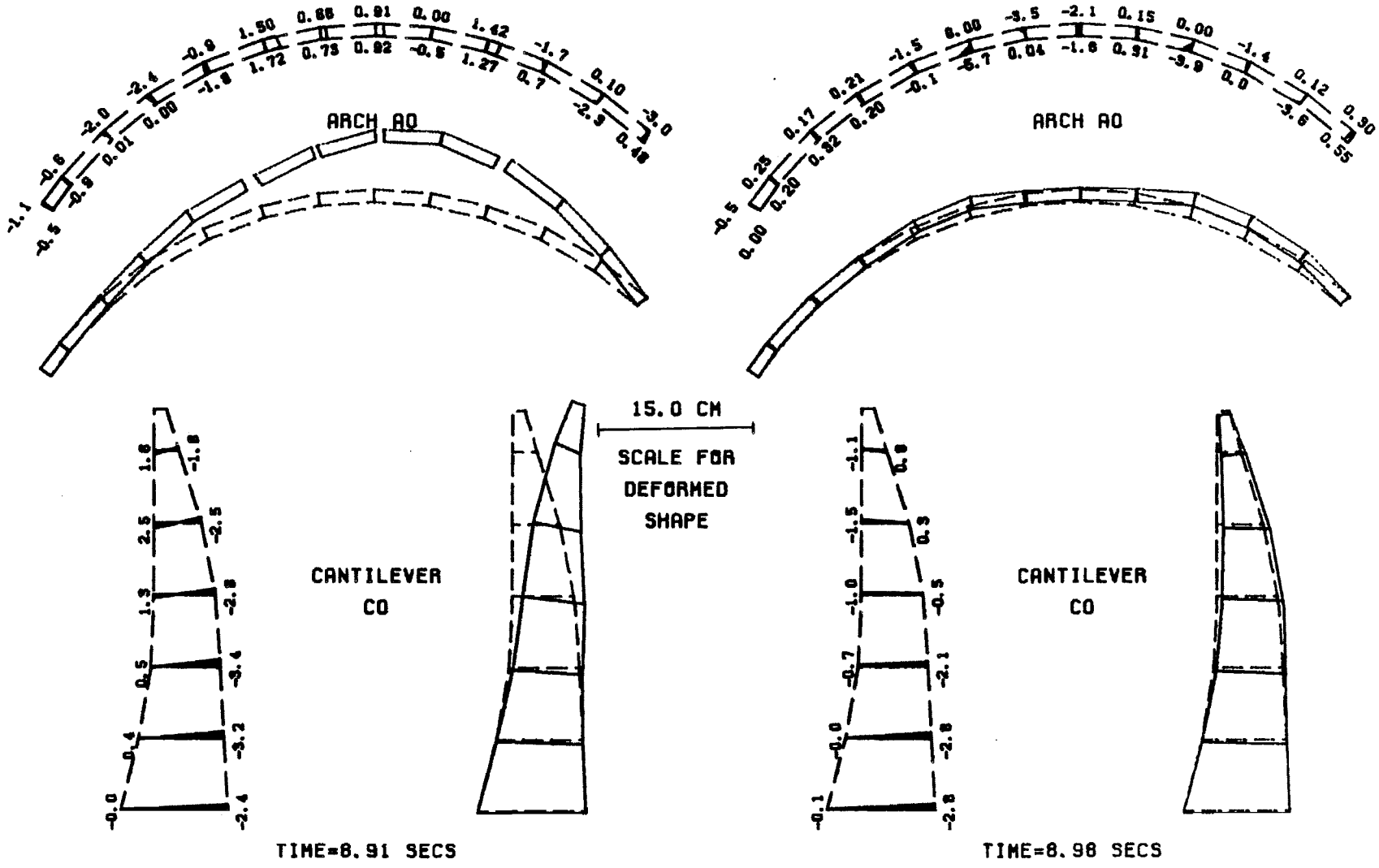

Figure 5.10 (continued, ground motion scale = 2/3, partially full reservoir).

Figure 5.11 (next 6 pages). Sequence of snapshots of arch A0 and cantilever C0 from the nonlinear earthquake response of Pacoima Dam to the records of Figure 5.1 scaled by 2/3. Results are for the full reservoir: normal stresses (shaded, tension positive, compression negative, amplitude given in MPa to one decimal place), joint openings (unshaded, amplitude given in cm to two decimal places), and deformed shape (solid line, original profile dashed line).

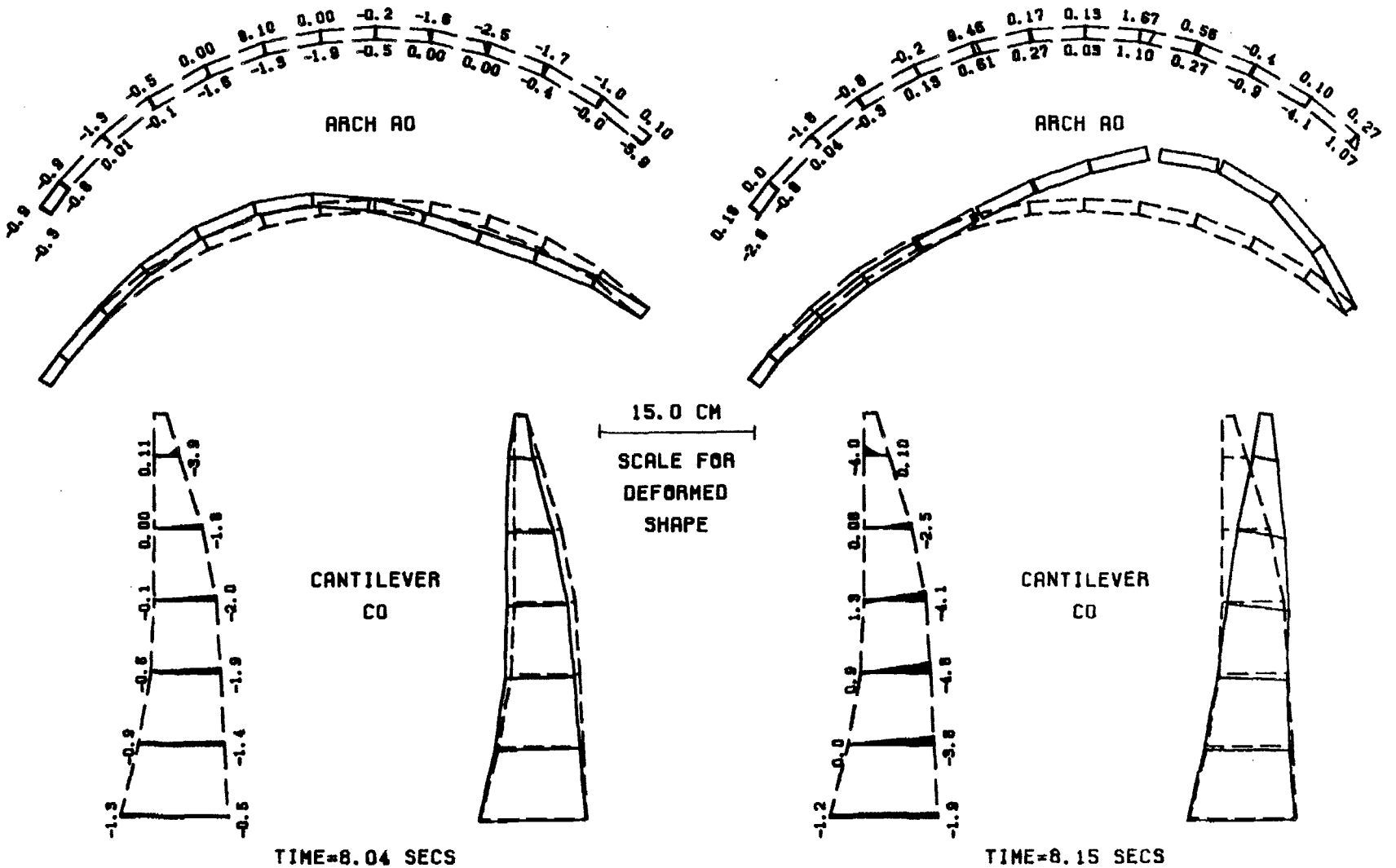

Figure 5.11 (ground motion scale = 2/3, full reservoir).

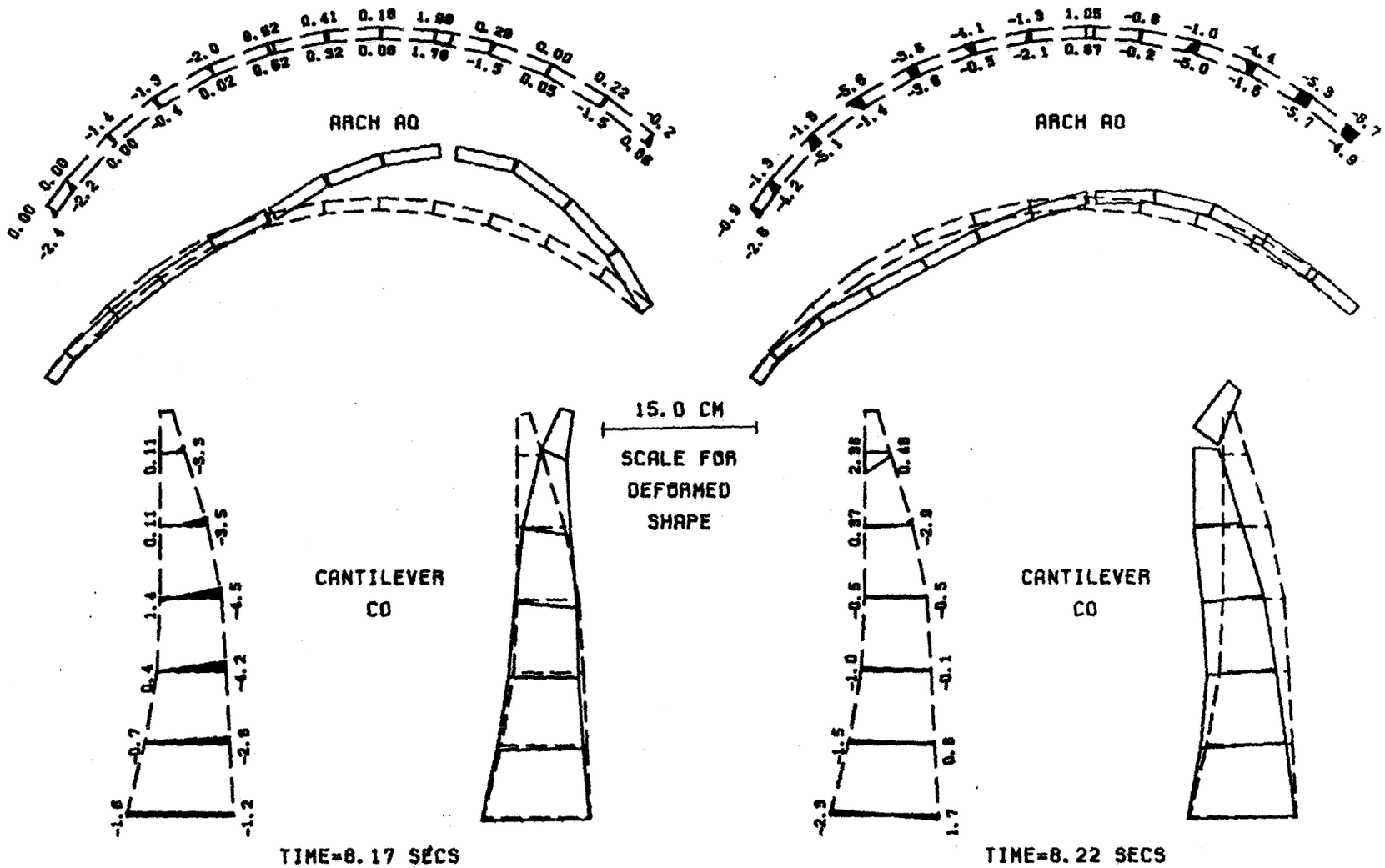

Figure 5.11 (continued, ground motion scale = 2/3, full reservoir).

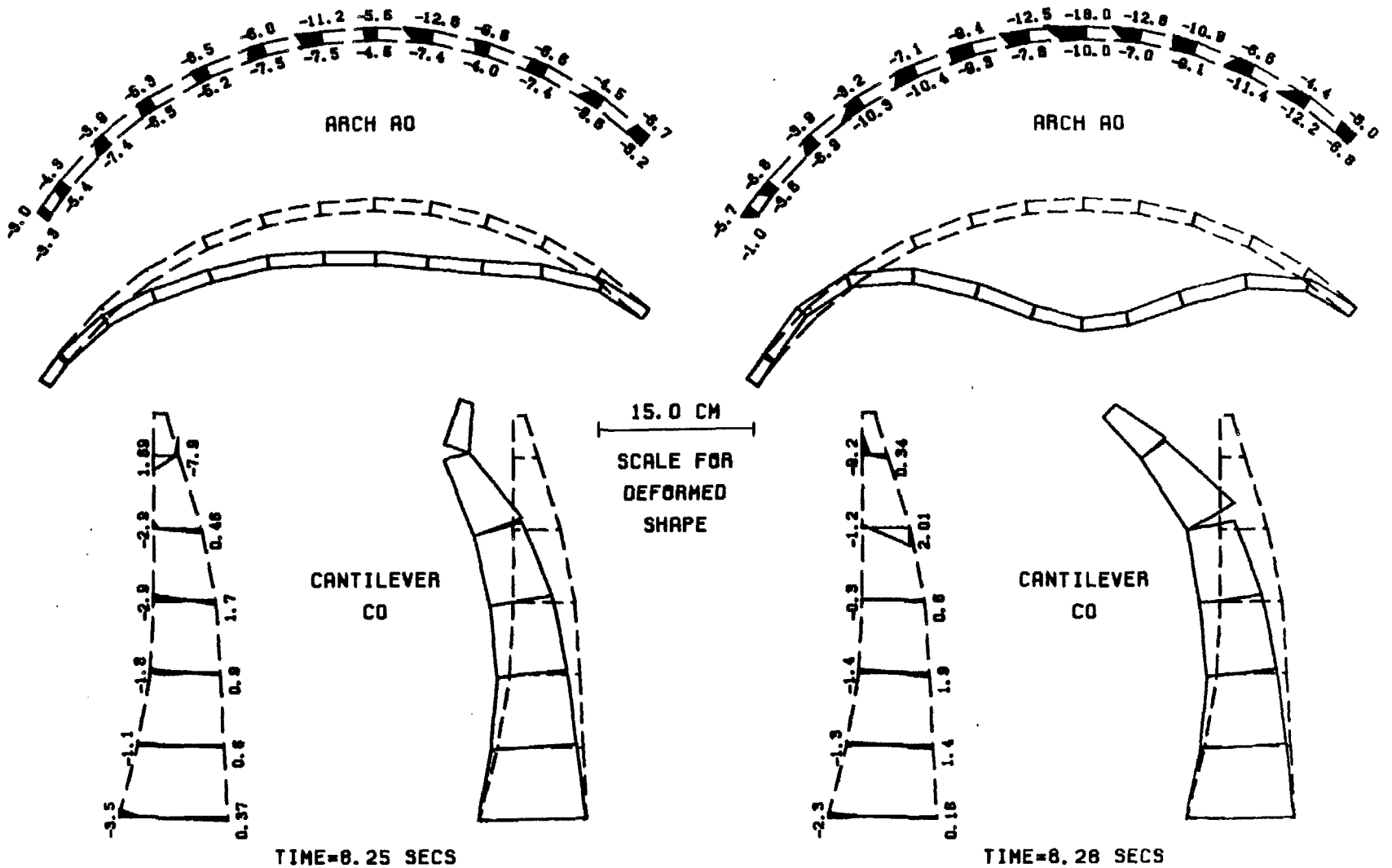

Figure 5.11 (continued, ground motion scale = 2/3, full reservoir).

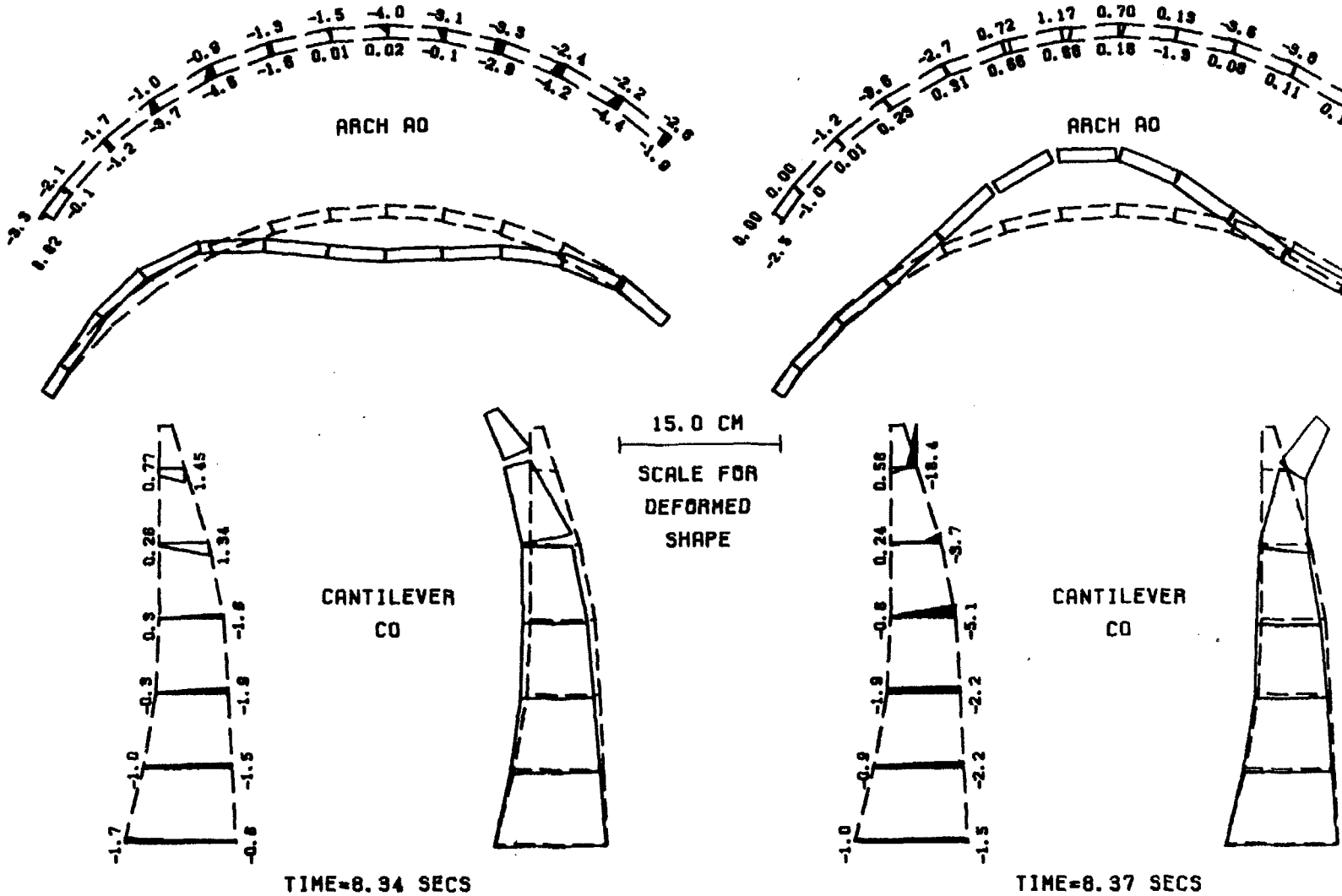

Figure 5.11 (continued, ground motion scale = 2/3, full reservoir).

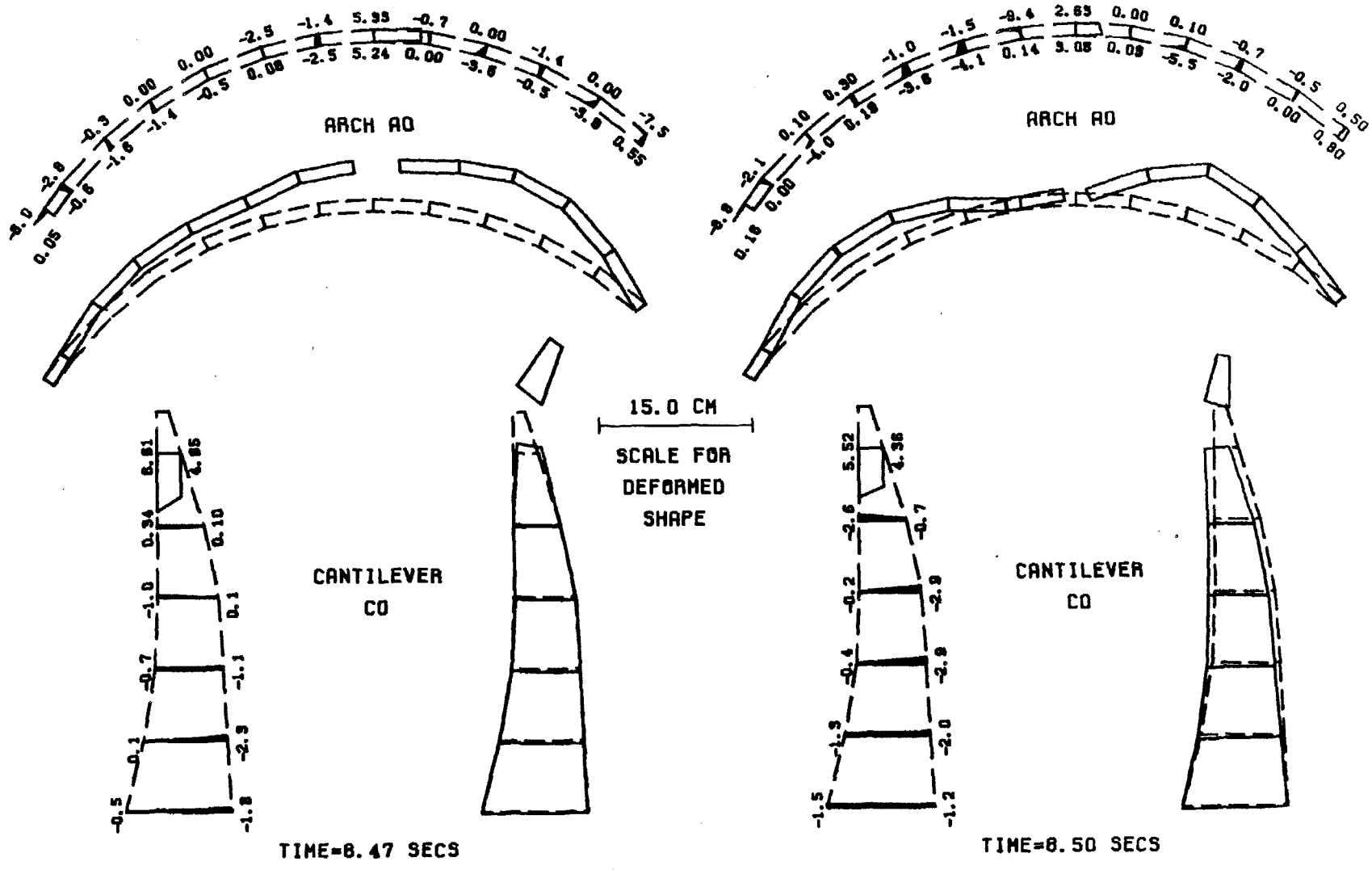

Figure 5.11 (continued, ground motion scale = 2/3, full reservoir).

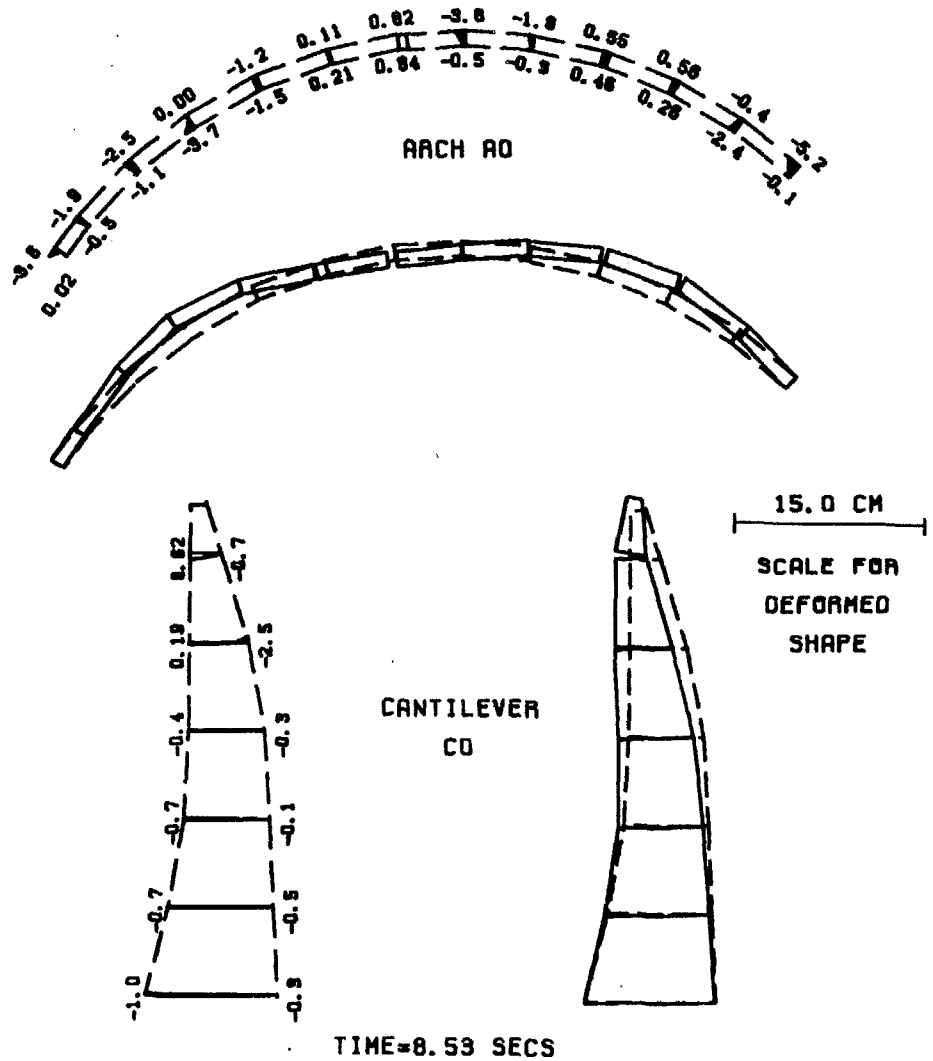

Figure 5.11 (continued, ground motion scale = 2/3, full reservoir).

Figure 5.12 a to f (next 7 pages). Selected time histories (6.0 to 10.0 seconds) from various analyses of Pacoima Dam using the records of Figure 5.1 scaled by 2/3.

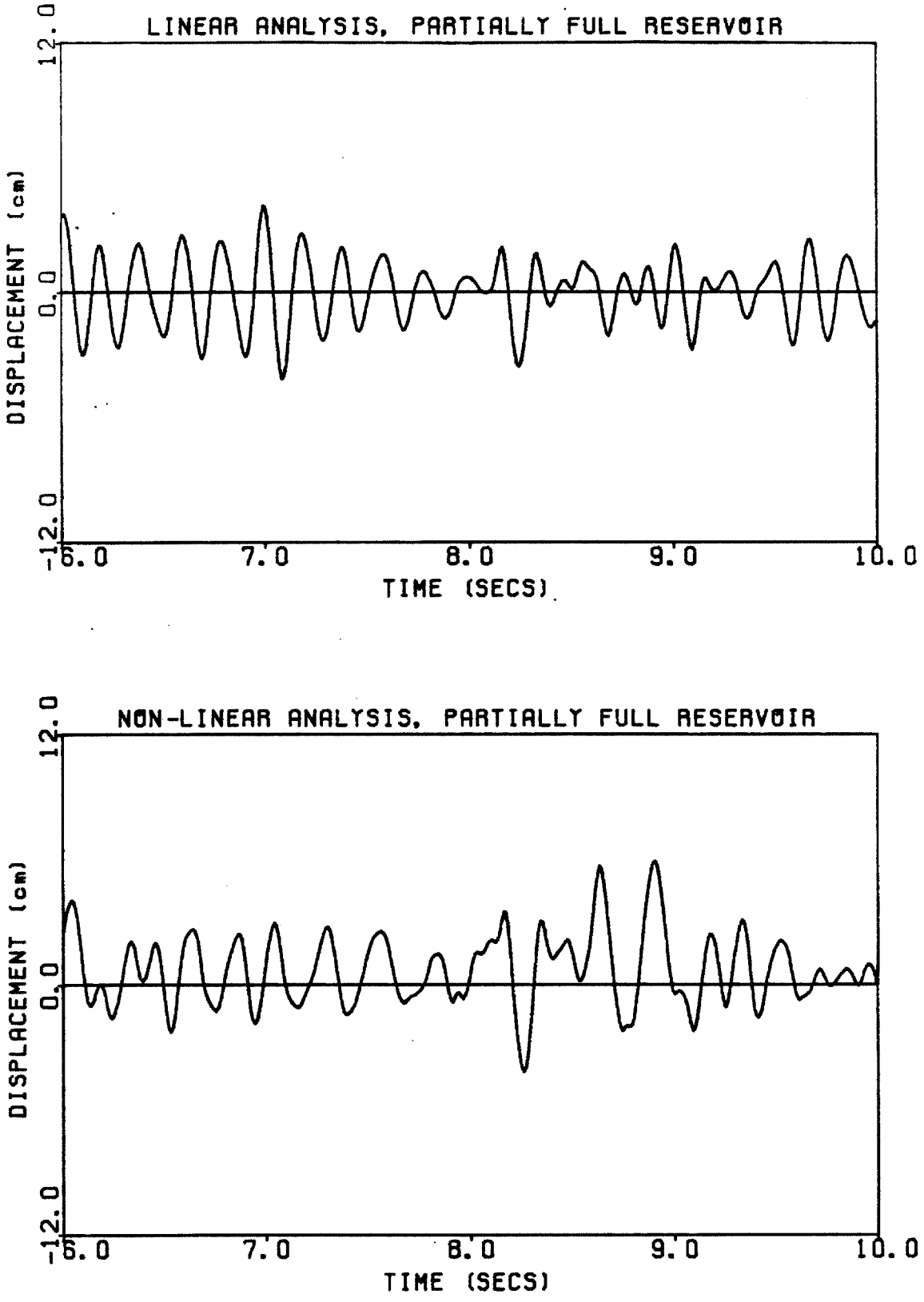

Figure 5.12a. Average dynamic radial displacement at node 29 (ground motion scale = 2/3).

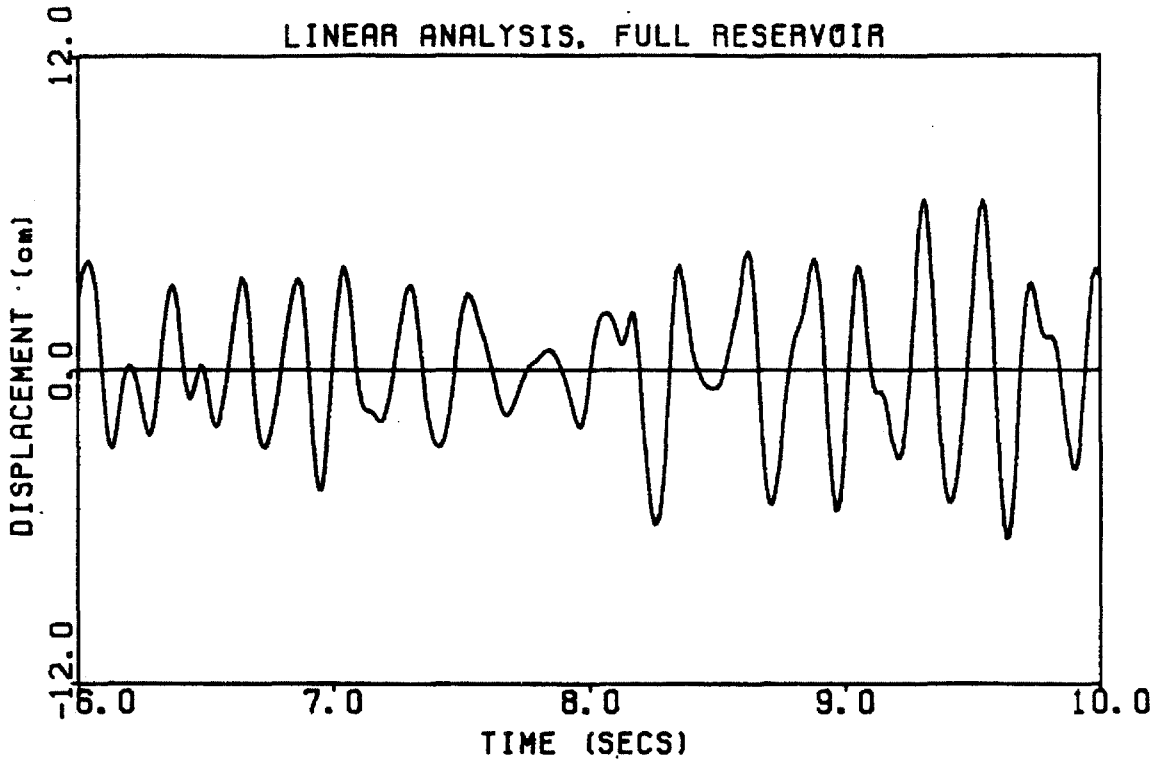

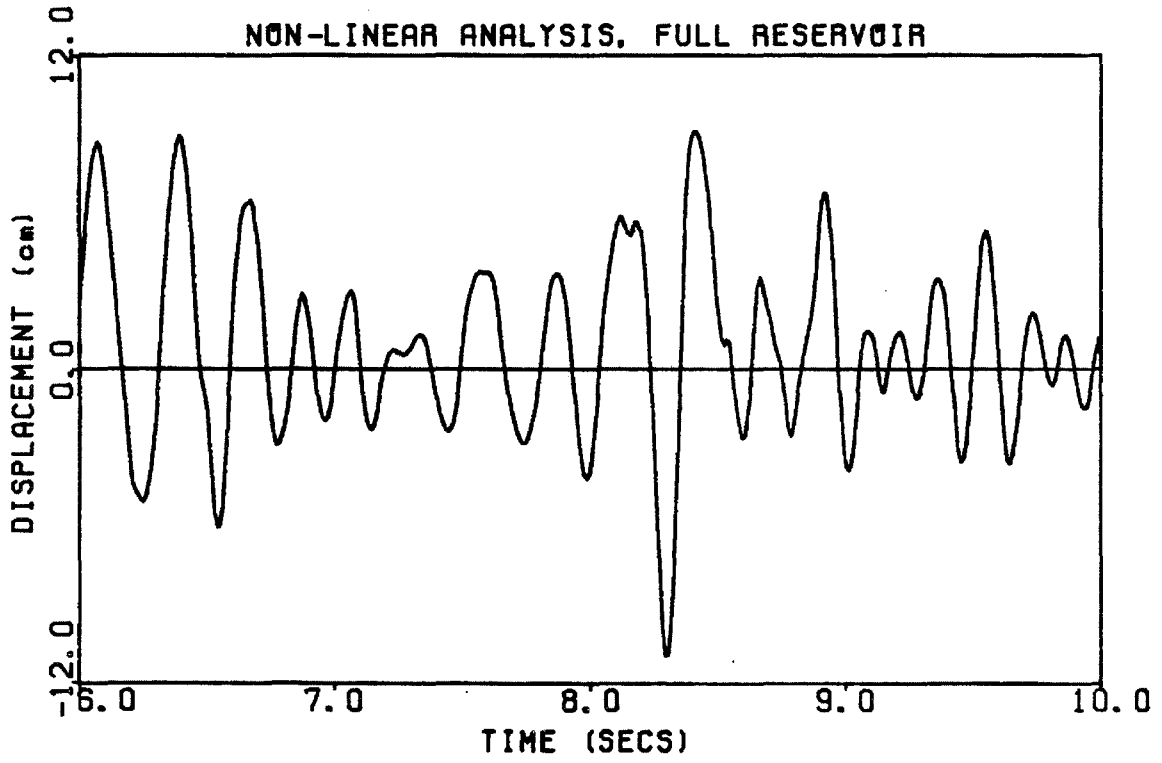

Figure 5.12a. (continued). Average dynamic radial displacement at node 29 (ground motion scale = 2/3).

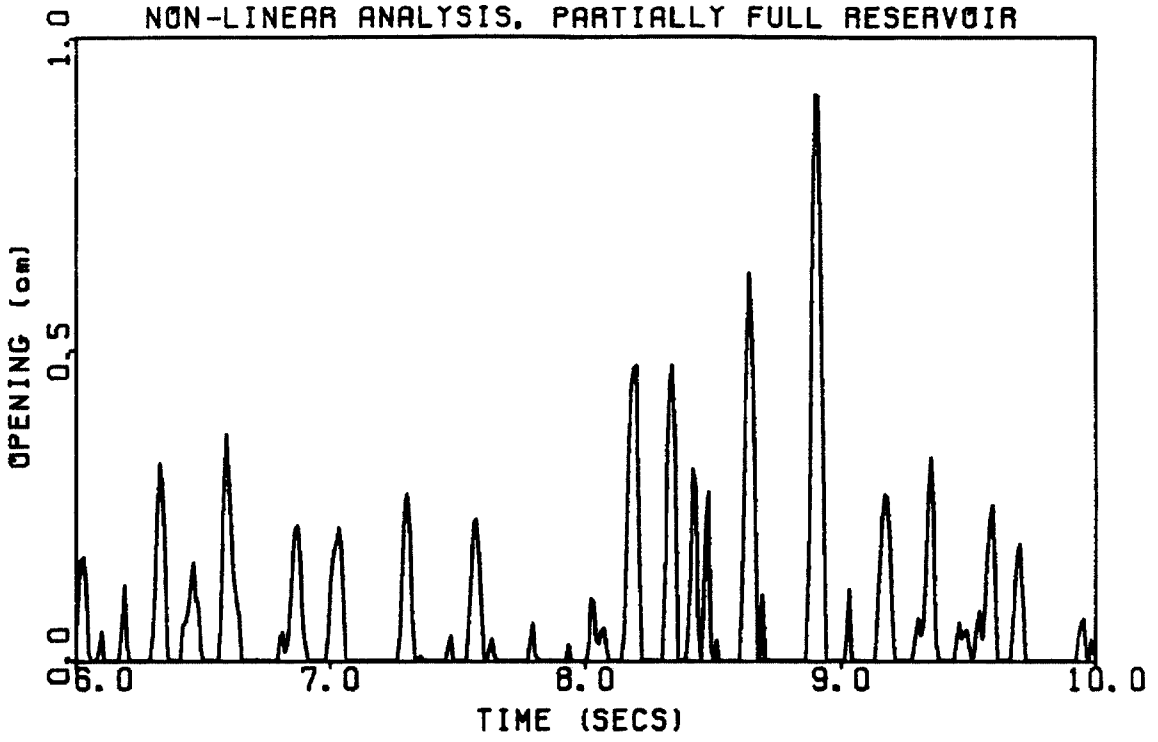

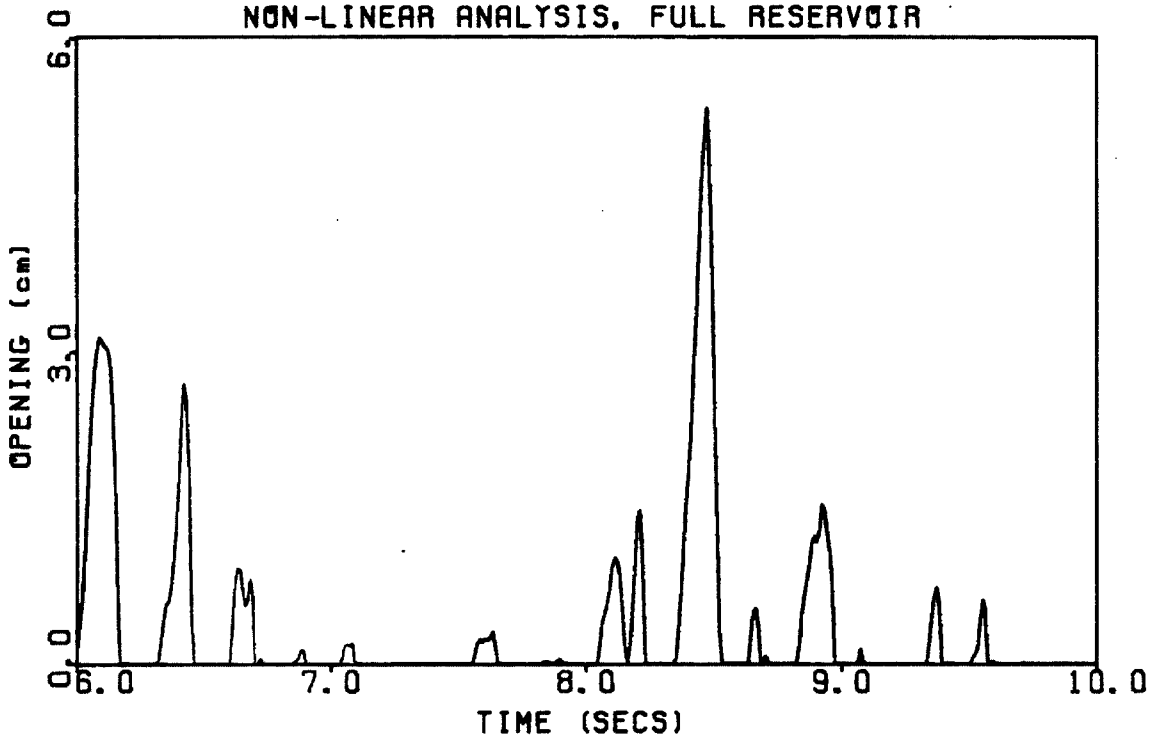

Figure 5.12b. Opening of vertical joint on upstream face at node 29 (ground motion scale = 2/3).

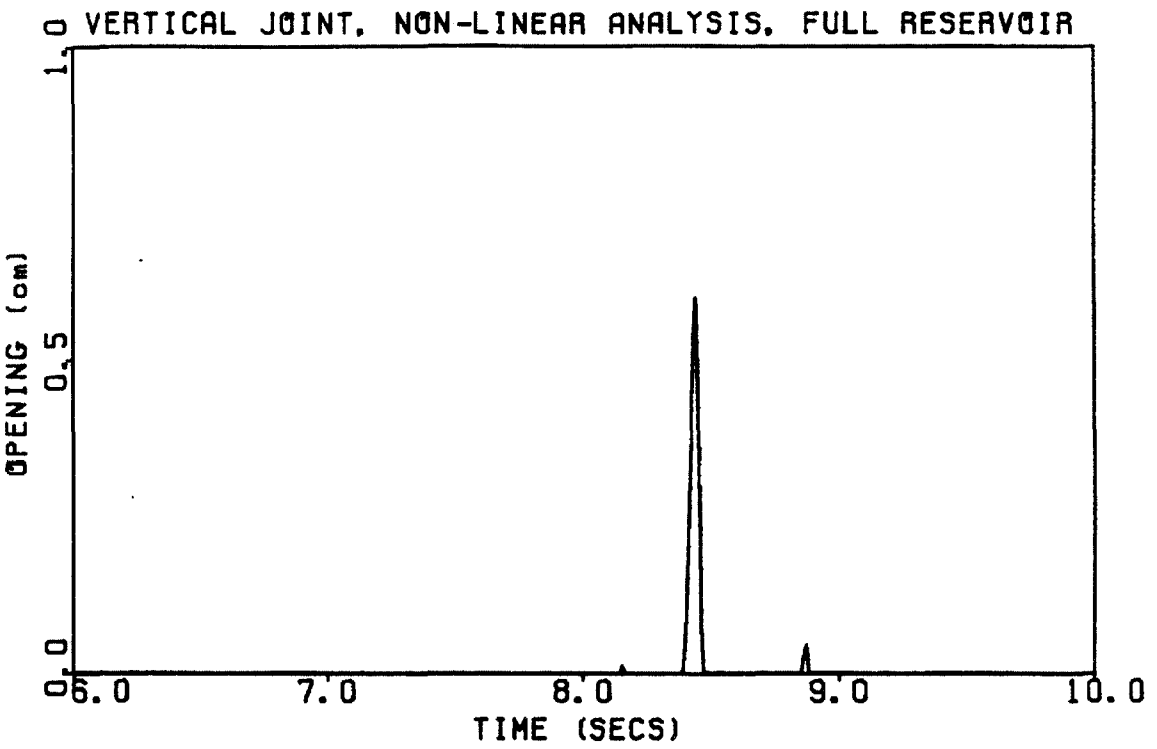

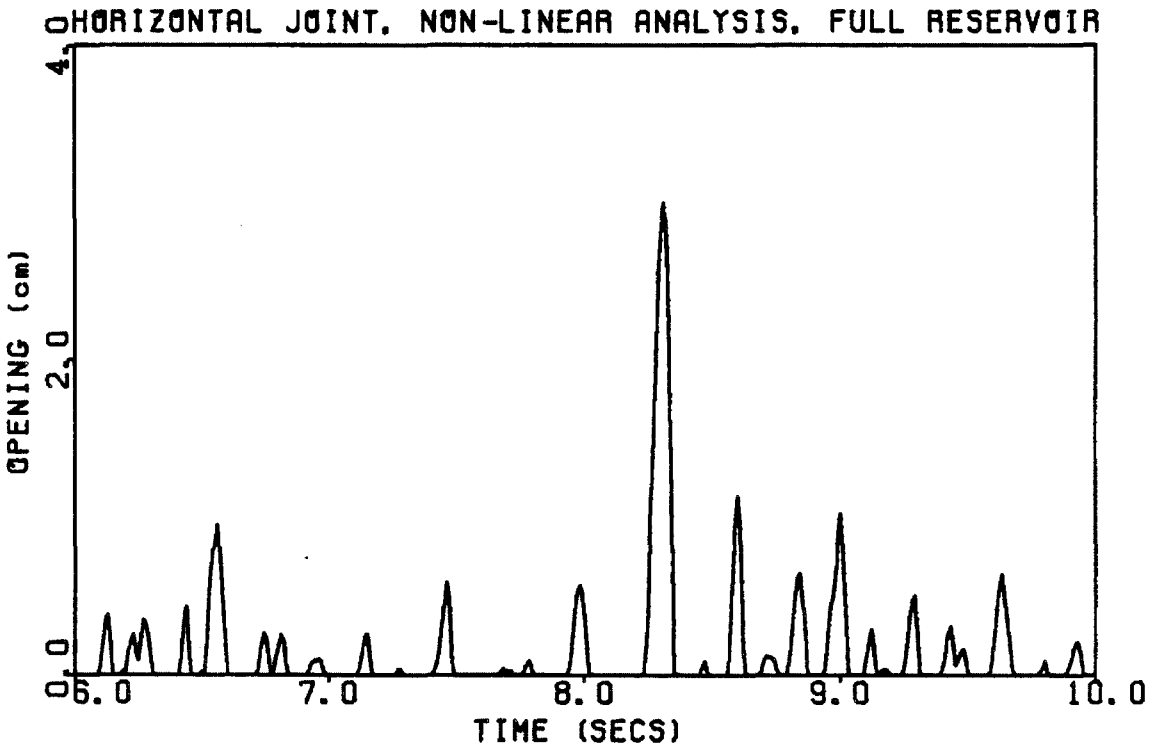

Figure 5.12c. Opening on upstream face at node 31 (ground motion scale = 2/3).

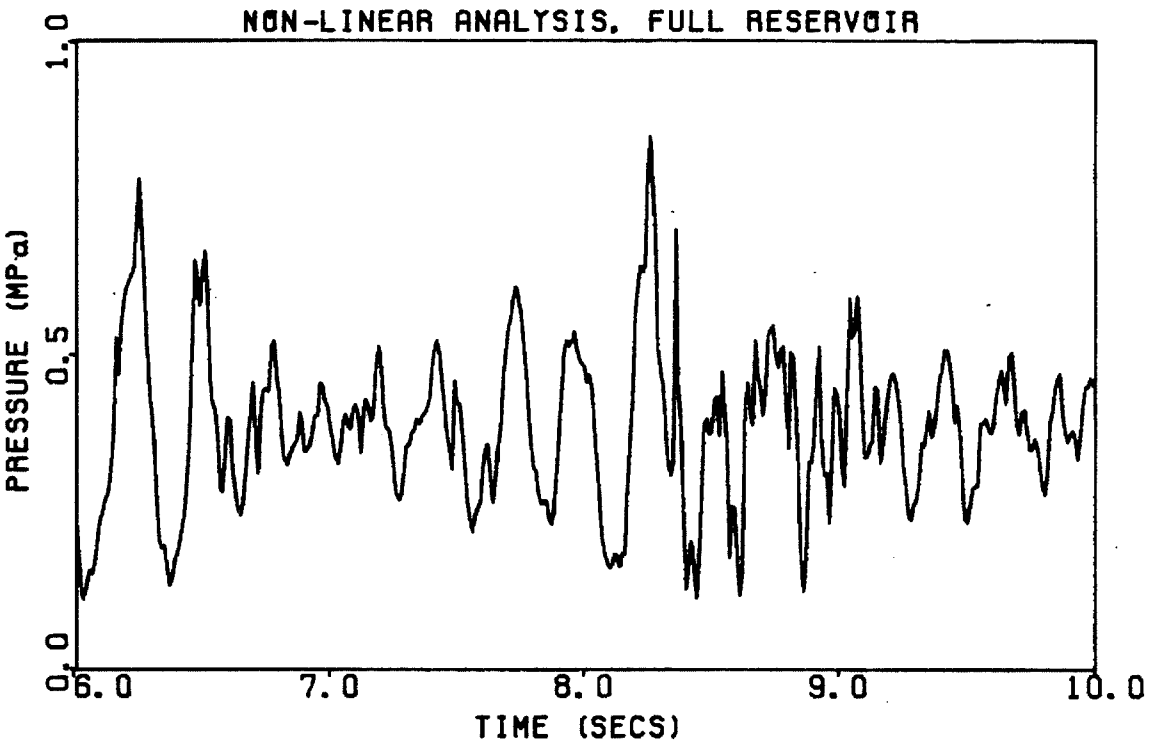

Figure 5.12d. Absolute water pressure at node 31 (ground motion scale = 2/3).

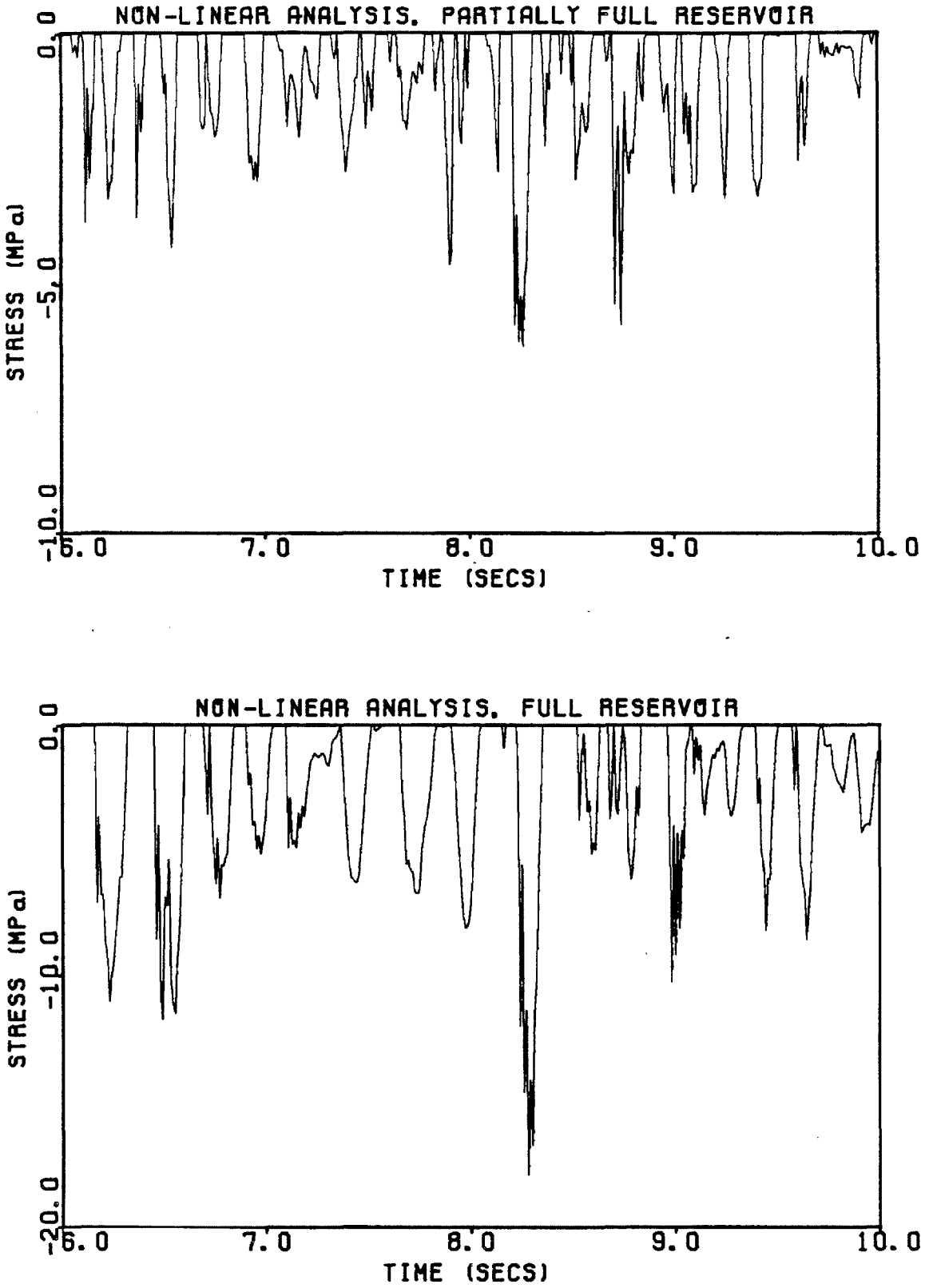

Figure 5.12e. Stress on upstream face on vertical joint at node 29 (ground motion scale = 2/3).

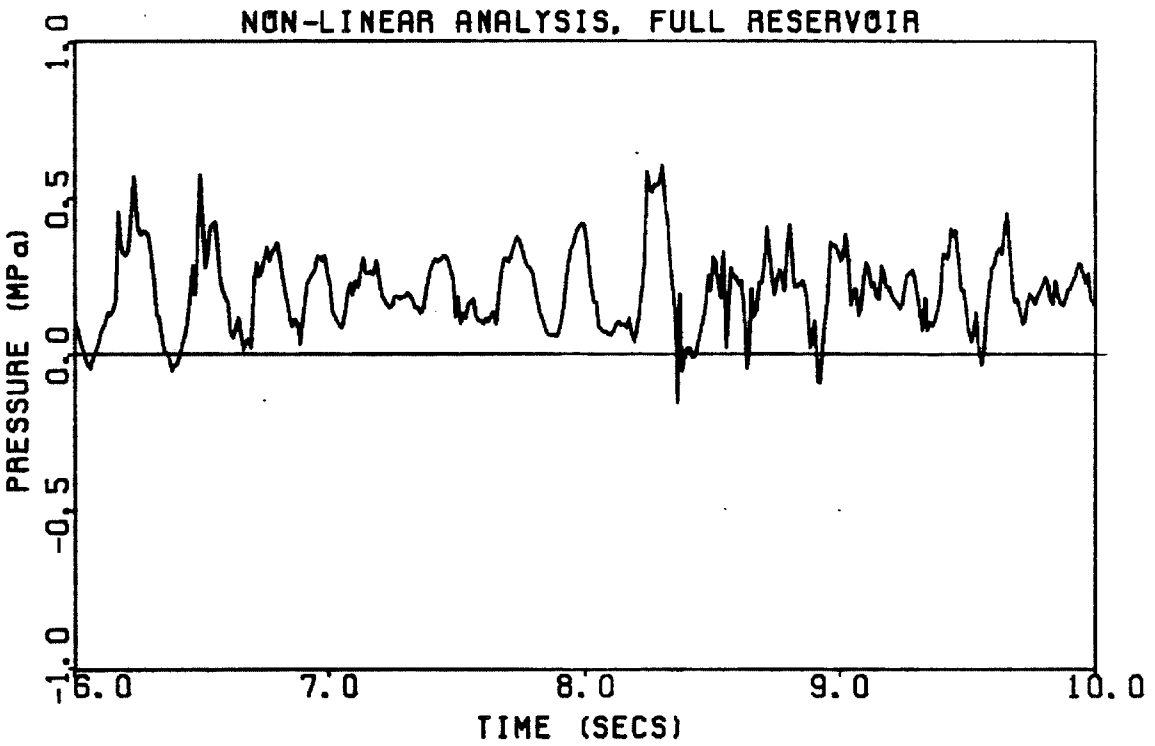

Figure 5.12f. Absolute water pressure at node 30 (ground motion scale = 2/3).

Figure 5.13 a to e (next 5 pages). Summary of the earthquake responses of Pacoima Dam to the records of Figure 5.1 scaled by 0.44. Results are for full reservoir: static stresses, maximum tensions for linear analysis, maximum openings for nonlinear analysis, and maximum compressions for linear and nonlinear analysis. Stresses (MPa) are shaded with amplitudes given to one decimal place. Openings (cm) are unshaded with amplitudes given to two decimal places.

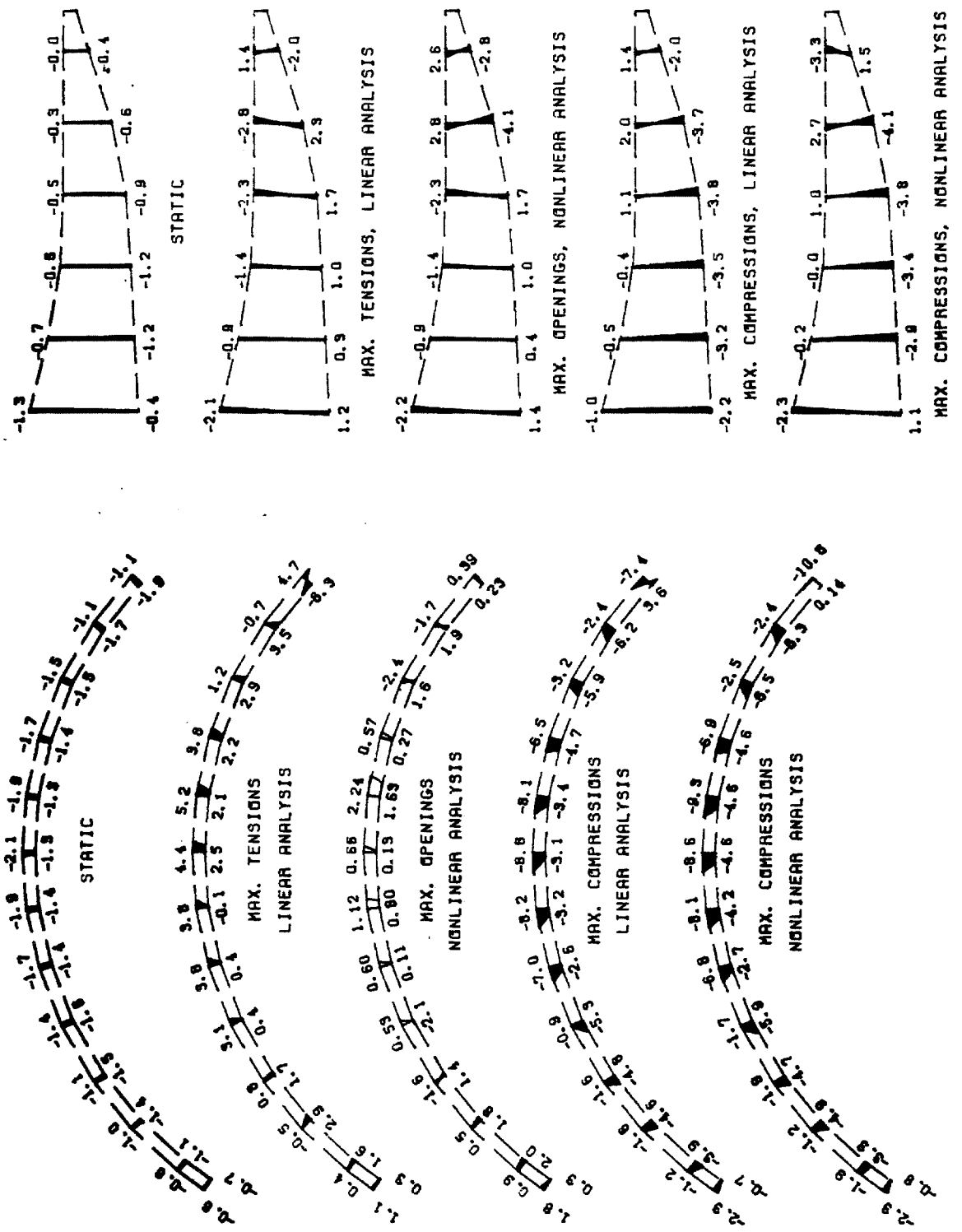

Figure 5.13a. Arch 0 and Cantilever 0 (ground motion scale = 0.44, full reservoir).

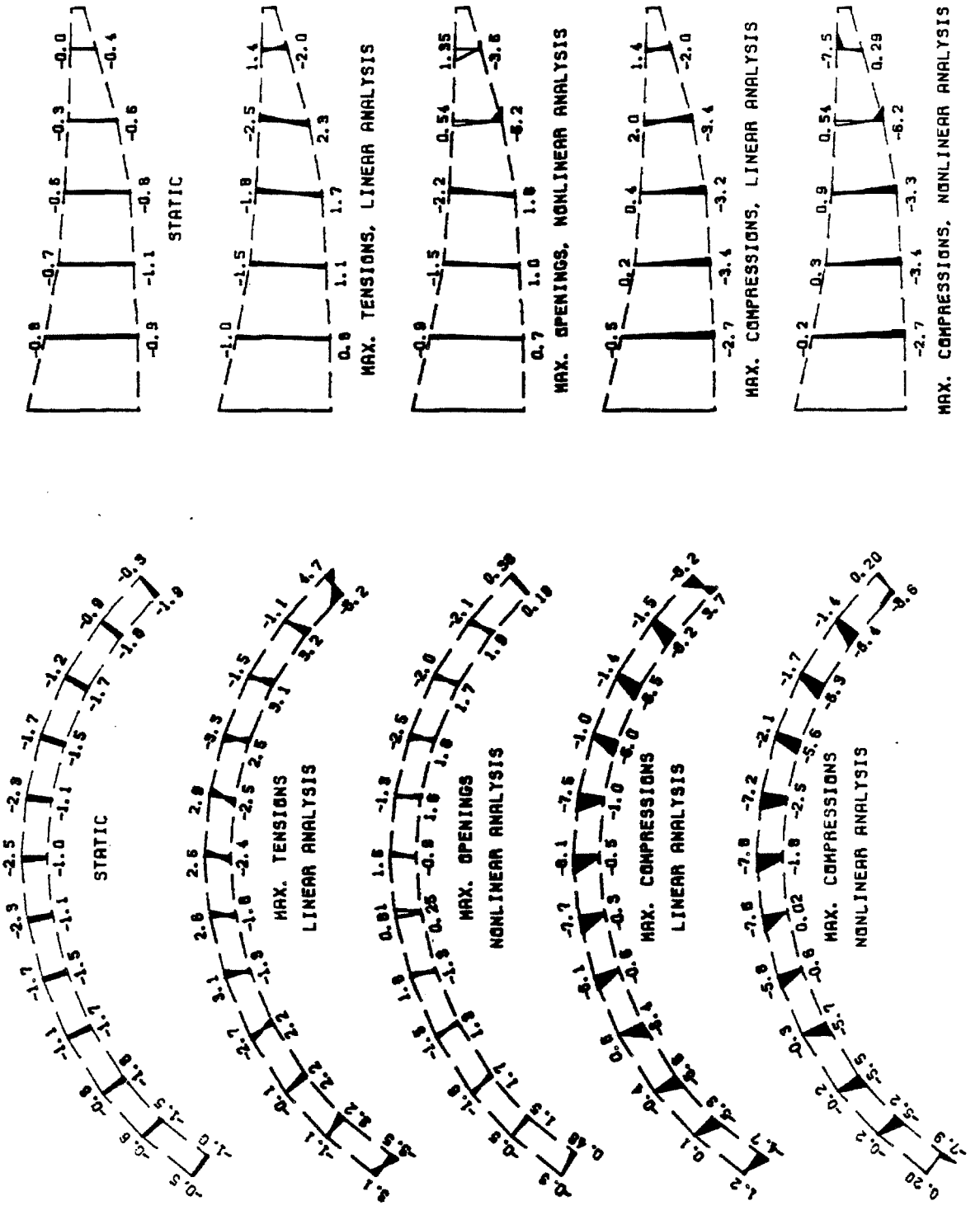

Figure 5.13b. Arch 1 and Cantilever −1 (ground motion scale = 0.44, full reservoir).

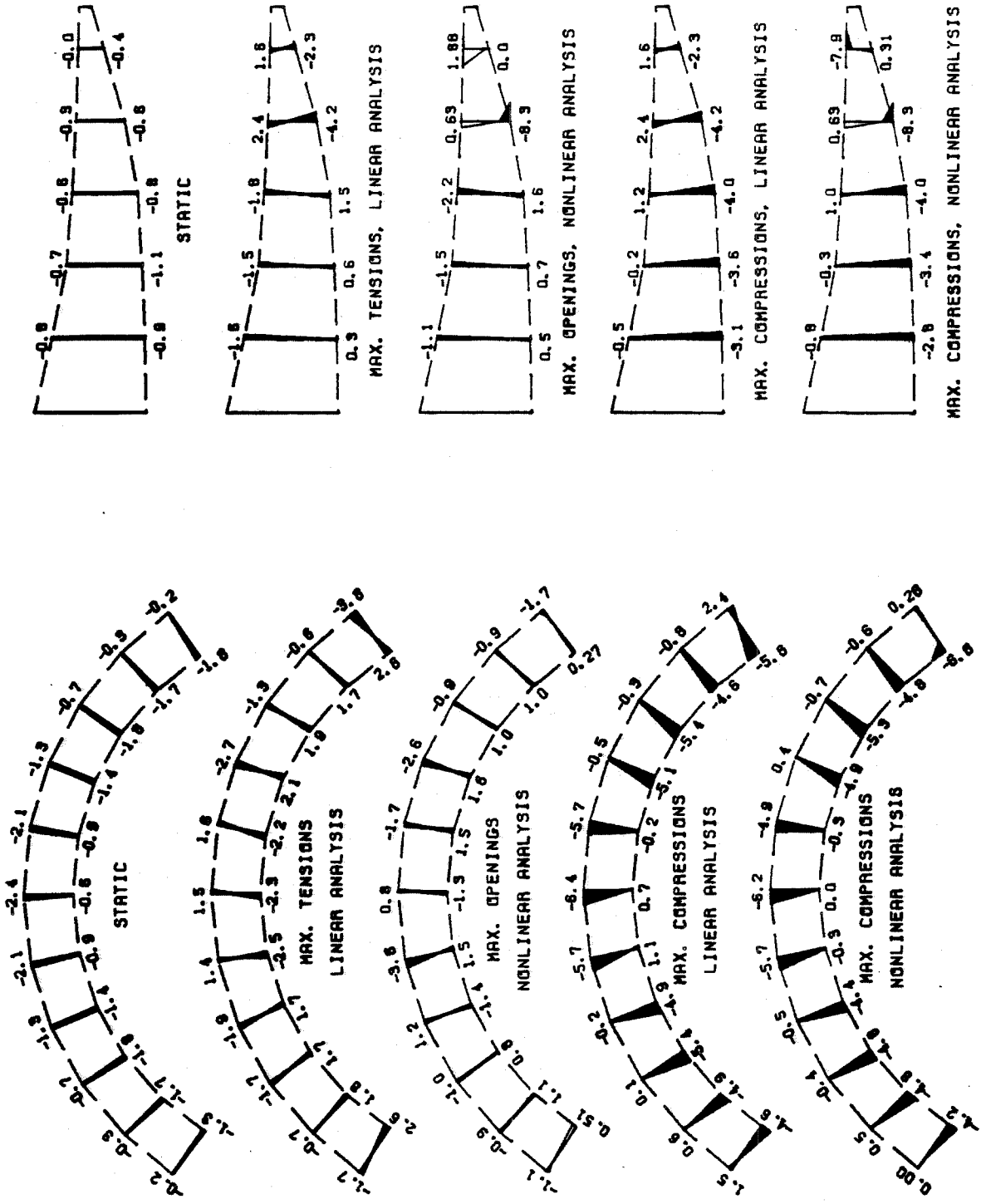

Figure 5.13c. Arch 2 and Cantilever 1 (ground motion scale = 0.44, full reservoir).

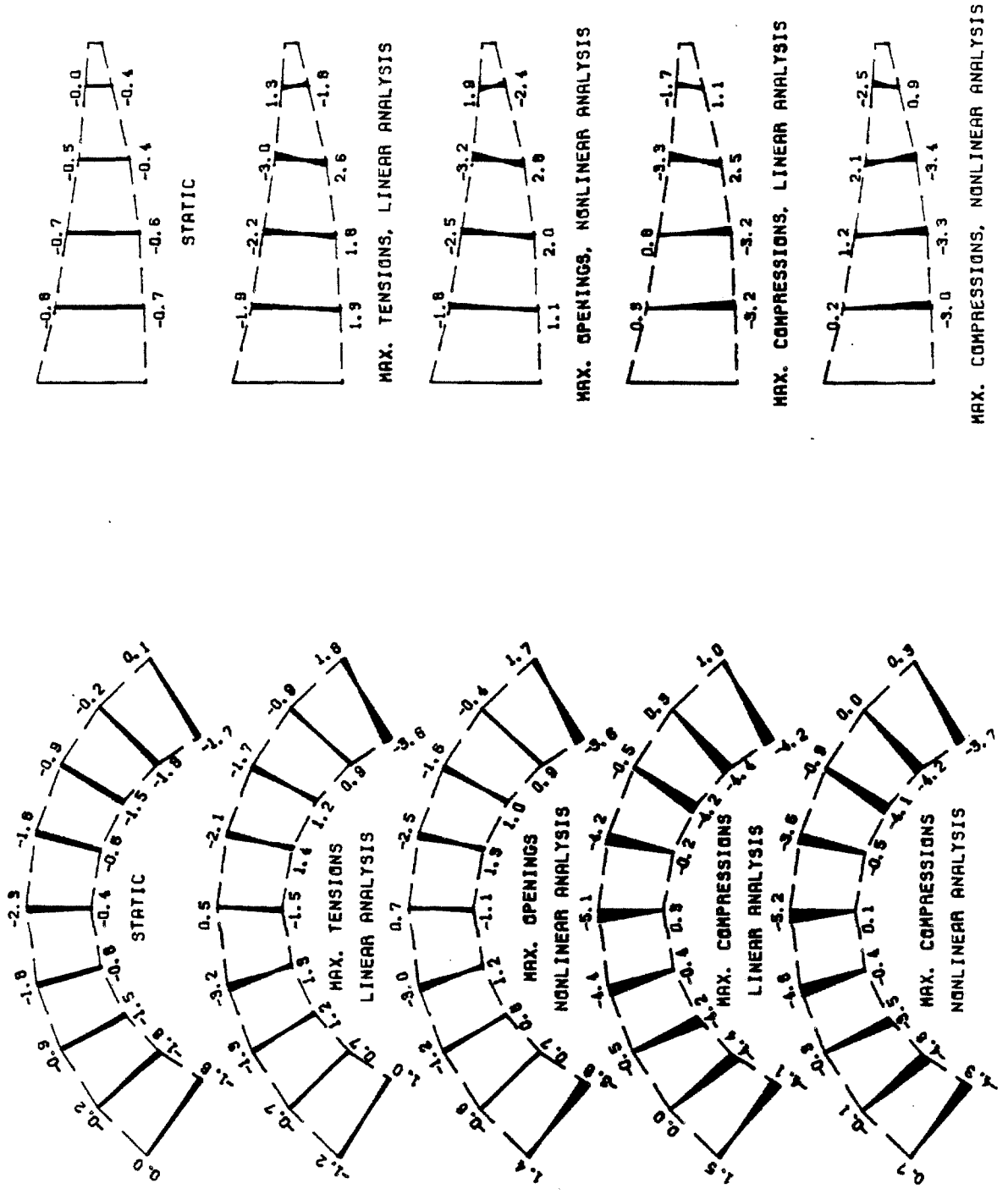

Figure 5.13d. Arch 3 and Cantilever −2 (ground motion scale = 0.44, full reservoir).

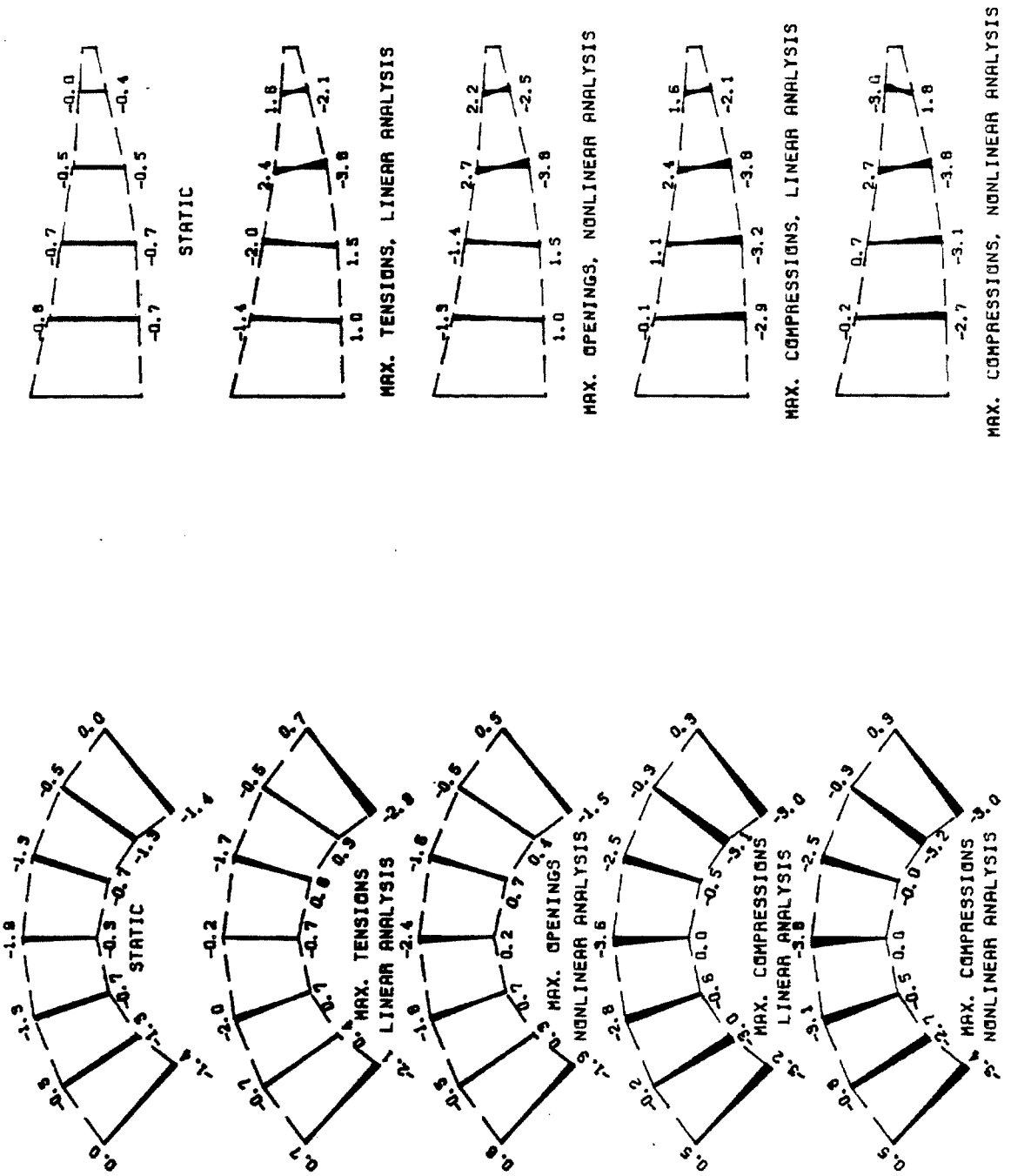

Figure 5.13f. Arch 4 and Cantilever 2 (ground motion scale = 0.44, full reservoir).

Figure 5.14 (next 6 pages). Sequence of snapshots of arch A0 and cantilever C1 from the nonlinear earthquake response of Pacoima Dam to the records of Figure 5.1 scaled by 0.44. Results are for the full reservoir: normal stresses (shaded, tension positive, compression negative, amplitude given in MPa to one decimal place), joint openings (unshaded, amplitude given in cm to two decimal places), and deformed shape (solid line, original profile dashed line).

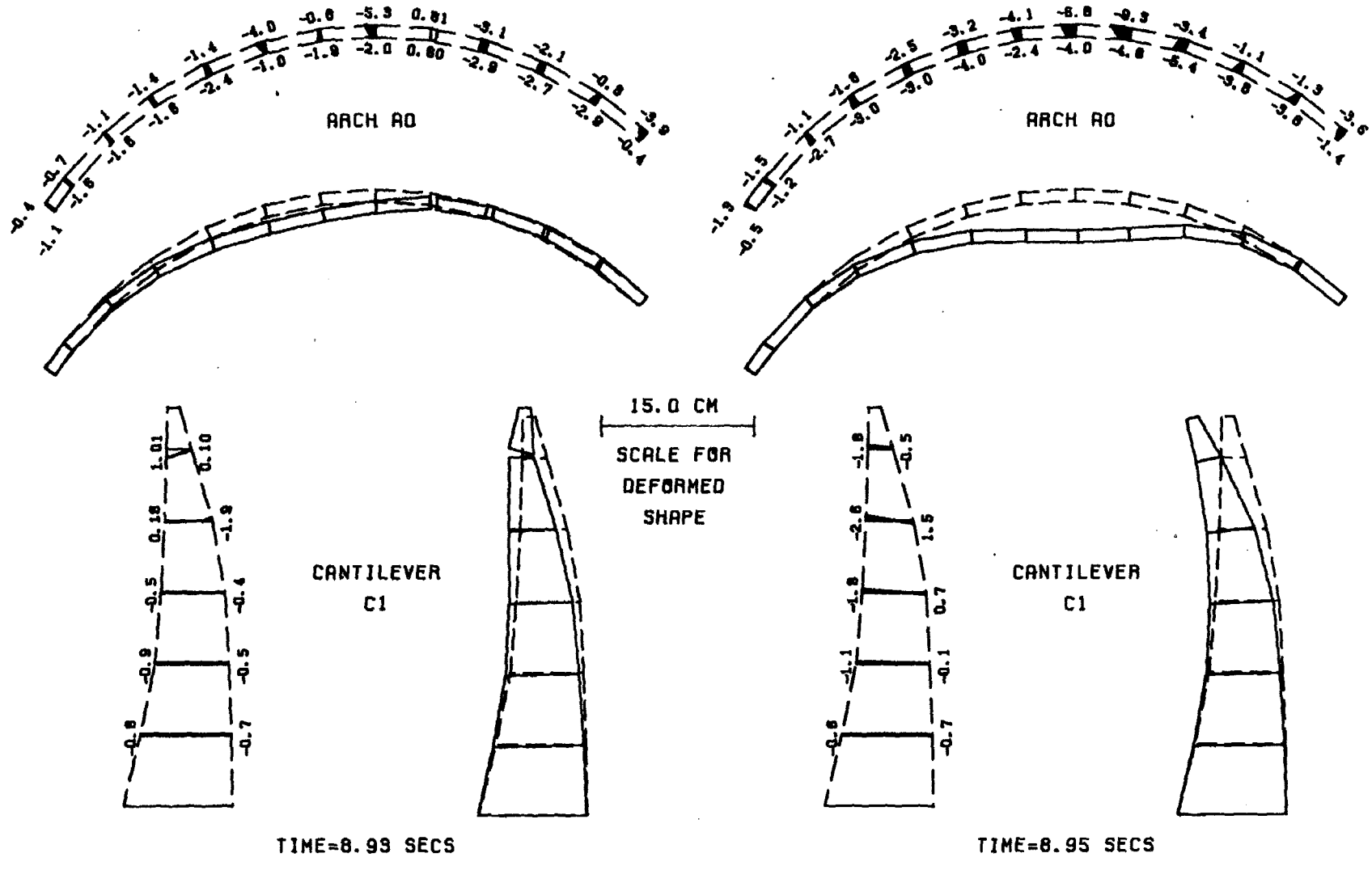

Figure 5.14 (ground motion scale = 0.44, full reservoir).

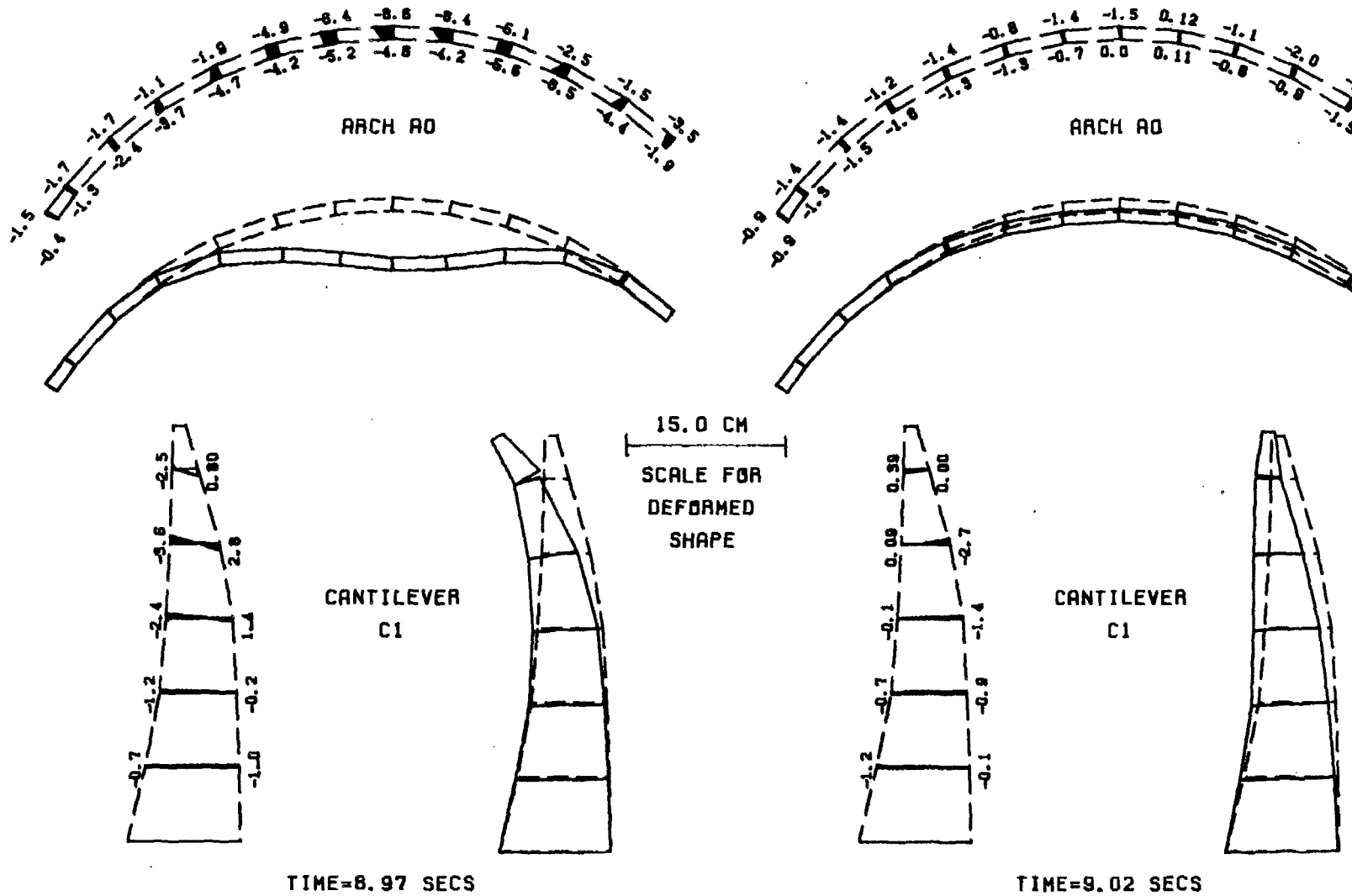

Figure 5.14 (continued, ground motion scale = 0.44, full reservoir).

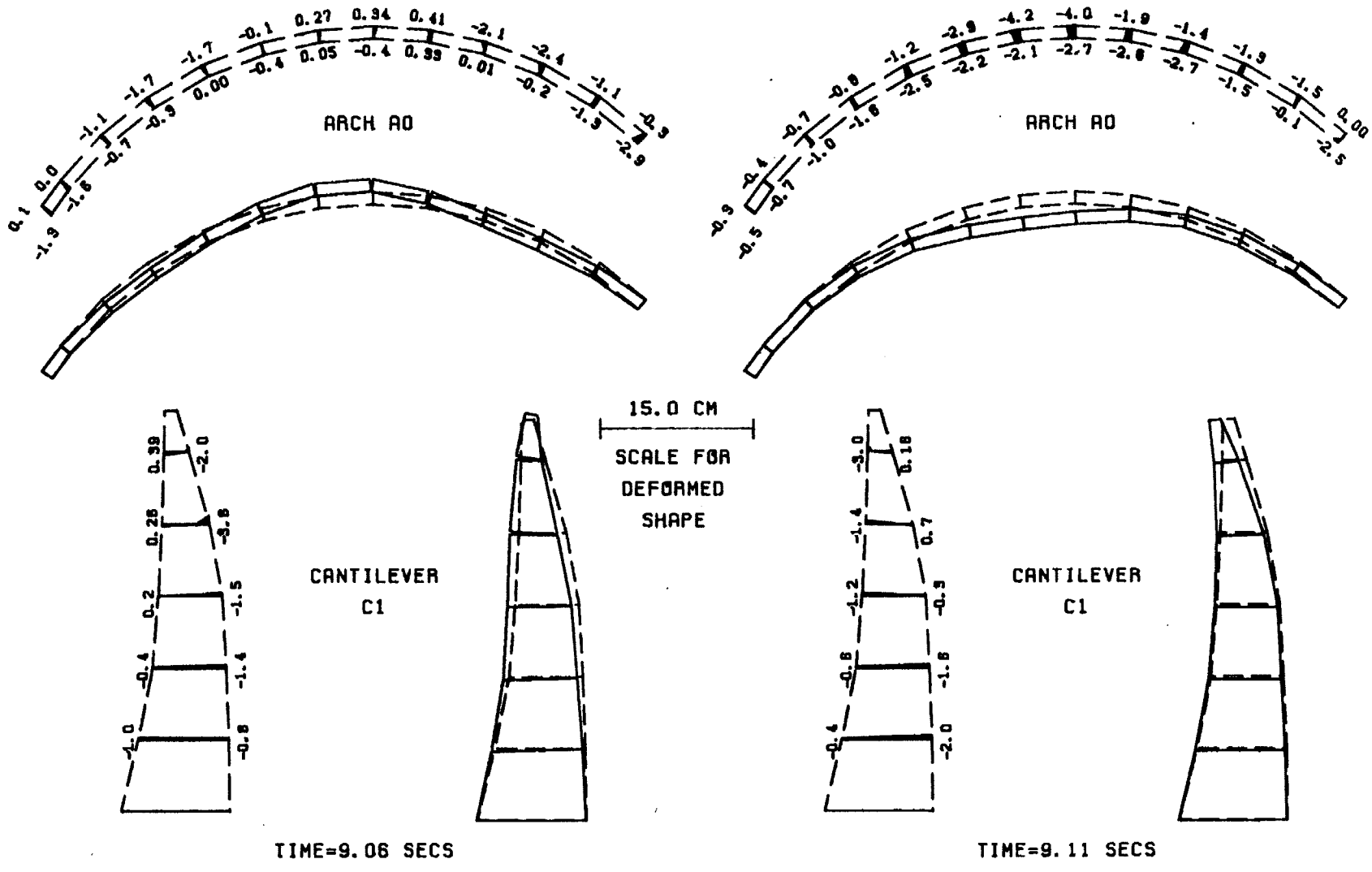

Figure 5.14 (continued, ground motion scale = 0.44, full reservoir).

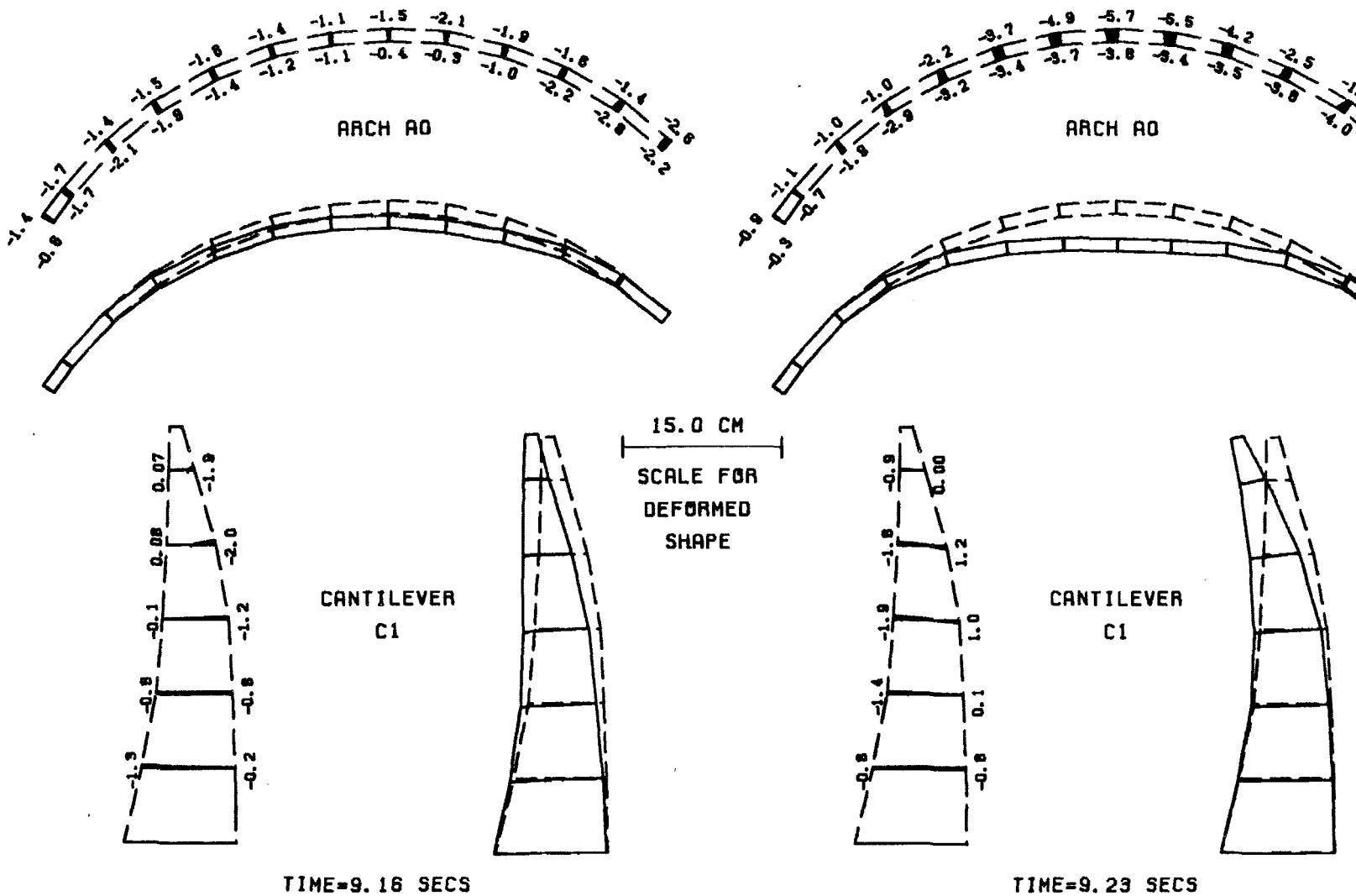

Figure 5.14 (continued, ground motion scale = 0.44, full reservoir).

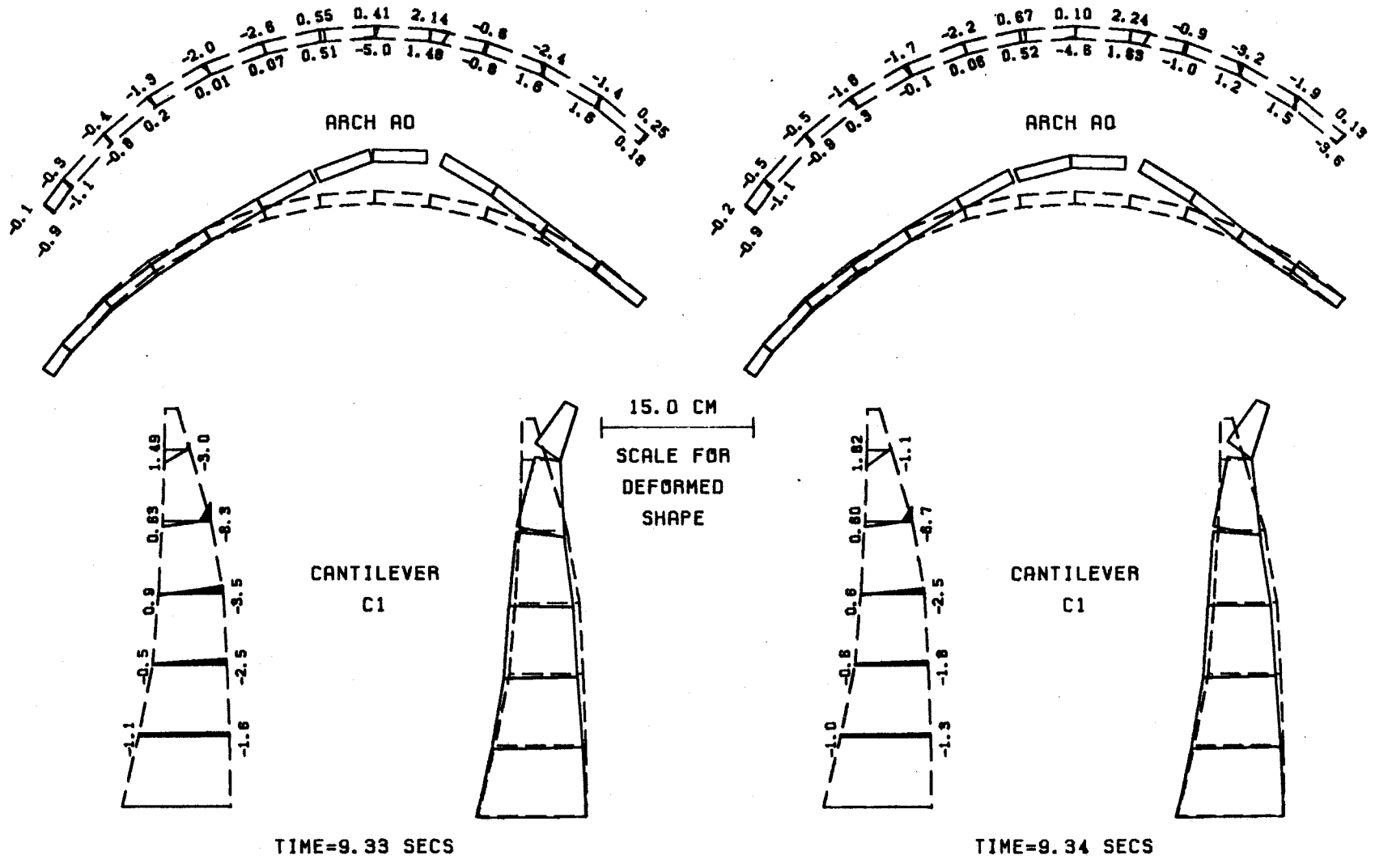

Figure 5.14 (continued, ground motion scale = 0.44, full reservoir).

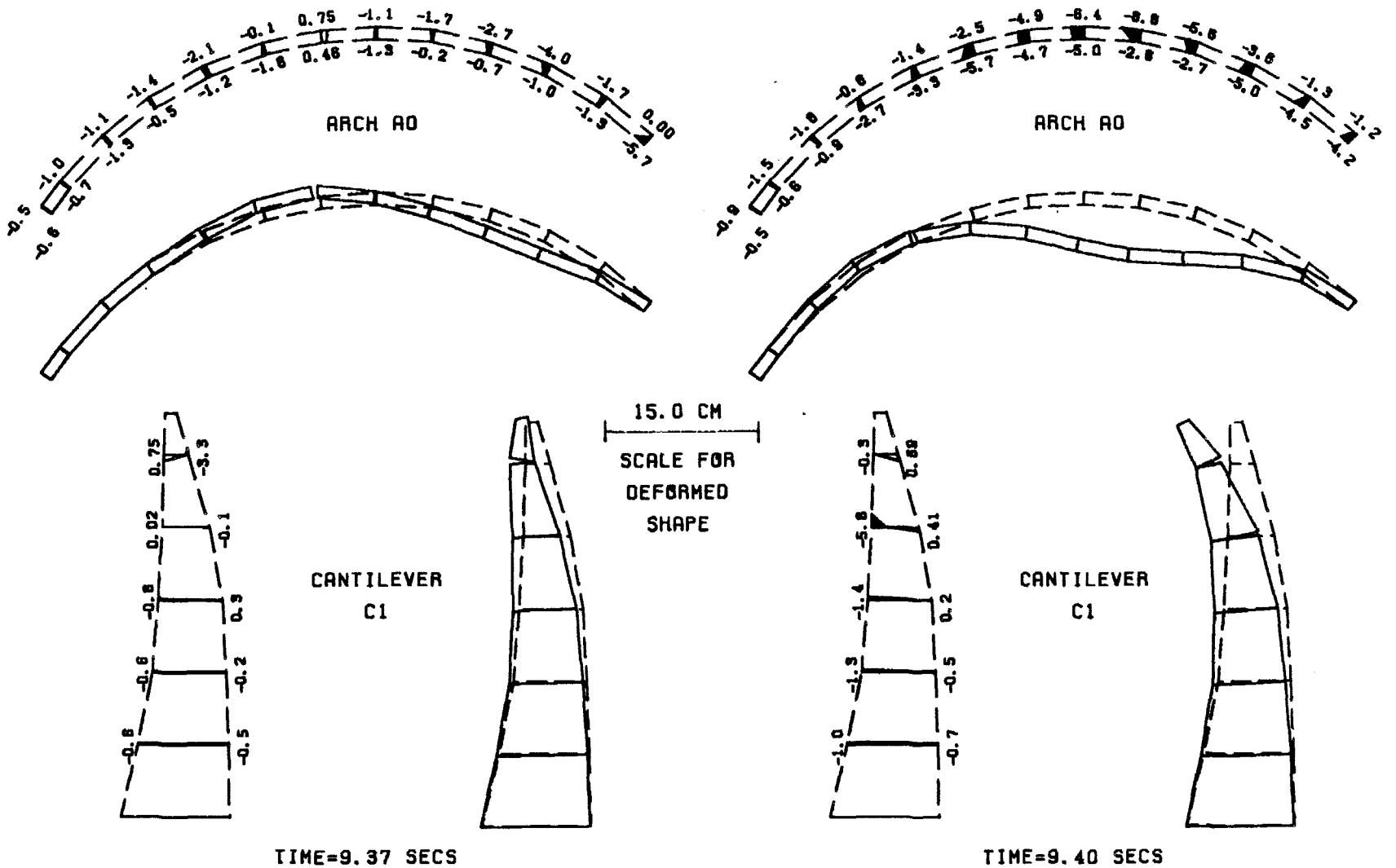

Figure 5.14 (continued, ground motion scale = 0.44, full reservoir).

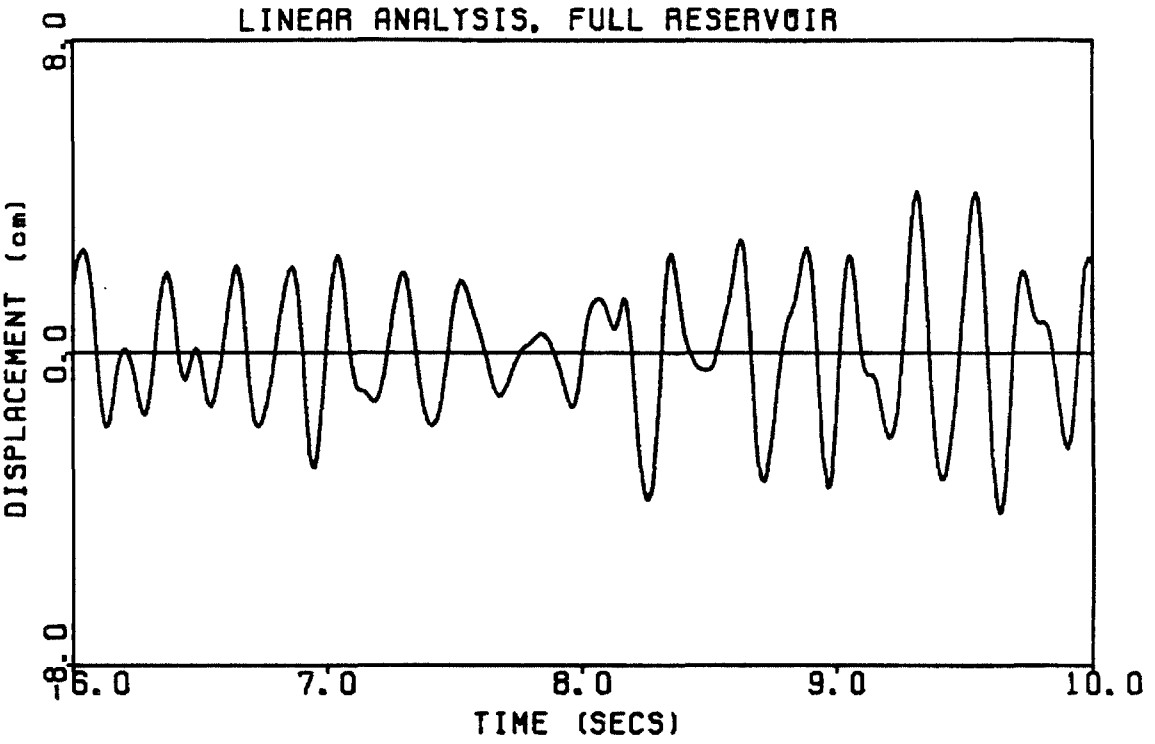

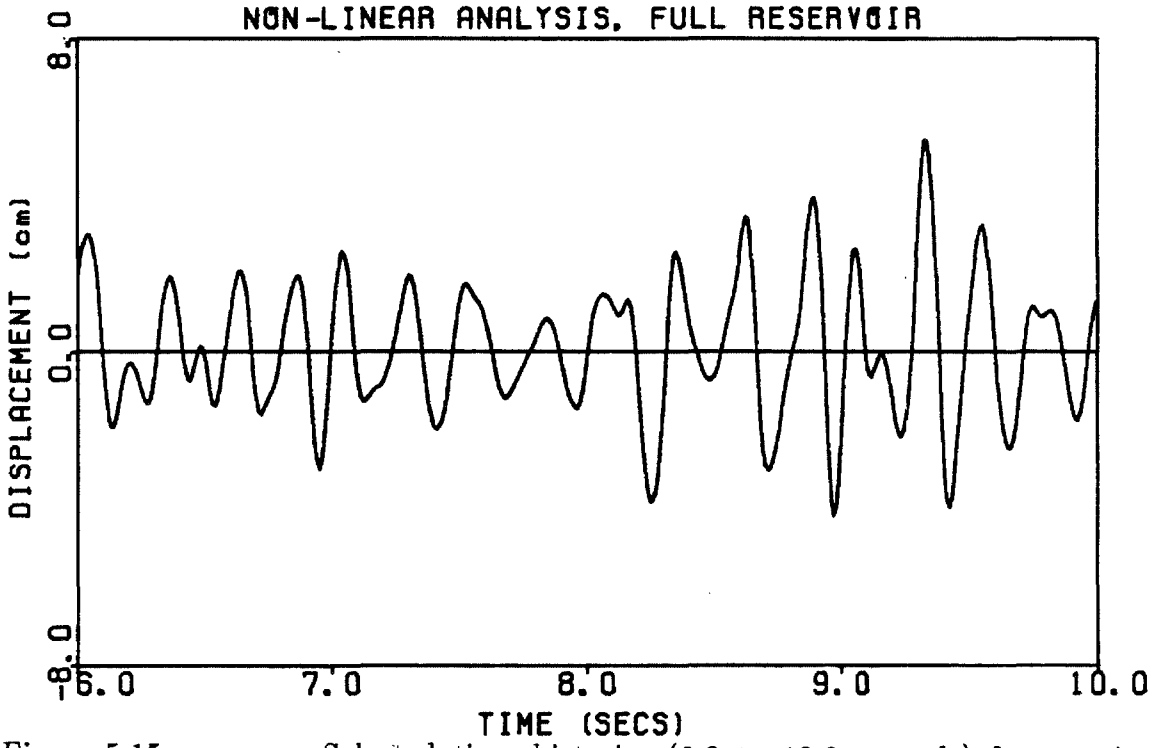

Figure 5.15 Selected time histories (6.0 to 10.0 seconds) from various analyses of Pacoima Dam using the records of Figure 5.1 scaled by 0.44. Average dynamic radial displacement at node 29.

Figure 5.16 a and b. (next 2 pages). Results of pseudo-static analysis of Pacoima Dam using a 1g ground acceleration in the downstream direction: compressive stresses (shaded, amplitude given in MPa to one decimal place), joint openings (unshaded, amplitude given in cm to two decimal places), and deformed shape (dashed line).

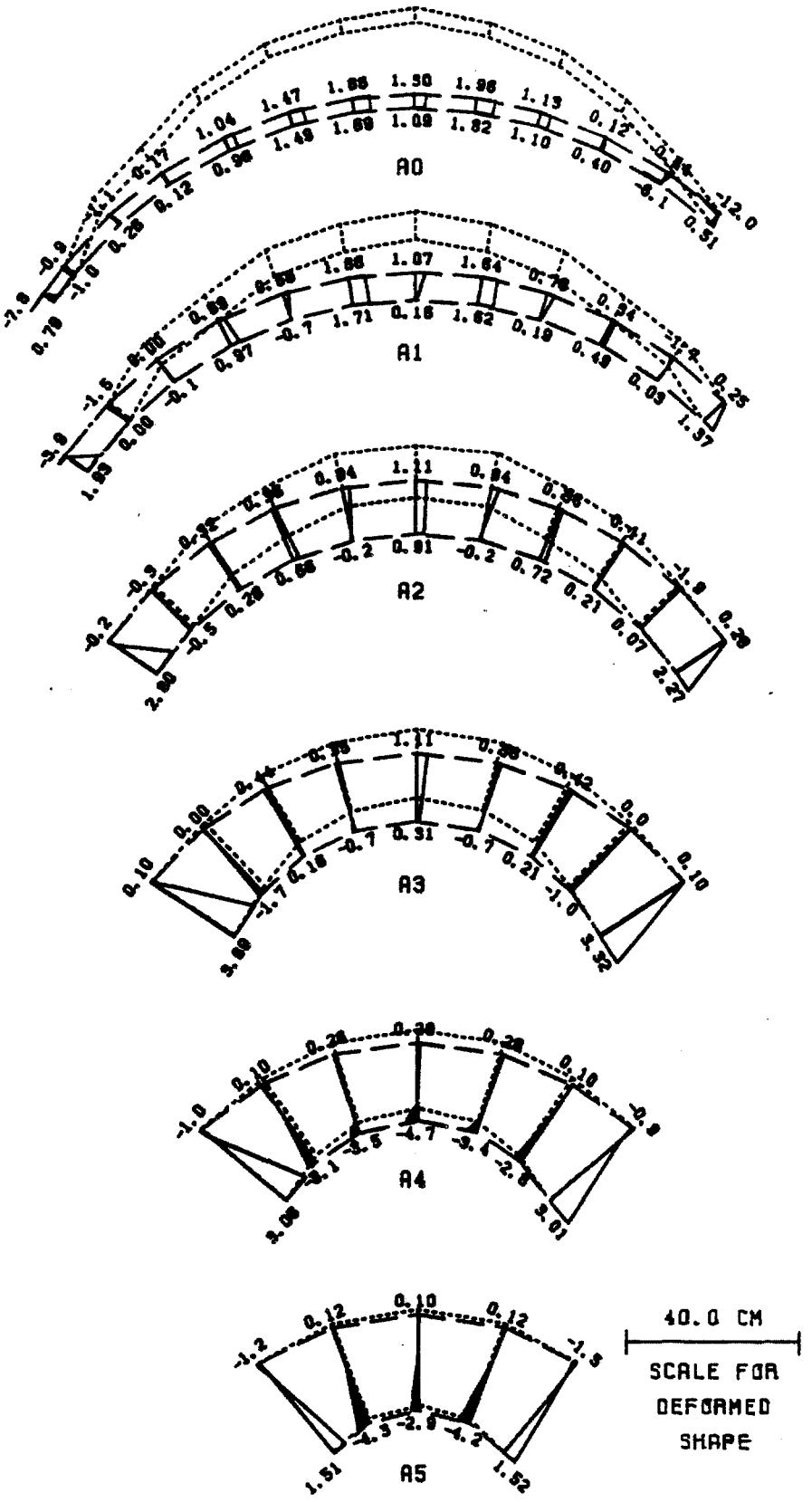

Figure 5.16a. Pseudo-static test. Arches A0 to A5.

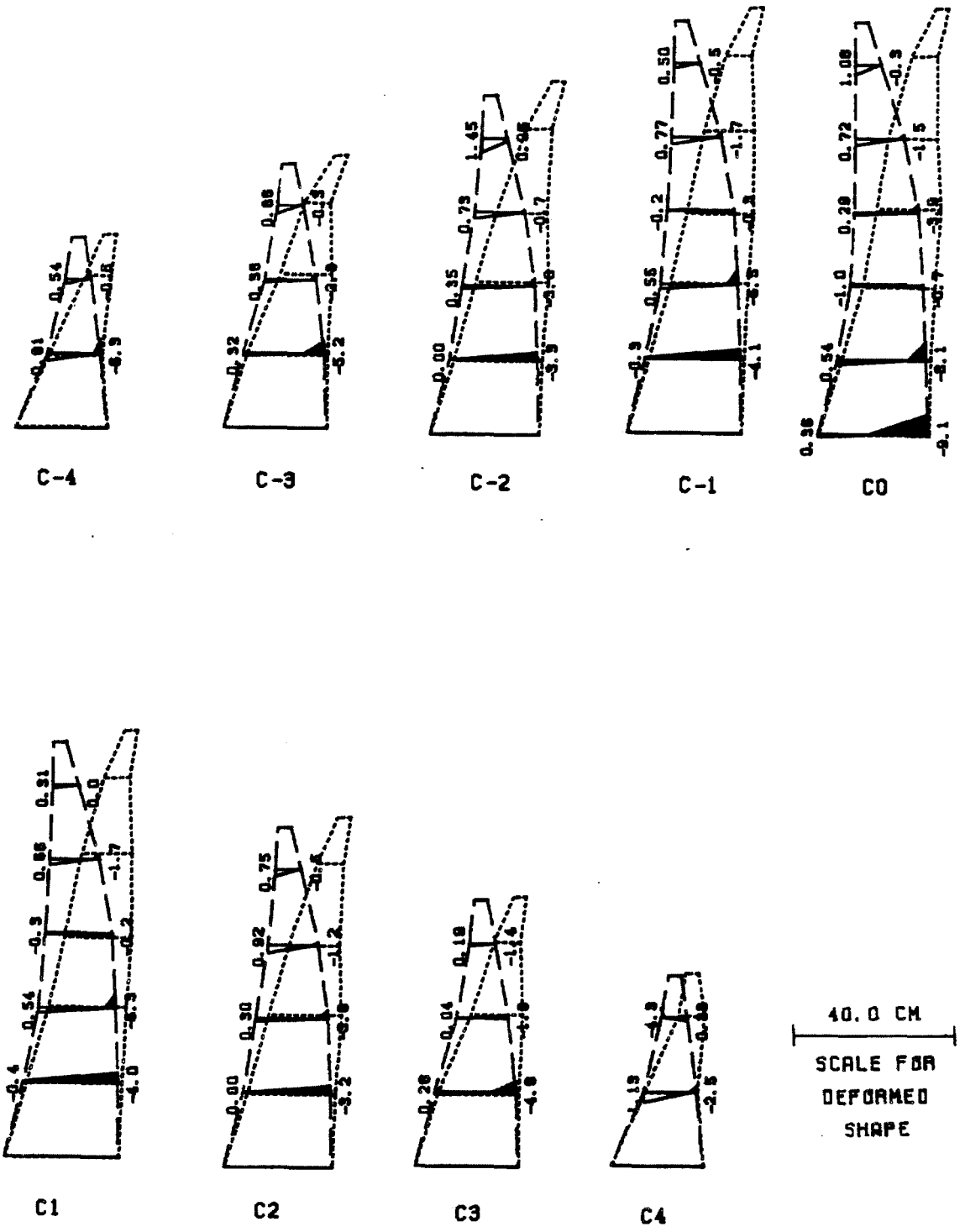

Figure 5.16b. Pseudo-static test. Cantilevers C−4 to C4.

CHAPTER VI
SUMMARY AND CONCLUSIONS

6.1 Summary

In this dissertation, the nonlinear response of jointed concrete arch dams to earthquake excitation is examined. The development of a two-dof nonlinear spring element to model the gradual opening and closing of joints in two-dimensional slabs and arches is first outlined. To demonstrate the accuracy and efficiency of this equivalent joint element, the results of static and dynamic analysis of a two dimensional arch, in one case modeled with slab finite elements connected by these joint elements, and in the other case modeled by a fine discretization through the depth of plane finite elements and joint springs, are compared. Further, an extensive analysis of the arch structure, using the slab element-equivalent joint element discretization, is carried out by subjecting the arch to a series of successively stronger ground motions in order to observe the increasing amout of joint opening which occurs and its effect on the dynamic response of the arch. Thereafter, the generalization of the two-dimensional joint element for use in a three-dimensional arch dam model is described, together with the treatment of some important features of the analysis, namely foundation-structure interaction, fluid-structure interaction and dead load application. Lastly, all these features are incorporated into a series of three-dimensional linear and nonlinear analyses of Pacoima Dam in which the dam-foundation-water system (full reservoir and partially full reservoir) is subjected to ground motions of various intensities.

6.2 Conclusions

The results of Chapter III show that the equivalent joint element, whose development is outlined in Chapter II, is capable of modeling with a reasonable degree of accuracy the gradual opening and closing mechanism of a two-dimensional interface joint. Further, the results show that the opening and closing of joints in a

two-dimensional arch has a significant effect on the dynamic response.

As shown in Chapter V, inclusion of a massless foundation region and an incompressible water domain can be accomplished efficiently and accurately for a three-dimensional arch dam by condensing out all dof not connected to the dam and then localizing the condensed matrices. However, there are still errors incurred from omitting foundation mass and water compressibility. Those arising from omitting foundation mass are thought to be tolerable, while water compressibility effects may be important in some cases. However, inclusion of water compressibility can only be accomplished with a great increase in computational effort.

Because of the dependence of the nonlinear dynamic response on the initial static solution, it is necessary to apply the dead weight of the dam in a more realistic manner than instantaneously to the continuous and completely finished structure. Simulation of the construction process considerably reduces the dead weight stresses in the upper part of the dam, especially near the abutments, and should have an important effect on the computed dynamic openings of the contraction joints.

The results of the dynamic analysis of Pacoima Dam in Chapter V show that, for moderate to severe ground shaking, several nonlinear phenomena are present with varying degrees of importance. Of these, the most important is the opening of the upper portions of the vertical contraction joints and dam-foundation interface joints. Opening and separation of these joints occurs even at moderate levels of excitation, even if the joints are grouted, and significantly affects the dam's response. The separations would most certainly be accompanied by appreciable joint slip, an effect not considered here, since typical shear keys have beveled geometries. The effect of the no-slip constraint is presently unknown. Slip in the contraction joints could be approximately included with the addition of perhaps three more relative dof per node. Although this would double the computational effort, it would greatly improve the validity of the analysis procedure.

Another important nonlinearity revealed in the analysis of Pacoima Dam, which is partly induced by the loss of arch stiffness, is cracking in the cantilevers. In addition, the analysis with full reservoir and intense ground motion predicts significant

lift-offs in the cracking planes, which, once again, violate the no-slip constraint. Generalization of the analysis technique to include slip in both the horizontal cracking planes and vertical contraction joints appears to be very difficult. The level of excitation, with full reservoir, which produces significant lift-offs in the cantilever cracking planes also results in compressive stresses in the nonlinear range. Nonlinear behavior in compression is another feature which appears to be very difficult to incorporate in the present scheme. Thus, the present analytical technique, generalized to include slip in the contraction joints, will have a legitimate range of applicability, but may be unable to model a dam subjected to intense ground motions under the full reservoir condition. On the other hand, the prediction of significant lift-offs in the cantilever cracking planes and compressive stresses in the nonlinear range may indicate that remedial action need be taken.

One way to extend the valid range of the analysis technique is to relieve some of the assumptions which may have increased the response level, i.e., no structural damping associated with the joints and uniform free-field ground motions. Structural damping in the joints involves inelastic impacts and friction. A procedure for inclusion of inelastic impacts is not clear at the present time due to the gradual nature of the impacts which arises from the varying contact area. Regarding friction, a mechanism could be incorporated in new provisions for slip in the contraction joints. Relieving the assumption of uniform free-field ground motions could not make use of the common pseudo-static and dynamic decomposition for nonuniform excitations because of the presence of nonlinearities, and the best procedure is not evident at present.

The importance of water cavitation was not indicated by the analyses performed as the negative excursions of water pressure were few in number and small in amplitude. However, because water compressibility may significantly affect the dynamic water pressures, the importance of water cavitation should ideally be judged when water compressibility is included.

Incorporation of water intrusion into open joints and cracks is a difficult assignment that would involve considerable fluid mechanics. One simplistic approach

would be to modify the stiffnesses of the joint elements to reflect an internal pressure which has the same time variation as the computed external pressure. Such an approach would be conservative regarding the amount of water intrusion into a joint or crack, but unconservative regarding the higher pressures generated when the water is squeezed out.

Finally, a few comments are in order regarding implications of the present study on the safety of Pacoima Dam. Certainly, results of the attempt to reproduce the 1971 earthquake event with full reservoir show the dam to be severely stressed, and, even though the dam response may have been overestimated by assuming uniform ground motion and neglecting dissipation in the joints, it would be prudent to consider restrictions on the water level if a similar event were possible in the future. However, the earthquake with greatest potential to effect Pacoima Dam in the next hundred years, either a magnitude 8+ on the San Andreas Fault 32 km distant or a repeat of the 1971 event on an adjacent segment of the same fault 20 km away [6], may be less severe, although a longer duration for the San Andreas earthquake would be of concern. Ground motion time histories estimated to be characteristic of these events and intended to be used as input in analyses had maximum accelerations slightly exceeding 0.3g for both [6]. Linear analyses for these possible, future motions were carried out in reference 6, but no analyses have been performed here. An additional consideration is that Pacoima Dam is primarily a flood control structure, and the possibility of an earthquake occurring simultaneously with a high water level is small. Lastly, a concern over the stability of the rock mass on the left abutment (for which much remedial action has been taken) has not been addressed here.

REFERENCES

1. Hatano, T. and T. Nakagawa, *Seismic Analysis of Arch Dams - Coupled Vibrations of Dam Body and Reservoir Water*, Technical Report of the Central Research Institute of Electric Power Institute, Tokyo, November 1972.
2. Bathe, K.-J., E.L. Wilson and F.E. Peterson, *SAP IV: Structural Analysis Program for Static and Dynamic Response of Linear Systems*, Earthquake Engineering Research Center Report No. EERC 73-11, University of California, Berkeley, 1973.
3. Clough, R.W., J.M. Raphael and S. Mojtahedi, *ADAP- A Computer Program for Static and Dynamic Analysis of Arch Dams*, Earthquake Engineering Research Center Report No. EERC 73-14, University of California, Berkeley, 1973.
4. Priscu, R., et al., *New Aspects in the Earthquake Analysis of Arch Dams*, **Criteria and Assumptions for Numerical Analysis of Dams**, D.N. Naylor, et al., editor, Swansea, September 1975.
5. Fok, K.-L., J.F. Hall and A.K. Chopra, *EACD-3D: A Computer Program for Three-Dimensional Earthquake Analysis of Concrete Dams*, Earthquake Engineering Research Center Report No. UCB/EERC 86/09, University of California, Berkeley, July 1986.
6. International Engineering Company, Inc., *Pacoima Arch Dam, Investigation and Evaluation of Effects of San Fernando Earthquake*, Report to Los Angeles County Flood Control District, August 1972.
7. Lindvall, Richter and Associates, *Final Report for Investigation and Re-analysis of the Big Tujunga Dam*, Report to Los Angeles County Flood Control District, October 1975.
8. International Engineering Company, Inc., *Final Report on Investigation and Re-analysis of Santa Anita Dam*, Report to Los Angeles County Flood Control District, August 1977.
9. *Design and Analysis of Auburn Dam, Volume Four, Dynamic Studies*, U.S. Bureau of Reclamation, Denver, April 1978.
10. Dungar, R., *Aseismic Design Considerations for a Large Arch Dam*, **Dams and Earthquake**, Institution of Civil Engineers London, 1980.
11. Bowes, D.E., A.X. Sison and A.L. O'Neill, *Hazard Assessment of Arch Dam in a Seismic Zone*, **Journal of the Hydraulics Division**, ASCE, February 1981.
12. Kreuzer, H.L., *The Design of El Cajon: A Retrospective View*, **Water Power and Dam Construction**, October 1983.
13. Tarbox, G.S., K.J. Dreher and L.R. Carpenter, *Seismic Analysis of Concrete Dams*, **Proceedings of the 13th International Conference on Large Dams**, Question 51, New Delhi, 1979.
14. Kolgaard, E.B. and R.P. Sharma, *Seismic Stability Evaluation of Existing Concrete Dams*, Paper presented at the Evaluation of Dam Safety Conference, sponsored by the Engineering Foundation, 1976.

15. Clough, R.W., *Nonlinear Mechanisms in the Seismic Response of Arch Dams*, **Proceedings of the International Research Conference on Earthquake Engineering**, Skopje, 1980.

16. Herzog, M.A.M., *Failure Mechanisms in Dams Subject to Earthquakes*, **Water Power and Dam Construction**, August 1980.

17. Oberti, G. and E. Lauletta, *Structural Models for the Study of Dam Earthquake Resistance*, **Proceedings of the 9th International Conference on Large Dams**, Question 35, Istanbul, 1967.

18. Gutidze, P.A., *Model Investigations of Seismic Action on the Concrete Arch Dam of the Inguri Hydroelectric Station*, **Gidrotekhnicheskoe Stroitel'stvo**, No. 11, November 1985.

19. Dungar, R. and R.T. Severn, *A Resume of Experience Gained in the Static and Dynamic Analysis of Arch Dams*, **Criteria and Assumptions for Numerical Analysis of Dams**, D.N. Naylor, et al., editor, Swansea, September 1975.

20. Pal, N., *Seismic Cracking of Concrete Gravity Dams*, **Journal of the Structural Division**, ASCE, September 1976.

21. Zienkiewicz, O.C., et al., *Computational Models for the Transient Dynamic Analysis of Concrete Dams*, **Dams and Earthquake**, Institution of Civil Engineers, London, 1980.

22. Hamon, M., P. Pouyet and A. Carrere, *Three Dimensional Finite Element Analysis of the Laparan Dam*, **Water Power and Dam Construction**, August 1983.

23. Norman, C.D. and F.A. Anderson, *Reanalysis of Cracking In Large Concrete Dams in the U.S. Army Corps of Engineers* , **Proceedings of the 15th International Conference on Large Dams**, Question 57, Lausanne, 1985.

24. Croucamp, W.S. and C. Grobbelaar, *The Three-Dimensional Evaluation of the Effects of Structural Discontinuities in an Arch Dam and a Multiple Dome Dam*, **Criteria and Assumptions for Numerical Analysis of Dams**, D.N. Naylor, et al., editor, Swansea, September 1975.

25. Ricketts, R.E. and O.C. Zienkiewicz, *Preformed 'Cracks' and their Influence on Behavior of Concrete Dams*, **Criteria and Assumptions for Numerical Analysis of Dams**, D.N. Naylor, et al., editor, Swansea, September 1975.

26. Row, D. and V. Schricker, *Seismic Analysis of Structures with Localized Nonlinearities*, **Proceedings of the 8th World Conference on Earthquake Engineering**, San Francisco, 1984.

27. O' Connor, J.P.F., *The Finite Element Analysis of Arch Dams in Wide Valleys Including the Effect of Crack Formation at the Concrete-Rock Interface*, **Proceedings of the Institution of Civil Engineering**, Part 2, September 1985.

28. O' Connor, J.P.F., *The Modeling of Cracks, Potential Crack Surfaces and Construction Joints in Arch Dams by Curved Surface Interface Elements*, **Proceedings of the 15th International Conference on Large Dams**, Lausanne, 1985.

29. Goodman, R.E., R.L. Taylor and T.L. Brekke, *A Model for the Mechanics of Jointed Rock*, **Journal of the Soil Mechanics and Foundations Division**, ASCE, May 1968.

30. Ghaboussi, J., E.L. Wilson and J. Isenberg, *Finite Element for Rock Joints and Interfaces*, **Journal of the Soil Mechanics and Foundations Division**, ASCE, October 1973.

31. Strikerud, P.E. and H. Bachmann, *Discrete Crack Modeling for Dynamically Loaded, Unreinforced Concrete Structures*, **Earthquake Engineering and Structural Dynamics**, Vol. 14, No. 2, March–April 1986.

32. Kuo, J. S.-H., *Joint-Opening Nonlinear Mechanism: Interface Smeared Crack Model*, Earthquake Engineering Research Center Report No. UCB/EERC 82/10, University of California, Berkeley, August 1982.

33. Graves, R., *Improved Interface Smeared Crack Model for Concrete*, U.S. Military Academy, West Point, 1986.

34. Aldstead, E. and P.G. Bergan, *Nonlinear Time-Dependent Concrete-Frame Analysis*, **Journal of the Structural Division**, ASCE, July 1978.

35. Hall, J. F. and M.J. Dowling, *Response of Jointed Arches to Earthquake Excitation*, **Earthquake Engineering and Structural Dynamics**, Vol. 13, No. 6, November–December 1985.

36. Niwa, A. and R.W. Clough, *Nonlinear Seismic Response of Arch Dams*, **Earthquake Engineering and Structural Dynamics**, Vol. 10, No. 2, March–April 1982.

37. Bathe, K.-J., **Finite Element Procedures in Engineering Analysis**, Prentice-Hall, 1982.

38. Hughes, T.J.R., **The Finite Element Method**, Prentice-Hall, 1987.

39. Adams, D.D. and W.L. Wood, *Comparison of Hilber-Hughes-Taylor and Bossak 'α–Methods' for the Numerical Integration of Vibration Equations*, **International Journal for Numerical Methods in Engineering**, Vol. 19, No. 5, 1983.

40. Clough, R.W. and J. Penzien, **Dynamics of Structures**, McGraw-Hill, New York, 1975.

41. Hall, J.F. and M.J. Dowling, *Analysis of the Nonlinear Seismic Response of Arch Dams*, **Proceedings of China–U.S. Workshop on Earthquake Behavior of Arch Dams**, Beijing, China, June 1987.

42. Clough, R.W., K.-T. Chang, et al., *Dynamic Response Behavior of Xiang Hong Dian Dam*, Earthquake Engineering Research Center Report No. UCB/EERC 84/02, University of California, Berkeley, April 1984.

43. Clough, R.W., K.-T. Chang, et al., *Dynamic Response Behavior of Quan Shui Dam*, Earthquake Engineering Research Center Report No. UCB/EERC 84/20, University of California, Berkeley, November 1984.

44. Fok, K.-L., and A.K. Chopra, *Earthquake Analysis and Response of Concrete Arch Dams*, Earthquake Engineering Research Center Report No. UCB/EERC 85/07, University of California, Berkeley, June 1985.

45. Duron, Z.H., *Experimental and Finite Element Study of a Large Dam*, Earthquake Engineering Research Laboratory Report No. EERL 87-02, Caltech, Pasadena, 1987.

46. Kuo, J. S.-H., *Fluid-Structure Interactions: Added Mass Computations for Incompressible Fluid*, Earthquake Engineering Research Center Report No. UCB/EERC 82/09, University of California, Berkeley, August 1982.

47. Zienkiewicz, O. C., **The Finite Element Method**, 3rd edition, McGraw-Hill Book Company, 1977.

48. Hall, J.F. and A.K. Chopra, *Dynamic Response of Embankment, Concrete-Gravity and Arch Dams Including Hydrodynamic Interaction*, Earthquake Engineering Research Center Report No. UCB/EERC 80/39, University of California, Berkeley, October 1980.

49. Priscu, R., D. Stematiu, L. Ilie and A. Popovici, *Critical Considerations on Arch Dam Mathematical Models*, **Criteria and Assumptions for Numerical Analysis of Dams**, D.N. Naylor, et al., editor, Swansea, September 1975.

50. Fitzpatrick M.D. and S. Giudici, *Gravity Loading of a Double Curvature Arch Dam*, **Criteria and Assumptions for Numerical Analysis of Dams**, D.N. Naylor, et al., editor, Swansea, September 1975.

51. Housner, G.W. and P.C. Jennings, *The San Fernando California Earthquake*, **Earthquake Engineering and Structural Dynamics**, Vol. 1, No. 1, July–September 1972.

52. Woodward-Lundgren and Associates, *Pacoima Dam, Determination of Rock In Situ Dynamic Elastic Foundation Properties*, Report to International Engineering Company, Inc., 1971.

53. *Design of Large Dams*, U.S. Bureau of Reclamation, Denver, 1977.

54. Reimer, R. B., *Deconvolution of Seismic Response for Linear Systems*, Earthquake Engineering Research Center Report No. EERC 73-10, University of California, Berkeley, 1973.

55. ANCO Engineers, Inc., *Dynamic Testing of Concrete Dams*, Report to National Science Foundation, June 1982.

56. Hall, J.F, and P.S. Nowak, *Effects of Nonuniform Seismic Input on Arch Dam Response*, paper submitted to the 9th World Conference on Earthquake Engineering, Tokyo, 1988.